UNIVERSITÉ DE STRASBOURG

Ecole Doctorale de Physique et Chimie Physique
Institut Pluridisciplinaire Hubert Curien (IPHC), UMR 7178

THÈSE présentée par:

Pathiranage Shamilka Deshan Sandanayake
soutenue le : **18 October 2024**

pour obtenir le grade de: **Docteur de l'Université de Strasbourg**
Discipline/ Spécialité: **Physique des Particules**

The Top Tracker of the JUNO neutrino experiment: Mitigating atmospheric muon-induced backgrounds

THÈSE dirigée par:
Dr. Marcos DRACOS   Institut Pluridisciplinaire Hubert Curien

RAPPORTEURS:
Dr. Dominique DUCHESNEAU   Laboratoire d'Annecy de Physique des Particules
Dr. Margherita BUIZZA AVANZINI   Laboratoire Leprince-Ringuet

PRESIDENT:
Dr. Boris HIPPOLYTE   Institut Pluridisciplinaire Hubert Curien

"In the beginning was the Word,
and the Word was with God, and the Word was God. He was in the beginning with God.
All things were made through Him, and without Him nothing was made that was made.
In Him was life, and the life was the light of men.
And the light shines in the darkness, and the darkness did not comprehend it."

– John 1:1-5, the Holy Bible (New King James Version) –

"Qu'est-ce donc que nous crie cette avidité et cette impuissance, sinon qu'il y a eu autrefois
dans l'homme un véritable bonheur, dont il ne lui reste maintenant que la marque et la trace
toute vide, et qu'il essaie inutilement de remplir de tout ce qui l'environne, recherchant
dans les choses absentes le secours qu'il n'obtient pas des présentes, mais qui en sont toutes
incapables, parce que ce gouffre infini ne peut être rempli que par un objet infini et
immuable, c'est-à-dire que par Dieu lui même."

– Blaise Pascal (1623-1662), Pensée 138 –

Dedication

To my dearest wife, Nayomi,
For being the calm in the storm of my thoughts,
the light in the dark hours of doubt,
and the joy when the path grew rough.

You endured the late nights, the scattered ideas,
and at times, this absent-minded, overworked Ph.D. mess.
Your laughter made this rugged journey a thousand times lighter,
and your comforting presence, a million times sweeter.

ACKNOWLEDGEMENTS

As I look back at my journey as a doctoral researcher, I see not just an achievement, a title, or a certification. I view it as a transformative experience–one that has shaped my ability to think critically, persevere in the face of challenges, and continuously learn.

In this spirit of reflection, my heart is filled with gratitude, and it is only fitting to begin by acknowledging the One who guided me through every phase of this path–God. It is to Him that I owe my deepest gratitude, for being my rock and my source of strength.

No journey of this magnitude is completed alone. I am but one thread in a rich tapestry woven by the contributions of many compassionate hearts and supportive souls. This work would not exist without them. I am extremely grateful to my lovely wife, Nayomi, for your countless sacrifices along the way. In a land far from home, away from comfort, you have bravely accompanied me in this quest. I am forever indebted to you for your sweet love that never ran out on me, your limitless patience that never gave up on me, and the endless joy that you brought to me, day after day. I am filled with deep gratitude for our loving parents, Nimal Sandanayake, Beatrice Kusumalatha, Roger Rozairo and Rosi Perera for their unshaken support through constant prayers, well wishes, as well as through precious words of consolation and encouragement.

When I first set foot in Strasbourg, I was a stranger, far from the comfort of home and the embrace of those I held dear. Yet, by God's grace, I found a place of belonging in the Trinity International Church of Strasbourg (TICOS). They welcomed me with open arms, in the name of Jesus, and became my family away from family–a source of warmth, fellowship, and spiritual support during this chapter of my life. I am thankful to every TICOS family member from all around the globe for your prayers, encouragement, and the warmth of your embrace.

I am profoundly grateful for the invaluable opportunity to pursue a 2-year Master's degree in Physics, fully funded by the prestigious Quantum Sciences and Nanomaterials (QMat) scholarship from the QMat International Graduate School of the Université de Strasbourg. Without this invaluable assistance which paved my way towards doctoral research, none of this would have been possible. My sincere thanks to all the teachers who taught me during my Master's degrees for their dedicated efforts towards my inspiration to pursue higher studies.

I would also like to take this opportunity to express my sincere gratitude to my supervisor, Marcos Dracos. Your broad expertise, vast experience and boundless enthusiasm has left a profound impact on me. Your insight broadened my perspective, your wisdom guided me through challenges, and your passion ignited a deeper drive within me to push boundaries. João Pedro Athayde Marcos de André, you have been a constant source of wisdom and counsel guiding me forward. Your rigour, availability, and attention to detail has constantly motivated me to push myself to pursue the best version of me. Through countless discussions you have clarified many of my doubts, developing in me a broader understanding and a deeper appreciation of scientific research. I am sincerely thankful to you for all of that. I owe my gratitude to current as well as former members of IPHC Neutrino group who has

CONTENTS

Introduction

The neutrino is one of the most intriguing and mysterious particles in the universe. A fundamental component of the Standard Model of particle physics, neutrinos are electrically neutral, massless, and interact with matter so weakly that they are notoriously almost impossible to detect. Yet, despite their elusiveness, neutrinos are extraordinarily abundant. Trillions of these ghostly particles pass through every square centimetre of our bodies every second, a constant, invisible flux that permeates the entire cosmos. This sheer abundance of neutrinos underscores their profound significance in the universe, shaping everything from the fusion reactions that power stars to the evolution of the universe itself.

The history of neutrino physics showcases the determination of scientists to unravel these elusive particles. Wolfgang Pauli proposed the neutrino in 1930 to explain energy conservation in nuclear β-decay. In 1934, Enrico Fermi developed the first theoretical framework for β-decay [1], naming the particle "neutrino" and establishing the basis for weak interaction theory. Despite predictions by physicists like Hans Bethe and Rudolf Peierls that neutrino detection would be nearly impossible [2], Clyde Cowan and Frederick Reines successfully detected neutrinos from a nuclear reactor [3] for the first time ever in 1956, a breakthrough that earned Reines the Nobel Prize in 1995. The Homestake experiment [4], led by Raymond Davis Jr. in the 1960s, first detected solar neutrinos, revealing a deficit that became known as the solar neutrino problem. In the late 1980s and early 1990s, the Kamiokande experiment [5] observed a deficit of atmospheric neutrinos, termed the atmospheric neutrino anomaly. These anomalies could not be explained by detector inaccuracies or theoretical errors but pointed to an unaccounted physical phenomenon–neutrino flavour oscillations. The theoretical framework for neutrino flavour oscillations had been developed earlier by Ziro Maki, Masami Nakagawa, and Shoichi Sakata [6] in 1962, followed by Bruno Pontecorvo [7] in 1968. In 1998, the Super-Kamiokande (SK) [8] experiment provided strong evidence for neutrino oscillations, showing that the atmospheric neutrino deficit is consistent with this phenomenon [9]. In 2000, by detecting solar neutrinos through different interaction channels, the Sudbury Neutrino Observatory (SNO) [10] experiment demonstrated that the apparent solar neutrino deficit was also due to neutrino oscillations [11]. These discoveries opened new research avenues and led the respective leaders of SK and SNO, Takaaki Kajita and Arthur B. McDonald, being awarded the 2015 Nobel Prize in Physics "for the discovery of neutrino oscillations, which shows that neutrinos have mass".

Despite significant progress in neutrino physics, several key questions remain unresolved. One of the most pressing is the neutrino mass ordering, which seeks to determine which neutrino mass state is the heaviest. Resolving it is vital for understanding neutrino properties with significant implications for particle physics and cosmology. The absolute mass scale of neutrinos remains unknown and could reveal new physics beyond the Standard Model. Additionally, determining whether neutrino oscillations violate $\mathcal{CP}$ symmetry could explain the matter-antimatter asymmetry in the universe. Whether neutrinos are Majorana particles–meaning they are their own antiparticles–also remains unresolved, with profound implications for mass generation and lepton number violation. Neutrinos' role in astrophysical processes, such as supernovae and the early universe formation, is another active area of research. Solving these mysteries could unlock fundamental insights into the universe.

Chapter 1 reviews theoretical and experimental progress toward understanding neutrinos and their flavour oscillations.

Located deep underground in China, the Jiangmen Underground Neutrino Observatory (JUNO) [12, 13] is an upcoming multi-purpose 20 kt liquid scintillator experiment designed to meet a baseline energy resolution requirement of 3% at 1 MeV. JUNO aims to determine the neutrino mass ordering with 3σ significance over 6 years of operation by precisely measuring the oscillation patterns of reactor antineutrinos. JUNO's Central Detector [14], which holds the liquid scintillator, serves as the neutrino target. It is encircled by a cylindrical pool filled with ultrapure water that serves as a Water Čerenkov detector [15], with a high-precision muon tracker, the Top Tracker (TT), positioned above it [16]. Together, the TT and the Water Cherenkov detector form the muon veto system. JUNO's findings could provide crucial insights into neutrino oscillations and enhance our understanding of neutrino physics, with the potential to influence future experiments and theoretical models in particle physics and cosmology. Chapter 2 provides a detailed overview of the JUNO detector's design and its associated physics program.

This doctoral research focuses on the JUNO TT, a 3-layer array of plastic scintillator strips re-purposed from the OPERA Target Tracker [17]. A detailed introduction to the TT is presented in the chapter 2. The TT tracks atmospheric muon flux at the JUNO site, which aids the mitigation of muon-induced backgrounds. Scintillation from muons traversing the TT scintillator strips is collected by wavelength-shifting fibres and transmitted to photomultiplier tubes. The ensuing signal from the photomultipliers is digitized by front-end electronics boards (FEB). The TT FEBs were individually validated and graded through multiple characterization tests. A prototype of the TT was constructed at IPHC Strasbourg using suboptimal OPERA strips, serving as a demonstrator and validating the electronics under realistic conditions. Signal attenuation through the fibres was estimated using muon flux measurements from this prototype. Chapter 3 details the FEB and fibre validation results. The concentrator boards in the TT handle data aggregation, x-y coincidence selection, and event timestamping. Chapter 4 describes the rigorous tests conducted to validate the performance of these concentrator boards during their development and production.

The final objective of the doctoral research was concerned with the estimation of background due to atmospheric muon-induced ^{9}Li/^{8}He using the TT. The ^{9}Li/^{8}He decays in the JUNO detector imitates the signal due to reactor antineutrinos, posing a serious threat to JUNO's physics program. Hence, a precise validation of the ^{9}Li/^{8}He background is crucial for the success of JUNO's primary mission. Using a dataset simulated and reconstructed using the JUNO official simulation and reconstruction software [18], a data-driven template to estimate the ^{9}Li/^{8}He background to the JUNO antineutrino spectrum is presented. Furthermore, the impact of the ^{9}Li/^{8}He background uncertainty on the JUNO neutrino mass ordering sensitivity was also explored. The respective results are presented in detail under chapter 5.

The work presented in this thesis, through the meticulous testing, calibration, and validation of the Top Tracker's electronics, along with the data-driven estimation of atmospheric muon-induced backgrounds, contributes directly to JUNO's readiness to achieve its major scientific goals. By ensuring the Top Tracker's optimal operation, this research not only supports JUNO's primary mission but also sets the stage for future discoveries that could reshape our understanding of particle physics as well as other branches of physics.

Part I

State-of-the-art

CHAPTER 1

PHYSICS OF THE NEUTRINO

1.1 The Standard Model

Throughout recorded history, humanity has been perpetually motivated by an insatiable curiosity to understand the essential constituents of the universe and the forces that govern its existence. Over decades of rigorous experimental validations as well as meticulous theoretical progress, scientists have achieved an elusive quantum field theory that combines quantum mechanics and special relativity, known as the Standard Model of particle physics. It provides a comprehensive depiction of the interactions among fundamental particles, encompassing the electromagnetic, strong, and weak forces.

Figure 1.1 : *The table of elementary particles in the standard model. Adapted from [19].*

1.1.1 The classification of the fundamental particles

The table of elementary particles in the standard model is shown in figure 1.1. Fundamental particles can be categorized into two main groups: fermions and bosons. Fermions are half-integer spin particles which make up matter, obeying Fermi-Dirac statistics [20, 21] and the Pauli exclusion principle [22]. Bosons are integer spin particles which mediate interactions, obeying Bose-Einstein statistics [23, 24]. They consist of the gauge bosons of the electromagnetic, strong, and weak forces. Additionally, they include the scalar H boson, which provides a mechanism through which all particles gain mass, except neutrinos and photons.

While all the fermions can interact via the weak force, these particles can also be distinguished by their sensitivity to the electromagnetic force and the strong force. The fermions can be subdivided into two groups, namely quarks and leptons, based on whether they are sensitive to the strong force or not, respectively. Similarly, the quarks and leptons can be grouped further into two rows each, depending on their electric charge. The upper row of quarks, referred to as up-type quarks, carries an electric charge of $+\frac{2}{3}$, while the lower row, identified as down-type quarks, bears an electric charge of $-\frac{1}{3}$. Regarding the upper row of leptons, all three have an electric charge of -1. The lower row of leptons consists of electrically-neutral neutrinos that interact exclusively through the weak force. Each of these neutrinos is associated with the lepton flavour of its charged counterpart. The quarks and leptons can be categorized into three generations in the ascending order of masses of the quarks and the charged leptons, spanning from the 1st generation to the 3rd generation. The neutrinos are massless in the framework of the standard model [25], although experimental observations [9, 26] proved otherwise, as is presented under section 1.2. Although the exact mass of the neutrinos is yet unknown, experimental searches have constrained it to be on the sub-eV level [25], which is extremely light compared to other massive fundamental

particles. A discussion of neutrino masses is presented in section 1.1.4.

Charge conjugation ($\mathcal{C}$), Parity ($\mathcal{P}$), and Time reversal ($\mathcal{T}$) are fundamental symmetries of the standard model framework. $\mathcal{C}$ symmetry refers to whether the reversal of the discrete additive quantum numbers (such as electric charge, baryon number, lepton number, etc.) that describe the quantum state of a particle affects the physics of the system. Such a reversal of discrete additive quantum numbers of a particle yields what is known as its antiparticle state, which has the same mass as the respective particle. $\mathcal{P}$ symmetry deals with whether a system behaves differently under the inversion of spatial coordinates. A system is said to be symmetric under a $\mathcal{T}$ transformation if it is invariant under the reversal of the direction of time flow. Reversal of time also reverses the linear and angular momenta of a given system. The works of Julian Schwinger, Gerhart Lüders and Wolfgang Pauli showed that any Lorentz invariant local quantum field theory with a Hermitian Hamiltonian, such as the standard model of particle physics, must preserve $\mathcal{CPT}$ symmetry [27–29]. As a consequence, the application of the combined $\mathcal{CPT}$ operation on a particle state yields its corresponding antiparticle state, governed by the same physics laws as the particle state. Therefore, the picture of the table of the elementary particles broadens to include the antiparticles.

This thesis aims to discuss the physics of the neutrinos. Therefore, the details discussed under this section will be limited to the details of the Electroweak theory.

1.1.2 The Electroweak Theory

In 1930, Wolfgang Pauli introduced the idea that in nuclear β-decays, alongside the electron, a light neutral particle is emitted. Pauli suggested that this elusive particle, which later came to be known as the neutrino, carries away energy equivalent to the discrepancy between the observed energy of an electron and the maximum energy found in the continuous β-spectrum. This proposal aimed to uphold the energy conservation law in these processes. Incorporating the neutrino, Enrico Fermi published his theory of β-decay [1], laying the foundation for the theory of the weak interaction.

Electroweak unification and the spontaneous symmetry breaking

The theoretical studies of Sheldon Glashow, Abdus Salam, and John Clive Ward in 1959 aimed to generalize the U(1) gauge group of electromagnetic interaction [30, 31]. Steven Weinberg extended this work in 1967 to produce a unified description of electromagnetism and the weak force [32]. Mathematically, the unification of electromagnetism and weak interactions is expressed as a Yang-Mills field with an SU(2)×U(1) gauge group. Each gauge group gives rise to associated gauge bosons. There are 3 gauge bosons A^i such that $i = \{1, 2, 3\}$ with the SU(2) gauge group and a single gauge boson B with the U(1) gauge group. Under this formalism, the 4 bosons of the Electroweak model are massless, in contrary to what is physically observed. In 1964, three independent teams published somewhat related approaches to explain how mass could appear in gauge theories. These proposals were made by Robert Brout and François Englert [33], Peter Higgs [34] and Gerald Guralnik, Carl Richard Hagen, and Tom Kibble [35]. In order to generate mass, as well as
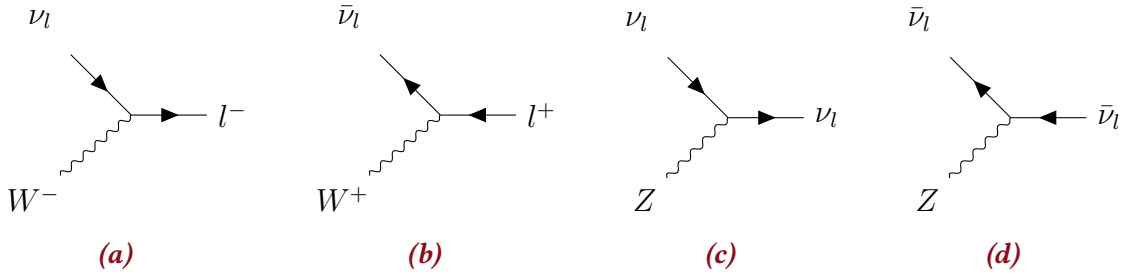
Figure 1.2 : *Standard neutrino interaction vertices for the CC interactions via the exchange of (a) W^-, and (b) W^+ bosons, and for NC interactions via the exchange of Z boson for (c) neutrinos, and (d) antineutrinos.*

the $U(1)_{em}$ gauge group of electromagnetism through spontaneous symmetry breaking, a complex scalar doublet

$$\phi = \begin{pmatrix} \phi^+ \\ \phi^0 \end{pmatrix} \tag{1.1}$$

is introduced to the model. This mechanism results in the mixing of the A^i and B boson fields to produce the massive $W^\pm$, Z bosons and the massless γ boson. Moreover, ϕ simplifies to a single neutral scalar field denoted as ϕ^0, known as the Brout-Englert-Guralnik-Hagen-Higgs-Kibble field, commonly referred to as the Higgs field. This field corresponds to its associated scalar particle, the H boson.

Charged current and Neutral current interactions

Weak interactions that occur through the exchange of W^+ or W^- as shown in figures 1.2a and 1.2b are known as a charged current (CC) weak interactions. In CC interactions, the quantum numbers of the original particles are subject to change, and involve a transmission of electric charge via the charged weak bosons. Since the $W^\pm$ bosons have charges of ± 1, to conserve electric charge, only the pairs of fermions that differ by one unit of electric charge are coupled via the CC interaction. In the case of the leptons, by definition, the CC interaction couples a charged lepton with its corresponding neutrino,

$$\begin{pmatrix} \nu_l \\ l^- \end{pmatrix}, \quad l = \{e, \mu, \tau\}. \tag{1.2}$$

Probing CC interactions involving neutrinos allow distinguishing between different neutrino flavours. For the quarks, CC interaction couples all possible combinations of pairs of quarks differing by a unit of charge,

$$\begin{pmatrix} q_u \\ q_d \end{pmatrix}, \quad q_u = \{u, c, t\}, \quad q_d = \{d, s, b\}. \tag{1.3}$$

The weak interactions mediated by Z bosons are known as neutral current (NC) weak interactions. NC interactions do not involve an exchange of electrical charges. Standard NC interaction vertices for neutrinos are shown in figures 1.2c and 1.2d. NC interactions
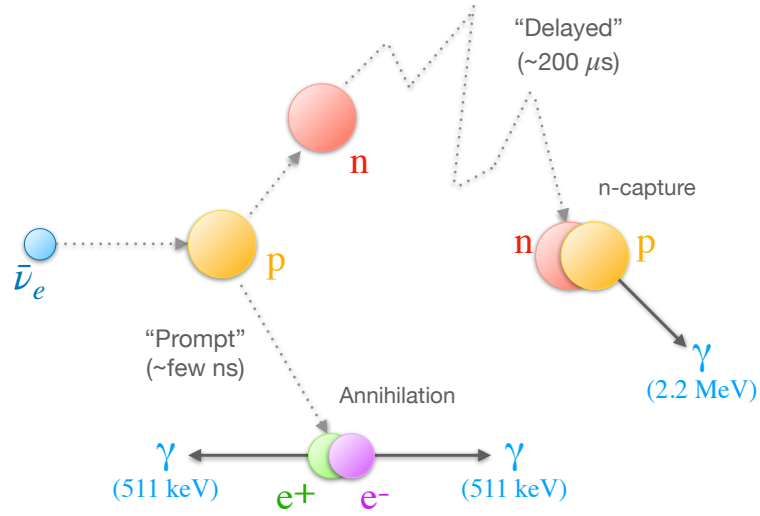
Figure 1.3 : *Illustration of the inverse β-decay, and the resulting prompt-delayed signals. The delayed signal illustrated here is the one relevant to JUNO.*

involving neutrinos do not allow distinguishing between different neutrino flavours.

In 1934, Hans Bethe and Rudolph Peierls estimated that the interaction cross section σ of the neutrino is such that $\sigma < 10^{-44}\text{cm}^{-2}$ [2]. As a result, for many years since then, the neutrino was considered an undetectable particle. In 1946, Bruno Pontecorvo put forward the possibility to detect neutrinos using the inverse β-decay process ($\bar{\nu}_e + p \rightarrow e^+ + n$) [36], illustrated in the figure 1.3. In 1956, Clyde Cowan and Frederick Reines set up an experiment that utilized the detection of reactor electron antineutrinos via the inverse β-decay process, experimentally confirming the existence of the neutrino [3].

Chiral structure of the weak interaction

Chirality is an inherent characteristic of fundamental particles. It can be understood along with helicity (h), which is the normalized projection of a particle's spin ($\vec{s}$) along its direction of momentum ($\vec{p}$), given by,

$$h = \frac{\vec{p} \cdot \vec{s}}{|\vec{p}|}. \tag{1.4}$$

At the ultra-relativistic limit, helicity and chirality can be considered equivalent. This is particularly applicable to neutrinos, given their exceptionally small masses compared to the other fundamental particles. Chirality originates from the representation theory of the Lorentz group, that describes the space-time. A particle can be either left-chiral (L) or right-chiral (R). The practical effect of chirality can be observed in how particles with different chiralities engage in CC weak interactions. Since $W^{\pm}$ only couples to left-chiral particles and right-chiral antiparticles, the CC interactions fully violate the $\mathcal{C}$ symmetry (particle $\leftrightarrow$ antiparticle) and $\mathcal{P}$ symmetry (left-chiral $\leftrightarrow$ right-chiral). The CC weak interaction only affects the left-chiral particles and right-chiral antiparticles. It does not affect

right-chiral particles or left-chiral antiparticles. In 1957, Maurice Goldhaber, Lee Grodzins and Andrew Sunyar experimentally concluded that the neutrino must be left-handed [37]. Therefore, we can interpret the left-chiral leptons as a SU(2) doublet and right-chiral leptons as a singlet of SU(2) as

$$\mathfrak{l}_L = \begin{pmatrix} \nu_l \\ l \end{pmatrix}_L, \quad \mathfrak{l}_R = \begin{pmatrix} l \end{pmatrix}_R. \tag{1.5}$$

The 3 lepton families appear to have identical properties as a result of gauge symmetry, and only differ among themselves by mass and the lepton flavour quantum number.

1.1.3 Fermion masses in the standard model

Let us consider a Dirac particle field $\psi = \psi_L + \psi_R$ and its corresponding antiparticle field $\bar{\psi}$. Attempting to generate fermion masses via the introduction of the term

$$-m\bar{\psi}\psi = -m(\bar{\psi}_R\psi_L + \bar{\psi}_L\psi_R) \tag{1.6}$$

in the Dirac Lagrangian of the standard model is not feasible, because it is not invariant under the SU(2)×U(1) gauge symmetry. It was discussed under section 1.1.2 that the spontaneous symmetry breaking induced by the Higgs mechanism on the SU(2)×U(1) gauge symmetry group generates the masses of the weak bosons. The same mechanism is responsible for the generation of fermion masses. Since the Higgs field $\phi \equiv \phi(x)$ is an SU(2) doublet, it transforms under an infinitesimal SU(2) gauge transformation as

$$\phi \longrightarrow \phi' = (I + ig_W\boldsymbol{\epsilon}(x) \cdot \mathbf{T})\phi \tag{1.7}$$

where I is the unit matrix, g_W is the weak coupling strength of the SU(2) gauge symmetry, $\mathbf{T} = \frac{1}{2}\boldsymbol{\sigma}$ are the 3 generators of the SU(2) gauge symmetry ($\boldsymbol{\sigma}$=Pauli matrices) and $\boldsymbol{\epsilon}(x)$ is an infinitesimal arbitrary function of x. The same transformation applies to $\mathfrak{l}_L$, the left-chiral lepton doublet. Therefore, the effect on $\bar{\mathfrak{l}}_L$ is

$$\bar{\mathfrak{l}}_L \longrightarrow \bar{\mathfrak{l}}'_L = \bar{\mathfrak{l}}_L(I - ig_W\boldsymbol{\epsilon}(x) \cdot \mathbf{T}). \tag{1.8}$$

As a result, the combination $\bar{\mathfrak{l}}_L\phi\mathfrak{l}_R$ (as well as its Hermitian conjugate $\bar{\mathfrak{l}}_R\phi^\dagger\mathfrak{l}_L$), with the right-chiral SU(2) singlet, is gauge invariant under SU(2) and U(1). This property can be exploited to introduce a SU(2)×U(1) invariant term of the form

$$\mathcal{L}_f = -g_f(\bar{\mathfrak{l}}_L\phi\mathfrak{l}_R + \bar{\mathfrak{l}}_R\phi^\dagger\mathfrak{l}_L) \tag{1.9}$$

to the standard model Lagrangian, where g_f is the Yukawa coupling of the fermion to the Higgs field. The spontaneous symmetry breaking, as was discussed under section 1.1.2, reduces $\phi(x)$ to

$$\phi(x) = \frac{1}{\sqrt{2}} \begin{pmatrix} 0 \\ v + h(x) \end{pmatrix} \tag{1.10}$$

where v is the vacuum expectation value of the Higgs field ($v = 246$ GeV) and $h(x)$ is the Higgs field. It is important to note that, as the upper component of $\phi(x)$ is null, all the

neutrino terms of the equation 1.9 disappear after the matrix multiplication, and only the terms for the charged leptons remain. As a result, a Lagrangian term of the form given in equation 1.9 cannot generate neutrino masses. By substituting equations 1.5 and 1.10 in equation 1.9 yields a Lagrangian term $\mathcal{L}_l$ for the leptons

$$\mathcal{L}_l = -\frac{g_l}{\sqrt{2}}(v + h)(\bar{l}_L l_R + \bar{l}_R l_L), \tag{1.11}$$

where g_l is the Yukawa coupling of the charged lepton to the Higgs field. Since the Higgs mechanism does not predict the Yukawa coupling constants for fermions, their values can be chosen based on the observed fermion masses, such that $g_f = \frac{\sqrt{2}m_f}{v}$. Therefore, replacing g_f and applying the property shown in equation 1.6, the equation 1.11 becomes

$$\mathcal{L}_l = -m_l \bar{l}l - \frac{m_l}{v}\bar{l}lh, \tag{1.12}$$

where m_l is the mass of the charged lepton. The first and the second term of equation 1.12 correspond to the coupling of the charged lepton to the Higgs field and the coupling between the charged lepton and the H boson itself, respectively. This indicates the coupling of the left-chiral and right-chiral massless charged lepton fields with the Higgs field to acquire mass. A similar mechanism yields the masses of the quarks. Notice that, since the neutrinos are only left-chiral in the standard model, a Lagrangian term for the neutrino masses in the form 1.11, vanishes. Therefore, the masses of the Dirac fermions can be explained as a consequence of the coupling of the Dirac fermions with the H boson and the Higgs field, except for the neutrinos. This suggests that the mechanism through which the neutrinos acquire mass might be different from the other fermions.

1.1.4 Neutrino mass

Prior to the late 1990s, various experiments hinted at potential irregularities in the interaction rates of atmospheric and solar neutrinos. A transformative shift in our knowledge of the nature of neutrinos occurred following the measurements that unveiled compelling experimental proof of neutrino flavour oscillations occurring across long distances [9, 26]. As will be discussed in more details under section 1.2, it indicated that the neutrino masses are not degenerate, and hence not all of them are null as was predicted by the standard model. Neutrino mass was the first discovery that signalled the existence of physics beyond the standard model.

Neutrino mass models

Several extensions to the Standard Model attempted to describe the neutrino mass. As was shown in equation 1.12, to produce a Dirac neutrino mass term, the standard model Lagrangian must include a coupling between left and right-chiral neutrino fields. One extension [38] suggests the introduction of a right-chiral neutrino field, which does not interact via the weak force, permitting the generation of Dirac mass to neutrinos, analogous
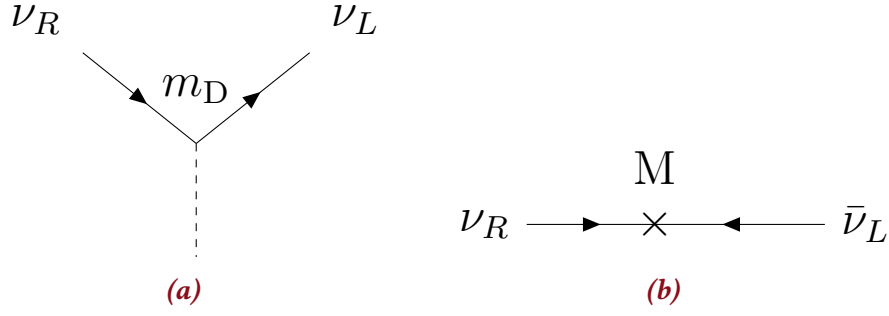
Figure 1.4 : *Feynman diagrams for (a) Dirac and (b) Majorana mass terms.*

to other leptons.

As the right-chiral neutrinos and left-chiral antineutrinos transform as singlets under Standard Model gauge transformations, any supplementary terms in the Lagrangian formed solely from these fields can be included without compromising the gauge invariance of the Standard Model. Therefore, a gauge-invariant mass term ($\mathcal{L}_M$) can be constructed using the right-chiral neutrino field ν_R such that

$$\mathcal{L}_M = -\frac{1}{2}M(\overline{\nu_R^c}\nu_R + \overline{\nu_R}\nu_R^c). \tag{1.13}$$

$\nu_R^c \equiv \hat{C}\hat{P}\nu_R$ represents the $\mathcal{CP}$-conjugate field of ν_R which corresponds to the left-chiral antineutrino field. M is known as Majorana mass, in honour of Ettore Majorana who proposed this mechanism in 1937 [39]. Such a Lagrangian term would indicate a direct coupling of a fermion and its corresponding anti-fermion, allowing particle$\leftrightarrow$antiparticle transitions. Although conservation of charge prohibits such an operation for charged fermions, the same does not apply for neutrinos which are neutral. Therefore, this formalism suggests that neutrinos can be their own antiparticle. Such particles are known as Majorana particles, opposed to Dirac particles, and the corresponding Feynman vertices are shown in figure 1.4. Further, a Dirac mass term can be constructed using the right-chiral neutrino singlet ν_R, left-chiral antineutrino singlet $\overline{\nu_L}$ and their corresponding $\mathcal{CP}$-conjugates, given by

$$\mathcal{L}_D = -\frac{1}{2}m_D(\overline{\nu_L}\nu_R + \overline{\nu_R^c}\nu_L^c) + h.c., \tag{1.14}$$

where m_D is the Dirac neutrino mass, and $h.c.$ stands for the corresponding Hermitian conjugate terms. A more general form of a Lagrangian term for the neutrino masses can be formed by including both the Dirac and Majorana components as

$$\mathcal{L}_{MD} = -\frac{1}{2}(m_D\overline{\nu_L}\nu_R + m_D\overline{\nu_R^c}\nu_L^c + M\overline{\nu_R^c}\nu_R) + h.c., \tag{1.15}$$

which yields the neutrino mass eigenvalues

$$m_\pm = \frac{M \pm M\sqrt{1 + \frac{4m_D^2}{M^2}}}{2}. \tag{1.16}$$

It follows from equation 1.16 that, if $M \gg m_D$, then

$$m_{\pm} \simeq \frac{1}{2}M \pm \frac{1}{2}\left(M + \frac{2m_D^2}{M}\right),$$

(1.17)

resulting in a heavy neutrino mass $m_+ \simeq M$ and a light neutrino mass $m_- \simeq \frac{m_D^2}{M}$. In this formalism, it is assumed that the Dirac mass term m_D for the neutrinos is comparable to that of other fermions (of the order of 1 MeV to about 100s of GeV). Then, by observing the light neutrino solution m_-, the corresponding Majorana mass term M has to be scaled up in order to yield a sub-eV mass for the neutrino as experimentally observed. This yields $M \sim 10^{11}$ GeV. Therefore, if a Majorana mass term exists, then the aforementioned mechanism called the see-saw mechanism, suggests that for every neutrino generation, there exists a left-chiral neutrino whose mass is much smaller than the standard model fermions, and a right-chiral neutrino which is much heavier than the standard model fermions. However, it is important to note that Majorana mass or the see-saw mechanism are still hypotheses, that require a solid experimental evidence to support their validity. One experimental technique to determine whether neutrinos are actually Majorana is to search for the phenomenon of neutrinoless double-beta ($\beta\beta 0\nu$) decays, as illustrated in figure 1.5a. This process is forbidden in the standard electroweak theory, as it violates the lepton number conservation.

(a)

(b)
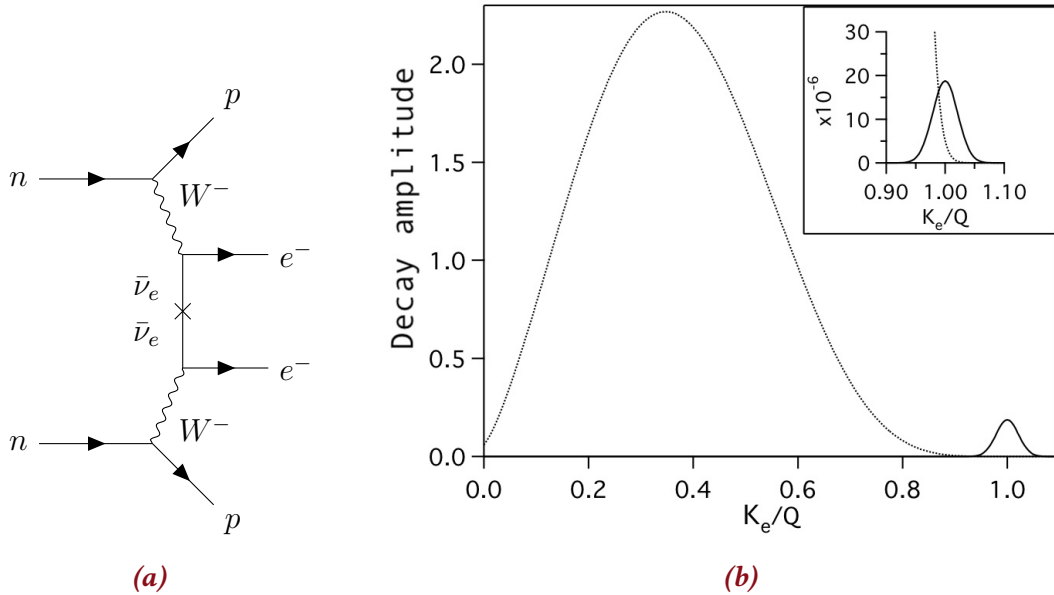
Figure 1.5 : *(a) Feynman diagram illustrating Neutrinoless double-beta decay interaction. Notice that the two antineutrinos produced in two different interactions annihilate each other because they are their own antiplarticles, assuming that they are Majorana. (b) The energy spectrum of the total kinetic energy of the emitted electrons (K_e) normalized to the endpoint energy (Q, equivalent to the mass difference between the parent and daughter nuclei). Neutrinoless double-beta decay yields a unique peak at 1 (also shown zoomed in the inset), whereas the double-beta decay involving the emission of 2 neutrinos yields a continuum as the neutrinos carry away a portion of the total energy. Adapted from [40].*

Neutrino mass measurements

Currently there are several techniques that can serve as pathways to measure the mass of the neutrino.

- **Neutrinoless double-beta decays**: Double-beta ($\beta\beta2\nu$) is rare allowed transition between two nuclei where 2 neutrons of the same nucleus undergo weak decay to protons, emitting 2 neutrons and 2 electron antineutrinos. The leading-order Feynman diagram for the $\beta\beta2\nu$ process is shown in figure 1.5a. The expected electron kinetic energy spectra for $\beta\beta2\nu$ and $\beta\beta0\nu$ are shown in figure 1.5b, assuming neutrinos are Majorana particles. The rate of $\beta\beta0\nu$ decay is proportional to the square of the effective Majorana mass $m_{ee} = |\sum_j U_{ej}^2 m_j|$. m_j is the mass of the jth neutrino mass eigenstate and U is the neutrino mixing matrix that describes the mixing between neutrino mass eigenstates and flavour eigenstates, which will be introduced in detail in section 1.2.3. The energy from electrons is measured with either ionization, scintillation, or through phonons. Among the experiments detecting ionization, ultrapure ^{76}Ge detectors such as GERDA-LEGEND [41] provide the best sensitivity thanks to high energy resolution and low background. To search for $\beta\beta0\nu$ decays via the detection of scintillation light, experiments such as KamLAND-Zen [42] and SNO+ [43] use liquid scintillator loaded with ^{136}Xe and ^{130}Te, respectively. EXO-200 [44] used a liquid Xenon time projection chamber to detect both ionization and scintillation. CUORE [45] uses a cryogenic TeO$_2$ bolometer to measure decay energy via detecting the heat generated by the ^{130}Te decay. AMoRE [46] deploys ^{100}Mo-enriched and ^{48}Ca-depleted CaMoO$_4$ crystals to simultaneously detect the scintillation and heat signals of ^{100}Mo decay. NEMO-3 [47] deploys a ^{100}Mo source hosted within a tracking detector and a calorimeter for a tracker-calorimeter technique. The best limit on m_{ee} at the time of writing this thesis comes from the KamLAND-Zen experiment, at m_{ee} < 28–122 meV (90%CL) [42].

- **Kinematics of weak decays**: A model-independent technique to determine neutrino mass can be developed by considering the energy-momentum conservation of weak decays involving a neutrino or an antineutrino. In 1934, Fermi proposed such a kinematic method to search for the mass of the neutrino by observing the tail-end of the β-decay spectrum of ^{3}H [1], as depicted in figure 1.6. Constructing on the experience of past experiments such as Mainz [48] and Troitsk [49], the KATRIN experiment has provided the most recent result that adopted this technique. So far, it has not excluded non-null neutrino masses, but imposes an upper limit $m_{\nu_e}^{eff}$ < 0.45 eV (95%CL) [50], where $m_{\nu_e}^{eff} = \sqrt{\sum_j |U_{ej}|^2 m_j^2}$. The ongoing KATRIN experiment estimates a neutrino mass sensitivity limit of ∼0.2 eV [51]. Concurrent experiments such as ECHo [52], HOLMES [53], and NuMECS [54] make complementary measurements to ^{3}H-based experiments. They all use an alternative isotope, ^{163}Ho, which decays by emitting a ν_e, as opposed to ^{3}H which decays by emitting a $\bar{\nu}_e$.

- **Cosmology**: The sum of all neutrino masses, Σm_j is measured by observing the size of cosmological fluctuations at different scales using cosmic microwave background and large-scale structure data. The shape of the cosmic microwave background spectrum is primarily influenced by the physical processes preceding the recombination phase
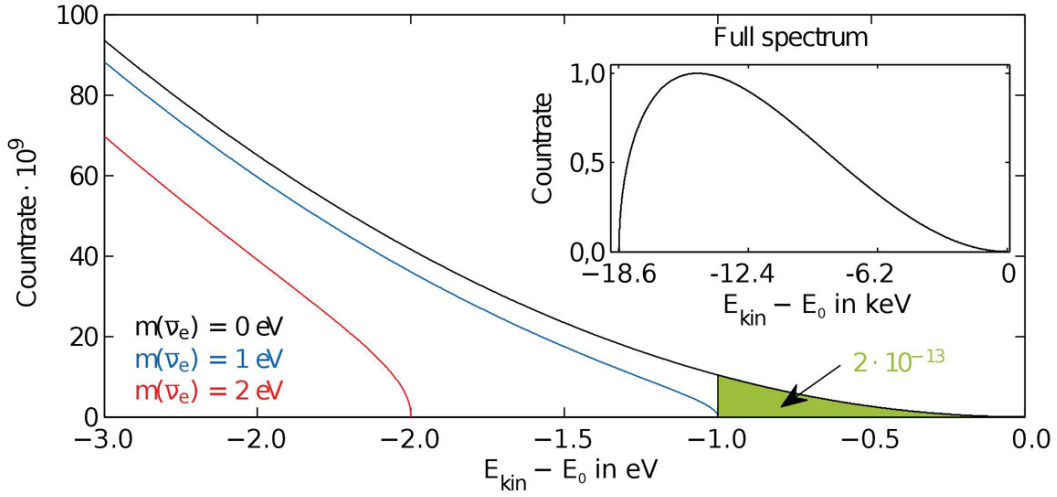
Figure 1.6 : *Emitted electron energy spectrum E_{kin} of β-decay of ^{3}H. E_0 is equal to the maximum electron kinetic energy, assuming neutrinos have no mass. Only a fraction of 2×10^{-13} events are expected to have an energy higher than $(E_0\text{-}1)$ eV. The curves shown in different blue and red indicate expected spectra if the neutrino mass is 1 eV or 2 eV, respectively. The inset shows the full spectrum [55].*

of evolution of the universe. Hence, the impact of neutrino mass may manifest through a modified background evolution and secondary anisotropy corrections. As a result, the shape of the matter power spectrum at small scales is sensitive to the sum of the neutrino masses. By combining the most recent Planck data [56] with the baryon acoustic oscillation data from the Dark Energy Spectroscopic Instrument [57], the strongest bound to date for the mass of the neutrino has been established at $\Sigma m_j <0.072$ eV (95% CL) [58].

While the most strict limit for the neutrino mass is deduced via cosmological constraints, it is currently not considered as the best limit due to its model dependency. Similarly, the limits posed by the $\beta\beta 0\nu$ decay experiments are also not quoted as the reference value for the mass of the neutrino, as these measurements follow from the assumption that the neutrino is a Majorana particle, which is not yet experimentally confirmed [25]. Hence, the upper limit for the neutrino mass determined by fitting the shape of the β-decay spectrum by the KATRIN experiment is considered the best accepted limit.

1.2 Neutrino Oscillations

In 1958, inspired by Gell-Mann and Pais' suggestion of the possibility of $K^0 \rightleftarrows \bar{K}^0$ [59], Bruno Pontecorvo introduced the possibility of $\nu \rightleftarrows \bar{\nu}$ [60]. The works of Ziro Maki, Masami Nakagawa and Shoichi Sakata in 1962 [6] followed by Pontecorvo in 1968 [7] laid the foundational work for a theory of neutrino flavour oscillations, introduced under section 1.2.3. The possibility for the neutrino to oscillate from one flavour to another implied that the neutrinos have non-degenerate masses.
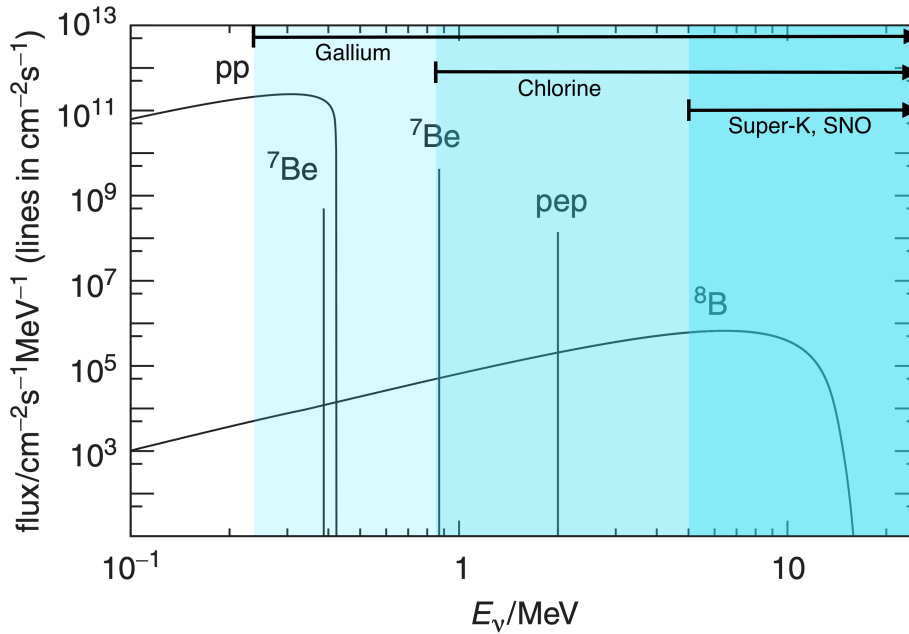
Figure 1.7 : *The flux of solar neutrinos from the main processes in the Sun. The horizontal arrows indicate the sensitive energy ranges for the Gallium, Chlorine and Kamiokande/SNO experiments. Adapted from [61].*

1.2.1 Solar neutrino deficit

The Sun, our radiant celestial neighbour, is the dominant source of neutrinos on Earth, showering us with an average neutrino flux of about $7 \times 10^{10}\ \nu \cdot \mathrm{cm}^{-2} \cdot \mathrm{s}^{-1}$ [25]. Under the immense temperature and pressure within the Sun's core, a number of nuclear fusion reactions burn hydrogen into helium, fuelling the Sun. The resulting solar neutrino energy spectrum is shown in figure 1.7. Although the neutrino interaction cross sections are extremely small and the Sun is located very far away from the Earth, solar neutrinos can be observed with a sufficiently massive detector.

In 1946, Bruno Pontecorvo proposed a radiochemical technique to experimentally detect the neutrino [36]. Based on Pontecorvo's proposal, in the 1960s, Ray Davis and John N. Bahcall designed the Homestake Experiment [4] to directly and quantitatively test the standard solar model [62] by measuring the solar neutrino flux. They placed a tank containing C_2Cl_4 deep underground in a mine. The solar neutrinos interact with ^{37}Cl via inverse β-decay process, producing ^{37}Ar. By bubbling He gas through the tank once every few weeks, they extracted the Ar gas that had formed. Then, the solar neutrino flux was calculated by counting the ^{37}Ar atoms that subsequently underwent radioactive decay. Only 1.7 interactions per day were expected. However, they measured only 0.48 ± 0.04 neutrinos per day [63]. Subsequent experiments such as SAGE [64] and GALLEX [65] too reported a deficit in the measured solar neutrino flux. This apparent deficit of solar neutrinos is famously known as the solar neutrino problem, that perplexed physicists for several decades.

The Sudbury Neutrino Observatory (SNO) [66] began operations in 1999 with the aim of measuring both the flux of solar electron neutrinos (ϕ_e) and the total solar neutrino flux
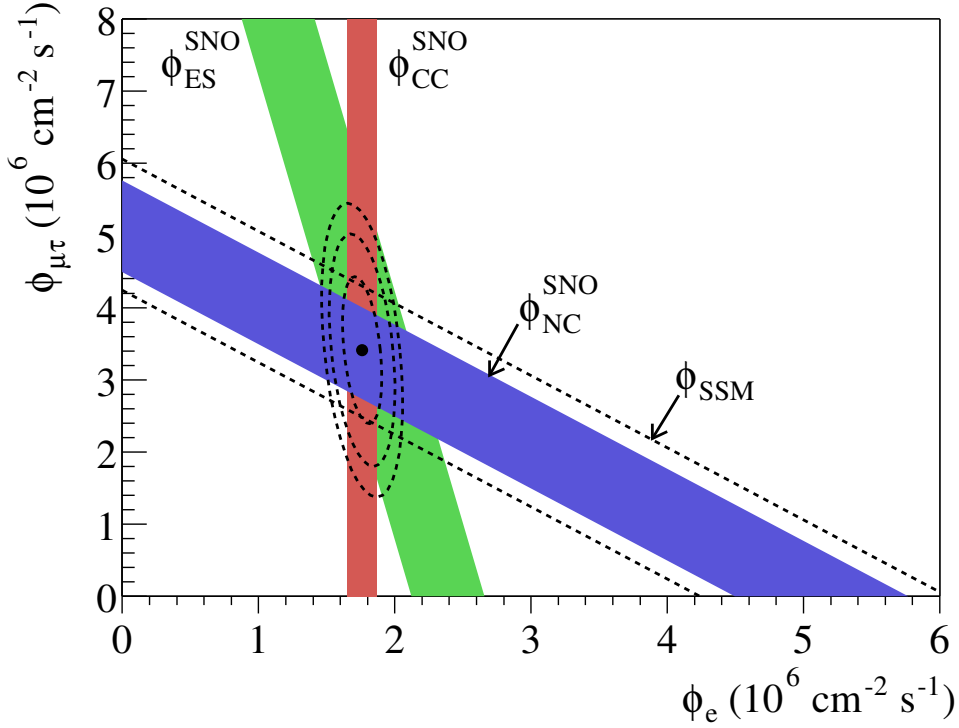
Figure 1.8 : *Flux of ^{8}B solar neutrinos which are μ or τ flavour ($\phi_{\mu\tau}$) vs flux of electron neutrinos (ϕ_e) deduced from the three neutrino reactions in SNO. The diagonal bands show the total ^{8}B flux (ϕ_{SSM}) as predicted by the standard solar model (dashed lines) and that measured via neutral current, charged current and elastic scattering reactions (ϕ_{NC}, ϕ_{CC} and ϕ_{ES}, respectively) in SNO (solid bands). The intercepts of these bands with the axes represent the $\pm 1\sigma$ errors [66].*

($\phi_{\text{tot}} = \phi_e + \phi_\mu + \phi_\tau$). SNO neutrino target is a 12 m diameter vessel containing 1 kton of heavy water (D_2O). ϕ_e can be measured by tagging the CC weak interaction of ν_e with D in the neutrino target. NC weak interaction of neutrinos with D is equally sensitive to all neutrino flavours. In addition, neutrinos can undergo elastic scattering (ES) from the atomic electrons in the neutrino target, favouring the ν_e more than the other flavours. Therefore, by combining the observed neutrino rates from the CC, NC and ES processes, ϕ_e and $\phi_{\mu\tau} = \phi_\mu + \phi_\tau$ fluxes can be constrained as shown in the figure 1.8. Combined with the high-statistics ES measurements from Super-Kamiokande [67], this provided direct evidence of a non-ν_e component in the solar neutrino flux. The NC measurement result in 2002 [11] established it with a statistical significance of 5.3σ. This confirmed that the ϕ_{tot} obtained from the NC processes is consistent with the predictions of the standard solar model. Since the production of ν_μ and ν_τ via the fusion reactions in the Sun are kinematically prohibited, this measurement serves as strong evidence of long-range neutrino flavour transformations. Hence, the long-stood question of the solar neutrino deficit was finally solved.

1.2.2 Atmospheric neutrino anomaly

When primary cosmic rays collide with atomic nuclei in the Earth's atmosphere, it leads to the production of hadrons which eventually decay, producing neutrinos. About two-thirds

of all atmospheric neutrinos and antineutrinos are of μ-flavour, while the remainder are of e-flavour. Atmospheric neutrinos are observed in a wide range of energies from 100 MeV to as high as few PeVs following a power-law spectrum.

When an energetic charged particle passes through a dielectric medium at a speed greater than that of light in the same medium, it results in the emission of electromagnetic radiation, known as Cherenkov radiation. In the 1980s, Kamioka Nucleon Decay Experiment (Kamiokande) [5] and Irvine-Michigan-Brookhaven (IMB) [68] water Cherenkov detectors were active players in the search of nucleon decay, and atmospheric neutrinos were an important source of background, at a rate of approximately 10^2 events·year^{-1}·kt^{-1}. The atmospheric neutrinos interact with the water molecules via elastic scattering, resulting in relativistic electrons that generate Cherenkov radiation. The direction of propagation of the scattered neutrinos and the electrons are isotropic in the center-of-mass frame of reference. However, in the laboratory frame of reference, the center-of-mass frame is boosted in the direction of the neutrino. Hence, water Cherenkov detectors are capable of retaining the directionality information of the neutrino.

In 1988, the Kamiokande experiment reported a substantial deficit in the number of μ-like events compared to the Monte Carlo prediction, while the number of e-like events aligned well with expectations [69]. Comparable findings were later published in the early 1990s by the IMB experiment [70]. This observation was known as the atmospheric neutrino anomaly. Given the significance of the discrepancy, it was concluded that the observed data could not be attributed to systematic detector effects or uncertainties in atmospheric neutrino fluxes alone, but to yet-unaccounted physics phenomena, such as neutrino flavour transformations.
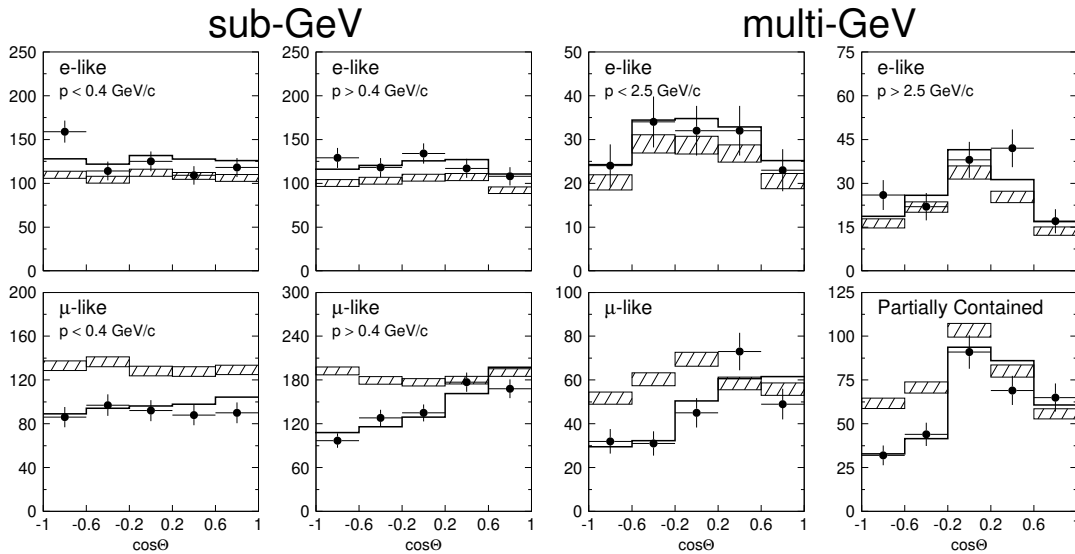
Figure 1.9 : *Zenith angle distributions of e-like and μ-like events for sub-GeV and multi-GeV data sets observed in Super-Kamiokande Experiment. Upward-going particles have $\cos\theta < 0$ and downward-going particles have $\cos\theta > 0$. The hatched region shows the Monte Carlo expectation for no oscillations normalized to the data live time with statistical errors. The bold line is the best-fit expectation for $\nu_\mu \leftrightarrow \nu_\tau$ oscillations with the overall flux normalization fitted as a free parameter [9].*

In the perspective of a detector near the Earth's surface, down-going neutrinos travel about 15 km through the atmosphere, while up-going neutrinos travel about 13000 km through the Earth before reaching the detector. In 1998, the Super-Kamiokande collaboration reported a zenith angle dependent deficit of up-going muon neutrinos, with a statistical significance better than 6σ, which is strongly consistent with two-flavour $\nu_\mu \leftrightarrow \nu_\tau$ oscillations [9, 71], as shown in figure 1.9.

1.2.3 Neutrino oscillations in vacuum

Neutrinos produced in CC weak interactions associated with a charged lepton are labelled as weak-eigenstates ($|\nu_\alpha\rangle$ where $\alpha = \{e, \mu, \tau\}$). The weak eigenstates do not have a well-defined mass and can be identified as coherent linear superpositions of mass eigenstates ($|\nu_j\rangle$ where $j = \{1, 2, 3\}$):

$$|\nu_\alpha\rangle = \sum_j U^*_{\alpha j}|\nu_j\rangle. \tag{1.18}$$

U is a 3×3 unitary mixing matrix known as the Pontecorvo-Maki-Nakagawa-Sakata (PMNS) matrix, which describes the mixing of flavour eigenstates and mass eigenstates. The PMNS matrix is parametrized with three mixing angles $\theta_{12}, \theta_{23}, \theta_{13} \in [0, \frac{\pi}{2}]$ and the $\mathcal{CP}$-violating phase $\delta_{CP} \in [0, 2\pi]$ as

$$U = \begin{pmatrix} c_{12}c_{13} & s_{12}c_{13} & s_{13}e^{-i\delta_{CP}} \\ -s_{12}c_{23} - c_{12}s_{13}s_{23}e^{i\delta_{CP}} & c_{12}c_{23} - s_{12}s_{13}s_{23}e^{i\delta_{CP}} & c_{13}s_{23} \\ s_{12}s_{23} - c_{12}s_{13}c_{23}e^{i\delta_{CP}} & -c_{12}s_{23} - s_{12}s_{13}c_{23}e^{i\delta_{CP}} & c_{13}c_{23} \end{pmatrix} \tag{1.19}$$

where $s_{jk} = \sin\theta_{jk}$ and $c_{jk} = \cos\theta_{jk}$. The unitarity of U follows from the orthogonalities of flavour eigenstates and mass eigenstates. If U is non-diagonal, it is a clear indication of the existence of flavour oscillations.

Consider that the neutrino is in the flavour eigenstate $|\nu_\alpha\rangle = |\nu(0)\rangle$ at time $t = 0$, with a three-momentum vector $\vec{p}$. Since the propagation of the mass eigenstates are described by a plane wave, their time evolution is characterized by a phase factor $e^{-iE_j t}$. In this case, the energy of $|\nu(0)\rangle$ is not well-defined, as each component of $|\nu(0)\rangle$ will have an energy $E_j = \sqrt{p^2 + m_j^2}$. Therefore, after time t, the neutrino flavour state evolves to

$$|\nu(t)\rangle = \sum_j U^*_{\alpha j}e^{-iE_j t}|\nu_j\rangle. \tag{1.20}$$

Hence, the probability of observing the neutrino at time t as a flavour state $|\nu_\beta\rangle$ is

$$P(\nu_\alpha \to \nu_\beta; t) = ||\langle \nu_\beta | \nu(t)\rangle||^2 = \sum_{j,k} U_{\beta j}U^*_{\alpha j}U_{\beta k}U^*_{\alpha k}e^{-i(E_j - E_k)t}. \tag{1.21}$$

Because $m_j \ll E_j$, $E_j = \sqrt{p^2 + m_j^2} \simeq p\left(1 + \frac{m_j^2}{2p^2}\right)$. Further, $p \simeq E_\nu$ where E_ν is the energy of the neutrino, and $t \simeq L$ (in natural units, where L is the distance travelled by the neutrino

during a time interval t). Thus, equation 1.21 becomes

$$P(\nu_\alpha \to \nu_\beta; t) = \sum_{j,k} U_{\beta j} U^*_{\alpha j} U_{\beta k} U^*_{\alpha k} e^{-i\Delta m^2_{jk}\frac{L}{2E_\nu}}, \quad \Delta m^2_{jk} = m^2_j - m^2_k. \qquad (1.22)$$

The result in equation 1.22 has very interesting implications. First, it implies that the probability of observing a given neutrino flavour oscillates as a function of $\frac{L}{E_\nu}$. Secondly, the oscillations vanish if the squared-mass difference term $\Delta m^2_{jk} = 0$. Thus, the experimental observation of neutrino oscillations are a clear indication that the neutrino masses are not null as predicted by the standard model.

From the general expression for the oscillation probability shown in 1.22, the three-flavour oscillation probability can be derived in the form

$$P(\nu_\alpha \to \nu_\beta; t) = \sum_{j} |U_{\beta j}|^4 |U_{\alpha j}|^4 + \sum_{j<k} 2\Re\mathfrak{e}[U_{\beta j} U^*_{\beta k} U^*_{\alpha j} U_{\alpha k}] \cos\left(\frac{\Delta m^2_{jk} L}{E_\nu}\right)$$
$$+ \sum_{j<k} 2\Im\mathfrak{m}[U_{\beta j} U^*_{\beta k} U^*_{\alpha j} U_{\alpha k}] \sin\left(\frac{\Delta m^2_{jk} L}{E_\nu}\right). \qquad (1.23)$$
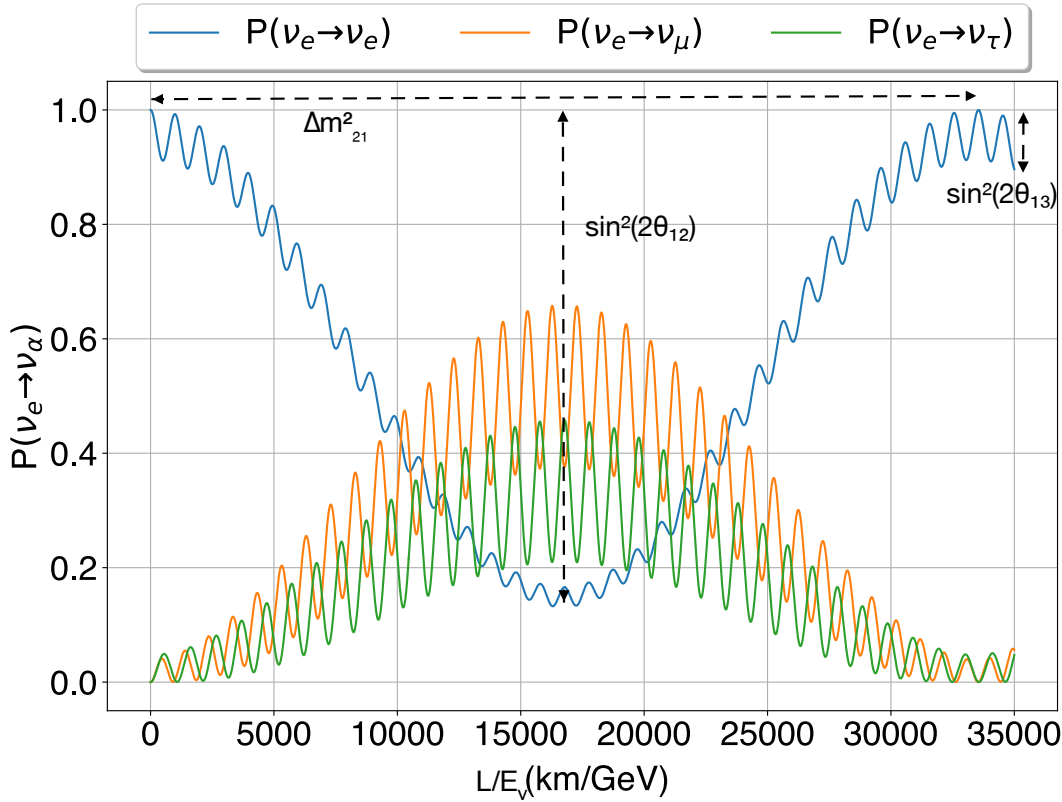
Figure 1.10 : *The variation of the three-flavour neutrino oscillation probabilities as a function of the ratio $\frac{L}{E_\nu}$ for an initial electron neutrino. The illustration was made using θ_{12}=33.44°, θ_{13}=8.57°, θ_{23}=49.0°, Δm^2_{21}=7.42×10⁻⁵, Δm^2_{31}=2.514×10⁻³, and, δ_{CP}=195°. The parameter values are from [72].*

The resulting oscillation probabilities for an initial electron neutrino as a function of $\frac{L}{E_\nu}$ are plotted in figure 1.10. The best-fit oscillation parameter values [72] at the time of writing of this thesis were used to plot the figure 1.10. The three squared-mass differences are related such that $\Delta m_{31}^2 = \Delta m_{21}^2 + \Delta m_{32}^2$. Hence, in addition to the three mixing angles and the $\mathcal{CP}$-violating phase, the three-flavour neutrino oscillations in vacuum are parametrized by only two independent squared-mass difference terms. Note that the oscillations appear as a "slow" oscillation component driven by Δm_{21}^2 and modulated by θ_{12}, as well as a "fast" oscillation component driven by Δm_{31}^2 and modulated by θ_{13}.

The corresponding oscillation probability for antineutrinos ($P(\bar{\nu}_\alpha \rightarrow \bar{\nu}_\beta; t)$) is derived by replacing $U \leftrightarrow U^*$ in equation 1.23. The replacement $U \leftrightarrow U^*$ is equivalent to replacing the matrix elements with their corresponding complex conjugates. As a result, the sign of the imaginary part (sine terms) of equation 1.23 is inverted, while leaving the real part (cosine terms) unchanged. Therefore, $P(\nu_\alpha \rightarrow \nu_\beta; t) \neq P(\bar{\nu}_\alpha \rightarrow \bar{\nu}_\beta; t)$ if and only if the mixing matrix has a non-zero imaginary part (i.e. $\delta_{CP} \neq \{0, \pi\}$). Thus, three-flavour neutrino oscillations violate $\mathcal{CP}$ symmetry, if and only if the aforementioned condition is met.

Replacing the indices $\alpha \leftrightarrow \beta$ of the oscillation probability $P(\nu_\alpha \rightarrow \nu_\beta; t)$ corresponds to the reversal of the direction of the time coordinate, $t \rightarrow -t$. This operation inverts the sign of the phase term of the sine terms and the cosine terms. This again affects only the sign of the sine terms, leaving that of the cosine terms invariant. Therefore, three-flavour neutrino oscillations violate the $\mathcal{T}$ symmetry (i.e. $P(\nu_\beta \rightarrow \nu_\alpha; t) \neq P(\nu_\alpha \rightarrow \nu_\beta; t)$) if and only if the mixing matrix has a non-zero imaginary part.

However, a combined replacement of ν with $\bar{\nu}$ followed by an interchange of initial and final flavours, leaves equation 1.23 invariant. Hence, although three-flavour neutrino oscillations can lead to a potential violation of $\mathcal{CP}$ and $\mathcal{T}$ symmetries, it preserves the combined $\mathcal{CPT}$ symmetry. Therefore, $P(\nu_\alpha \rightarrow \nu_\beta; t) = P(\bar{\nu}_\beta \rightarrow \bar{\nu}_\alpha; t)$. It is clear that the sine terms of equation 1.23 determines the $\mathcal{CP}$ and $\mathcal{T}$ violation effects.

Substituting $\alpha = \beta$ yields the ν_β disappearance probability $P(\nu_\beta \rightarrow \nu_\beta; t)$. This move leads to the cancellation of all the coefficients of the imaginary terms. The resulting expression is free from $\mathcal{CP}$ and $\mathcal{T}$ violating effects.

1.2.4   Neutrino oscillations in matter

Lincoln Wolfenstein's studies published in 1978 and 1979 led to the understanding that neutrino oscillations can be affected when propagating through matter [73, 74] due to coherent forward scattering of neutrinos from the surrounding particles. This phenomenon is described as the presence of an effective potential

$$V_{\text{eff}} = \pm\sqrt{2}G_F \left(-\frac{N_n}{2} + N_e\delta_{e\alpha} \right), \tag{1.24}$$

where G_F, N_n and N_e represent the Fermi constant, neutron density and the electron density of the medium, respectively. $\delta_{e\alpha}$ is 1 for ν_e or $\bar{\nu}_e$ and 0 otherwise. The sign of V_{eff} is $(+)$ for neutrinos and $(-)$ for antineutrinos. Flavour-independent NC scatterings generate the 1st

term of equation 1.24 only from interactions with neutrons, as the corresponding potentials due to electrons and protons in a charge-neutral matter distribution are equal and opposite, hence cancelling each other out.

For simplicity, consider two neutrino flavour states ($|\nu_\alpha\rangle$ and $|\nu_\beta\rangle$ as defined by equation 1.18) expressed as a linear superposition of two neutrino mass eigenstates ($|\nu_1\rangle$ and $|\nu_2\rangle$). The corresponding neutrino mixing matrix U can be expressed in terms of a single mixing angle θ as,

$$\begin{pmatrix} \nu_\alpha \\ \nu_\beta \end{pmatrix} = \begin{pmatrix} \cos\theta & \sin\theta \\ -\sin\theta & \cos\theta \end{pmatrix} \cdot \begin{pmatrix} \nu_1 \\ \nu_2 \end{pmatrix}. \tag{1.25}$$

The propagation of the neutrino in vacuum is described using a time-dependent Schrödinger equation $i\frac{\partial}{\partial t}|\nu(t)\rangle = \mathcal{H}_{vac}|\nu(t)\rangle$, where

$$\mathcal{H}_{vac} = \frac{\Delta m^2}{4E_\nu} \begin{pmatrix} -\cos 2\theta & \sin 2\theta \\ \sin 2\theta & \cos 2\theta \end{pmatrix} \tag{1.26}$$

is the corresponding Hamiltonian in vacuum, and $\Delta m^2 = m_2^2 - m_1^2$. The corresponding appearance probability $\mathrm{P}_{vac}(\nu_\alpha \to \nu_\beta; t)$ in vacuum is

$$\mathrm{P}_{vac}(\nu_\alpha \to \nu_\beta; t) = \sin^2(2\theta)\sin^2\left(\frac{\Delta m_M^2 \mathrm{L}}{\mathrm{E}_\nu}\right). \tag{1.27}$$

In a matter medium of constant density, V_{eff} effectively modifies $\mathcal{H}_{vac} \to \mathcal{H}_M$ and $\mathrm{P}_{vac}(\nu_\alpha \to \nu_\beta; t) \to \mathrm{P}_M(\nu_\alpha \to \nu_\beta; t)$ such that

$$\mathcal{H}_M = \frac{\Delta m^2}{4E_\nu} \begin{pmatrix} -\cos 2\theta_M & \sin 2\theta_M \\ \sin 2\theta_M & \cos 2\theta_M \end{pmatrix} \tag{1.28}$$

and

$$\mathrm{P}_M(\nu_\alpha \to \nu_\beta; t) = \sin^2(2\theta_M)\sin^2\left(\frac{\Delta m_M^2 \mathrm{L}}{\mathrm{E}_\nu}\right). \tag{1.29}$$

That is, the Hamiltonian $\mathcal{H}_M$ in matter and the oscillation probability $\mathrm{P}_M(\nu_\alpha \to \nu_\beta; t)$ in matter take the same form as their counterparts in vacuum, except that the vacuum parameters Δm^2 and θ are replaced by Δm_M^2 and θ_M, given by

$$\Delta m_M^2 = \sqrt{\sin^2(2\theta) + (\cos 2\theta - K)^2} \tag{1.30}$$

and

$$\sin^2(2\theta_M) = \frac{\sin^2(2\theta)}{\sin^2(2\theta) + (\cos 2\theta - K)}. \tag{1.31}$$

The parameter K is a measure of the matter effects, given by

$$K = \frac{2\mathrm{E}_\nu \mathrm{V}_{eff}}{\Delta m^2}. \tag{1.32}$$

Notice that when $K \to \cos 2\theta$, $\mathrm{P_M}(\nu_\alpha \to \nu_\beta; \mathrm{t})$ experiences an enhancement, irrespective of the value of θ. When $\cos 2\theta = K$, this enhancement reaches its maximum. In 1985, Stanislav Mikheyev and Alexei Smirnov predicted that a slow decline of matter density along the direction of the propagation of neutrinos leads to a dynamical modification of the mixing angle θ_M [76]. If the matter density decline is slow enough, the effect is negligible. Considering this effect for solar neutrinos propagating through the solar interior, the vacuum oscillations dominate the mixing at lower-end of the solar neutrino energies ($\leq$0.5 MeV), while matter-enhanced oscillations dominate the mixing at the higher-end of the solar neutrino energies ($\geq$3 MeV). As a result, the neutrinos at relatively higher energies experience an enhanced mixing with respect to the low-energy neutrinos. This is known as the MSW effect. It can be tested experimentally by making accurate measurements of neutrinos with energies above and below the transition region. The experimental measurements of solar neutrino disappearance probability from different processes at different solar neutrino energies by the Borexino Experiment, shown in figure 1.11, clearly demonstrates the effect of enhanced neutrino mixing at energies above 3 MeV.

Solar neutrinos are produced as electron neutrinos with energies of the order of few MeVs. Therefore, for solar neutrinos reaching the Earth, $\frac{\mathrm{L}}{\mathrm{E}_\nu} \ggg 35$ km/MeV. As a result, the individual effects of all the oscillation terms of the electron neutrino disappearance probability $\mathrm{P}\left(\nu_e \to \nu_e; t\right)$ are averaged out over the full energy spectrum. As shown in equations 1.31 and 1.32, the observed average electron neutrino disappearance probability depends on the solar neutrino energy E_ν, with this dependence reflected in the measured amplitude of θ_{12}. The parameter K that quantifies the degree of matter effects is contingent upon the
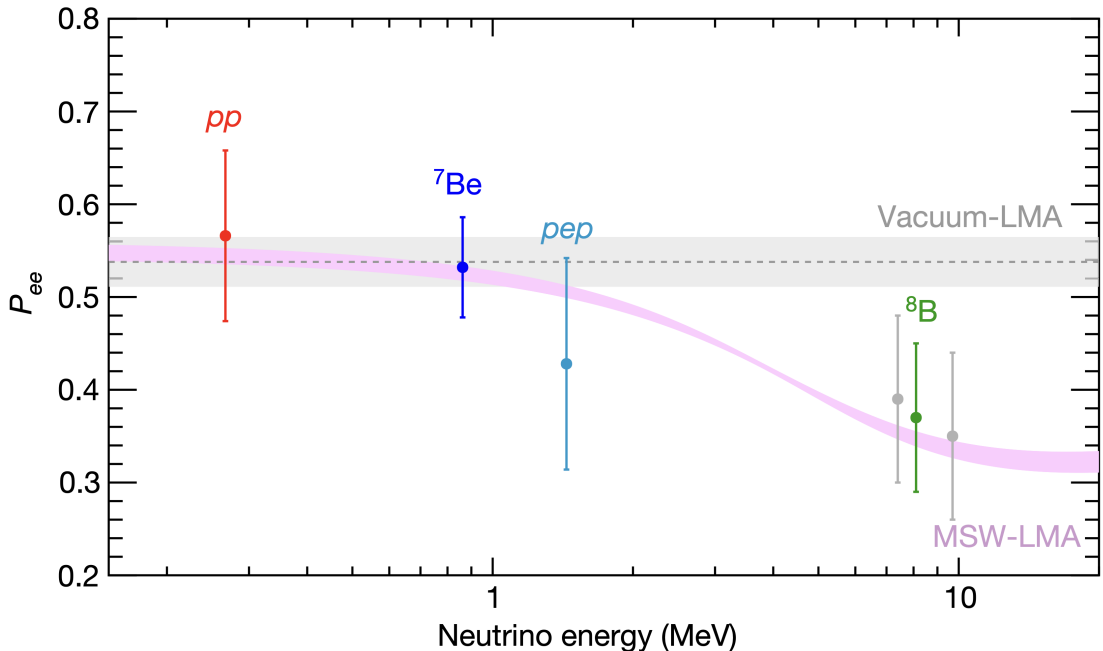
Figure 1.11 : *Disappearance probability* $\mathrm{P_{ee}}$ *of electron neutrinos produced in the Sun as a function of neutrino energy. The pink band represents the $\pm 1\sigma$ interval for MSW-LMA solution. Data points represent Borexino measurements of solar neutrinos due to different processes. The grey band represents $\pm 1\sigma$ interval around the vacuum LMA prediction [75].*

sign of Δm_{21}^2. Hence, observing the MSW effect and measuring the amplitude of θ_{12} using solar neutrinos provides a unique opportunity to determine the sign of Δm_{21}^2.

1.2.5 Present knowledge

The PMNS matrix shown in equation 1.19 is usually decomposed into a product of three rotation matrices as

$$
U = \begin{pmatrix} 1 & 0 & 0 \\ 0 & c_{23} & s_{23} \\ 0 & -s_{23} & c_{23} \end{pmatrix} \cdot \begin{pmatrix} c_{13} & 0 & s_{13}e^{-i\delta_{CP}} \\ 0 & 1 & 0 \\ -s_{13}e^{i\delta_{CP}} & 0 & c_{13} \end{pmatrix} \cdot \begin{pmatrix} c_{12} & s_{12} & 0 \\ -s_{12} & c_{12} & 0 \\ 0 & 0 & 1 \end{pmatrix}. \tag{1.33}
$$

The measured values of neutrino oscillation parameters quoted below are based on the latest publication by nuFIT [72], unless stated otherwise. Values quoted there are based on global analyses of existing neutrino data at the time of composition of this thesis.

Solar sector

The observation of solar neutrino deficit as evidence for neutrino flavour oscillations were discussed under section 1.2.1. In section 1.2.4, the MSW effect during the propagation of neutrinos through the solar interior was also introduced as an additional contribution to be accounted. The combined analysis incorporating solar neutrino experiments with KamLAND reactor neutrino experiment data [77] provides the dominant contribution to the determination of θ_{12} and Δm_{21}^2. The values of θ_{12} and Δm_{21}^2 are found to be $\theta_{12} = \left(33.44^{+0.78}_{-0.75}\right)°$ and $\Delta m_{21}^2 = \left(7.42^{+0.21}_{-0.20}\right) \times 10^{-5}\text{eV}^2$. Figure 1.12 illustrates the determination of these parameters from the global solar analysis in comparison with that of KamLAND. The results of the solar neutrino analyses are shown for the two latest versions of the Standard Solar Model, namely the GS98 and the AGSS09 models [78] obtained with two different determinations of the solar abundances. It must be noted that the MSW enhancement is sensitive to the sign of the Δm_{21}^2, as shown in equation 1.32. Therefore, experimental measurement of mixing enhancement due to MSW effect allows the determination of the sign of Δm_{21}^2 to be $(+)$, indicating that the mass eigenvalue of ν_2 (m_2) is larger than that of ν_1 (m_1).

Atmospheric sector

The observation of atmospheric neutrino anomaly as evidence for neutrino flavour oscillations was discussed under section 1.2.2. The oscillation of atmospheric neutrinos are dominated by $\nu_\mu \to \nu_\tau$. Therefore, ν_μ beam experiments can be used to measure the atmospheric neutrino oscillation parameters θ_{23} and Δm_{32}^2, as implemented by K2K [80], MINOS [81], T2K [82], NOνA [83], etc. In addition, neutrino telescopes built primarily for the detection of high-energy neutrino astrophysics such as ANTARES [84] and IceCube [85] are also sensitive to atmospheric neutrino oscillations. Further, combined data sets from the Daya Bay, RENO and Double-Chooz reactor experiments also play a
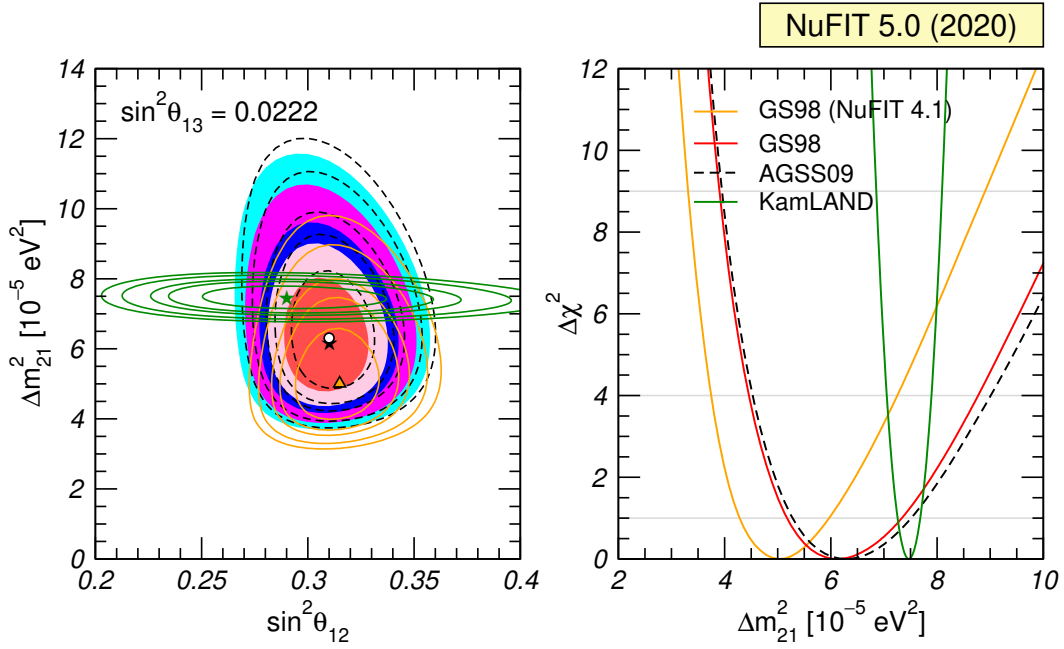
Figure 1.12 : *Left: Allowed parameter regions (at 1σ, 90%, 2σ, 99%, and 3σ CL) for θ_{12} and Δm_{21}^2 from the combined analysis of solar data for GS98 model (full regions with the best fit marked by black star) and AGSS09 model (dashed void contours with the best fit marked by a white dot), and for the analysis of KamLAND data (solid green contours with the best fit marked by a green star) for fixed $\sin^2 \theta_{13} = 0.0224$ ($\theta_{13} = 8.6°$). The orange contours the previous results of the global analysis for the GS98 model. Right: $\Delta\chi^2$ dependence on Δm_{21}^2 for the same four analyses [72].*
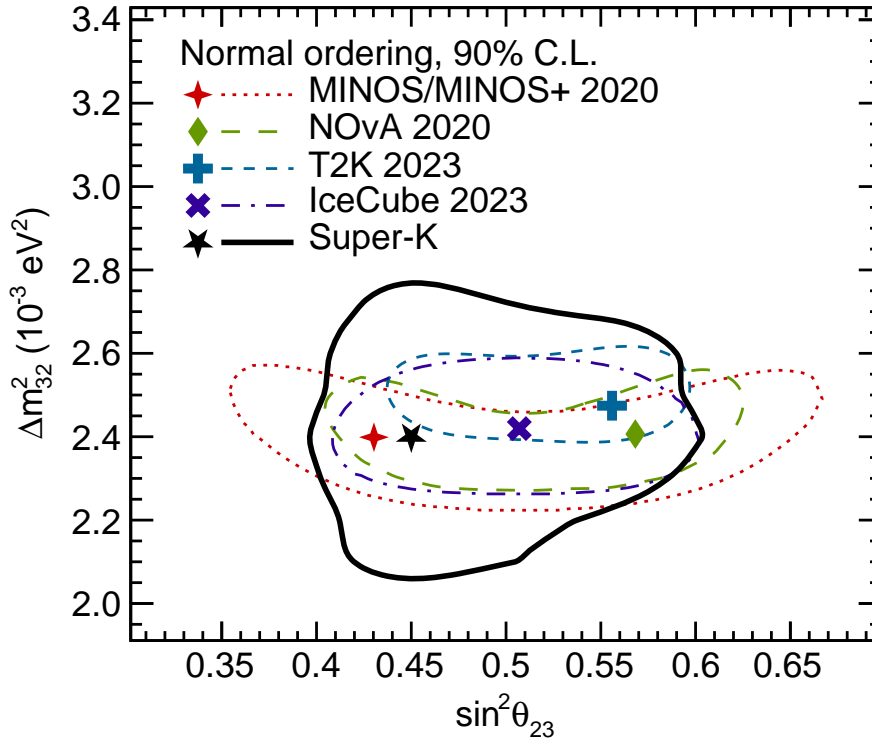
Figure 1.13 : *Comparison of the 90% confidence regions in $\sin^2(\theta_{23})$ - Δm_{32}^2 for normal mass ordering with data from MINOS+, NOνA, T2K, IceCube and Super-Kamiokande [79].*

role in constraining Δm_{32}^2 in the global fits [25, 72]. The value of θ_{23} is measured to be $\theta_{23} = \left(49.0_{-1.4}^{+1.1}\right)^\circ$. The value of $\Delta m_{31}^2 = \left(2.514_{-0.027}^{+0.028}\right) \times 10^{-3} \text{ eV}^2$ assuming normal ordering, and $\Delta m_{31}^2 = \left(-2.497_{-0.028}^{+0.028}\right) \times 10^{-3} \text{ eV}^2$ assuming inverted ordering. A comparison of measurements of θ_{23} and Δm_{32}^2 from several experiments is shown in figure 1.13.

Reactor sector

By the early 2000s, following the solid evidence provided by atmospheric, solar, reactor and neutrino beam experiments, an urge to determine the mixing angle θ_{13} emerged. In 2011, T2K reported the first indication of $\nu_\mu \rightarrow \nu_e$ oscillation with a statistical significance of 2.5σ, indicating the detection of a non-zero amplitude generated by θ_{13} [87]. In contrast to long-baseline neutrino beam experiments, a reactor neutrino experiment with a baseline of ~ 1 km can make an almost pure measurement of $\sin^2(2\theta_{13})$ from the disappearance of $\bar{\nu}_e$. To improve sensitivity by overcoming the systematic uncertainties in the understanding of the reactor neutrino flux, a near-far detector approach was suggested. As a result, Double-
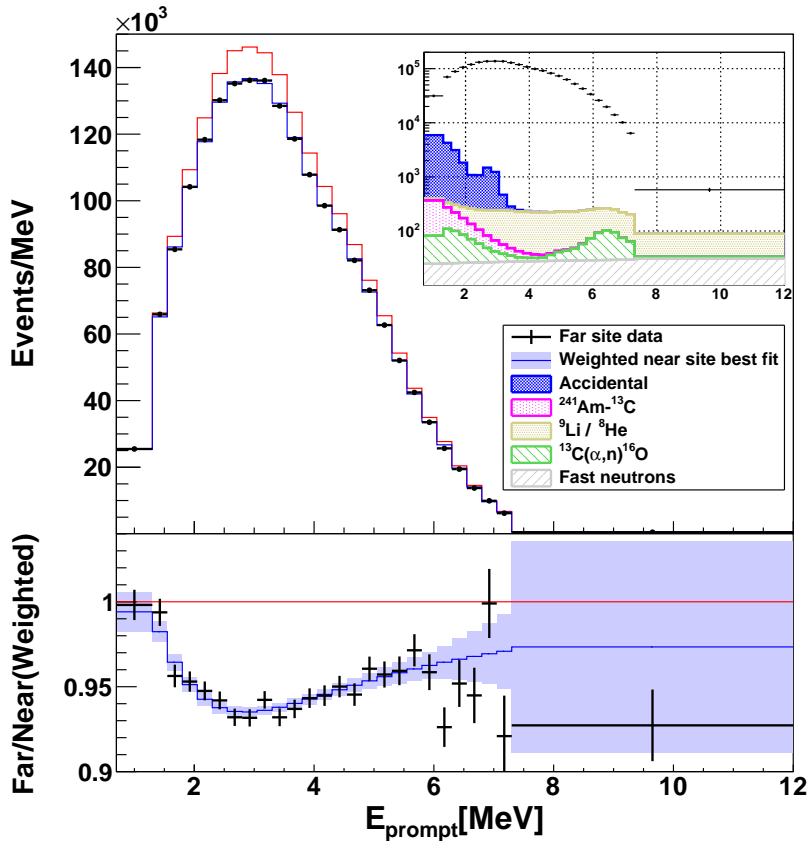
Figure 1.14 : *The background-subtracted spectrum at the far site (black points) and the expectation derived from near-site measurements excluding (red line) or including (blue line) the best-fit oscillation for the Daya Bay experiment. The bottom panel shows the ratios of data over predictions with no oscillation. The shaded area is the total uncertainty from near-site measurements and the extrapolation model. The error bars represent the statistical uncertainty of the far-site data. The inset shows the background components on a logarithmic scale [86].*

Chooz [88], Daya Bay [89], and RENO [90] commenced their pursuits for θ_{13} in 2011. The next year, Double-Chooz ruled out the no-oscillation hypothesis at 94% CL [91], RENO reported a non-zero value for θ_{13} at 4.9σ significance [92], and Daya Bay measured a non-zero value for θ_{13} at 5.2σ significance [93]. An updated comparison of background-subtracted spectrum of the Daya Bay far detector with the expected best-fit oscillated and unoscillated spectra derived from the near-site measurements is shown in figure 1.14. The value of θ_{13} is measured to be $\theta_{13} = \left(8.57^{+0.13}_{-0.12}\right)^\circ$.
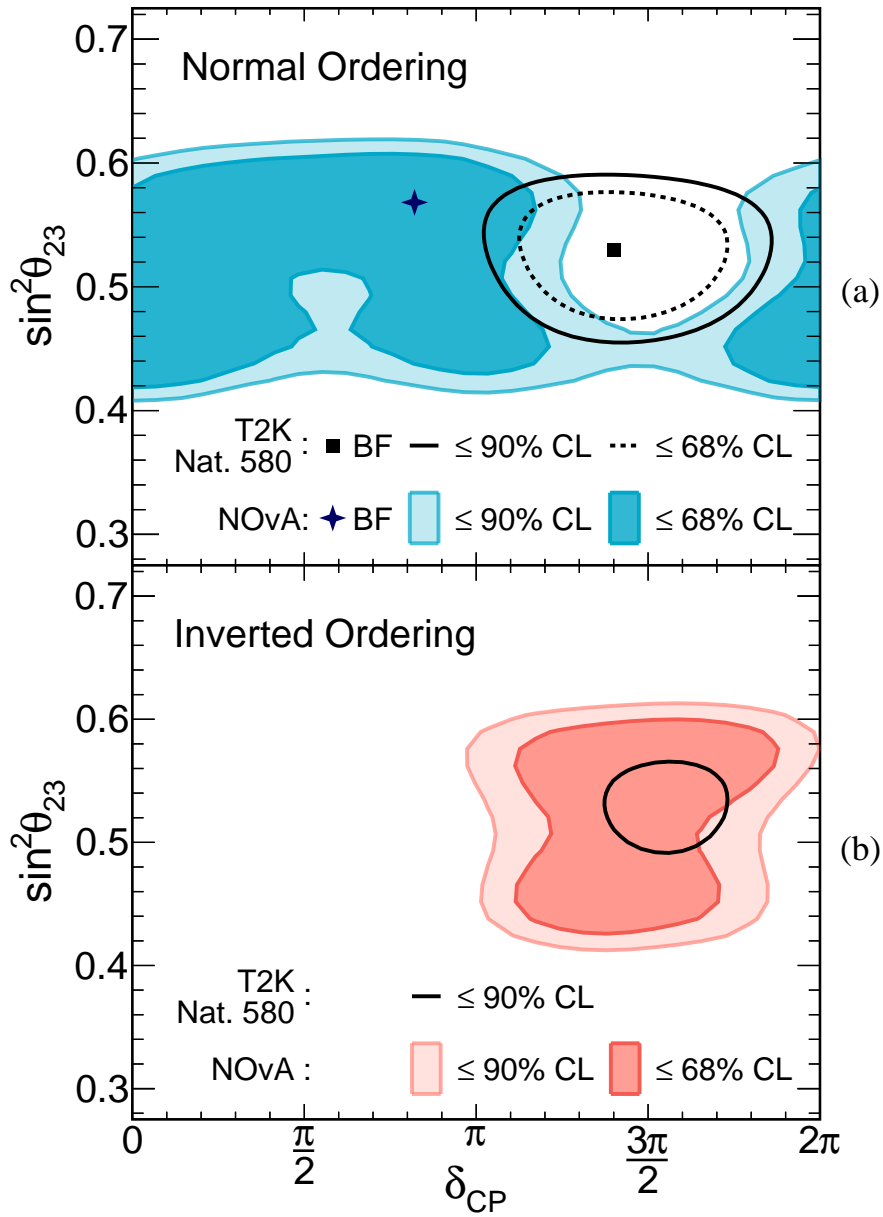
Figure 1.15 : *Comparison of 68% and 90% confidence level contours in $\sin^2(2\theta_{23})$ - δ_{CP} over both mass orderings with NOvA and T2K [94].*

$\mathcal{CP}$ violating phase δ_{CP}

In Section 1.2.3, a brief overview of the $\mathcal{CP}$ violation in three-flavour neutrino oscillations was presented. Long-baseline neutrino beam experiments can separately measure the $\nu_\mu \to \nu_e$ and $\bar\nu_\mu \to \bar\nu_e$ appearance to assess the $\mathcal{CP}$ violation in neutrino mixing. The T2K experiment, initiated in 2010, was the first long-baseline neutrino experiment to employ a 2.5° off-axis neutrino beam. The neutrino energy peaks at 0.6 GeV, tailored to observe the first oscillation probability maximum at a baseline of 295 km. In 2021, T2K reported a slight indication of $\mathcal{CP}$ violation at a 2σ significance level [95]. The NOvA experiment, which commenced in 2014, also adopts an off-axis configuration, with its neutrino beam energy peaking at about 2 GeV. Its far detector observes the first oscillation probability maximum at a distance of 810 km. A comparison incorporating data from T2K and NOvA, plotted in the figure 1.15, reveals significant overlap among the allowed regions in the $\sin^2(2\theta_{23})$ - δ_{CP} parameter space, although T2K and NOvA exclude the best-fit value of each other at >90% CL, in the normal ordering case [94]. The value of δ_{CP} is measured to be $\delta_{CP} = (195^{+51}_{-25})°$.

1.3 Open questions in Neutrino Physics

Over the last few decades, the field of neutrino physics has experienced a remarkable surge forward. From groundbreaking discoveries such as the discovery of neutrino oscillations to the precision measurement of oscillation parameters, the once obscure neutrino landscape is steadily coming into focus. Yet, amidst this progress, a host of unanswered questions linger. Excitingly, a wave of new experiments equipped with cutting-edge hardware, refined designs, and innovative strategies is on the horizon, displaying great potential to resolve some of the mysteries. Finding solutions to these enigmas will not just deepen our understanding of the neutrino itself, but holds promise to fundamentally transform our perception of the universe we inhabit.

Do neutrino oscillations violate $\mathcal{CP}$ symmetry?

In the PMNS matrix, the parameter δ_{CP} appears in conjunction with θ_{13}. The experimental measurement of non-zero value of θ_{13} has opened the pathway to explore the possibility of $\mathcal{CP}$ violations in the three-flavour neutrino oscillation picture. A δ_{CP} value different from 0 or π would indicate that the universe treats the three-flavour oscillations of neutrinos and antineutrinos differently, violating $\mathcal{CP}$ symmetry. The value of δ_{CP} still remains a significant open question in the field of neutrino physics. So far, long-baseline neutrino beam experiments employing measurements of the θ_{13}-driven neutrino oscillations using neutrino and antineutrino beams such as T2K and NOvA have been in the forefront of the search of the value of δ_{CP}. While the latest release of their respective measurements of δ_{CP} from T2K and NOvA are in agreement with each other in the inverted ordering case, they are in tension with each other in the normal ordering case. These experiments are not expected to reach 5σ sensitivity for δ_{CP}. However, next-generation high-precision long-baseline neutrino experiments are expected to perform conclusive measurements at high significance.
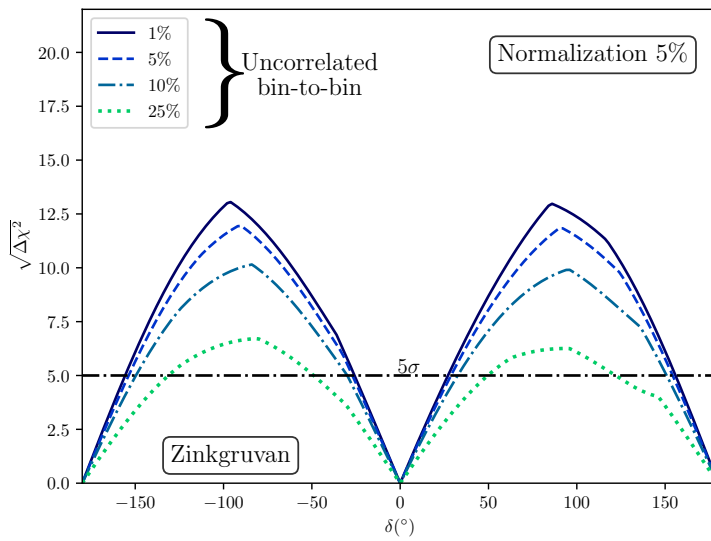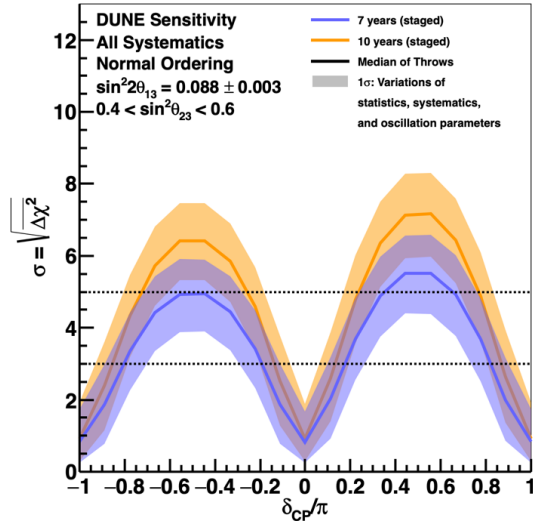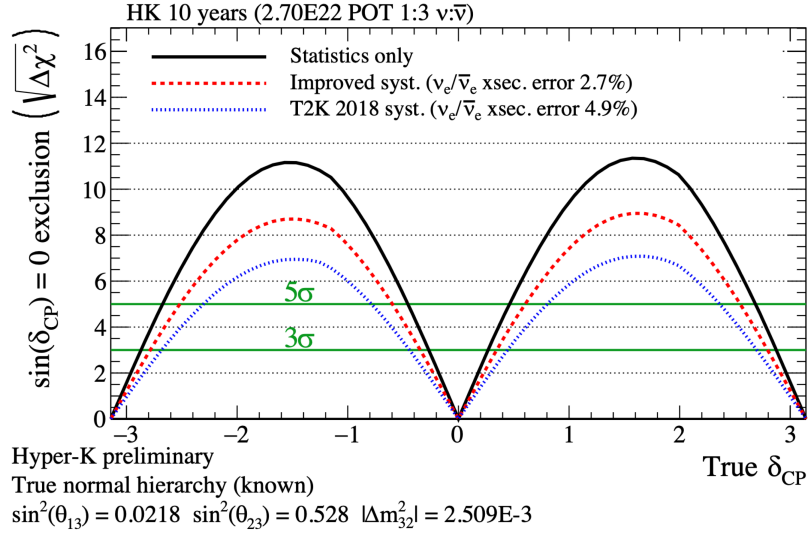
Figure 1.16 : δ_{CP} *sensitivity of Hyper-Kamiokande (top), DUNE (middle), and ESSνSB assuming a baseline at 360 km (Zinkgruvan, bottom) after 10 years of data collection, assuming normal ordering* [96–98].

The Hyper-Kamiokande experiment, a proposed successor to T2K, will use a similar off-axis, narrow-band beam setup. It is set to begin data acquisition in 2027, with a 25-fold increase in fiducial volume (190 ktons) and enhanced photocathode coverage in the far detector. It aims to measure δ_{CP} with better than 5σ significance within 10 years for 55% of all δ_{CP} values [99]. Concurrently, the Deep Underground Neutrino Experiment (DUNE) is slated to begin in the early 2030s. Using an on-axis, high-intensity, wide-band, 2.5 GeV neutrino beam setup, DUNE aims to detect both the first and second oscillation maxima at a baseline of 1285 m. It seeks δ_{CP} observation with better than 5σ significance within 10 years for 50% of δ_{CP} values [97]. As a second-generation experiment with respect to Hyper-Kamiokande and DUNE, the European Spallation Source Neutrino Super Beam (ESSνSB) plans to start operations in the late 2030s, aiming to produce the world's most intense neutrino beam. Preliminary studies suggest that placing a far detector at a baseline of 360 km will allow ESSνSB to measure δ_{CP} with better than 5σ significance within 10 years for 70% of all δ_{CP} values [100]. Combining data from multiple experiments will further constrain δ_{CP} [101]. The sensitivities of Hyper-Kamiokande, DUNE, and ESSνSB are shown in figure 1.16. Discovering δ_{CP} is significant for addressing key questions in particle physics, such as explaining the universe's matter-antimatter asymmetry.

Are neutrinos Majorana particles?

The nature of neutrinos, whether they are Majorana or Dirac particles, is a fundamental open question in particle physics. While the Dirac interpretation implies an unnaturally small Yukawa coupling to the Higgs field, the Majorana interpretation implies that the neutrinos are their own antiparticles. If neutrinos are Majorana particles, it implies the possibility of neutrinoless double-beta decay. Many experiments, as was introduced in detail under section 1.1.4 are currently underway in search of neutrinoless double-beta decay, but no conclusive evidence has been found yet. Figure [102] shows the allowed regions in the parameter space defined by the effective Majorana mass ($m_{\beta\beta}$) and the mass of the lightest neutrino eigenstate (m_{light}), assuming that neutrinos are Majorana particles. As shown, the allowed regions in the parameter space depends on the correct neutrino mass ordering, which is another open question in the field of neutrino physics. Thus, the potential of neutrinoless double-beta decay experiments to determine whether neutrinos are Majorana or Dirac particles depends on the neutrino mass ordering, which is introduced below.

What is the correct mass ordering?

Section 1.2.5 introduced that the sign of Δm_{21}^2 is known thanks to the MSW effect. However, the sign of Δm_{32}^2 remains unknown. Therefore, it is not yet clear if the mass eigenvalue of ν_3 (m_3) is greater or lesser compared to that of ν_1 (m_1). This gives rise to two orders to arrange the mass eigenvalues based on their magnitudes: normal ordering (NO) where $m_3 > m_2 > m_1$, and inverted ordering (IO) where $m_2 > m_1 > m_3$, as shown in figure 1.18. Determining which of these orders is correct is referred to as resolving the neutrino mass ordering (NMO). Knowledge of the neutrino mass ordering impacts our understanding of the neutrino mass scale, determination of the neutrino oscillation parameters and the value of δ_{CP}.
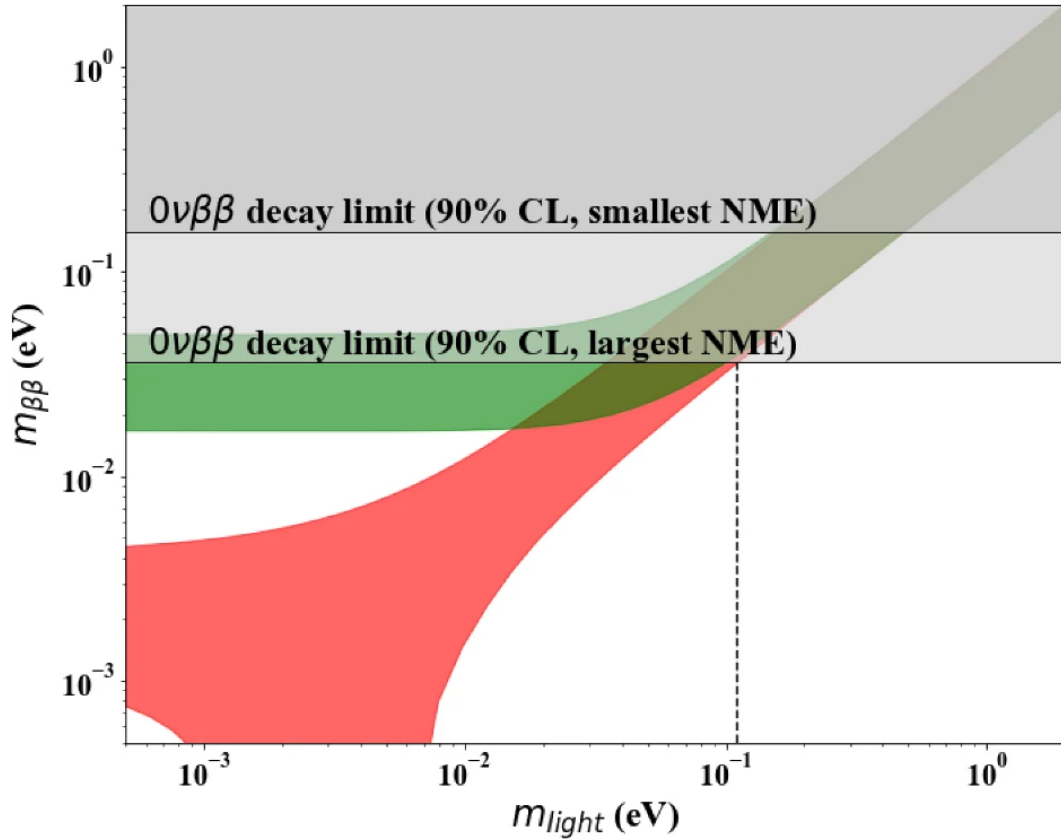
Figure 1.17 : *The effective neutrino Majorana mass ($m_{\beta\beta}$) as a function of the lightest neutrino mass (m_{light}). The red (green) band corresponds to the normal (inverted) mass ordering, respectively, in which case m_{light} is equal to m_1 (m_3). The horizontally excluded region comes from neutrinoless double-beta decay constraints [102].*
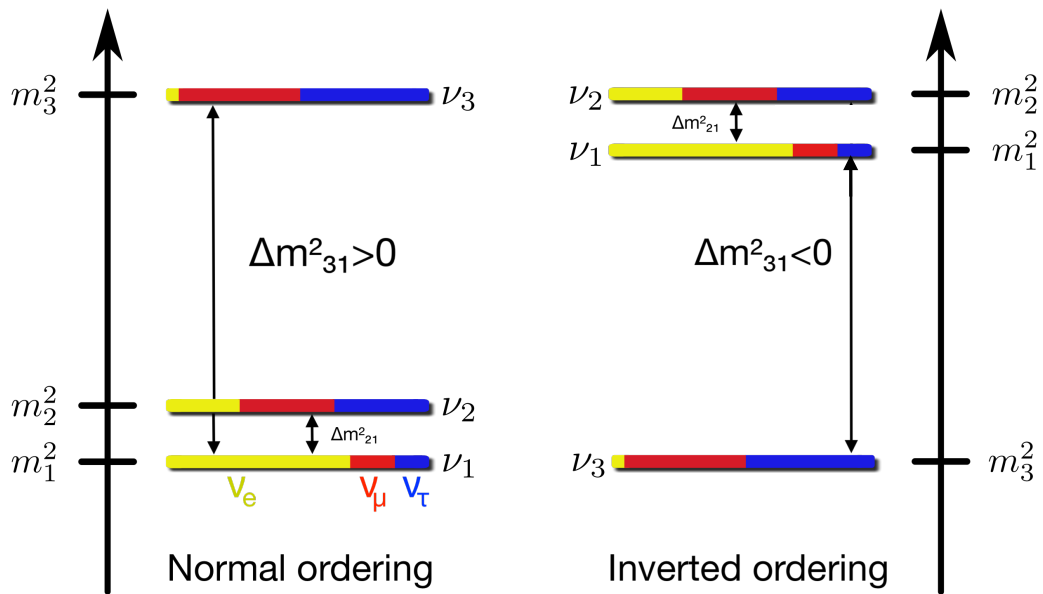
Figure 1.18 : *The two possible neutrino mass orderings in terms of neutrino flavour states, under a three-neutrino oscillation paradigm. Adapted from [103].*

Long-baseline neutrino beam experiments and atmospheric neutrino experiments involve neutrinos propagating through the Earth over long distances. As the degree of matter effects is sensitive to the sign of Δm^2_{32}, neutrino beam and atmospheric neutrino experiments hold potential to resolve NMO. In all current three-flavour neutrino oscillation analyses, the best-fit is found when NO is assumed. The latest combined fits driven by long-baseline neutrino beam experiment data and short-baseline reactor data slightly disfavour IO at >1.5σ significance. IO is further disfavoured at 2.5σ when the Super-Kamiokande atmospheric data is included [25]. Future long-baseline neutrino beam experiments such as DUNE [104] and Hyper-Kamiokande [105], as well as future atmospheric neutrino experiments such as ORCA [106] show great promise to definitively resolve NMO.

Chapter 2 presents a detailed overview of the upcoming medium-baseline reactor electron antineutrino experiment know as JUNO, primarily aimed at determining the correct neutrino mass ordering. Currently, JUNO is the only experiment in the horizon to utilize vacuum oscillations to determine NMO, introducing a whole different insight in the landscape of NMO determination strategy. Contrary to the aforementioned approaches, JUNO relies on the precision measurement of the reactor antineutrino spectrum. The complementarity of JUNO and other experiments on the hunt for NMO will facilitate the NMO determination much sooner [107–110].

Résumé : La physique des neutrinos

Le modèle standard de la physique des particules est une théorie quantique des champs qui unifie la mécanique quantique et la relativité restreinte, expliquant les interactions entre les particules fondamentales. Ces particules sont divisées en fermions (particules de matière) et en bosons (médiateurs des interactions fondamentales). Les fermions comprennent les quarks et les leptons, les quarks étant sensibles à la force forte et les leptons ne l'étant pas. Les quarks se subdivisent en quarks (u, c, t) avec une charge de $+\frac{2}{3}$, et en quarks (d, s, b) avec une charge de $-\frac{1}{3}$. Les leptons se subdivisent entre les leptons chargés et les leptons neutres. Les leptons chargés (e, μ, τ) ont une charge de -1. Les leptons neutres, aussi appellés neutrinos (ν_e, ν_μ, ν_τ) qui interagissent uniquement par le biais de la force faible, ce qui leur permet généralement de traverser la matière sans entrave. Ces fermions sont classés en trois générations en fonction de leur masse. Les bosons comprennent le photon (γ), le gluon (g), les bosons de l'intéraction faible (W^+, W^-, Z) et le boson de Higgs (H). L'image des particules fondamentales s'élargit encore pour inclure les antiparticules, en conséquence de la conjugaison de la charge ($\mathcal{C}$), de la parité ($\mathcal{P}$) et de la symétrie de renversement du temps ($\mathcal{T}$) du modèle standard. Comme le focus de cette thèse sont les neutrinos, ils séront discutés plus en détaille par la suite.

En 1930, Wolfgang Pauli a proposé l'existence d'une particule légère et neutre pour expliquer la violation apparente de la conservation de l'énergie observée dans les désintégrations nucléaires. En 1932, Enrico Fermi a intégré cette idée dans sa théorie des désintégrations nucléaires β, dans laquelle il a nommé cette nouvelle particule « neutrino ». Ce travail a été la base de la théorie de l'interaction faible. En 1956, Clyde Cowan et Frederick Reines ont confirmé expérimentalement l'existence du neutrino. Le prix Nobel de physique 1995 a été attribué à Reines pour cette découverte du neutrino. En 1957, Maurice Goldhaber, Lee Grodzins et Andrew Sunyar concluent expérimentalement que le neutrino doit être gaucher.

Les progrès théoriques réalisés entre la fin des années 1950 et le début des années 1960 ont abouti au modèle électrofaible, qui unifie l'électromagnétisme et la force faible, représentée par un groupe de jauge SU(2)×U(1). Dans ce cadre, les quatre bosons sont sans masse, contrairement aux observations physiques. En 1964, le mécanisme de la brisure spontanée de symétrie a été introduit dans le modèle électrofaible pour expliquer comment les particules acquièrent une masse. Les masses des fermions de Dirac proviennent de leur interaction avec le boson H et le champ de Higgs. Comme les neutrinos droitiers n'existent pas dans le modèle standard, les neutrinos sont considérés comme sans masse dans ce cadre. Cela suggère que le mécanisme par lequel les neutrinos acquièrent une masse pourrait être différent de celui des autres fermions. La construction de Majorana, proposée en 1937, permet d'obtenir un terme de masse invariant en couplant un neutrino gaucher avec son conjugué $\mathcal{CP}$, ce qui implique que les neutrinos pourraient être leurs propres antiparticules. Un terme de Lagrange plus complet pour les masses des neutrinos peut être construit en incorporant à la fois les composantes de Dirac et de Majorana. Le mécanisme susmentionné, connu sous le nom de mécanisme de la balançoire, suggère que chaque génération de neutrinos comporte un neutrino léger gaucher et un neutrino beaucoup plus lourd droitier. Cependant, la construction de Majorana et le mécanisme de la balançoire restent théoriques et attendent une confirmation expérimentale.

Plusieurs techniques permettent de mesurer la masse du neutrino. En supposant que les neutrinos sont des particules de Majorana, les expériences de désintégration double bêta sans neutrinol ($\beta\beta 0\nu$) telles que GERDA-LEGEND, KamLAND-Zen, EXO-200, et CUORE cherchent à déterminer la masse du neutrino de Majorana en mesurant le taux de désintégration $\beta\beta 0\nu$. Parallèlement, des expériences telles que KATRIN, ECHo, HOLMES et NuMECS, analysent la conservation de l'énergie-momentum dans les désintégrations faibles impliquant des neutrinos ou des antineutrinos en observant la fin du spectre de désintégration de β afin d'en déduire la masse du neutrino. La masse du neutrino peut également être sondée en analysant les fluctuations cosmologiques à différentes échelles en utilisant le fond diffus cosmologique et les données de structure à grande échelle dans l'univers. En raison de la dépendance du modèle des mesures cosmologiques et de l'hypothèse selon laquelle les neutrinos sont de Majorana dans les recherches $\beta\beta 0\nu$, il est usuel de faire plus confiance à la méthode cinématique pour évaluer la masse du neutrino. Par conséquent, la limite supérieure établie par l'expérience KATRIN ($m_{\nu_e}^{eff}$<0,45 eV (95% CL)), obtenue en ajustant la forme du spectre de désintégration β, est considérée comme la meilleure limite acceptée.

Le déficit apparent des mesures du flux de neutrinos solaires rapporté dans les années 1960, ainsi que le déficit apparent des mesures du flux atmosphérique de ν_μ rapporté par Kamiokande en 1988 ont laissé les physiciens perplexes pendant des décennies. À l'aube du XXIe siècle, notre compréhension du neutrino s'est transformée. Des mesures détaillées du flux atmosphérique ν_μ par le détecteur Super-Kamiokande, ainsi que du flux de neutrinos solaires par le Sudbury Neutrino Observatory, ont fourni des preuves solides que les anomalies susmentionnées pouvaient être expliquées par un phénomène encore inconnu connu sous le nom d'oscillations de saveur des neutrinos. Ce phénomène a montré que la probabilité de détecter un neutrino d'une saveur spécifique change au fur et à mesure qu'il se propage. Takaki Kajita, de Super-Kamiokande, et Arthur McDonald, de Sudbury Neutrino Observatory, ont reçu conjointement le prix Nobel de physique de 2015 pour la découverte des oscillations de saveur des neutrinos.

Le phénomène des oscillations de saveur des neutrinos est un processus expliqué purement par la mécanique quantique. Les neutrinos peuvent être identifiés en fonction des états de saveur leptonique dans lesquels ils interagissent, ainsi qu'en fonction de leurs états propres de masse (ν_1, ν_2, ν_3 avec des valeurs propres de masse m_1, m_2, m_3 respectivement) dans lesquels ils se propagent. Chaque état propre de saveur est un mélange spécifique d'états propres de masse et vice versa. Le mélange est caractérisé par une matrice unitaire 3×3 connue sous le nom de matrice de Pontecorvo-Maki-Sakagawa-Nakata (PMNS). La matrice PMNS est caractérisée en termes de trois angles de mélange (θ_{12}, θ_{13}, θ_{23}) et de phase de violation $\mathcal{CP}$ (δ_{CP}). Par conséquent, la probabilité qu'un neutrino d'une saveur leptonique initiale donnée soit observé comme une certaine saveur leptonique lorsqu'il se propage sur une distance donnée peut être décrite en fonction des trois angles de mélange, δ_{CP}, et des séparations de masse au carré (Δm_{21}^2, Δm_{31}^2). L'amplitude de la probabilité d'oscillation des neutrinos est déterminée par les termes de la matrice PMNS, tandis que les différences des carrées des masses régissent les fréquences d'oscillation. La possibilité pour le neutrino d'osciller d'une saveur à l'autre implique que les neutrinos ont des masses non dégénérées, contrairement à ce que suggère le modèle standard.

Au cours des dernières décennies, le domaine de la physique des neutrinos a connu un essor

remarquable. De la découverte de l'oscillation de neutrinos à la mésure précise de leurs paramètres, le paysage des neutrinos est dévenu de plus en plus clair. Les expériences sur les neutrinos solaires, les expériences sur les neutrinos atmosphériques, les expériences sur les faisceaux de neutrinos à longue "baseline", ainsi que les expériences sur les réacteurs à courte "baseline" ont contribué de manière éclatante à la mesure précise de la plupart des paramètres d'oscillation des neutrinos, élargissant ainsi notre compréhension actuelle des neutrinos. Cependant, au milieu de ces progrès, une multitude de questions restent sans réponse. La valeur de δ_{CP}, qui quantifie si l'univers traite différemment les oscillations des neutrinos et des antineutrinos, reste une question ouverte. Les prochaines expériences sur les réacteurs à longue "baseline" sont très prometteuses pour déterminer δ_{CP}. La nature de la masse des neutrinos, qu'ils soient de Majorana ou de Dirac, est encore inconnue. Dans ce domaine, des recherches sur la désintégration double bêta sans neutrinol sont actuellement en cours. Bien que le signe et la magnitude de Δm_{21}^2 soient connus, seule la magnitude de Δm_{31}^2 est connue. Cela suggère donc deux ordres de masse possibles : $m_3 > m_2 > m_1$ (ordre normal), ou $m_2 > m_1 > m_3$ (ordre inversé). Les expériences sur les faisceaux de neutrinos à longue "baseline" et les expériences sur les neutrinos atmosphériques peuvent permettre de déterminer cet ordre grace à l'empreinte des effets de matière dans leur oscillation. En plus de cela, l'expérience en préparation utilisant les antineutrinos produits dans un réacteur de moyenne "baseline", connue sous le nom JUNO, adopte une stratégie unique pour déterminer l'ordre de masse des neutrinos. Pour le faire, JUNO s'appuie sur la mesure précise du spectre des antineutrinos du réacteur.

THE JUNO EXPERIMENT

2.1 Overview

The Jiangmen Underground Neutrino Observatory (JUNO) is an upcoming reactor electron antineutrino experiment under construction in an underground laboratory under the Dashi
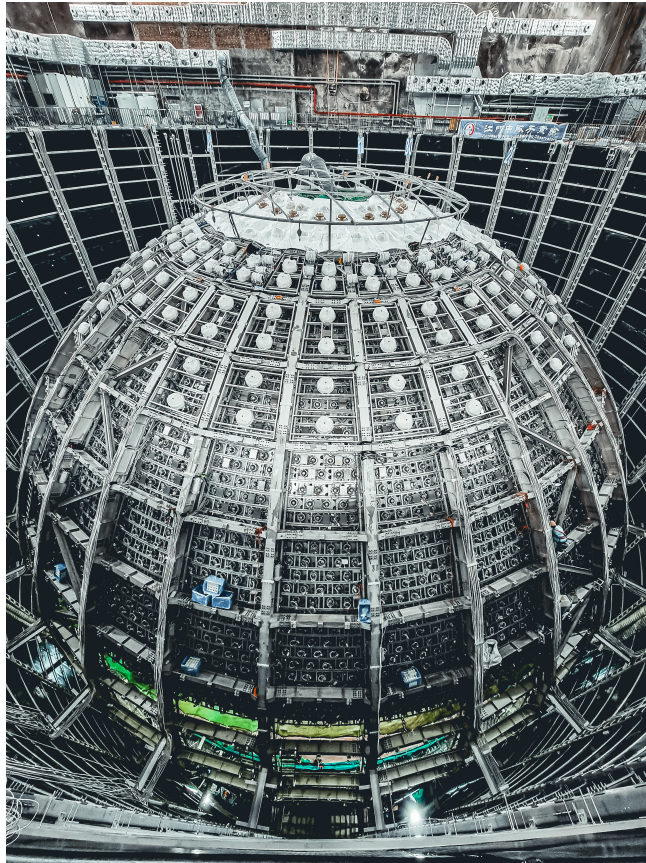
Figure 2.1 : *The JUNO detector under construction, as of July 2023.*

hill in Jiangmen, China. The civil construction commenced in 2015 [111], and was completed by December 2021. Figure 2.1 is a depiction of the detector under construction as of July 2023. The vertical overburden with respect to the detector center is about 700 m, which is about 1800 m.w.e. (meter water equivalent). A large spherical volume containing 20 ktons of Liquid Scintillator (LS) will be deployed as the neutrino target of the JUNO experiment. Thanks to its excellent energy resolution, JUNO offers exciting opportunities to address many important topics in neutrino physics and astrophysics. JUNO aims to determine the neutrino mass ordering at 3σ significance and to measure the neutrino oscillation parameters $\sin^2\theta_{12}$, Δm_{21}^2 and Δm_{31}^2 to a precision of 0.5% or better within 6 years of data taking [112]. Its success greatly relies on a detailed understanding of the reactor antineutrino spectrum as well as rigorous quantification and control of the associated backgrounds, as is described under section 2.3.

2.2   JUNO physics prospects

With its rich neutrino physics program, JUNO has great potential to become one of the most important players in the next-generation of neutrino experiments. Although JUNO's primary goal is the determination of the neutrino mass ordering, its physics potential extends further, as summarized below.
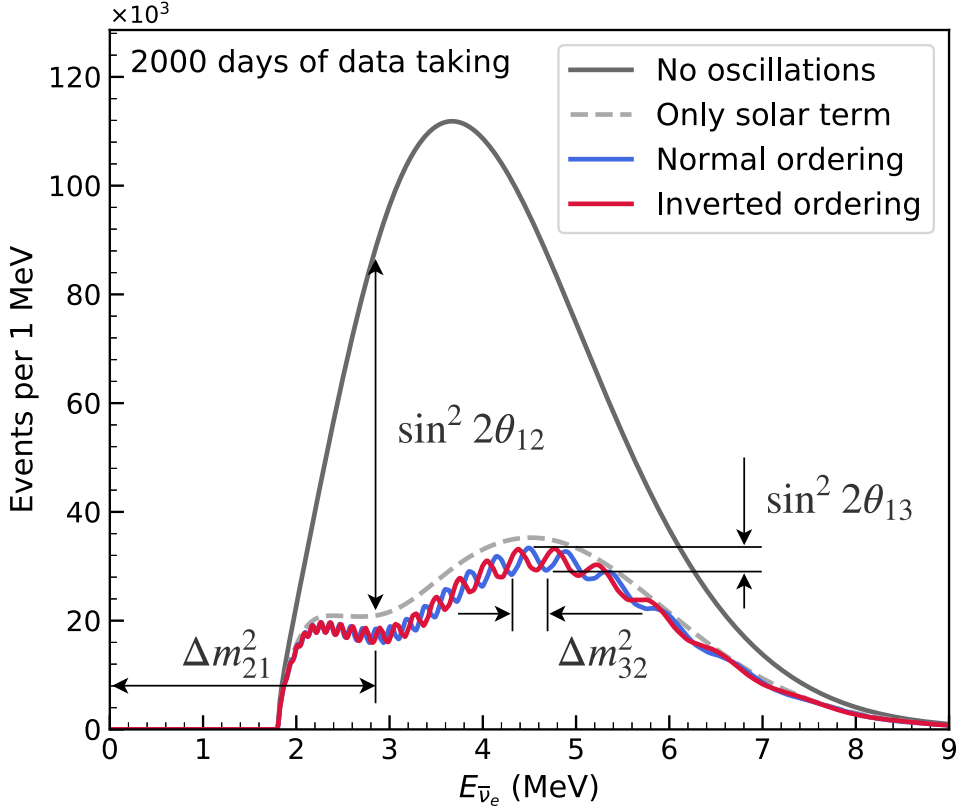
Figure 2.2 : *The expected antineutrino energy spectrum weighted by IBD cross section with and without (black) oscillation at the JUNO experiment for normal ordering (blue) and inverted ordering (red) assuming 2,000 days of data taking [13].*

2.2.1 Precision measurement of neutrino oscillation parameters

The channel used for the observation of reactor antineutrino oscillations in JUNO is the $\bar{\nu}_e \rightarrow \bar{\nu}_e$ disappearance. From equation 1.23, the $\bar{\nu}_e \rightarrow \bar{\nu}_e$ disappearance probability $\mathrm{P}\left(\bar{\nu}_e \rightarrow \bar{\nu}_e; \mathrm{E}_{\bar{\nu}_e}, \mathrm{L}_r\right) \equiv \mathrm{P}_{\bar{\nu}_e \rightarrow \bar{\nu}_e}$ for a neutrino energy of $\mathrm{E}_{\bar{\nu}_e}$ at a baseline L_r can be derived as

$$
\begin{aligned}
\mathrm{P}_{\bar{\nu}_e \rightarrow \bar{\nu}_e} = 1 &- \sin^2 2\theta_{12} \cos^4 \theta_{13} \sin^2 \left(\frac{\Delta m_{21}^2 \mathrm{L}_r}{4\mathrm{E}_{\bar{\nu}_e}}\right) \\
&- \sin^2 (2\theta_{13}) \left[\cos^2 \theta_{12} \sin^2 \left(\frac{\Delta m_{31}^2 \mathrm{L}_r}{4\mathrm{E}_{\bar{\nu}_e}}\right) + \sin^2 \theta_{12} \sin^2 \left(\frac{\Delta m_{32}^2 \mathrm{L}_r}{4\mathrm{E}_{\bar{\nu}_e}}\right)\right].
\end{aligned}
\tag{2.1}
$$

As shown in the figure 2.2, the antineutrino spectrum observed by JUNO is composed of a slow (low frequency) oscillation component that is responsible for most of the $\bar{\nu}_e$ disappearance, and a fast (high frequency) oscillation component. The former is driven by Δm_{21}^2 and modulated by θ_{12}, while the latter is driven by Δm_{32}^2 and modulated by θ_{13}. Note that the observed oscillation pattern will subtly differ, depending on the mass ordering. Thus, JUNO aims to determine the NMO via precise measurement of the reactor antineutrino spectrum. More details can be found under section 5.1.3. Hence, an unparalleled energy

Table 2.1 : *A summary of precision levels for the oscillation parameters. The results of PDG2020 [113] is compared with 100 days and 6 years of JUNO data taking [112].*

Parameter	Central value	PDG2020	100 days	6 years
Δm_{31}^2 (10^{-3}eV^2)	2.5283	± 0.034 (1.3%)	± 0.021 (0.8%)	± 0.0047 (0.2%)
Δm_{21}^2 (10^{-5}eV^2)	7.53	± 0.18 (2.4%)	± 0.074 (1.0%)	± 0.024 (0.3%)
$\sin^2 \theta_{12}$	0.307	± 0.013 (4.2%)	± 0.0058 (1.9%)	± 0.0016 (0.5%)

resolution is crucial for JUNO to resolve NMO. Moreover, it will offer JUNO the golden opportunity to become the world's first experiment to observe the slow and fast neutrino oscillations concurrently. The precision of this measurement will ascertain $\sin^2 \theta_{12}$, Δm_{21}^2, and $|\Delta m_{31}^2|$ to a precision of 0.5% or better within 6 years of data collection [112], as demonstrated in table 2.1. In fact, 100 days of data will already be sufficient to surpass the current precision on those three parameters. Achieving sub-percent level of precision on neutrino oscillation parameters will play an integral role in the future unitarity tests of the PMNS matrix.

2.2.2 Solar neutrinos

Solar nuclear fusion proceeds primarily through the proton-proton (pp) chain and the sub-dominant CNO cycle, which is catalysed by carbon, nitrogen, and oxygen, contributing about 1% of the energy output of the Sun. The solar neutrino flux is dominated by pp neutrinos (from the primary pp process) which have a maximum energy of 0.42 MeV. Other neutrinos from the pp chain include those from ^{7}Be electron-capture, proton-electron-proton reaction (pep), ^{8}B decay, and the hep reaction $\left[^3\mathrm{He} \, (p, e^+ \nu_e)^4 \, \mathrm{He} \right]$. ^{7}Be neutrinos have energies of 0.38 MeV and 0.86 MeV, pep neutrinos are mono-energetic at 1.44 MeV, and ^{8}B and hep neutrinos have broader spectra extending beyond 16 MeV. CNO neutrinos have a flux comparable to pep neutrinos and an energy spectrum up to 1.74 MeV.

Significant advancements have been made by Borexino and Super-Kamiokande through high-precision real-time spectroscopy of solar neutrinos via elastic scattering (ES) off electrons [75, 114]. However, the transition region of solar electron neutrino disappearance probability, as shown in figure 1.11, remains partially unexplored due to the challenge of reaching an analysis threshold for ES electrons below below 3 (3.5) MeV in Borexino (Super-Kamiokande). JUNO's low-energy threshold for ES electrons down to 2 MeV (provided that an LS radiopurity level of 10^{-17} g/g is achieved [115]), superior energy resolution, and larger target mass holds substantial promise for advancing solar neutrino physics. JUNO expects to detect about 60,000 ^{8}B solar neutrino events and 30,000 background events in the energy range above 2 MeV. The expected precision of the relevant oscillation parameters using ^{8}B solar neutrinos is shown in figure 2.3.

The neutrino energy threshold for neutrino CC interactions with ^{13}C is about 3.7 MeV, making it accessible for solar neutrinos, unlike ^{12}C, which has a much higher threshold
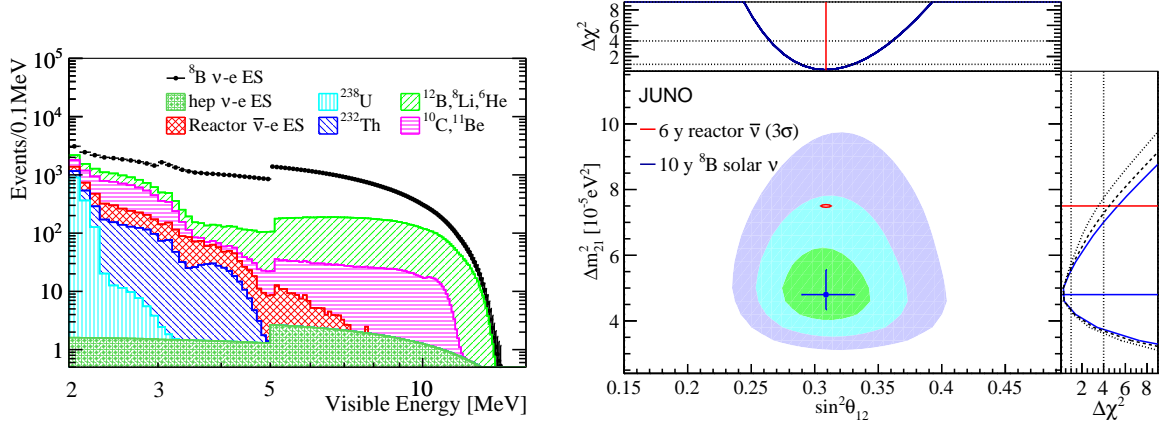
Figure 2.3 : *Signal and background spectra above 2 MeV expected in JUNO in 10 years after the selection cuts (left), and the expected precision of* $\sin^2\theta_{12}$ *and* Δm_{21}^2 *(right)* [115].

of over 15 MeV. The abundance of ^{13}C in the JUNO LS is 1.1%, amounting to 9×10^{30} ^{13}C targets, which is set to become the largest mass of ^{13}C nuclei in the history of LS detectors. Coupled with background levels as low as 10^{-17} g/g, JUNO will be able to experimentally observe ^{8}B solar neutrinos through CC and NC interactions on ^{13}C for the first time ever. Within 10 years, JUNO anticipates an additional 6,000 (3000) solar neutrino events from CC (NC) interactions with ^{13}C, which will lead to measure the ^{8}B solar neutrino flux to a precision of 5%. Through a JUNO+SNO combined analysis, a world-leading precision of 3% is anticipated [116].

JUNO's sensitivity to ^{7}Be, *pep* and CNO solar neutrinos has also been studied in the reference [117]. The results suggest that JUNO is expected to reach precisions of about 0.2%, 4% and 11% on the measurement of ^{7}Be, *pep* and CNO solar neutrino fluxes, respectively, within 6 years of data taking (assuming that the baseline LS radiopurity requirement of 10^{-16} g/g is achieved). It must be noted that JUNO will be able to significantly improve the current precisions on ^{7}Be and *pep* measurements with respect to that of Borexino within few years of data taking. JUNO's precision measurements of the neutrino flux from distinct solar processes offer detailed insights into the Sun's chemical composition and structure. This can lead to a comprehensive understanding of the fundamental processes governing the Sun's existence and evolution. Combined with future experiments such as Hyper-Kamiokande and DUNE, it may pave the way to shed new light on open issues in neutrino physics, such as non standard interactions of neutrinos.

2.2.3 Atmospheric neutrinos

Since the Earth is mostly transparent to neutrinos below the PeV energy scale, atmospheric neutrino detectors observe neutrinos from all directions, spanning diverse baselines (15 km to 1.3×10^4 km) and energies (0.1 GeV to 10 TeV), including all neutrino flavors. When they pass through the Earth, the MSW effect plays a key role, opening a unique opportunity to probe the NMO. Relevant oscillograms that depict the variation of oscillation probabilities $P_{\nu_\mu \to \nu_\mu}$ and $P_{\bar{\nu}_\mu \to \bar{\nu}_\mu}$ as a function of the energy of the neutrino and the zenith angle (θ)
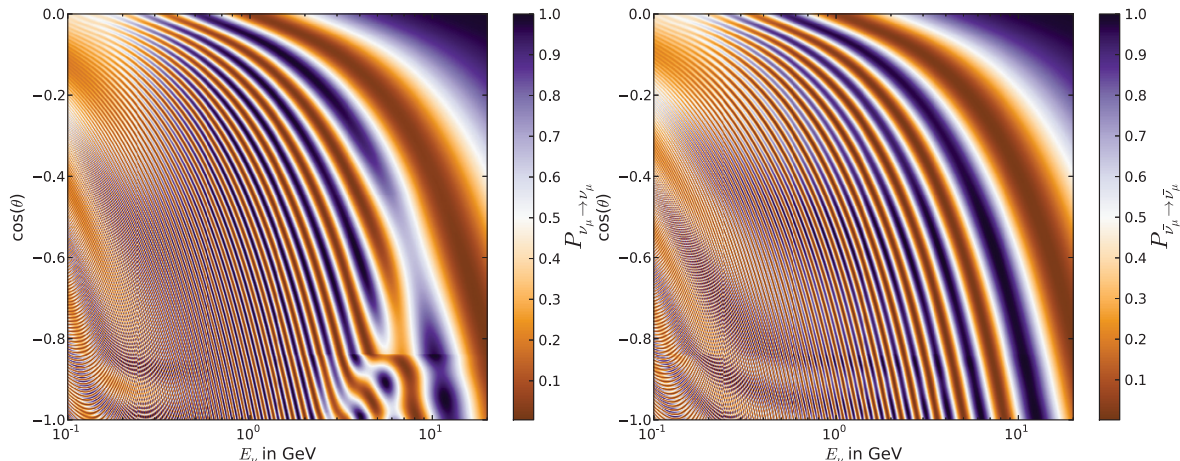
Figure 2.4 : *Variation of oscillation probabilities* $P_{\nu_\mu \to \nu_\mu}$ *and* $P_{\bar{\nu}_\mu \to \bar{\nu}_\mu}$ *as a function of the neutrino energy and the zenith angle, assuming normal ordering [12].*

assuming true normal ordering are shown in figure 2.4.

In the reference [12], the measurement of atmospheric neutrinos in JUNO and their contributions to the NMO determination has been investigated. To assess the reconstruction potential of the JUNO detector, a conservative selection of atmospheric ν_μ and $\bar{\nu}_\mu$ events with muon track length L_μ greater than 5 m and an angular resolution of $1°$ are used. These events are classified into fully contained (FC) ν_μ-like, FC $\bar{\nu}_\mu$-like, partially contained (PC) ν_μ-like, and PC $\bar{\nu}_\mu$-like samples based on the $\mu^\pm$ track and statistical charge separation. Considering different cross-sections, fluxes and oscillation probabilities, JUNO is foreseen to detect more than 20000 CC events and more than 12000 NC events during a period of 10 years. Numerical results indicate that JUNO's NMO sensitivity can reach 0.9σ for a 200 kton-year exposure with $\sin^2 \theta_{23} = 0.5$. Optimistically, sensitivity could reach 1.8σ over the span of 10 years, given the following assumptions: $\nu_e/\bar{\nu}_e$ CC events are well identified and reconstructed if the $e^\pm$ visible energy exceeds 1 GeV and the visible energy of accompanying hadrons is smaller than that of $e^\pm$; the selection condition for $\nu_\mu/\bar{\nu}_\mu$ CC events extends from $L_\mu > 5$ m to $L_\mu > 3$ m; and the charged lepton direction is replaced by the neutrino direction with a $10°$ angular resolution [13].

2.2.4 Core-collapse supernova neutrinos

Approximately 99% of the vast energy released in a core-collapse supernova (CCSN) is carried away by neutrinos within only few seconds. Only about 1% of the total energy of the CCSN manifests as the kinetic energy of the explosion. About 0.01% of the total CCSN energy is released as photons, which is still sufficient to outshine the host galaxy. While few CCSN events are estimated to occur every second throughout the visible universe, a detector like JUNO covers the events in our own galaxy and its satellites only [12].

CCSN neutrinos have energies in the range of several tens of MeV, allowing JUNO to detect all flavors of CCSN neutrinos through multiple channels: mainly via IBD, the elastic
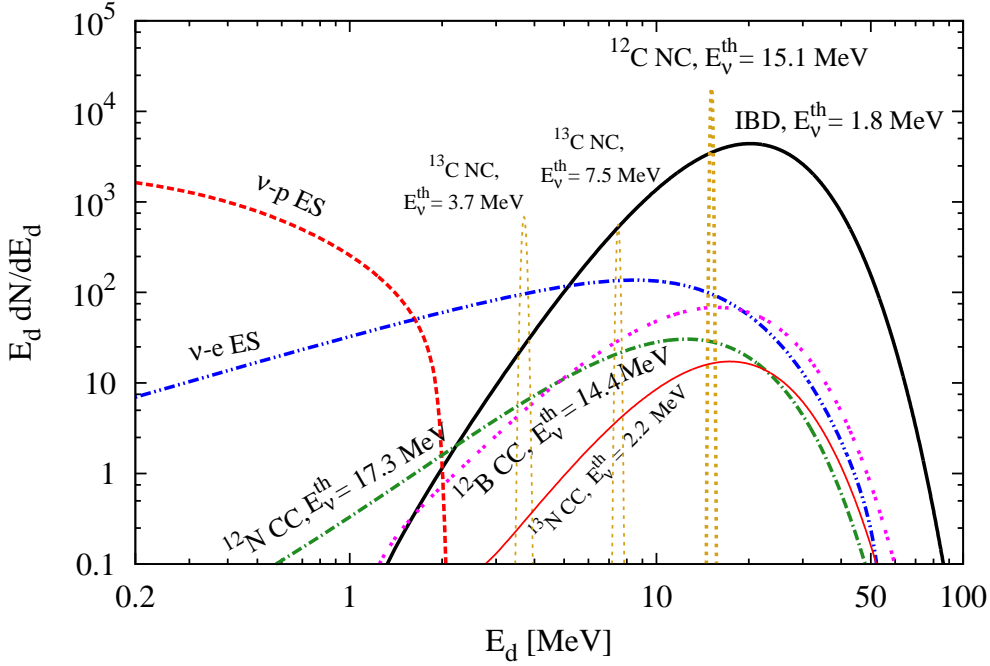
Figure 2.5 : *The neutrino event spectra with respect to the visible energy* E_d *in the JUNO detector for a typical SN at 10 kpC. (1) IBD (black, solid curve),* $E_d = E_\nu$ *- 0.8 MeV ; (2) Elastic neutrino-proton scattering (red, dashed curve),* E_d *= proton recoil energy; (3) Elastic neutrino-electron scattering (blue, double-dotted-dashed curve),* E_d *= electron recoil energy; (4) Neutral-current reaction* $^{12}C(\nu, \nu')^{12}C^*$ *(orange, dotted curve), with* $E_d = 15.1\,MeV$ *= energy of the* $^{12}C^*$ *de-excitation photon; (5) Charged-current reaction* $^{12}C(\nu_e, e^-)^{12}N$ *(green, dotted-dashed curve),* $E_d = E_\nu$ *- 17.3 MeV; (6) Charged-current reaction* $^{12}C(\bar{\nu}_e, e^+)^{12}B$ *(magenta, double-dotted curve),* $E_d = E_\nu$ *- 13.9 MeV [13].*

neutrino-electron scattering, and, the elastic neutrino-proton scattering. At a typical distance of 10 kpc and with typical CCSN parameters, JUNO is expected to detect approximately 5000 IBD events, around 300 elastic neutrino-electron scattering events, and roughly 2000 neutrino-proton scattering events. Additionally, the CC and NC interactions of neutrinos on ^{12}C nuclei will yield about 200 events and 300 events, respectively [13]. The interactions of pre-CCSN neutrinos with carbon nuclei are inaccessible because the energies of pre-CCSN neutrinos are of the order of few MeVs. At the same time, the visible energy of neutrino-proton elastic scattering events fall below the threshold owing to the significant proton quenching effect, limiting the available interactions for pre-CCSN neutrinos to only IBD and elastic neutrino-electron scattering interactions. Figure 2.5 depicts the neutrino event spectra with respect to the visible energy in the JUNO detector for a typical SN at 10 kpC.

Different backgrounds for detecting CCSN neutrinos exist, varying depending on the detector's location, type, and the signal channel utilized. Typically, background is not a significant issue during a supernova neutrino burst, lasting only around 10 seconds. Potential background sources for a specific signal channel include natural radioactivity (below 10 Hz at > 0.7 MeV), atmospheric muon-induced backgrounds (approximately 3 Hz muon rate in JUNO LS), the supernova neutrinos themselves, and other neutrinos [12].

A real-time monitoring system will detect the change in event rate due to pre-CCSN and

CCSN neutrinos, releasing an alert once it identifies a deviation from the steady event rate, indicative of a CCSN. Thus, JUNO will emerge as a significant contributor to the next-generation Supernova Early Warning System (SNEWS2.0) [118], for multi-messenger astronomy. Experimental observations of CCSN neutrinos with JUNO offer opportunities to explore various questions across astronomy, astrophysics, and particle physics, including stellar evolution, CCSN nucleosynthesis, as well as the neutrino mass scale and NMO.

2.2.5 Geo-neutrinos

Geo-neutrinos are electron antineutrinos that are produced from the beta decay of naturally occurring radioactive isotopes, primarily ^{238}U and ^{232}Th, found within the interior of the Earth. Detection of geo-neutrinos allow the measurement of the radiogenic heat generated by the decay of the aforementioned isotopes, shedding light on the formation and the chemical composition of the Earth. So far, only KamLAND [120] and Borexino [121] have measured geo-neutrinos, and none of them have sufficient sensitivity to determine the U/Th ratio to good accuracy, which is a crucial parameter to understand the specifics of the Earth's formation. JUNO will become part of the geo-neutrino experiment consortium, presenting an exceptional opportunity to measure geo-neutrinos.

JUNO can detect geo-neutrinos via the IBD interaction of geo-neutrinos with the JUNO LS. The primary challenge for JUNO's geo-neutrino measurement is the significant background from reactor antineutrinos. Additionally, other non-antineutrino backgrounds affect geo-neutrino detection, including atmospheric muons and the isotopes induced by them in the JUNO LS (such as ^{9}Li/^{8}He), fast neutrons, ^{13}C$(\alpha, n)^{16}$O reactions, and accidental coincidences. The geo-neutrino signal is derived from the observed IBD spectrum by applying a χ^2 fitting procedure using the least-squares method. The precision of this approach relies on the
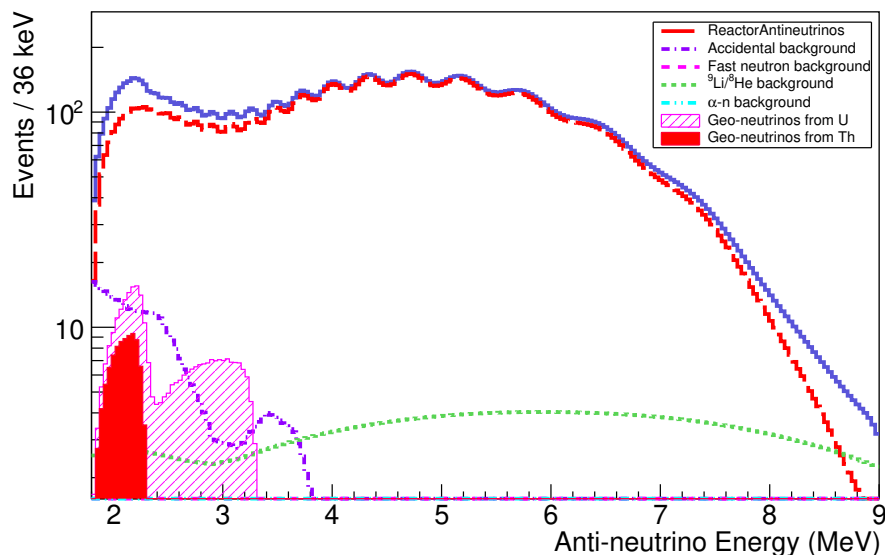
Figure 2.6 : *The energy spectra of geo-neutrinos, reactor antineutrinos, and other non-antineutrino backgrounds at JUNO for one year of data-taking. The blue solid line represents the total IBD spectrum [119].*

precise measurement of the reactor antineutrino spectrum, detailed understanding of the detector systematics, as well as the detailed understanding of different contributions from various sources of backgrounds. The energy spectra of geo-neutrinos, reactor antineutrinos, and other non-antineutrino backgrounds at JUNO for one year of data-taking is shown in the figure 2.6.

The expected geo-neutrino signal at JUNO has been calculated [122] adopting the reference Earth model [123]. The model uses a resolution of $1° \times 1°$ to set U and Th abundances based on geochemical and geophysical inputs. The geo-neutrino flux at JUNO experimental site is determined using a comprehensive regional lithospheric model that covers the nearest 500 km, which is integrated with a global model of the lithosphere and underlying mantle [119]. Within its inaugural year of operation, JUNO is projected to capture more geo-neutrino events than all other detectors combined up to that point, at a rate of about 400 events per year [12, 119]. The crust within a 500 km radius around JUNO contributes over 50% to the total signal. Therefore, detailed local geological models are essential for accurately estimating the crustal signal and separating it from the mantle signal. This effort presents an excellent opportunity for collaboration between geologists and particle physicists, allowing them to test predictions about the planet's interior.

2.2.6 Other physics

In addition to the above, JUNO bears potential to address a wide range of topics and open questions in particle physics, neutrino physics, astrophysics and cosmology. They span topics such as diffuse supernova neutrino background, nucleon decays, dark matter search, sterile neutrinos, search for exotic particles and many more, given the large target mass, low background, low energy threshold and excellent energy resolution of the JUNO detector.

2.3 JUNO reactor antineutrino signal and backgrounds

Understanding the reactor antineutrino spectrum is crucial for JUNO's main objectives. Accounting for experimental techniques and detector responses ensures accurate interpretation of observations. Additionally, comprehensive knowledge of background sources is necessary for efficient signal selection and background suppression. Under the following section, the reactor antineutrino flux, the signal and the associated backgrounds for the purpose of NMO determination and precision measurements of neutrino oscillation parameters is introduced.

2.3.1 The reactor antineutrino spectrum

As shown in figure 2.7, JUNO is situated at distances of about 52.5 km from the Yangjiang and Taishan nuclear power plants (NPP), which act as JUNO's primary antineutrino sources for the NMO determination and precision measurements of the neutrino oscillation parameters. The distance has been optimized to achieve the best sensitivity for the resolution of NMO. Yangjiang and Taishan NPPs have six and two reactor cores respectively, which provide a

Figure 2.7 : *Location of the JUNO experimental site, the nearest nuclear power plants and TAO [13].*

combined nominal thermal power of 26.6 GW$_{th}$. The next closest reactor to JUNO is the Daya Bay NPP, which is located about 215 km from the JUNO experimental site. All reactors in the vicinity of JUNO are commercial pressurized water reactors. More than 99% of the total antineutrino flux are generated through the fission reactions of the isotopes ^{235}U, ^{238}U, ^{239}Pu and ^{241}Pu isotopes in the reactor fuel. Accurate measurements of reactor power and fission fractions for each reactor core will be supplied by the NPPs over time once JUNO begins its data acquisition. The reactor antineutrino spectrum $\phi_r \left(\mathrm{E}_{\bar{\nu}_\mathrm{e}}, t \right)$ generated by a reactor r as a function of antineutrino energy $\mathrm{E}_{\bar{\nu}_\mathrm{e}}$ and time t [12] can be written as

$$\phi_r \left(\mathrm{E}_{\bar{\nu}_\mathrm{e}}, t \right) = \frac{\mathrm{W}_r \left(t \right)}{\sum_i f_{ir} \left(t \right) \mathrm{e}_i} \sum_i f_{ir} \left(t \right) s_i \left(\mathrm{E}_{\bar{\nu}_\mathrm{e}} \right), \tag{2.2}$$

where $\mathrm{W}_r \left(t \right)$ is the total thermal energy of the reactor r at time t, $f_{ir} \left(t \right)$ is the fission fraction of the isotope i at time t, e_i effective thermal energy per fission of the isotope i, and, $s_i \left(\mathrm{E}_{\bar{\nu}_\mathrm{e}} \right)$ is the antineutrino energy spectrum of the fission of isotope i. The spectra $s_i \left(\mathrm{E}_{\bar{\nu}_\mathrm{e}} \right)$ for different isotopes i mentioned earlier are shown in the figure 2.8.

A small satellite detector known as Taishan Antineutrino Observatory (TAO) [124] is being constructed at about 44 m away from one of the Taishan reactors, as mapped in figure 2.7. The TAO detector, shown in figure 2.9, aims to provide a precise reactor antineutrino spectrum which will be used as the reference spectrum for JUNO analyses. TAO consists of a spherical acrylic vessel containing 2.8 ton Gadolinium-doped LS which is expected to reach a photon detection efficiency of about 50% using 4024 silicon photomultipliers. TAO will measure the total antineutrino spectrum of the NPP core over multiple fuel cycles, with an excellent energy resolution better than 2% at 1 MeV. It anticipates detecting approximately 1000 IBD events per day, in comparison to the expected 57 IBD events per day projected for JUNO [125].

JUNO detects electron antineutrinos via the IBD process, where a $\bar{\nu}_e$ interacts with a proton
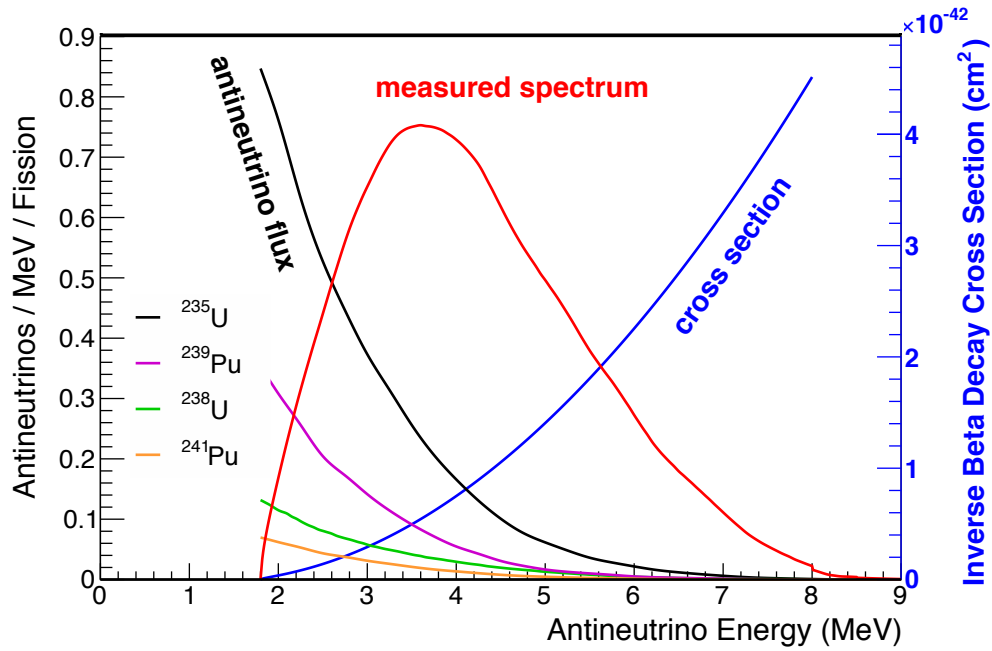
Figure 2.8 : *The reactor antineutrino flux from the individual isotopes, weighted by their typical contribution to the total flux in a commercial reactor (black/purple/green/orange), the IBD cross section (blue, axis on the right), and the product of the total reactor antineutrino flux and the IBD cross section that gives the measured unoscillated antineutrino spectrum (red) [126].*
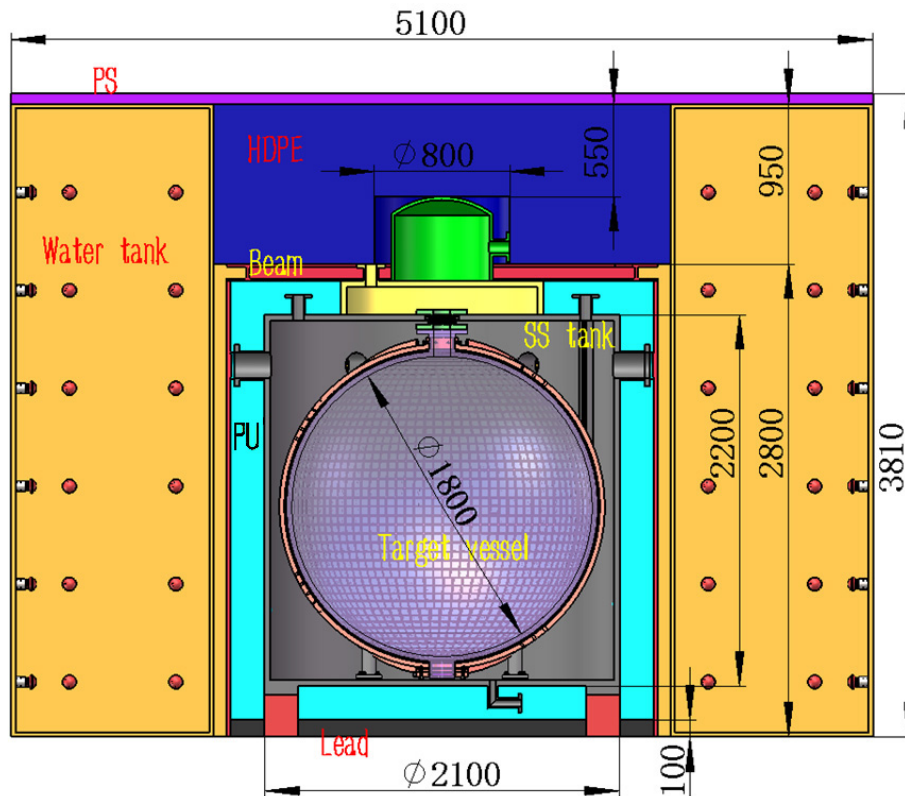
Figure 2.9 : *Schematic diagram of TAO. All dimensions are in mm [124].*

in the JUNO LS, as illustrated in the figure 1.3. The e^+ carries the majority of the energy of the incident $\bar{\nu}_e$ because the neutron is significantly heavier than the e^+. In a matter of a few nanoseconds, the e^+ rapidly transfers its kinetic energy to the medium and annihilates with an e^- in the medium, resulting in the production of a pair of 0.511 keV photons. The collective signal generated in the detector due to these processes is referred to as the prompt signal. The neutron scatters within the medium, traversing tens of centimeters over around 200 microseconds until it is thermalized enough to be captured, resulting in the emission of a photon that constitutes the delayed signal.

The cross section of the IBD interaction [127] can be expressed as

$$\sigma\left(\mathrm{E}_{\bar{\nu}_e}\right) = 0.0952 \times 10^{-42} \mathrm{cm}^2 \left(\frac{\mathrm{E}_{e^+} \cdot p_{e^+}}{1 \ \mathrm{MeV}^2}\right), \tag{2.3}$$

where E_{e^+} and p_{e^+} are the total energy and the momentum of the e^+, respectively. The IBD cross section, the antineutrino flux from different fission isotopes of the NPPs, as well as the total unoscillated antineutrino spectrum as a function of the antineutrino energy is illustrated in figure 2.8. Assuming that the neutron recoil energy is negligible, E_{e^+} can be written as $\mathrm{E}_{e^+} = \mathrm{E}_{\bar{\nu}_e} - (\mathrm{M}_n - \mathrm{M}_p)$, where M_n and M_p are the neutron and proton masses, respectively. The IBD interaction is initiated when the energy $\mathrm{E}_{\bar{\nu}_e}$ surpasses a threshold of approximately 1.806 MeV, attributed to the mass difference between the reactants and the products involved. By taking into account the IBD cross section, IBD detection efficiency of the detector (ϵ) and the number of proton targets of the detector (N_p), the total unoscillated antineutrino spectrum $\Phi\left(\mathrm{E}_{\bar{\nu}_e}, t\right)$ observed by a detector at time t at a baseline L_r from various reactors is given by

$$\Phi\left(\mathrm{E}_{\bar{\nu}_e}, t\right) = \epsilon \mathrm{N}_p \sigma\left(\mathrm{E}_{\bar{\nu}_e}\right) \sum_r \frac{\phi_r\left(\mathrm{E}_{\bar{\nu}_e}, t\right)}{4\pi \mathrm{L}_r^2}. \tag{2.4}$$

2.3.2 The expected reactor antineutrino signal for JUNO

Therefore, the total oscillated antineutrino spectrum as observed by the detector at a baseline L_r at time t can be expressed as

$$\Phi_{osc}\left(\mathrm{E}_{\bar{\nu}_e}, t\right) = \epsilon \mathrm{N}_p \sigma\left(\mathrm{E}_{\bar{\nu}_e}\right) \sum_r \frac{1}{4\pi \mathrm{L}_r^2} \mathrm{P}_{\bar{\nu}_e \to \bar{\nu}_e} \phi_r\left(\mathrm{E}_{\bar{\nu}_e}, t\right). \tag{2.5}$$

The reactor antineutrino visible energy (i.e. the prompt energy) spectrum expected in JUNO is shown in the figure 2.10. It indicates that the majority of the IBD events have their prompt energies in the range 0.7 MeV up to 8 MeV. The neutron that leads to the delayed signal is predominantly captured by protons ($\sim$99%), releasing a 2.2 MeV photon and much less frequently on carbon ($\sim$1%), leading to the emission of a 4.9 MeV photon. By selecting pairs of prompt-delayed signals that fall within the respective energy ranges and occur within short spatial and temporal intervals from each other as described, true IBD events can be efficiently identified while significantly suppressing uncorrelated backgrounds.
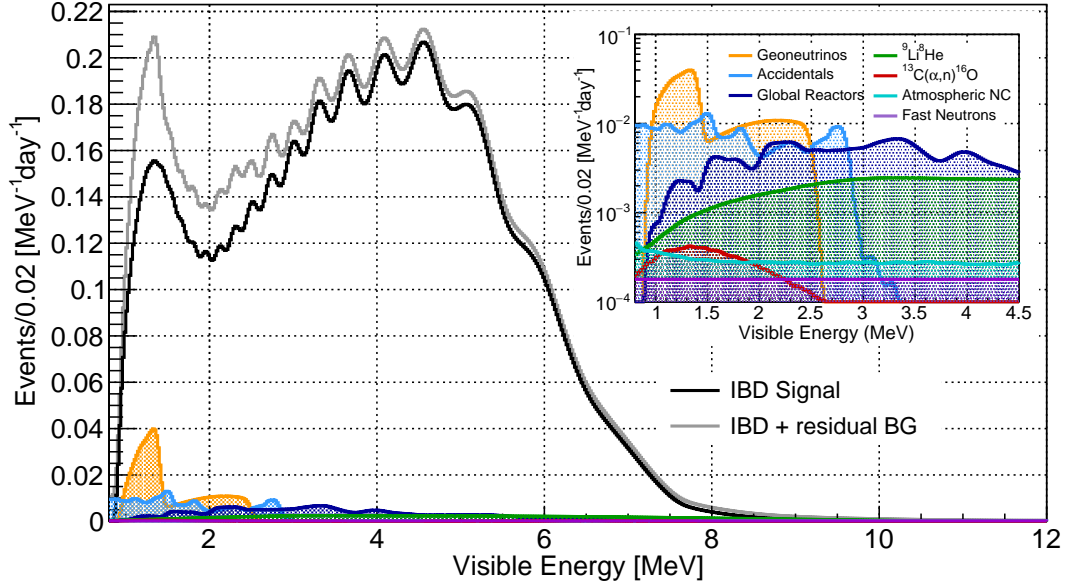
Figure 2.10 : *Visible energy spectrum expected in JUNO as measured with (grey) and without (black) backgrounds. The inset shows the spectra of the expected backgrounds, which amount to about 7% of the total IBD candidate sample and are mostly localized below ~3 MeV. The rates of different backgrounds in JUNO and the associated rate and shape uncertainties are presented in the table 5.3 [112].*

2.3.3 Backgrounds to the JUNO reactor antineutrino spectrum

The rate of antineutrino interactions in JUNO is expected to be about 60 counts per day. The main sources of background to the JUNO reactor antineutrino spectrum originate from natural radioactivity within and from the surroundings of the detector, by-products generated when atmospheric muons traverse through the detector and its environment, as well as the electron antineutrinos emitted by other sources such as distant reactors and geo-neutrinos. These backgrounds could generate detector signatures that mimic prompt-delayed IBD coincidences, as detailed below.

^{9}**Li**/^{8}**He**: The atmospheric muons that manage to penetrate the overburden and reach the JUNO LS can lead to spallation of carbon atoms in the LS, inducing a variety of radioisotopes. Some of them, most notably ^{9}Li and ^{8}He, undergo radioactive decay producing an e^- and a n. The energy deposited by e^- from muon spallations span almost the entirety of the energy range of interest for the IBD spectrum. Additionally, the topology of the scintillation produced by the e^- and that produced by a e^+ are indistinguishable in the JUNO detector. Hence, the deposition of energy by the e^- in the JUNO LS followed by the n-capture produces correlated prompt-delayed signals which imitate the IBD signature in the JUNO detector.

Accidental background: Uncorrelated single energy depositions that appear to be a prompt-delayed IBD signal pair are known as accidental background events. It consists of three main types: accidental correlation of two natural radioactive decays, a natural radioactive decay and the decay of a radioisotope induced by atmospheric muon spallations, and, a natural

radioactive decay and the capture of neutrons induced by atmospheric muon spallations.

Fast neutrons: The atmospheric muons that pass through the rock and other materials that surrounds the detector can induce spallation neutrons. The energetic neutrons produced in this manner can create a signal resembling an IBD signature by scattering off a proton before being captured in the JUNO LS.

^{13}**C$(\alpha, n)^{16}$O background**: The α particles from the radioactive decays of ^{238}U and ^{232}Th can interact with the ^{13}C in the LS. It can result in the generation of correlated signals that appear as IBD coincidences if the neutron is energetic enough or if a photon is produced via ^{16}O de-excitation.

Geo-neutrinos and $\bar{\nu}_e$ from distant reactors: The background due to $\bar{\nu}_e$ from geo-neutrinos and distant reactors is indistinguishable from a genuine JUNO reactor IBD. The geo-neutrino background is predominantly from the decays of ^{238}U and ^{232}Th, each contributing to about 77% and 23% of the total geo-neutrino background, respectively. These geo-neutrinos typically have energies below 2.4 MeV [128]. The energy spectrum of antineutrinos emitted by distant nuclear reactors is uniquely defined by the mixture of decaying isotopes. However, neutrino oscillations alter this spectrum as observed by the detector, with the distortion depending on the distance from each reactor. The antineutrinos from these distant reactors generally have energies below 10 MeV [129].

Atmospheric neutrino NC interactions: High-energy atmospheric neutrinos of all flavors can induce NC interactions with the JUNO LS, producing particles such as neutrons, protons, α particles, and excited light nuclei. These particles deposit their energy either immediately or shortly after production, potentially mimicking the IBD signature when followed by the capture of a spallation neutron.

The 700 m overburden suppresses the atmospheric muon flux reaching the JUNO detector down to 4.1×10^{-3} Hz·m^{-2} [112]. According to the final background budget for the main materials used for JUNO [130], via strict radiopurity control of materials, rigorous maintenance of cleanliness, and a careful arrangement of experimental apparatus, the single event rate in the sensitive volume of the detector due to natural radioactivity can be maintained below 10 Hz. In addition, implementation of atmospheric muon veto cuts is necessary for the efficient rejection of ^{9}Li/^{8}He and fast neutron backgrounds. The JUNO muon veto system is introduced under section 2.4. The visible energy spectrum for IBD interactions expected in JUNO and the contributions of different residual backgrounds following JUNO antineutrino selection is shown in the figure 2.10. JUNO's antineutrino selection criteria includes an IBD prompt-delayed coincidence search coupled with muon veto conditions, which will be introduced in detail under chapter 5. This strategy is capable of reducing background event rates down to about 4.11 counts per day, while maintaining an 82.2% efficiency in selecting genuine reactor IBD events [112].

2.4 The JUNO detector

The JUNO detector comprises two main components: namely, the neutrino target, and, the muon veto system. The neutrino target of the JUNO detector is the Central Detector (CD),

Top Tracker and calibration house

Water pool

Earth magnetic field compensation coils

Photomultiplier tubes

Acrylic spherical vessel filled with liquid scintillator

Acrylic supporting nodes
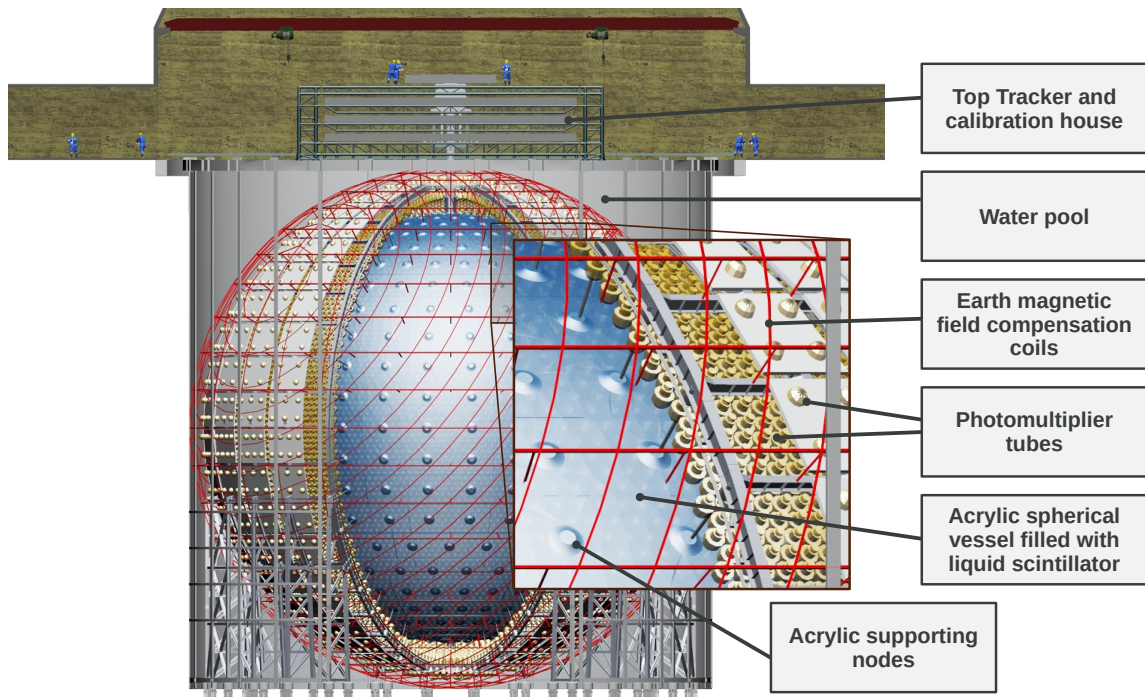
Figure 2.11 : *Schematic of the main JUNO detector [112].*

which is a spherical acrylic vessel of diameter 35.4 m that holds 20 ktons of LS viewed by 17,612 20-inch photomultiplier tubes (PMT), and 25,600 3-inch PMTs. The muon veto system is composed of two sub-detectors, namely, the Water Cherenkov Detector (WCD), and the Top Tracker (TT). The CD, WCD, and the TT are illustrated in the figure 2.11. The CD is fully immersed within the WCD, which is a cylindrical pool of ultrapure water. Serving as a protective barrier against external radioactivity and fast neutron background, a 1.4 m thick water buffer separates the acrylic vessel from the PMT photocathodes, shielding the LS from any radioactivity emitted by the PMT glass. The WCD and CD are optically isolated from each other. Atop the WCD lies the TT which is a three-layer plastic scintillator array, used for the precise tracking of a portion of the muon flux through the detector.

2.4.1 The Central Detector

The 20 kton liquid scintillator detector, known as the Central Detector, is designed to have an effective energy resolution of 3% at 1 MeV, which is one of the crucial requirements to achieve JUNO's primary mission. The CD construction is a significant challenge in JUNO, particularly owing to its large size. Housed within a spherical acrylic vessel with an inner diameter of 35.4 m and thickness of 120 mm, the LS is supported by a stainless steel (SS) structure via 590 connecting bars, which rests on a bearing consisting of 30 pairs of supporting legs rooted in the concrete floor of the WCD [14], as shown in the figure 2.12. The SS structure also accommodates 17,612 20-inch and 25,600 3-inch PMTs pointing inward to detect scintillation light. The 20-inch PMTs provide a photocathode coverage of 75.2%, while the 3-inch PMTs provide a coverage of 2.7%. All PMTs have undergone mass-testing
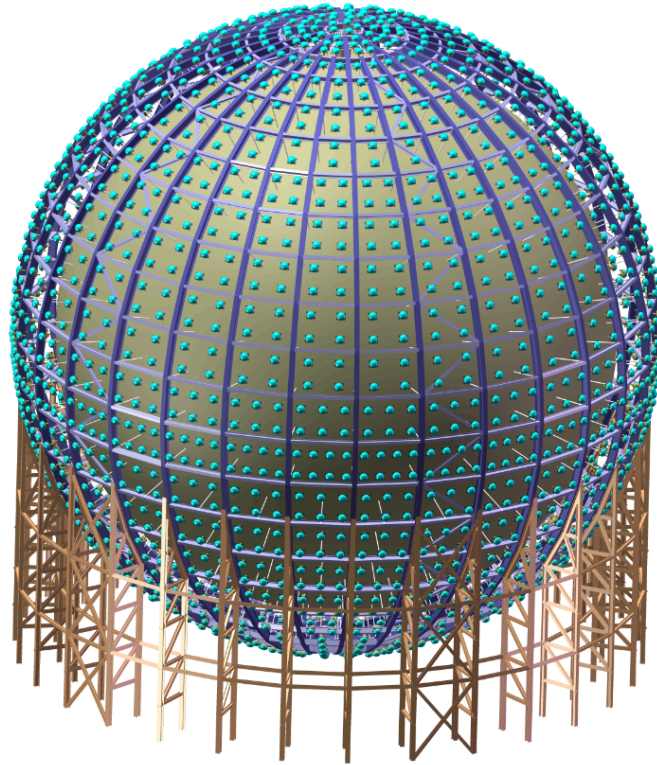
Figure 2.12 : *The arrangement of WCD PMTs on the JUNO SS structure [131].*

and characterization using dedicated setups [132, 133]. The photon detection efficiency of the PMTs is measured using a photon counting method applied to charge spectra generated following the injection of light using stabilized, low-intensity pulsed LEDs. The average photon detection efficiency of 20-inch and 3-inch CD PMTs is found to be 30.1% [134] and 24% [135] respectively.

Furthermore, special protection measures have been implemented for the large PMTs to safeguard against implosion. Compensation coils are installed on the SS structure to dampen the geomagnetic field and mitigate its influence on the photoelectron collection efficiency of the PMTs [136]. Additionally, the SS structure supports front-end electronics and cables, all requiring stability and reliability throughout JUNO's designed 30-year lifetime. Crafted through the bulk polymerization of 265 acrylic pieces, the acrylic vessel's formulation prioritizes optimal transparency, radiopurity, and durability. Supported by connection structures attached to the SS structure, the critical nodes on the vessel contribute significantly to stress management.

In recent LS experiments, a commonly utilized solvent is linear alkylbenzene (LAB), recognized for its exceptional transparency, high flash point, low chemical reactivity, and strong light yield, combined with 2,5-diphenyloxazole (PPO) as the fluor and p-bis-(o-methylstyryl)-benzene (bis-MSB) as the wavelength shifter. To enhance the light yield of the JUNO LS, various concentrations of the fluor and the wavelength shifter were evaluated using one

of the Daya Bay antineutrino detectors. After adjusting for differences in size between the JUNO and Daya Bay detectors, a new optical model was developed [137]. Relevant parameters were fine-tuned to determine the optimal composition for the JUNO LS: purified solvent LAB with 2.5 g/L PPO, and 3 mg/L bis-MSB [13, 138]. Before filling, the LS will undergo purification to enhance its radiopurity and transparency. JUNO also has an Online Scintilator Internal Radioactivity Investigation System (OSIRIS) which monitors the radiopurity of the JUNO LS during filling, which spans several months [139]. Results from a pilot plant test indicate that the LS's attenuation length can exceed 20 m. Based on preliminary simulations considering PMT detection efficiency and other detector parameters, a light yield of 1665 photoelectrons (PE) per MeV is projected [140].

2.4.2 The Water Cherenkov Detector

The JUNO Water Cherenkov Detector adopts a cylindrical shape with dimensions of 43.5 m in diameter and 44 m in height. Its side walls and the bottom are lined with 5 mm thick High-Density Polyethylene (HDPE) material, serving as a barrier against Radon gas from external sources and preventing water leakage. The detector is filled with 35 ktons of ultrapure water and features an outer surface equipped with 2400 20-inch MCP-PMTs facing outward, integrated into the SS frame, as shown in figure 2.12. The WCD serves a dual purpose: it acts as a shield to protect the CD from contaminants from the surroundings, as well as a muon veto that can reach a muon tagging efficiency of 99.5% [15]. To enhance light collection efficiency, a <1 mm thick white Tyvek film is applied as a reflector on the side walls, bottom, and the surface of the SS structure. The experiment utilizes a water system with a flow rate of 100 tons per hour to ensure high water quality as well as to maintain the CD at a temperature of 21℃. One detector volume can be circulated within 2–3 weeks.

2.5 The Top Tracker

The primary function of the Top Tracker is to track and precisely reconstruct atmospheric muons as they traverse it. Spanning approximately 60% of the surface area above the WCD, it can accurately track around 30% of the total muon flux at the CD. Chapter 5 presents a detailed study of how the TT's muon tracking capabilities allow the selection of a high-purity sample of ^{9}Li/^{8}He isotopes and the measurement of the visible energy spectrum of ^{9}Li/^{8}He in the JUNO detector. Furthermore, a well-reconstructed muon sample measured using the TT can be used for the calibration of the CD muon reconstruction.

2.5.1 The geometry and the components

In general terms, the TT is a three-layer array of plastic scintillator strips re-purposed from the OPERA Target Tracker [17]. The scintillator strips consist of polystyrene blended with 2% p-Terphenyl as the primary fluor, and 0.02% POPOP as the secondary fluor. A TiO$_2$ reflective coating around the scintillator material ensures efficient light collection. An embedded Kuraray Y11(175)-MJ [141] Wavelength-Shifting (WLS) double-cladding optical
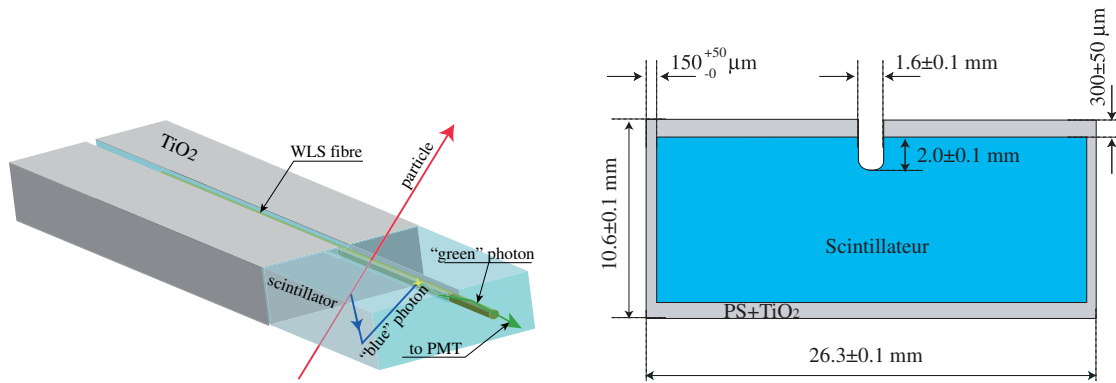
Figure 2.13 : *Particle detection principle (left), and the geometry (right) of a plastic scintillator strip [17].*
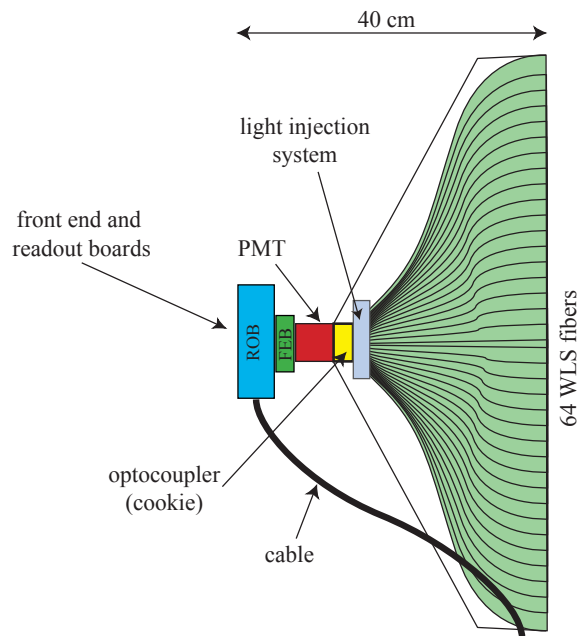
Figure 2.14 : *Schematic diagram of the end-cap of a TT module[17].*

fibre collects the scintillation light produced in the strips due to the energy deposition from ionizing particles such as muons traversing the strips, as illustrated in figure 2.13. A fundamental unit of the TT, known as a TT module, is formed by laying 64 plastic scintillator strips parallel to each other along the long edge of the scintillator strips. In a TT module, the strips are glued together using aluminum sheets that serve also as covers. At either end-cap of a TT module (shown in the figure 2.14), the optical signals transmitted by the WLS fibres are read-out using a 64-channel MultiAnode Photomultiplier (MA-PMT). The fibres are coupled to the MA-PMT using an optocoupler. The end-cap regions of the TT module also contains front-end electronics (that are introduced in detail under section 2.5.3) as well as a light injection system. The light injection system consists of two blue LEDs, straight PMMA light guides and a white painted diffusive box that is used to inject light to the region of WLS fibres just in front of the fibre-MA-PMT optocoupler, used for MA-PMT
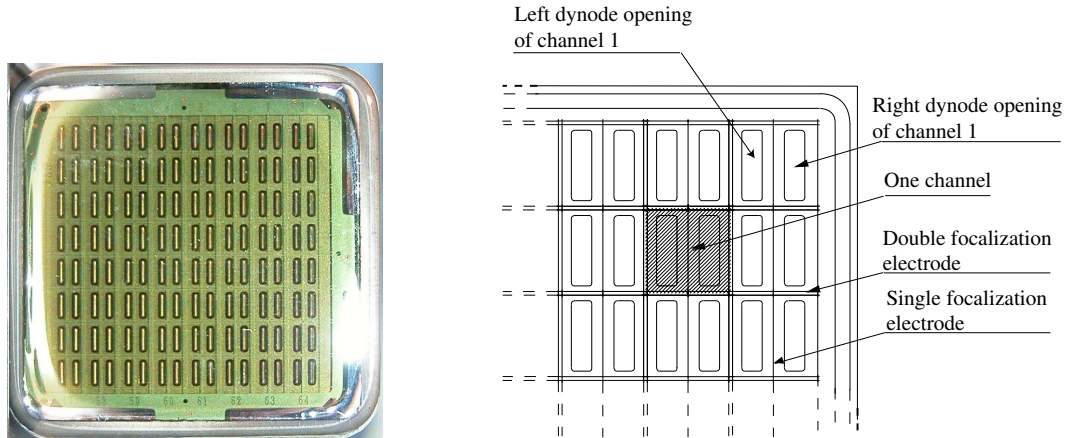
Figure 2.15 : *The front-face (left) and a schematic diagram of a Hamamatsu H7546 MA-PMT (right)* [17].

calibration tasks.

The TT employs Hamamatsu H7546 [142] 8×8-channel MA-PMTs shown in figure 2.15, whose individual performance is well known from their previous use in the OPERA Target Tracker [17]. It features channels with a surface area of 2.3 mm × 2.3 mm, each comprising two sets of 12 dynodes, as shown in figure 2.15 (right). It is powered by a negative-polarity high voltage of the range -800 V to -950 V, that corresponds to a gain of 10^6. Photoelectrons generated upon photon interactions with the photocathode are efficiently accelerated and directed towards the dynodes using focalization electrodes, enhancing the detection efficiency of the MA-PMT. Subsequently, the series of dynodes amplify the photoelectron signal through electron multiplication via secondary emission processes, resulting in a measurable quantity of charge.

An assembly of four TT modules laid side by side forms a TT plane that forms a sensitive surface area of 6.7 m^2×6.7 m^2. As depicted in figure 2.16, stacking two TT planes atop each other, such that the scintillator strips of each plane are aligned perpendicular to those of the other, enables the creation of a TT wall capable of providing 3D track information for particles crossing the TT wall. JUNO inherited 62 TT walls from the OPERA Target Tracker, amounting to 31,744 scintillating strips with 63,488 electronic channels.

The TT walls have been arranged in three horizontal layers to form the TT as shown in figure 2.17. The neighbouring TT walls overlap with each other by 150 mm at every edge to limit dead zones between them. A mechanical bridge constructed above the CD and WCD supports the TT detector. It constitutes two main beams of 48 m across the experimental hall, three layers of transverse girders separated by 20 m each, a support for the JUNO calibration system as well as support frames for the TT walls. The walls will be installed on their individual support frames. The frames are rigid enough to hold the walls flat during and after installation. Based on their placement, the modules of each wall are oriented either upwards or downwards, allowing their end caps and electronics to be accessible from the outside.

Distance between neighbouring TT layers is chosen to be 1.5 m as a compromise between
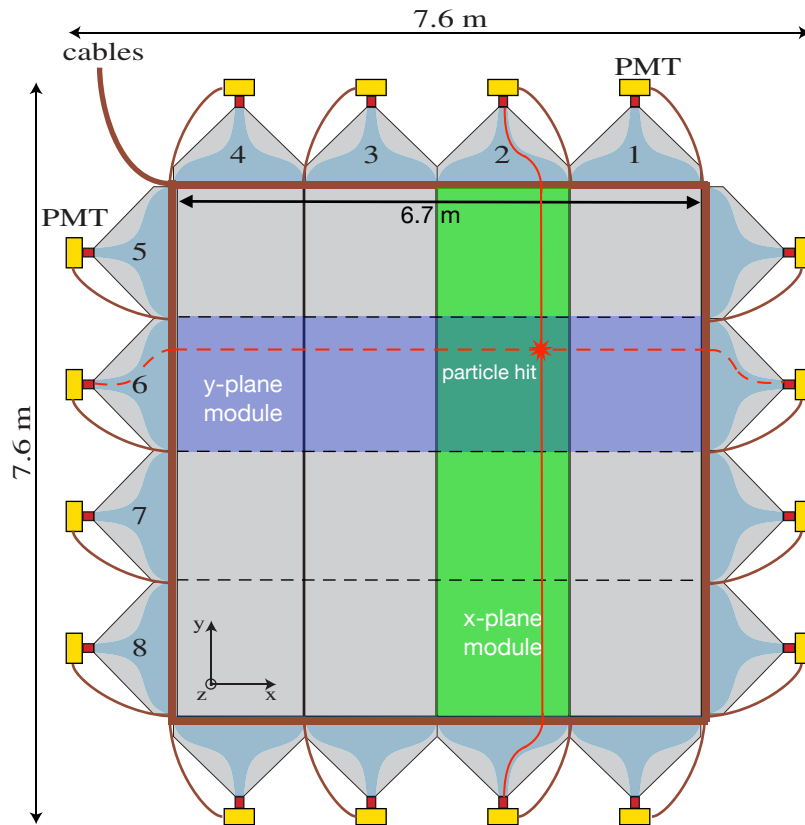
Figure 2.16 : *Schematic diagram of a TT wall. Adapted from [17].*
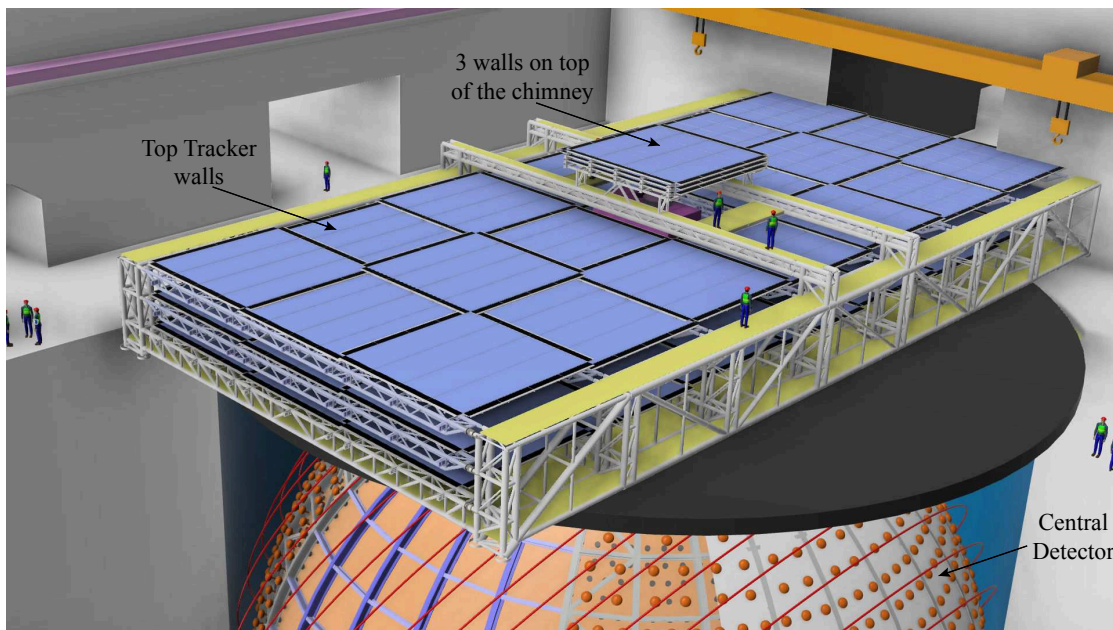
Figure 2.17 : *Schematic view of the JUNO Top Tracker on top of the Central Detector [16].*

56

the precision of muon tracking and the size of the mechanical support structure. In one horizontal direction, three walls are positioned over a 20 m span, while in the other direction, seven walls are situated across a 47 m span, leaving a void in the center for the JUNO chimney (comprising 20 walls per layer). This configuration utilizes 60 walls, with the modules of the remaining two walls rearranged and positioned atop the chimney, which is a section of the JUNO detector not enclosed by the WCD. The two remaining walls are rearranged to ensure three layers above the chimney as follows: one full TT wall is placed at the lowest section, while partial TT walls are positioned in the middle and upper sections, with each section separated by 23 cm. These partial walls over the chimney encompass only the two central modules in each layer, totalling four modules per wall, thereby covering the chimney's center.

2.5.2   Expected MA-PMT trigger rates of the Top Tracker

At the JUNO site, the expected muon rate crossing the entire TT is around 4 Hz. In contrast, the expected event rate following the MA-PMT trigger over the full TT detector is dominated by the radioactivity of the surrounding rock amounting to about 8 MHz. It is significantly larger than the overall rate of radioactivity of the components of the TT itself, which is about 9 kHz. During the JUNO site survey, measurements of radioisotope levels of the rock samples from JUNO site were realised at the Laboratoire de Physique des deux infinis[1], Bordeaux. It revealed that the radioisotope levels at the JUNO cavern are approximately two orders of magnitude higher than those at the Laboratori Nazionali del Gran Sasso (LNGS) cavern which hosted the OPERA experiment. In addition to that, the OPERA Target
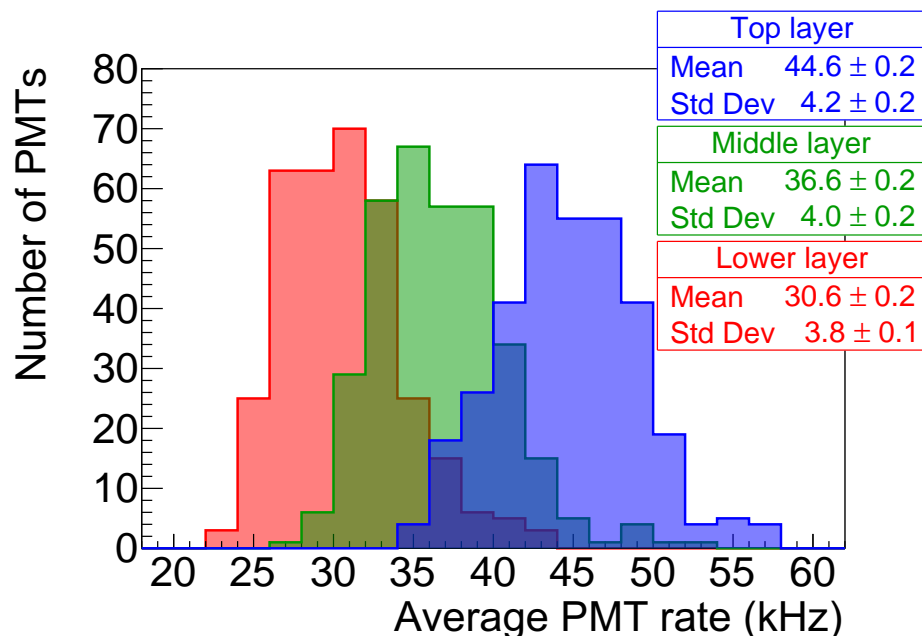
Figure 2.18 : *Trigger rate per MA-PMT for the three TT layers. An MA-PMT trigger threshold of 1/3 PE is assumed [16].*

---

[1]formerly known as Centre d'Etudes Nucléaires de Bordeaux Gradignan
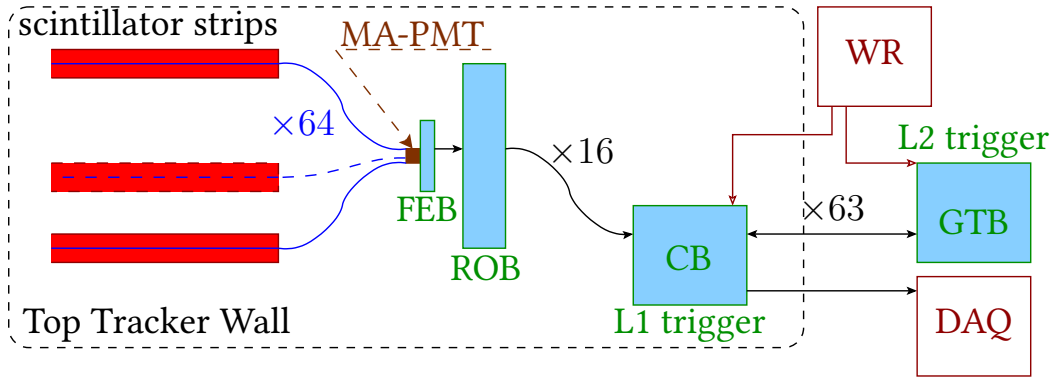
Figure 2.19 : *The TT electronics implementation (please refer to section 2.5.3 for more details) [16].*

Tracker modules were shielded by lead/emulsion bricks, whereas at the JUNO site, TT will be directly exposed to the rock. The MA-PMT trigger rate induced by rock radioactivity is estimated using JUNO's official simulation software [18, 143]. It shows varying trigger rates per MA-PMT, ranging from 20 kHz to 60 kHz. As indicated in figure 2.18, the MA-PMT trigger rates vary with respect to position as the TT walls nearer to the rock experience high exposure to radiation, while the upper layers offer some shielding to the lower ones.

2.5.3   The electronics

To cope with high trigger rates described above, dedicated electronics that are capable of efficient event selection, data readout, and timestamping have been designed. The conceptual implementation of the TT electronics is illustrated in figure 2.19. The Front-End Board (FEB) houses an application-specific integrated circuit (ASIC) known as Multi-Anode ReadOut Circuit (MAROC3) [144] which provides channel-by-channel charge and trigger information relevant to the MA-PMT signals. Based on the trigger information of the 64 MA-PMT channels, the MAROC3 provides a FAST-OR signal (the OR of all 64 trigger outputs). The Read-out Board (ROB) is positioned after the FEB to receive the MA-PMT data and transmit it to the Concentrator Board (CB). The CB aggregates the data from 16 FEB/ROBs within the TT wall. In the TT, the MA-PMT trigger threshold is foreseen to be kept at 1/3 PE (corresponding to a charge of about 50 fC for a MA-PMT gain of 10^6). When at least one MA-PMT channel is triggered (i.e. when the signal from at least one MA-PMT channel exceeds the trigger threshold), the MAROC3 sends the corresponding FAST-OR to the ROB. Then, the ROB issues a command to initiate charge measurement in the MAROC3, with a tunable delay and a time jitter of less than 1 ns. This approach ensures a charge measurement precision better than 1% [16].

The ROB transmits the FEB FAST-OR to the CB, which is utilized by the CB for data timestamping. Upon reception of the FAST-OR, the CB checks for x-y coincidences (L1 trigger) at the wall level. If no x-y coincidences are found, the CB sends a RESET signal to the ROB to minimize the dead-time of the MAROC3 due to the charge read-out, and to prepare it to accept a new signal. Upon detecting an x-y coincidence, the CB relays this information to the Global Trigger Board (GTB), which then searches for spatially aligned x-y coincidences across all three TT layers (L2 trigger) using a sliding window of 300 ns. The GTB
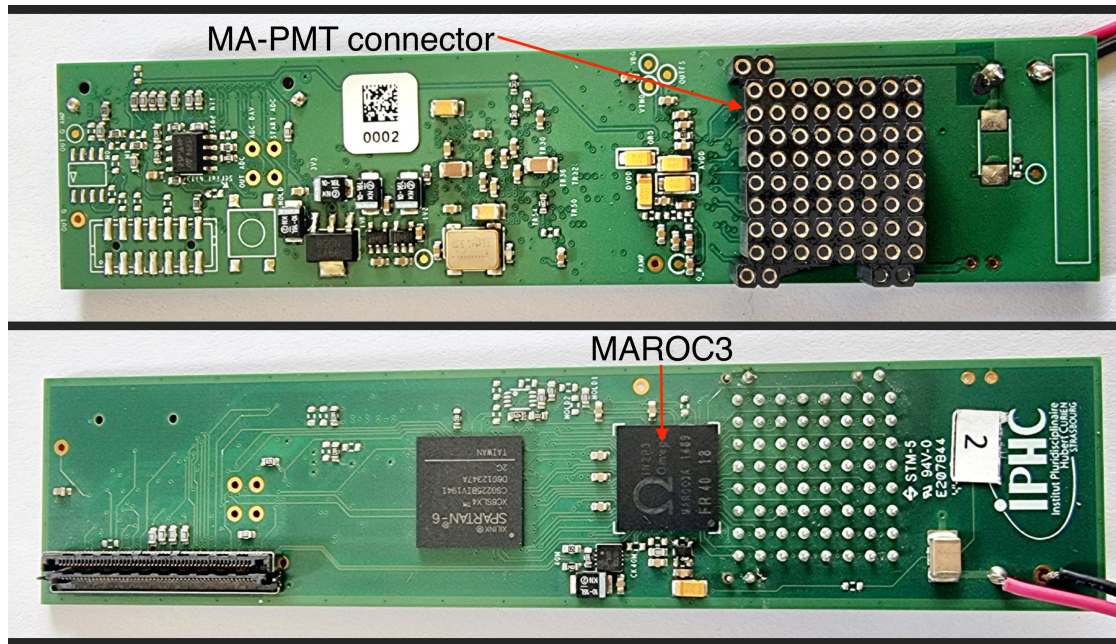
Figure 2.20 : *The Front-End Board of the JUNO Top Tracker.*

subsequently sends a validation or rejection signal back to the CBs, which correspondingly either transmits the related data to the JUNO data acquisition system or issue a RESET signal to the relevant ROBs. Both trigger levels play a crucial role in significantly reducing the TT data rate, as previously discussed, and minimizing the detector dead-time of the FEB MAROC3. The CB then transmits the validated events to the Data Acquisition (DAQ) system. To maintain synchronization across all CBs and the GTB, a timing system based on the White Rabbit (WR) [145] standard is used.

Front-End Board (FEB) and the Read-Out Board (ROB)

Figure 2.20 depicts a photograph of a FEB. The output signal from the MA-PMTs is read by the FEBs, which act as a fast-triggering electronic interface to the MA-PMTs. The MAROC3 chip of the FEB accounts for most of the tasks of the FEB. Each MA-PMT channel's signal is amplified by a variable gain preamplifier within the MAROC3, while maintaining electronic cross-talk levels among neighbouring channels below 0.25% [144]. The MA-PMT high voltage is common to all the channels. However, this does not translate to uniform response to incoming signals across all MA-PMT channels. Hence, tuning individual preamplifier gains in the MAROC3 make it possible to compensate for gain non-uniformities, ensuring uniform sensitivity across all channels. These preamplifier gains are encoded within a linear scale of the range [0,255] where 0 represents that the channel is turned off, 64 represents a gain amplification factor of 1, and so on [144]. The MAROC3 digitizes the gain-adjusted MA-PMT signal, providing channel-by-channel trigger and charge information. The trigger threshold is set by the internal 10-bit Digital-to-Analog Converters (DAC) of the MAROC3.

The FEBs transfer the digitized information to the ROBs that aid MA-PMT interfacing, MAROC3 control, high voltage regulation and TT calibration. Figure 2.21 depicts a pho-
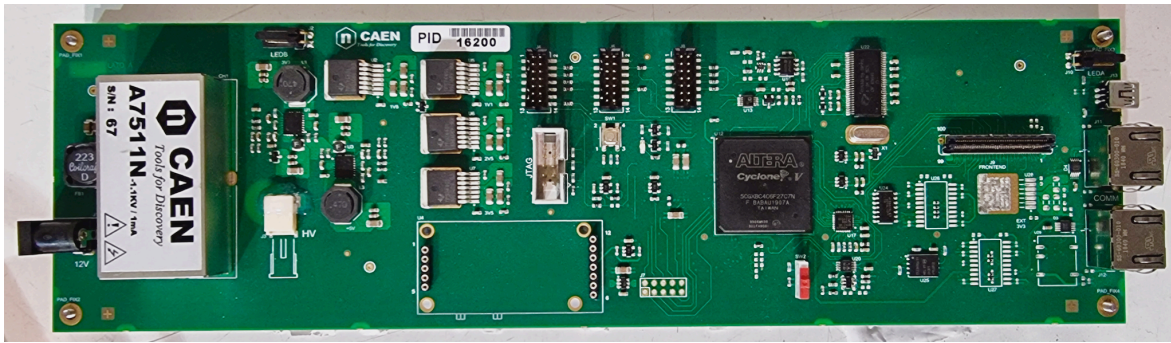
Figure 2.21 : *The Read-Out Board of the JUNO Top Tracker.*
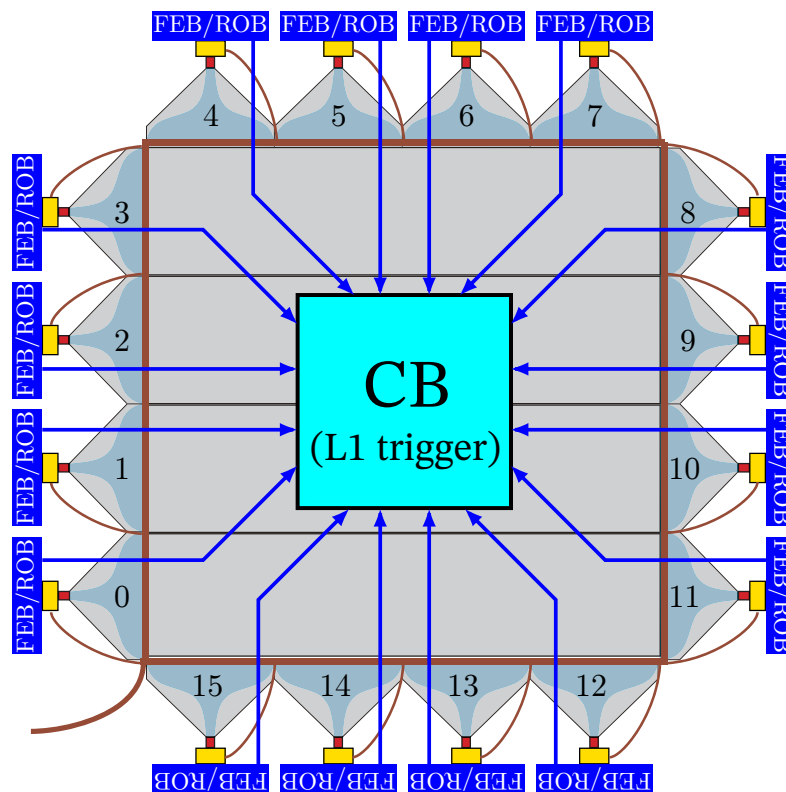
Figure 2.22 : *The Concentrator board placement in a TT wall. Adapted from [16].*

tograph of a ROB. The MAROC3 can output the digitized charges via an internal 8-bit Wilkinson Analog-to-Digital Converter (ADC), which spends about 14 μs per charge read-out. However, the ROB features a 12-bit Flash ADC (FADC) [146] for the charge read-out from the MAROC3, which takes only about 7 μs per charge read-out. The MAROC3 will not be available to measure the charges from subsequent signals that arrive during the electronics read-out time window, constituting a dead-time for the MAROC3. However, the dead-time does not affect the functioning of the MAROC3 trigger functions. The FADC will be used for the charge measurements in the JUNO TT, owing to its lower dead-time and

higher precision.

The ROB also has pulse generators that power the blue LEDs installed in the light injection system in the end-caps that are useful for the TT electronics calibration tasks. More details about electronics calibration can be found in chapter 3. While the TT needs 992 ROBs and 992 FEBs, 1160 FEBs and 1020 ROBs have been tested and validated.

Concentrator Board (CB)

A CB is installed at the centre of each TT wall, as shown in figure 2.22. The CB aggregates data from 16 MA-PMT/FEB/ROBs in the TT wall, and performs selection of x-y coincidences at the TT wall level (L1 trigger). An x-y coincidence is defined as the detection of 2, 3, or 4 FEB/ROB triggers within a 100 ns sliding time window, linked with two perpendicular modules within the same wall. L1 trigger selection suppresses the accidental correlations, leading to a reduction of the data rate by about an order of magnitude. The CB is also responsible for the transmission of the reduced data stream to the DAQ system. Implementation of a CB per wall reduces the number of data streams to DAQ from 992 FEB/ROBs down to only 63 data streams. The TT requires 63 CBs, with 80 CBs currently available.

Global Trigger Board (GTB)

Figure 2.23 shows a schematic view of the TT Trigger boards. The main task of the GTB is the application of a global trigger on the events selected by the L1 trigger of each TT wall. The GTB combines the trigger information from all 63 CBs in order to validate an event. It aims to identify alignments of x-y coincident events detected in different TT walls across the three TT layers within a sliding time window of 300 ns. As a result, the L2 trigger enhances the removal of background noise. The TT requires 1 GTB, while 2 GTBs are available.
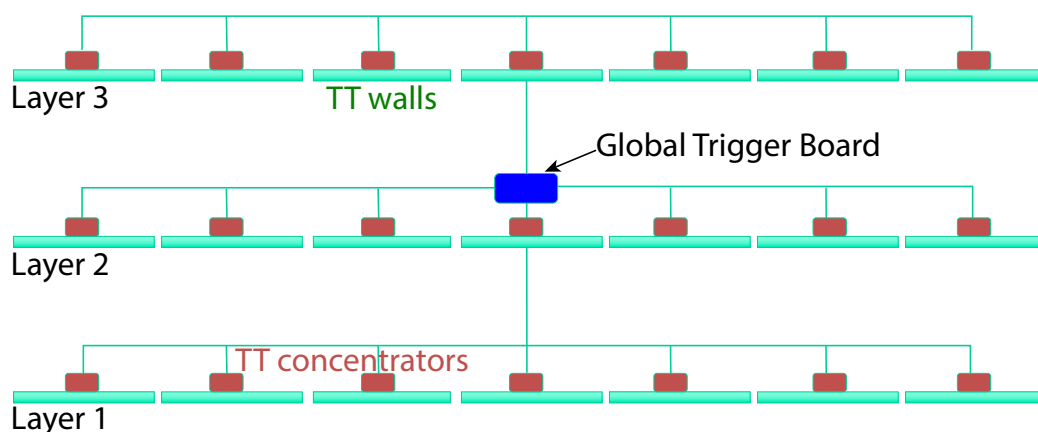
Figure 2.23 : *The schematic view of the TT global trigger strategy [16].*

2.5.4 Top Tracker operation modes

Four distinct modes have been envisioned for TT operation, aiming to facilitate stability monitoring, calibration, and data acquisition. Each mode may feature additional configurable options to enhance flexibility while maintaining the TT objective.

- **Trigger rate test (TRT) mode**: This mode is employed to measure the trigger rate per channel, aiming to characterize electronic noise, establish trigger thresholds, and detect light leaks in the TT modules. In the TRT mode, the acquisition is configured in auto-trigger mode without charge acquisition, returning only the number of triggers per channel within a specified time window (typically 1 s). The primary advantage of accessing this data is to minimize latency in these measurements for immediate use during the aforementioned calibration, as well as to assess the performance of MA-PMT channels and to check for light leaks.

- **Pedestal mode**: This mode is employed to ascertain the recorded charge in the absence of a signal. This is accomplished by measuring the charge with a consistent trigger frequency instead of relying on the MA-PMT signal for triggering detection.

- **LED light injection mode**: This mode functions similarly to the Pedestal mode, but with measurements taken concurrently with the light injection into the WLS fibres using the light injection system at each end-cap, as was previously outlined. Following a configurable delay from the LED pulse to accommodate the time required for the LED to flash, an external trigger is generated to execute the charge measurement in the MAROC3. The data corresponding to the light injection is collected at a fixed trigger frequency, with the LED being pulsed independently of the MA-PMT trigger. The intensity of the LED can be adjusted to produce a signal with an average intensity around the level of 1 PE. By analysing the observed charge spectra, useful information about each MA-PMT channel such as the MA-PMT channel gain can be extracted. This can then be used for the calculation of preamplifier gain factors in order to maintain uniform MA-PMT channel response, as well as to monitor the stability of the MA-PMT gain over long periods.

- **Normal run mode**: This is the mode in which regular data acquisition is performed. In this mode, a trigger is produced when the MA-PMT signal exceeds the threshold, as was described earlier. The MA-PMT trigger threshold used in this mode is 1/3 PE, unless otherwise stated. Moreover, zero-suppression (not saving the charge information of the channels that did not trigger) in the ROB can be activated in this mode to reduce the data size.

Prior to being installed in the TT, it is crucial to validate each electronics component with respect to different aspects, such as stability, durability, response to basic commands, firmware, etc. Because not all cards exhibit the same behaviour, it is essential to individually characterize and grade each component based on its performance. This process enables the installation of the optimal selection of electronics components, ensuring a homogeneous response throughout the entire TT detector during data acquisition. Chapter 3 presents

testing, calibration and validation activities relevant to the FEBs. Chapter 4 presents a summary of the CB testing and validation activities performed during the doctoral tenure. The data and the expertise thus gained have been instrumental in the process of comprehending, debugging and enhancing the performance of the electronics as well as for the development of the JUNO official simulation [18, 143]. Further, the characteristic information regarding each electronics component has not only been useful during the development and planning stages, but will be crucial during the commissioning and data acquisition stages of the TT detector.

2.5.5 Top Tracker muon reconstruction algorithm

JUNO official reconstruction software consists of an algorithm to reconstruct muons passing through the TT. A muon track in the TT is a straight line defined by at least three 3D points. The event builder of the JUNO official software searches for groups of x-y coincidences (i.e. 3D points) in all three TT layers within a sliding window of 100 ns. The number of 3D points per group (i.e. TT muon event), as determined by the event builder, can vary due to inefficiencies in detecting true muon hits on the scintillator strips, as well as due to accidental coincidences and muon showers, among others. When an $n(\geq 3)$ number of 3D hits satisfying the aforementioned conditions are found, the reconstruction algorithm follows a combinatorial process in which it considers all possible permutations among different 3D hits to form all possible tracks. Then, it calculates the χ_k^2 value with respect to each 3D point i for the track k, defined by

$$\chi_k^2 = \sum_{i=1}^{n} \frac{|(\mathbf{r}_i - \mathbf{r}_{0,k}) \times \mathbf{v}_k|^2}{|\mathbf{v}_k|^2 \sigma_i^2}, \tag{2.6}$$

where each possible track is parametrized in the form

$$\mathbf{r}_t(\lambda_k) = \mathbf{r}_{0,k} + \lambda_k \mathbf{v}_k. \tag{2.7}$$

$\mathbf{r}_{0,k} = (x_{0,k}, y_{0,k}, z_{0,k})$ and $\mathbf{v}_k = (v_{x,k}, v_{y,k}, v_{z,k})$ describe the cartesian coordinate and the direction vector that define the track along with the free parameter λ_k. σ_i, the uncertainty on the position, is fixed to 13 mm, equal to the half-width of a scintillator strip. The TT muon reconstruction algorithm currently does not utilize TT timing information, making it impossible to distinguish up-going muons from down-going ones. Consequently, the parameter $v_{z,k}$ is set to -1, assuming all muons in the TT are down-going. Parameter $z_{0,k}$ is fixed to the average z value of the 3D points. Hence the algorithm fits only the parameters $v_{x,k}$, $v_{y,k}$, $x_{0,k}$, and $y_{0,k}$. The algorithm considers a track as successful if it finds $\chi_k^2 < 3$. Then it proceeds to save the $\mathbf{r}_{0,k}$ and $\mathbf{v}_k$ values that describe successful tracks.

Résumé : L'expérience JUNO

L'Observatoire souterrain de neutrinos de Jiangmen (JUNO) est une expérience sur les antineutrinos electroniques de réacteur actuellement en cours de construction dans une installation souterraine à Jiangmen, en Chine, à une profondeur d'environ 700 m. Son objectif principal est de déterminer l'ordre de masse des neutrinos (NMO) avec une signification de 3σ avec six années de données. JUNO vise également à obtenir des mesures très précises des paramètres de l'oscillation des neutrinos, avec la possibilité d'atteindre une précision inférieure à un pour cent pour trois des paramètres (θ_{12}, Δm_{21}^2, Δm_{31}^2) dans un délai de 6 ans.

Le détecteur JUNO a deux éléments principaux : la cible de neutrinos et le système de veto. La cible de neutrinos de JUNO est un volume sphérique de 35,4 m de diamètre contenant 20 kt de scintillateur liquide appelé Détecteur Central (CD), qui est vu par 17612 tubes photomultiplicateurs (PMT) de 20 pouces et 25600 PMT de 3 pouces. Le système veto est composé de deux sous-détecteurs, à savoir le détecteur Tcherenkov à eau (WCD) et le Top Tracker (TT). Le CD est entièrement immergé dans le WCD, qui est une piscine cylindrique contenant 35 kt d'eau ultrapure, qui sert de barrière protectrice contre le bruit de fond externe.

Avec son grand volume de cible de neutrinos, sa résolution énergétique exceptionnelle de 3% à 1 MeV, sa grande pureté radiologique et sa non-linéarité énergétique minimale (<1%), JUNO étend son champ d'action à divers domaines de la physique. Il devrait effectuer des mesures de précision des flux de neutrinos ^{8}B, ^{7}Be, pep et CNO, ce qui permettra de mieux comprendre les processus solaires et la composition du Soleil. JUNO réalisera également des études sur les neutrinos atmosphériques, que pourra complémenter l'etude pour la determination de la NMO utilisant des réacteurs et ainsi amméliorer la sensibilité de l'expérience. Ses observations des neutrinos de supernova permettraient d'étudier l'évolution stellaire, la nucléosynthèse et l'échelle de masse des neutrinos. Pouvant détecter plus d'événements géo-neutrinos au cours de sa première année que tous les détecteurs précédents réunis, JUNO est appelé à devenir un acteur clé de la recherche sur les géo-neutrinos, offrant des informations cruciales sur le pouvoir radiogénique de la Terre et sur sa formation. En outre, JUNO explorera un large éventail de sujets, notamment le bruit de fond diffus des neutrinos de supernova, la désintégration des nucléons, la matière noire, les neutrinos stériles et la recherche de particules exotiques, pour n'en citer que quelques-uns.

JUNO est situé à environ 52,5 km des centrales nucléaires de Yangjiang et de Taishan, qui ont une puissance thermique combinée de 26,6 GW$_{th}$. Ces centrales constituent la principale source d'antineutrinos électroniques pour les principaux objectifs de physique de JUNO. En outre, un petit détecteur satellite appelé Observatoire d'antineutrinos de Taishan (TAO) est en cours de construction à environ 44 m de l'un des réacteurs de Taishan afin de fournir un spectre d'antineutrinos de réacteur précis, qui servira de spectre de référence pour les analyses de JUNO. JUNO détecte les antineutrinos électroniques par le biais du processus inverse à la désintégration bêta ($\overline{\nu}_e + p \rightarrow e^+ + n$). Le e^+ transporte la majorité de l'énergie du $\overline{\nu}_e$, produisant un signal rapide en quelques ns, tandis que la capture ultérieure du n à environ 200 μs produit un signal retardé, utilisé pour identifier ce type d'intéraction.

Les principales sources de bruit de fond dans les mesures du spectre antineutrino du réacteur JUNO proviennent de la radioactivité naturelle à l'intérieur et autour du détecteur, et des sous-produits générés par les muons atmosphériques qui traversent le détecteur et son environnement. Grâce à un contrôle rigoureux de la radioprotection, à des protocoles de propreté et à une disposition minutieuse des équipements, la radioactivité naturelle dans le volume sensible du détecteur est maintenue en dessous de 10 Hz, tandis que la couverture de 700 m réduit le flux de muons atmosphériques à $4,1 \times 10^{-3}$ Hz·m^{-2}. La sélection des candidats IBD sur la base des coïncidences spatiales, temporelles et énergétiques entre les signaux prompts et retardés permet de supprimer de manière significative les bruits de fond non corrélés. Cependant, les désintégrations $e^- + n$ des isotopes ^{9}Li/^{8}He induits par les muons génèrent des signaux corrélés qui imitent la signature de l'IBD à des taux comparables à ceux des véritables événements IBD, ce qui pose le plus grand défi en matière de bruit de fond. Pour atténuer ce problème, JUNO utilise un veto cylindrique autour des muons bien reconstruits dans le CD. Suite à l'application des critères de sélection des événements IBD pour l'analyse NMO, JUNO devrait observer 47,1 événements par jour, tout en réduisant efficacement les taux de bruit de fond à 4,1 événements par jour.

La fonction principale du Top Tracker est de reconstruire avec précision les muons atmosphériques qui le traversent. Cela permet d'étudier la production de bruits de fond induits par les muons atmosphériques dans le spectre des antineutrinos du réacteur. S'étendant sur environ 60% de la surface au-dessus de la WCD, il peut suivre environ 30% du flux total de muons traversant le CD avec une granularité de 2,6 cm×2,6 cm et une résolution angulaire médiane de 0,2 degrées. La capacité de reconstruction précise de muon du TT peut être utilisée pour améliorer les algorithmes de reconstruction des muons des CD et WCD. Le TT est un détecteur à trois couches de bandes de scintillateur plastique provenant de l'OPERA Target Tracker. Chaque bande de scintillateur contient une fibre optique intégrée qui collecte et transmet les signaux de scintillation dus aux rayonnements ionisants. L'unité fondamentale du TT, appelée module TT, est constituée de 64 bandes de scintillateur plastique disposées parallèlement les unes aux autres. Les signaux transmis par les fibres optiques sont lus à l'aide d'un photomultiplicateur multi-anodes (MA-PMT) à 64 canaux situé à chaque extrémité d'un module TT. Un assemblage de quatre modules TT forme un plan TT qui constitue une surface sensible de 6,7 m×6,7 m. L'empilement de deux plans TT l'un sur l'autre, de sorte que les bandes de scintillateur de chaque plan sont placées perpendiculairement à celles de l'autre, permet de créer un mur TT capable de fournir des informations sur la trajectoire en 3D des particules qui traversent le mur TT. Chaque couche de TT est une grille de murs de TT de 3×7.

Le taux de muons attendu traversant l'ensemble du TT est d'environ 4 Hz. En revanche, le taux d'événements attendu après le déclenchement du MA-PMT sur l'ensemble du détecteur TT est dominé par la radioactivité de la roche environnante, qui s'élève à environ 8 MHz. Les niveaux de radio-isotopes dans la caverne JUNO sont environ deux ordres de grandeur plus élevés que ceux de la caverne qui a accueilli l'expérience OPERA. C'est pourquoi une électronique dédiée, capable de faire face à des taux de radioactivité aussi élevés, a été conçue pour JUNO. La chaîne électronique du TT se compose de quatre cartes électroniques. La carte frontale (FEB) sert d'interface pour le MA-PMT. Ses fonctions principales, telles que le réglage du seuil de déclenchement du MA-PMT et la compensation des fluctuations de gain canal par canal, sont pilotées par une puce intégrée spécifique à l'application, connue sous

le nom de puce de lecture multi-anode version 3 (MAROC3). La carte de lecture (ROB) qui se connecte à la FEB facilite l'achèvement de la lecture du MA-PMT et fournit l'alimentation en haute tension du MA-PMT. Il y a une paire FEB/ROB pour chacun des 16 MA-PMT dans un mur TT. La carte concentrateur (CB) de chaque mur TT regroupe les données des 16 FEB/ROB et effectue la sélection des coïncidences x-y, ainsi que l'horodatage des événements. Une seule carte de déclenchement globale (GTB) sélectionne les coïncidences x-y alignées sur les trois couches de TT.

Part II

Top Tracker hardware validation

CHAPTER 3

TOP TRACKER FRONT-END HARDWARE VALIDATIONS

3.1   Front-end electronics calibration

In the Top Tracker electronics chain, the role of the FEB is pivotal, serving as the interface for optical signals from the MA-PMT channels. The core functionality of the FEB relies on the MAROC3 chip, which furnishes essential tools for interfacing with MA-PMTs, compensating for inherent gain variations among different MA-PMT channels, and providing channel-specific charge and trigger information. Hence, meticulous calibration of each FEB is essential for the accurate interpretation of the detected signals across the entire TT detector. A proper calibration facilitates precise interpretation of the signals measured by the detector.

At IPHC Strasbourg, an automated test bench was established to swiftly and comprehensively characterize all FEBs. The charge measurements on the test bench were performed using

the internal 8-bit Wilkinson ADC of the FEBs, coupled with a version of the ROB developed by IPHC Strasbourg that is capable of digitizing charge information in 9 bits. Under this discussion, the unit of charge as measured by the Wilkinson ADC is thus labelled as WADC. However, the ROBs that will be used in the JUNO experiment are also capable of performing charge readout using a 12-bit Flash ADC. More information on different ROB versions and ADCs is provided under chapter 4.

Using the test bench, the performance of the FEBs was evaluated based on various criteria, including:

- the high voltage interface to the MA-PMT,

- pedestal levels,

- cross-talk (i.e. signal leakage to surrounding channels),

- electronics trigger threshold setting, and,

- response to different injected charges.

This rigorous testing process resulted in the selection of 1160 FEBs out of 1200 FEBs produced to be used for the TT. Some of the FEBs identified to have issues have been repaired such that they can be used for other tests. However, the TT only requires 992 out of the 1160 selected FEBs, while the remaining, including some of the repaired ones, can serve as reliable spares. Through comprehensive data analysis of the test results, it becomes feasible to enhance the characterization of the FEBs based on their performance. This allows for the selection of 992 TT FEBs for installation in a manner that aims to achieve a more uniform response across the entire TT detector. This grading process not only ensures homogeneity but also facilitates prompt and confident identification of replacement FEBs if needed. Consequently, any replacements can be seamlessly managed with minimal disruption to the original TT electronics configuration. This section presents some of the in-depth analyses and the strategy for grading the FEBs that will be installed in the TT.

3.1.1 Determination of the pedestal levels

The pedestal denotes the measure when no input signal is present, establishing the baseline of measured signals. It constitutes background events stemming from inherent electronics noise of the MA-PMT or the FEB itself, as well as electromagnetic interferences from the surrounding electronics, among others. Pedestal level measurements are considered an integral task to fulfil during FEB calibrations and testing, as well as during physics data acquisitions. Based on the experience from OPERA, the pedestal levels are expected to be very stable. Consequently, there is no need to pause the JUNO physics data runs specifically for TT electronics pedestal level measurements. Instead, the pedestal levels can be measured on a monthly basis when the JUNO physics data runs are stopped for CD calibrations. The pedestal information thus gathered can be monitored over time to look for any evolution in the pedestal levels, as well as for any possible defects in the FEBs or the MA-PMTs.
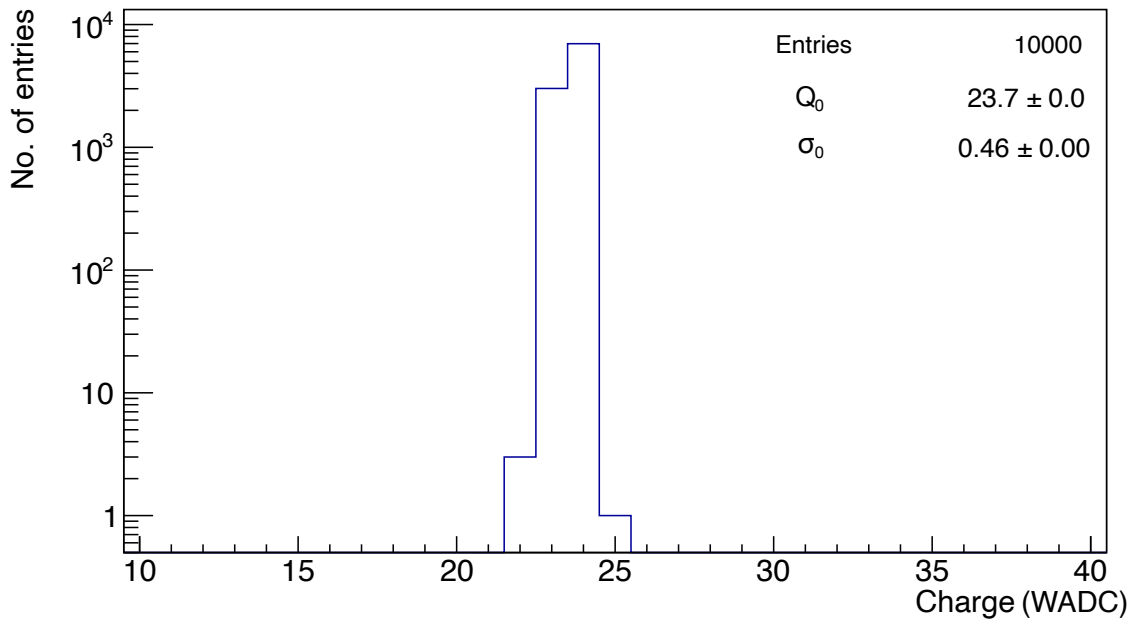
Figure 3.1 : *A pedestal distribution of one of the FEB channels.*
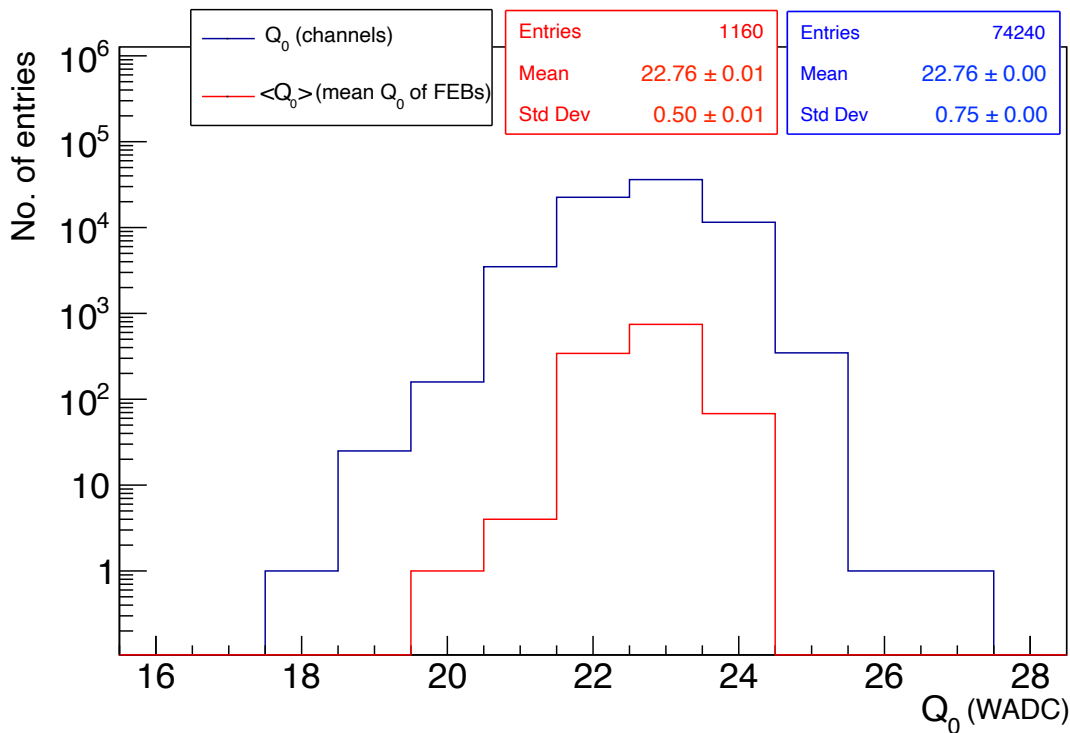
Figure 3.2 : *The distribution of Q_0 of the pedestals of the TT FEBs. The blue (red) histograms depict the distribution of Q_0 of all FEB channels (mean value of Q_0, $\langle Q_0 \rangle$ across all the channels of each FEB).*
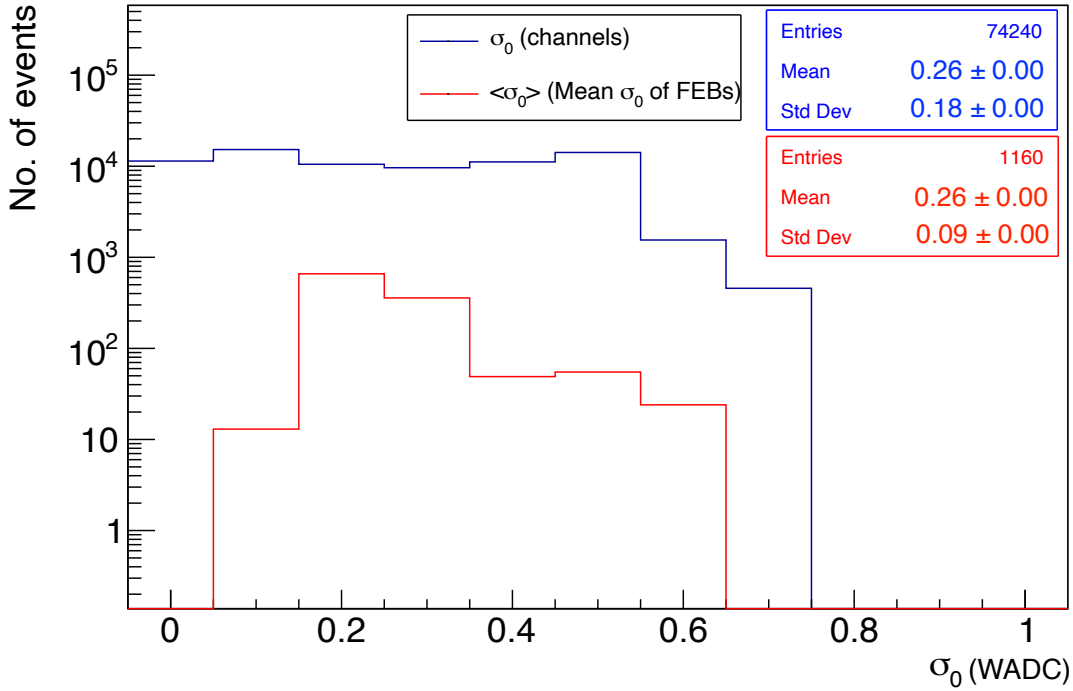
Figure 3.3 : *The distribution of σ of the pedestals of the TT FEBs. The blue (red) histograms depict the distribution of σ of all FEB channels (mean value of σ, $\langle \sigma \rangle$ across all the channels of each FEB).*

To determine the pedestal levels, data acquisition was performed in Pedestal mode which was introduced under section 2.5.4. Figure 3.1 depicts the observed pedestal distribution for one FEB channel. As shown, the pedestal distribution is characterized by its mean and standard deviation, labelled Q_0 and σ_0, respectively. Figures 3.2 and 3.3 present the results of the pedestal level determination tests performed on the FEBs using the test bench. The results highlight the level of homogeneity among the TT FEBs with respect to the pedestal levels. The mean of the standard deviation of the pedestal is 0.26 WADC ($\sim$0.03 PE at an MA-PMT gain of 10^6). Note that the precision of the standard deviation is limited by the bin size of the measurement. The relative standard deviation of the mean of the pedestal is 3.3%. Hence, this measurement indicates a high level of stability in the pedestal across all the TT FEBs.

3.1.2   Determination of the FEB electronics noise level

The trigger level corresponding to a given physical charge is set by the Digital-to-Analog Converter (DAC) of the MAROC3 in terms of an arbitrary electronics unit. It is common to all the channels of a given FEB. The distribution of electronics noise inherent to the FEB is expected to conform to a Gaussian distribution, characterised by its mean μ and the standard deviation σ. Therefore, out of N total events in the electronics noise distribution, the number of events $S(x)$ that overcome a trigger threshold value of x is expected to follow the form of a Gaussian error function, given by

Figure 3.4 : *The variation of the number of triggers observed as a function of the DAC threshold value for a FEB channel in the absence of charge injection.*
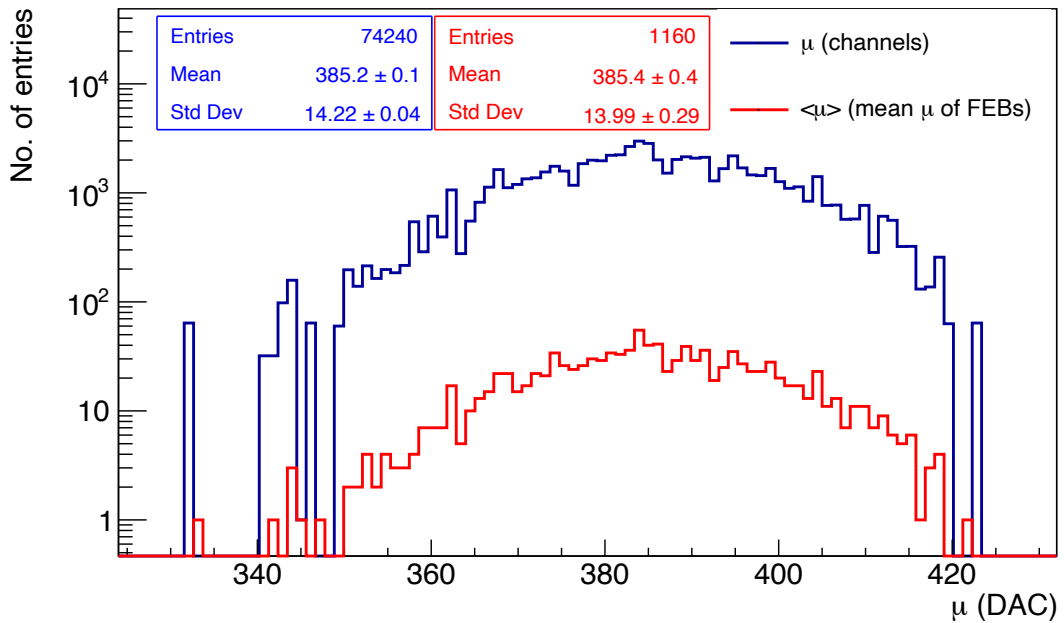
Figure 3.5 : *The distribution of Q_0 from the trigger threshold tests of all FEBs in the absence of charge injection. The blue (red) histograms depict the distribution of Q_0 of all FEB channels (mean value of Q_0, $\langle Q_0 \rangle$ across all the channels of each FEB).*
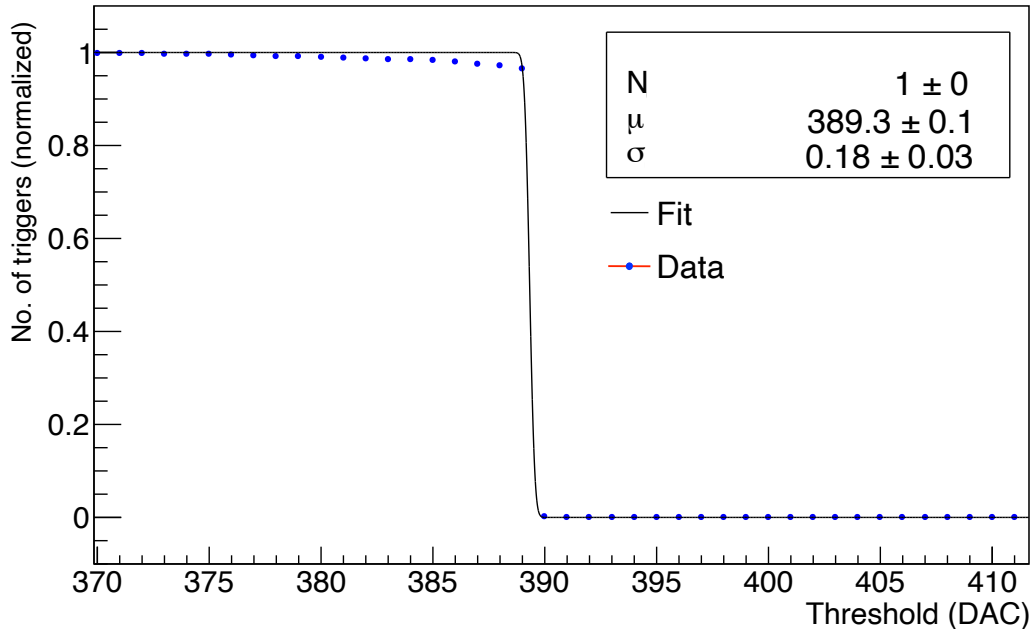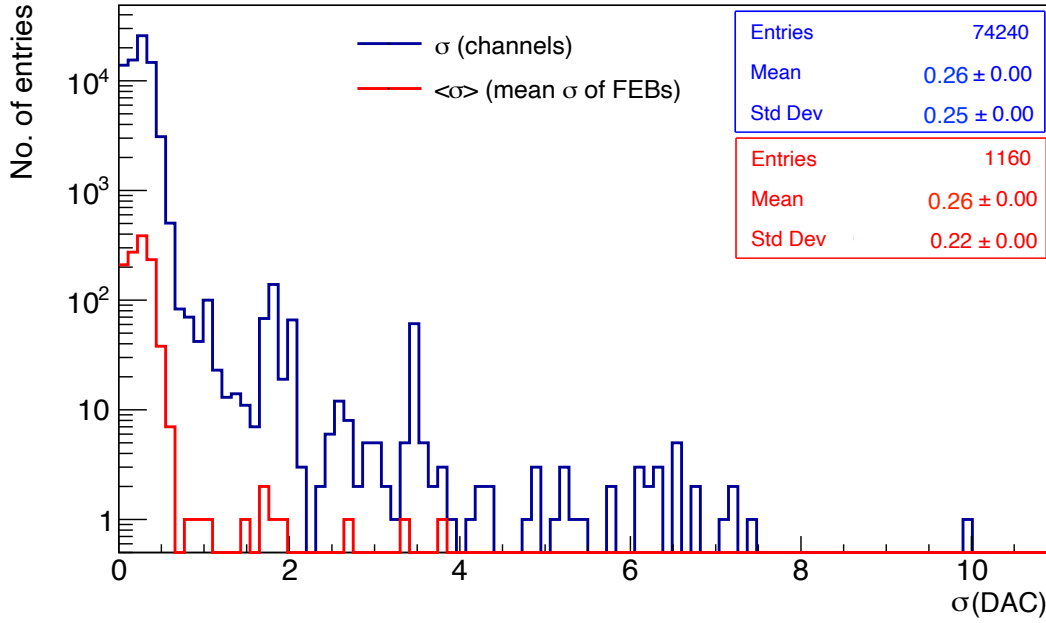
Figure 3.6 : *The distribution of σ_0 from the trigger threshold tests of all FEBs in the absence of charge injection. The blue (red) histograms depict the distribution of σ_0 of all FEB channels (mean value of σ_0, $\langle\sigma_0\rangle$ across all the channels of each FEB).*

$$S(x) = \frac{N}{2}erfc\left(\frac{x-\mu}{\sqrt{2}\sigma}\right).\tag{3.1}$$

μ corresponds to the value of x at which the number of triggers is 50% of N. At each DAC value, the number of triggers observed within a duration of 100 ms at a trigger frequency of 8 MHz were recorded. The variation of the (normalised) number of triggers observed as a function of the DAC threshold value for a particular FEB channel is depicted in the figure 3.4. The distributions thus measured at different DAC values were fitted with the function described in the expression 3.1 to extract the corresponding values of μ and σ that describe, respectively, the mean value and the spread of the pedestal distribution. The resulting distributions of μ and σ of all the channels as well as their mean values per each FEB, denoted $\langle\mu\rangle$ and $\langle\sigma\rangle$, are shown in figures 3.5 and 3.6. The relative standard deviations of μ and $\langle\mu\rangle$ are 3.7% and 3.6% respectively. The mean values of σ and $\langle\sigma\rangle$ are both 0.26 DAC. The precision of the standard deviation is limited by the bin size of DAC units. These results collectively highlight that the FEBs demonstrate a high level of agreement in terms of the intrinsic electronics noise levels among different channels within the same FEB as well among different FEBs.

3.1.3 Electronics trigger threshold determination

Soon after being produced, OPERA measured a mean charge deposition of 5.9 PE for atmospheric muons crossing the middle of the scintillator strips [17]. Based on the results, from their production (about 20 years ago) up to the beginning of JUNO data taking, a

20% decrease in the mean charge deposition is anticipated due to scintillator strip ageing. Therefore, the mean charge deposited by atmospheric muons observed at the middle of the TT plastic scintillator strips at the JUNO site is expected to be 4.8 PE [16]. Following the knowledge gained from the OPERA Target Tracker, placing a threshold at 1/3 PE ensures that the true signals due to muons crossing the scintillator strips are selected with >99% efficiency. Therefore, a MA-PMT trigger threshold of 1/3 PE is foreseen for the TT during JUNO data acquisition. Since the trigger threshold set by the DAC is common to all 64 FEB channels, it is also important to quantify the spread of the threshold value across the 64 channels of that FEB. Furthermore, the trigger threshold level must be optimized such that it strikes a healthy balance between the efficient selection of the events of interest and the purity of the selected sample. Consequently, the trigger threshold of each FEB must be maintained at the same physical charge value to ensure uniform trigger response across all FEBs to the incoming signals.

To determine the corresponding trigger threshold value of each FEB, a well-calibrated charge of 1/3 PE ($\sim$56 fC at 10^6 MA-PMT gain) was repeatedly injected to all the FEB channels using the test bench. The FEBs were configured to perform data acquisition in TRT mode. The charges were injected at a frequency of 50 kHz. For each FEB, at each DAC value, the number of triggers observed within a duration of 100 ms was recorded. During the entirety of these tests, the preamplifier gain factors of all the channels of all the FEBs were set to 64 (corresponding to a gain amplification factor of 1).

At each DAC value, the trigger efficiency $\varepsilon \in [0,1]$ is calculated using the number of events k that initiate a trigger and the total number of injections n as

$$\varepsilon = \frac{k}{n}. \tag{3.2}$$

Furthermore, since the trigger rate measurement follows a binomial process, the probability $\mathrm{P}(k; \varepsilon, n)$ that k events will initiate a trigger, given the conditions that ε is the true efficiency, and there are n events in total, is

$$\mathrm{P}(k; \varepsilon, n) = \binom{n}{k} \varepsilon^k (1 - \varepsilon)^{n-k}. \tag{3.3}$$

The corresponding standard error σ_ε on the efficiency is

$$\sigma_\varepsilon = \sqrt{\frac{\varepsilon(1 - \varepsilon)}{n}}. \tag{3.4}$$

It is important to note that the expression 3.4 yields absurd results in limiting cases. When $\varepsilon \to 0$ then $\sigma_\varepsilon \to 0$, and when $\varepsilon \to 1$ then $\sigma_\varepsilon \to 0$. This result is unphysical, as the total number of events n is a finite value, and additional events might slightly change the efficiency from either 0 or 1. Hence, in this study, the associated uncertainties on ε are treated using a Bayesian approach [147]. Starting with the Bayesian theorem, the following ansatz is established:

$$\mathrm{P}(\varepsilon; k, n) = \frac{\mathrm{P}(k; \varepsilon, n)\, \mathrm{P}(\varepsilon; n)}{\mathrm{P}(k; n)}, \tag{3.5}$$

where $P\left(\varepsilon; k, n\right)$ gives the probability function of ε for a given n and k. The term $P\left(\varepsilon; n\right)$ is the probability function of ε for a given n, prior to the consideration of data. The term $P\left(k; n\right)$ gives the probability function of k for a given n, irrespective of the value of ε. For a given measurement, $P\left(k; n\right)$ is a constant. Since ε is independent of n, $P\left(\varepsilon; n\right) = 1$. Therefore, the application of the normalization condition

$$\int_{-\infty}^{\infty} P\left(\varepsilon; k, n\right) d\varepsilon = 1 \tag{3.6}$$

yields

$$P\left(\varepsilon; k, n\right) = \frac{1}{n+1}. \tag{3.7}$$

Furthermore, the most probable value of ε is calculated by solving $\frac{dP(\varepsilon;k,n)}{d\varepsilon} = 0$, which yields

$$\varepsilon = \frac{k}{n} \tag{3.8}$$

as expected. Concurrently, the standard error σ_ε is calculated such that

$$\begin{aligned}
\sigma_\varepsilon &= \sqrt{\overline{\varepsilon^2} - \overline{\varepsilon}^2} \\
&= \sqrt{\int_0^1 \varepsilon^2 P\left(\varepsilon; k, n\right) d\varepsilon - \left(\int_0^1 \varepsilon P\left(\varepsilon; k, n\right) d\varepsilon\right)^2} \\
&= \sqrt{\frac{(k+1)(k+2)}{(n+2)(n+3)} - \frac{(k+1)^2}{(n+2)^2}}.
\end{aligned} \tag{3.9}$$

As expected, σ_ε from the expression 3.9, unlike that from the expression 3.4, behaves as expected in both the extreme cases. For $k = 0$ and $k = n$ (i.e. $\varepsilon=0$ and $\varepsilon=1$),

$$\sigma_\varepsilon|_{k=0,n} = \frac{1}{n+2}\sqrt{\frac{n+1}{n+3}} > 0. \tag{3.10}$$

It should be noted that when $n \gg 1$ and ε is not close to 0 or 1, expression 3.8 serves as a good approximation for expression 3.9. Therefore under the following analyses, the expression 3.9 is used for the proper estimation of errors in the threshold tests.

The observed variation of trigger efficiency ε as a function of the DAC threshold value, fit with the expression 3.1 for one FEB channel is shown in figure 3.7. The values of μ and σ thus extracted from all the FEB channels, as well as the distributions of their mean values per each FEB, are shown in figures 3.8 and 3.9. The above distributions show that there are some FEB channels that do not follow the predominant trend. Most of them, especially at lower values ($\mu \sim$360 DAC, σ<1.2 DAC), were found to be caused by some channels whose fits did not perform well. Upon close inspection, it was found that the fits fail because the μ values of such FEB channels lie very close to one end of the automated test range of DAC values. As a result, a portion of the full distribution is left beyond the scope of the measurement, leading to an unsuccessful fit. An example case is shown in the figure 3.10. Furthermore, a FEB as well as a few channels also demonstrate higher μ and σ compared to
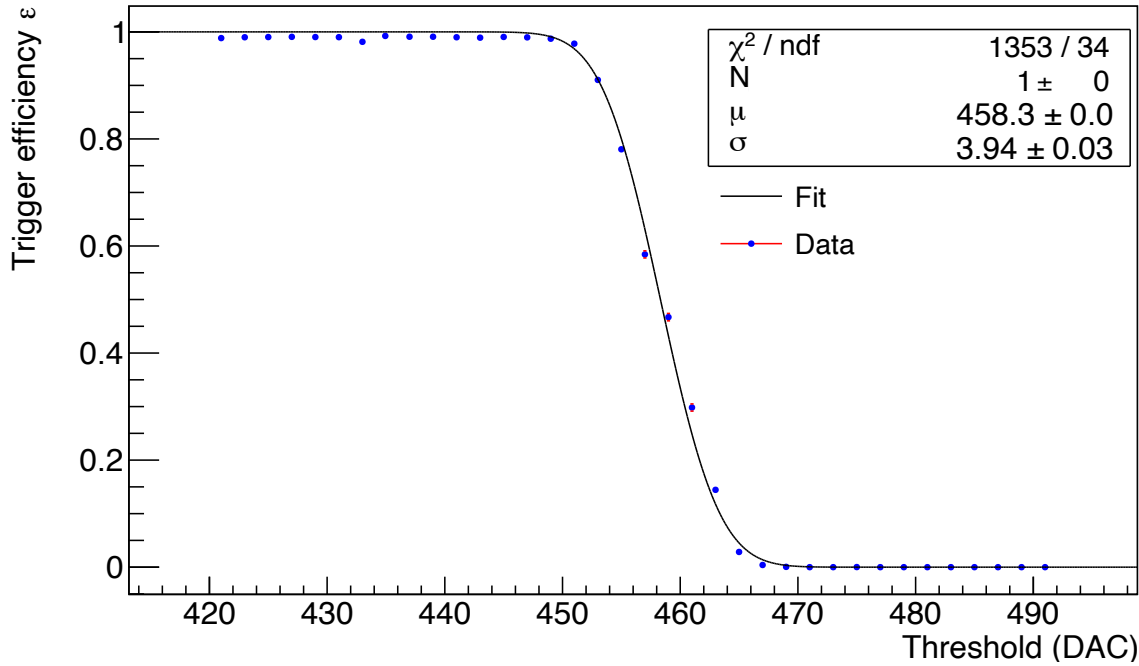
Figure 3.7 : *The variation of the trigger efficiency ε as a function of the DAC threshold value for a FEB channel for 1/3 PE charge injection.*
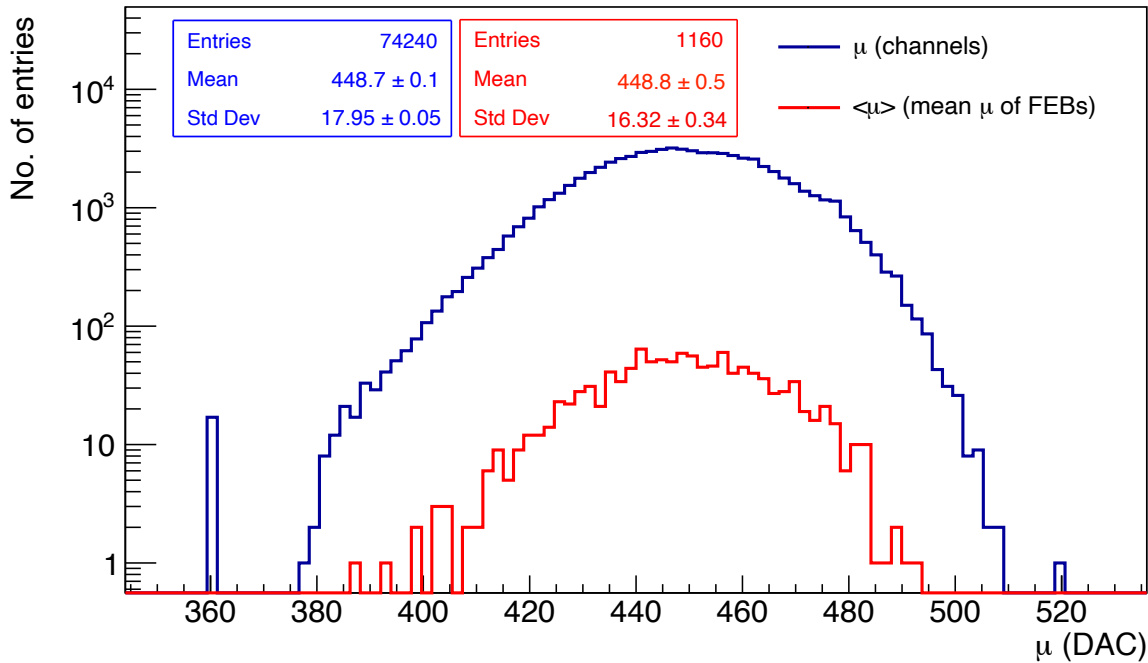
Figure 3.8 : *The distribution of μ from the trigger threshold tests of all FEBs for 1/3 PE charge injection. The blue (red) histogram depicts the distribution of μ of all FEB channels (mean value of μ, ⟨μ⟩ across all the channels of each FEB).*
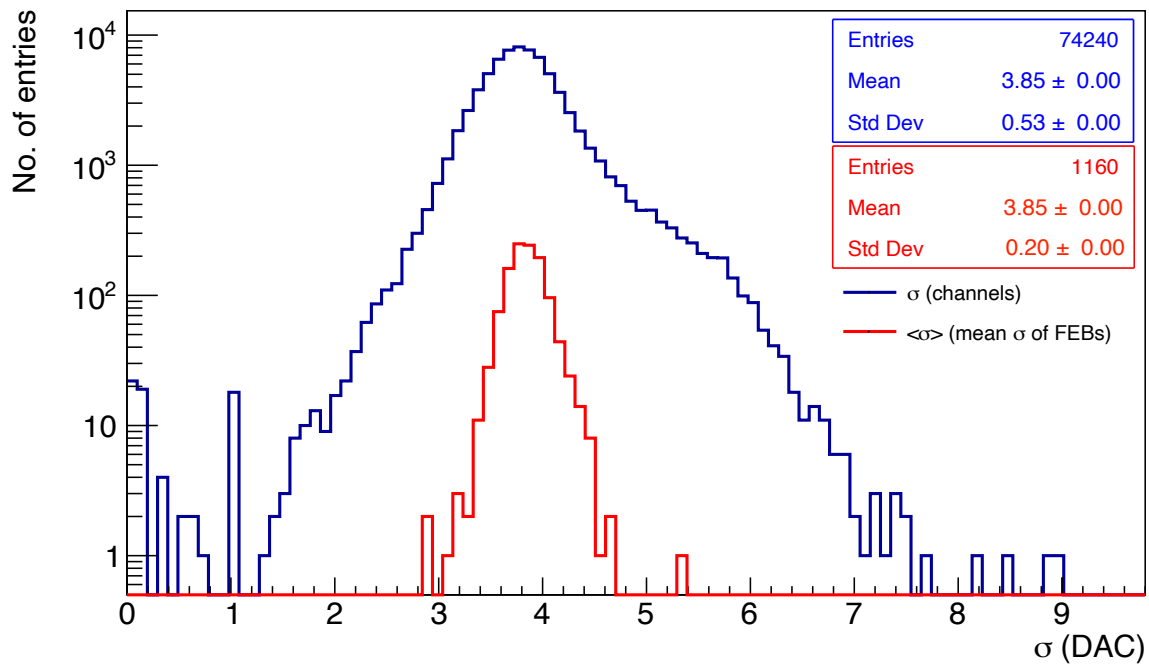
Figure 3.9 : *The distribution of σ from the trigger threshold tests of all FEBs for 1/3 PE charge injection. The blue (red) histogram depicts the distribution of σ of all FEB channels (mean value of σ, ⟨σ⟩ across all the channels of each FEB).*
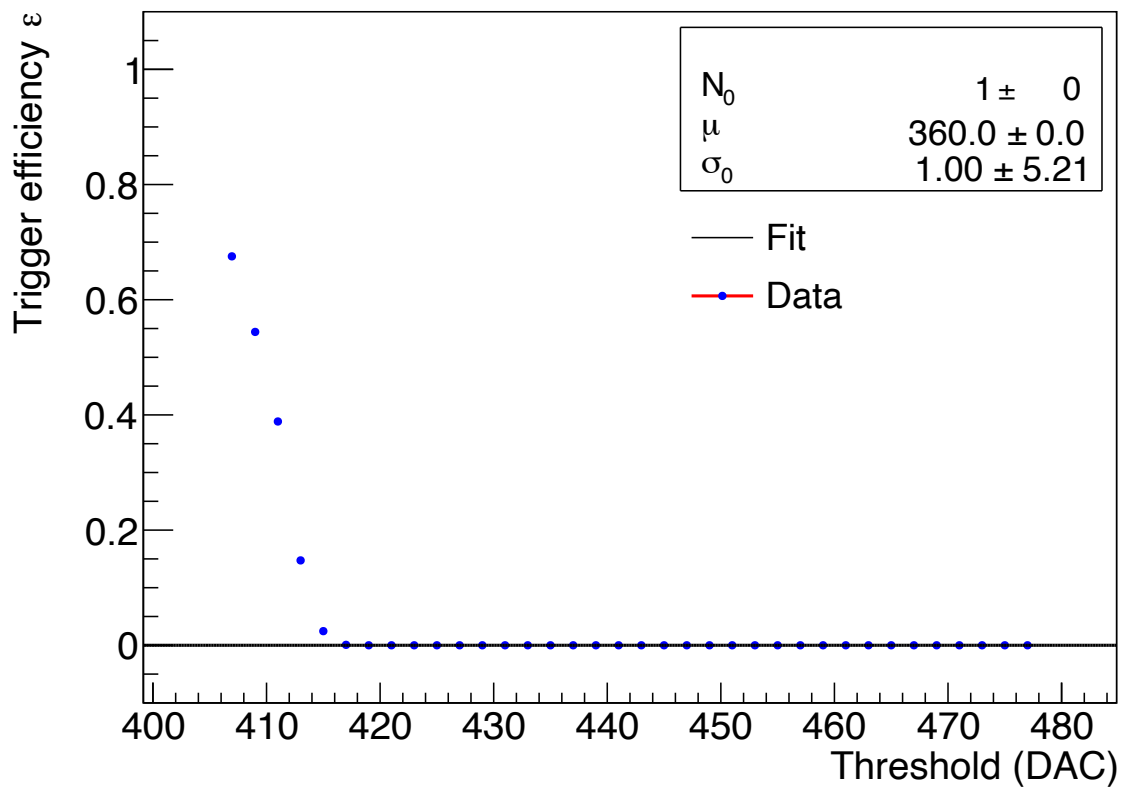
Figure 3.10 : *An example of a FEB channel where the fit to determine the DAC trigger threshold value failed.*
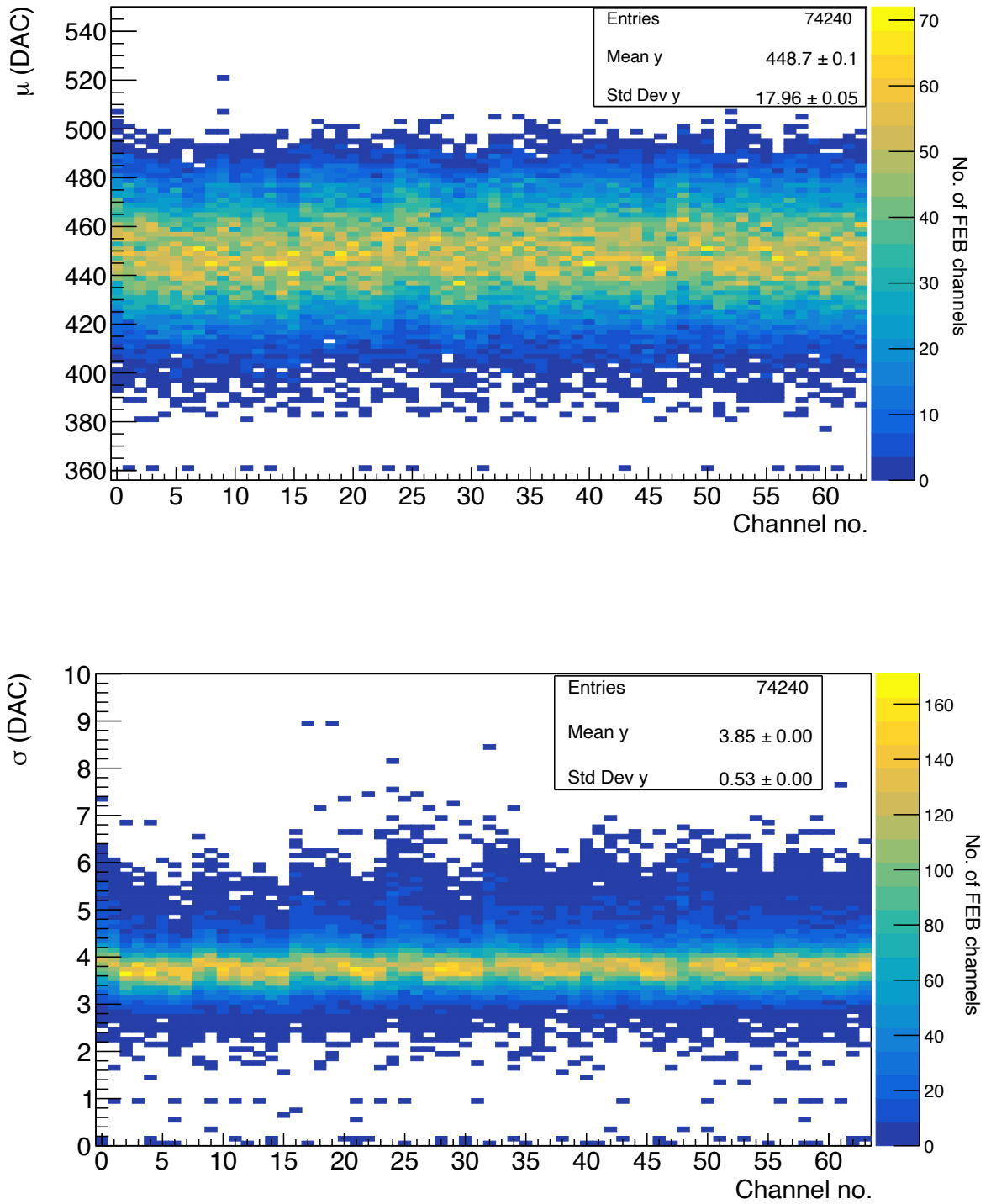
Figure 3.11 : *The distribution of μ (top) and σ (bottom) for all FEBs with respect to the FEB channel number, as observed from the trigger threshold tests for 1/3 PE charge injection.*
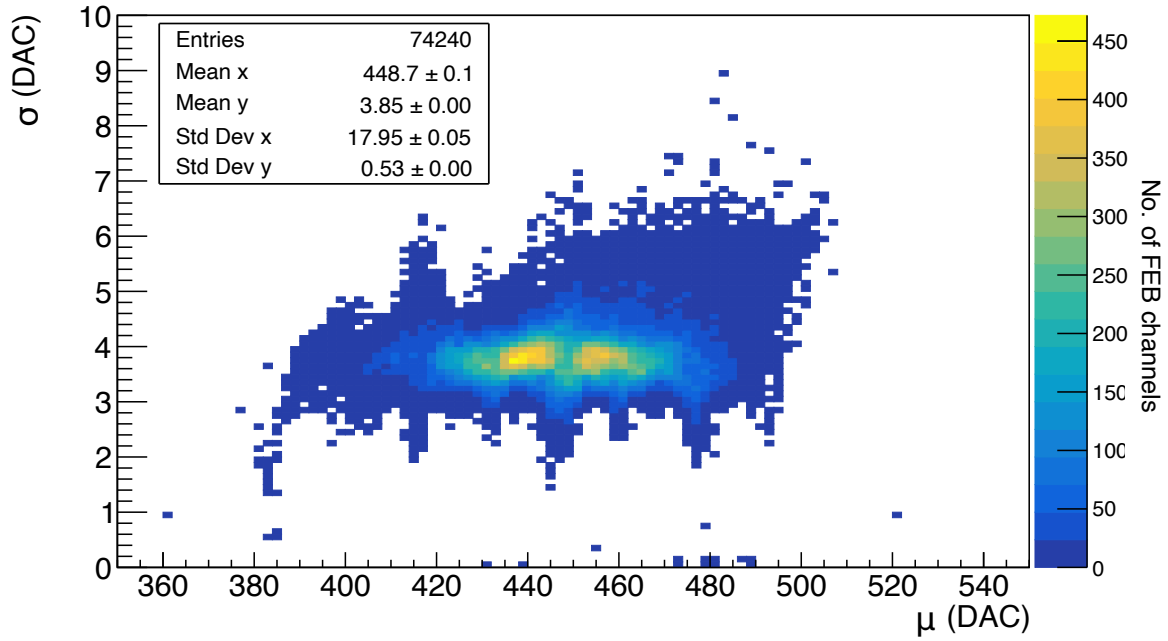
Figure 3.12 : *Comparison of μ and σ for 1/3 PE charge injection.*
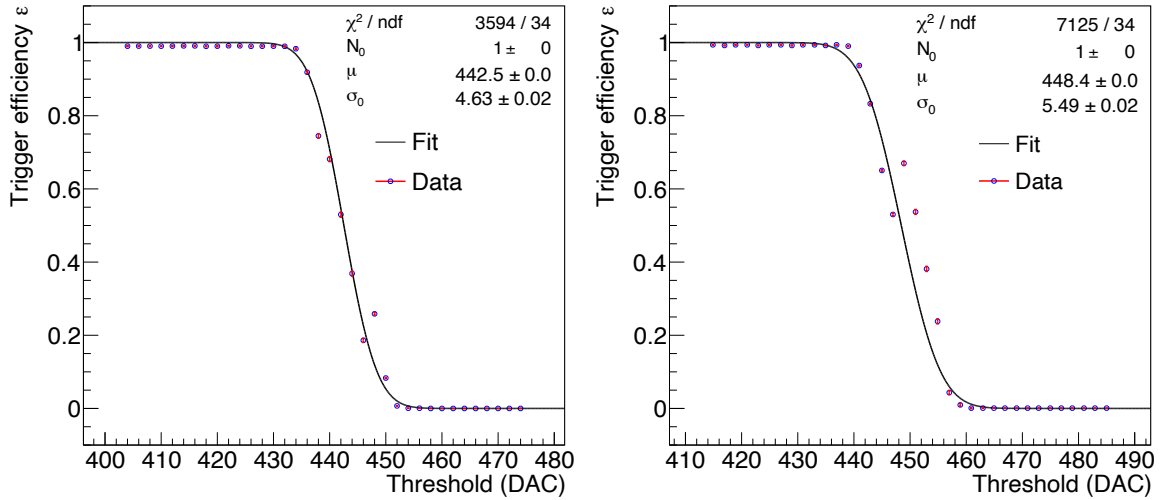
Figure 3.13 : *Example of two FEB channels that show an unusual shift in trigger efficiency around 450 DAC during the 1/3 PE charge injection test.*

other FEBs. Nevertheless, these problematic and outlier FEBs/FEB channels were well noted, and are taken into consideration during the grading process, discussed under section 3.1.5. Apart from the outliers and faulty FEBs/channels, it can be seen that the relative standard deviations of μ and $\langle\mu\rangle$ are 4.0% and 3.6% respectively. Both the mean values of σ and $\langle\sigma\rangle$ were determined to be 3.85 DAC, with σ<10 DAC units across all FEBs. Therefore, apart from statistical fluctuations, these results further endorse the consistency among different channels within the same FEB as well among different FEBs in terms of the DAC value corresponding to a 1/3 PE trigger threshold.

To further check for any undesired correlations between the DAC threshold value and the FEB channel number, the distribution of μ and σ was plotted as a function of the channel number, as shown in the figure 3.11. It demonstrates that, apart from statistical variations, there is no strong indication of a FEB channel-dependence on the values of μ and σ, as expected.

Furthermore, the data were checked for any correlations present among μ and σ, and the comparison is shown in figure 3.12. Although no correlation among μ and σ are observed, figure 3.12 indicates the presence of two apparently distinct favourable regions in the (μ, σ) space across all FEB channels. Upon further scrutiny, it was noted that in most FEB channels whose value of μ is close to 450 DAC, the measured trigger efficiency measurements have been significantly deviated from the expected trend. Two such example cases for different channels of two distinct FEBs are shown in figure 3.13. For these FEB channels, the presence of such deviations results in unexpected shifts in the standard deviation σ against the general trend. Therefore, although a single favourable region in the (μ, σ) space is expected, the aforementioned effect introduces a deviation around 450 DAC, resulting in the observation of two apparently distinct regions.

By the time of this analysis, all the FEBs were already shipped to the JUNO site. Hence it was practically impossible to retake data relevant to these observations. It is likely that this observation is associated with the MAROC3 itself. Less than 1% of the signals due to muons crossing the scintillator strips have charges as low as 1/3 PE. Therefore, the impact on the MA-PMT trigger efficiency due to such shits of σ as observed for trigger thresholds around 450 DAC is negligible. Furthermore, this effect is observed on only 5 FEBs. These FEBs are noted down, and it is accounted during the FEB grading process discussed under section 3.1.5.

3.1.4 Charge calibration

To physically interpret the digitised charges readout by the MAROC3, a pC↔WADC calibration is necessary[1]. This involves injecting accurately calibrated charges in a suitable range and comparing them with the corresponding ADC output values to establish the pC↔WADC calibration curve.

In the test bench setup, each channel of the FEB received injections of charges at five specific values: 0.056 pC, 0.158 pC, 0.5 pC, 2 pC, and 10 pC. These values approximately correspond to 0.3 PE, 1 PE, 3 PE, 12 PE, and 63 PE, respectively, at a MA-PMT gain of 10^6. The selection of charge injection values aimed to streamline the testing process while gathering sufficient information about each FEB for thorough characterization. Figure 3.14 (red points) illustrates the results from one such FEB channel, with pedestal levels subtracted. Additionally, the same FEB channel underwent manual injections with a broader range of distinct and precisely calibrated charge values, as depicted in figure 3.14 (green points).

---

[1]The charge calibration studies discussed here were obtained using 8-bit Wilkinson ADC. Since the 12-bit Flash ADC will be used for the MA-PMT charge readout in the JUNO experiment, an additional calibration between Wilkinson ADC ↔ Flash ADC is needed. This calibration will not be discussed here as it is beyond the scope of this thesis
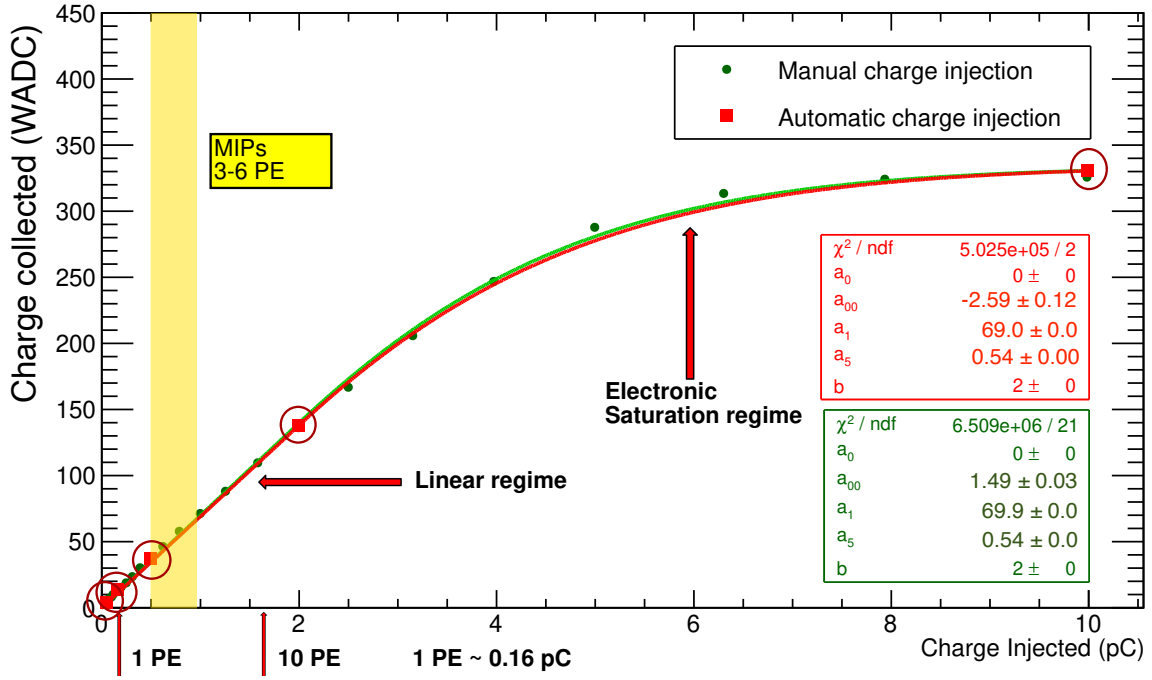
Figure 3.14 : *A pC↔WADC charge calibration measurements obtained for a prototype FEB channel using the test bench (red) and via manual charge injection (green). The respective curves are obtained by fitting the data with the function 3.11. The expected range of charges deposited by muons crossing the TT is also shown (yellow).*

The measurements indicate that the charge measured by the MAROC3 ADC increases in proportion to the increasing injected charge, prior to experiencing electronics saturation effects, distinguishing two distinct regions as labelled in the figure 3.14. As previously discussed, mean charge deposited by atmospheric muons observed at the middle of the TT plastic scintillator strips at the JUNO site is expected to be 4.8 PE.

A mathematical representation of the calibration curve enables quantitative analysis of various FEB characteristics, such as the pC↔WADC conversion factor in the linear regime, degree of electronics saturation, and linearity limit. This description serves as a crucial metric for characterizing individual FEBs and comparing them with one another. Moreover, it aids in predicting FEB performance under expected TT operational conditions. A higher order polynomial would serve as a smooth function that is capable of characterising the linear regime while providing a smooth transition from the linear region to the saturation region. Furthermore, by going to higher and higher orders, it is possible to find a function that fits the data well. However, this approach introduces significant risks such as instability in the fit and the possibility of the polynomial diverging at large values of Q_{pC}, leading to unreliable and non-monotonic results. Therefore, a piecewise function,

$$Q_{WADC}(Q_{pC}) = \begin{cases} a_0 + a_1 \cdot Q_{pC} & , Q_{pC} \leq b \\ a_{00} + a_2 \left(1 - e^{-a_3 \cdot Q_{pC}^{a_4}}\right) & , Q_{pC} > b \end{cases} \tag{3.11}$$

was developed to characterize the FEB pC↔WADC charge calibration curves. Q_{WADC}

represents the charge as seen by the MAROC3 in units of WADC, corresponding to a physical input charge Q_{pC}. The parameters a_0 and a_1 represents the pedestal and the pC $\leftrightarrow$WADC conversion factor (i.e. the gradient) in the linear regime. The function describing the range $Q_{pC} > b$ of the expression 3.11 is developed such that it undergoes an exponential retardation of the gradient and attains saturation. Parameter a_2 represents the degree of saturation (i.e. the WADC value at which the calibration curve fully saturates). Parameter b quantifies the value of Q_{pC} at which the calibration curve deviates from linearity, entering into saturation region. All the other parameters are used as tools for the purpose of handling a good fit.

By subtracting the corresponding pedestal value from each measurement of a given FEB, the value of a_0 can be set to 0 WADC. Since the fit function is a piecewise function, conditions of continuity and differentiability between the two pieces of functions at $x = b$ were taken into account. By applying the condition of continuity, one obtains

$$a_1 b = a_{00} + a_2 \left(1 - e^{-a_5}\right),\tag{3.12}$$

where

$$a_5 = a_3 b^{a_4},\tag{3.13}$$

yielding

$$a_2 = \left(\frac{a_1 b - a_{00}}{1 - e^{-a_5}}\right).\tag{3.14}$$

Furthermore, the condition of differentiability yields

$$a_4 = \frac{a_1 b}{a_2 a_5} e^{-a_5}.\tag{3.15}$$

Thus, the equation 3.11 can now be described using 5 parameters: a_0, a_{00}, a_1, a_5, and, b. Since the charge injection data from the test bench for all FEB channels consist of only five data points, it is necessary to sensibly reduce the degrees of freedom based on the available information to extract reliable results from the fits. Parameter a_0 for a given channel was fixed to a_0=0 WADC by subtracting the pedestal values measured for that channel from each of the five data points. By extensively comparing charge calibration data across different FEB channels, it was observed that b=2 pC was a reasonable value for all the FEB channels. This allowed the reasonable elimination of two degrees of freedom from the fit.

The comparison of the charge calibration curves obtained by fitting the data from the test bench charge injection tests (red curve) and that from the manual charge injection data (green curve) using the function 3.11 are shown in the figure 3.14. The maximum deviation of the red (green) fit curve with respect to the data from the manual charge injection data was found to be 3.2% (2.3%). This indicates a notable agreement between both curves with respect to the data from manual charge injection across both the linear and saturation regions, instilling confidence in the applicability of the described fit function to the test bench measurements of all FEBs. Hence, the test bench data for all the FEB channels were fit using the function 3.11, and the distributions of a_1 and a_2 as well as their mean values across the 64 channels of each FEB (labelled $\langle a_1 \rangle$ and $\langle a_2 \rangle$, respectively) thus obtained are depicted
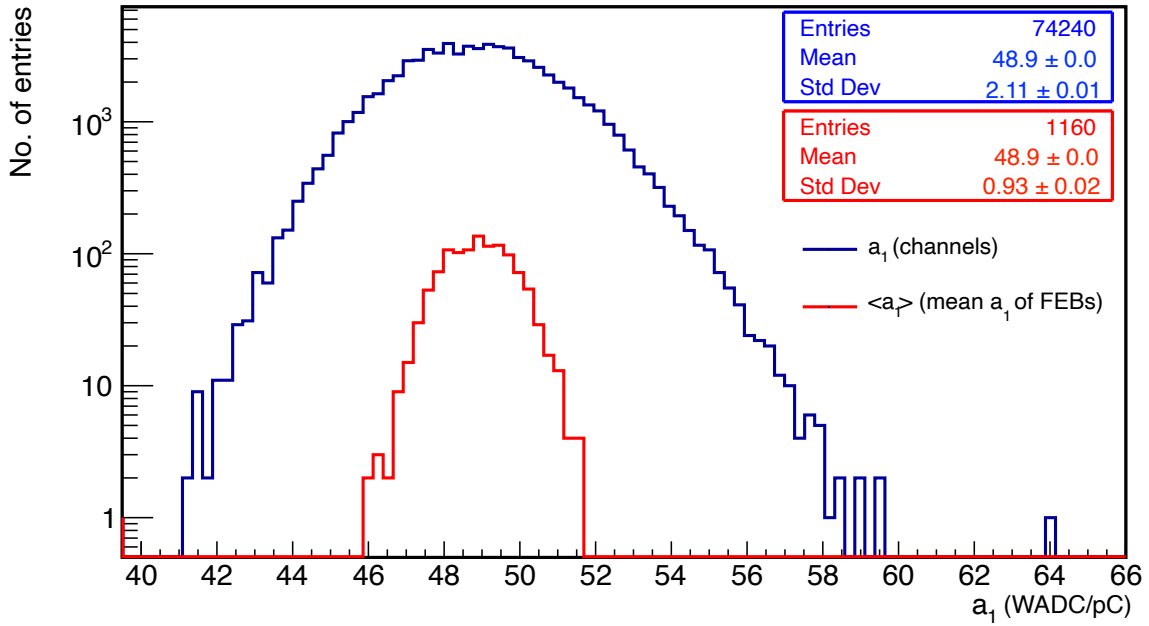
Figure 3.15 : *The distribution of the pC↔WADC conversion factor in the linear regime (a_1) from the charge calibration fits. The blue (red) histogram depicts the distribution of a_1 of all FEB channels (mean value of a_1, $\langle a_1 \rangle$ across all the channels of each FEB).*
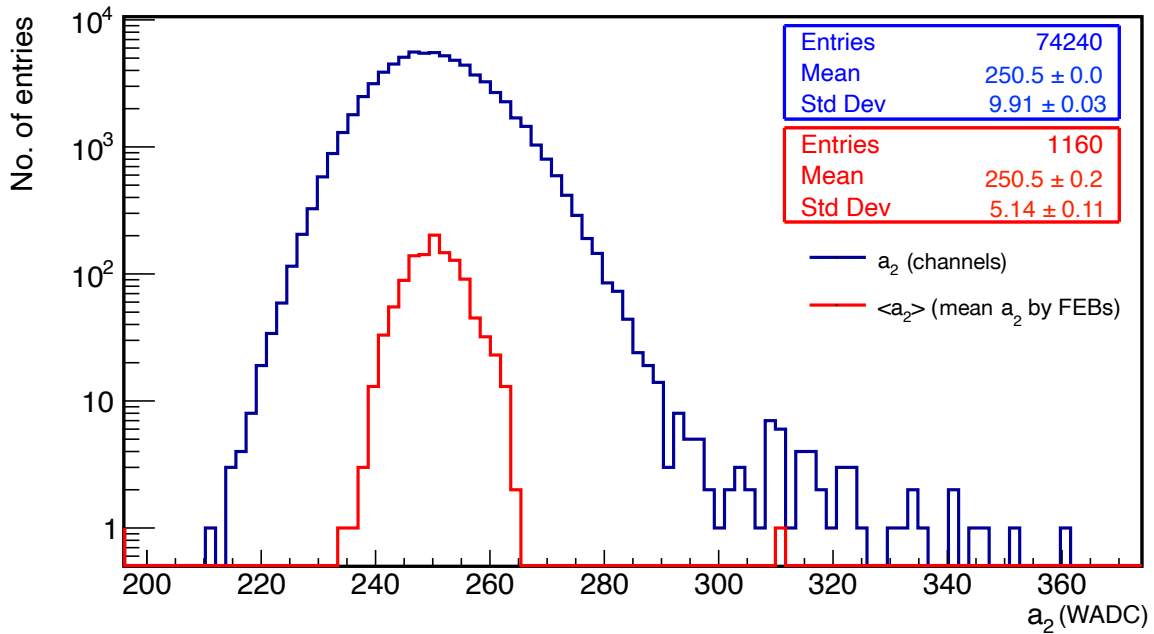
Figure 3.16 : *The distribution of the degree of saturation (a_2) from the charge calibration fits. The blue (red) histogram depicts the distribution of a_2 of all FEB channels (mean value of a_2, $\langle a_2 \rangle$ across all the channels of each FEB).*
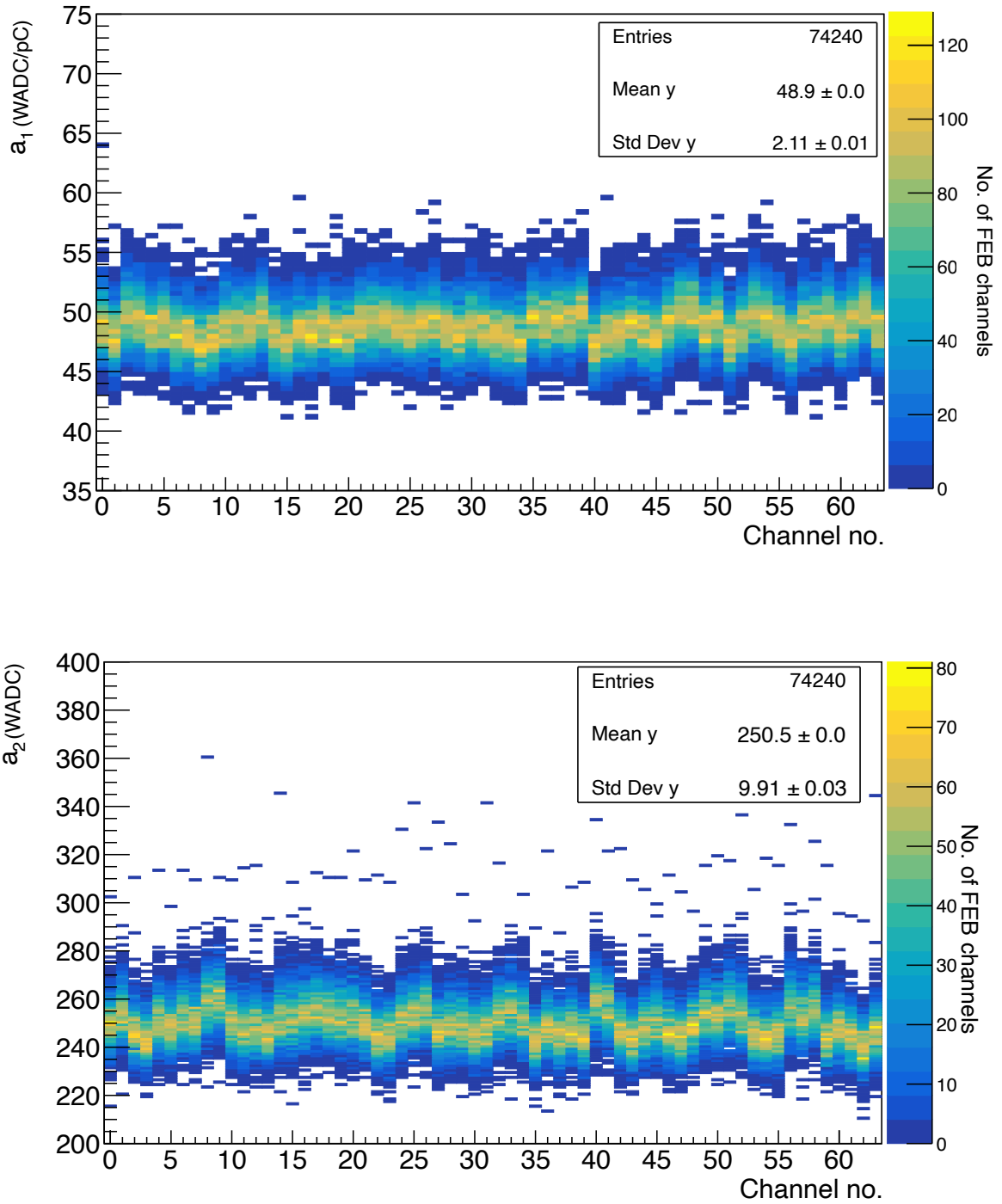
Figure 3.17 : *The comparison of the distributions of pC↔WADC conversion factor in the linear regime (a_1, top), and, the comparison of the distributions of the degree of saturation (a_2, bottom) across different FEB channels.*

in the figures 3.15 and 3.16, respectively. It reveals that the relative standard deviations of the distributions of a_1 and a_2 across all the FEB channels are 4.3% and 4.0% respectively, while the corresponding distributions of $\langle a_1 \rangle$ and $\langle a_2 \rangle$ are of 1.9% and 2.1% respectively. The value of $\langle a_1 \rangle$ is 48.9 WADC/pC, which indicates that 1 WADC unit corresponds to 0.02 pC. One FEB is seen to display saturation at a relatively high value compared to the rest of the FEBs. However, a higher saturation level is not a concern for the use case of the TT, given that the mean charge deposition from atmospheric muons crossing the center of a scintillator strip at the JUNO site is approximately 4.8 PE, which is well within the linear regime. However, muon hits on regions of the scintillator strips which are closer to the MA-PMTs may result in higher charges that could approach the saturation regime, though this is usually not a major issue since most charges are relatively smaller. For the sake of homogeneity of performance among the FEBs installed in the TT at a given instance, it is desired to use FEBs with similar characteristics. Apart from the outlying FEB, the distributions shown in the figures 3.15 and 3.16 are a clear indication of the excellent consistency in performance among different FEBs as well as different FEB channels within a given FEB in terms of charge calibration results.

Furthermore, the results were plotted against the FEB channel number as shown in the figure 3.17 to check for any possible dependencies on the FEB channel number. Although some non-uniformities are apparent, these fluctuations are within the order of 4% relative uncertainty mentioned earlier. These fluctuations are possible due to innate uncertainties of the charge injection system itself, inherent differences among different charge processing streams within the MAROC3, or a combination of both.

Figure 3.18 depicts a two-dimensional distribution of a_2 vs. a_1. It displays no significant correlation among the two parameters. However, a clear cluster of channels that lie outside the majority of the distribution is visible. Upon closer checks, these channels were identified
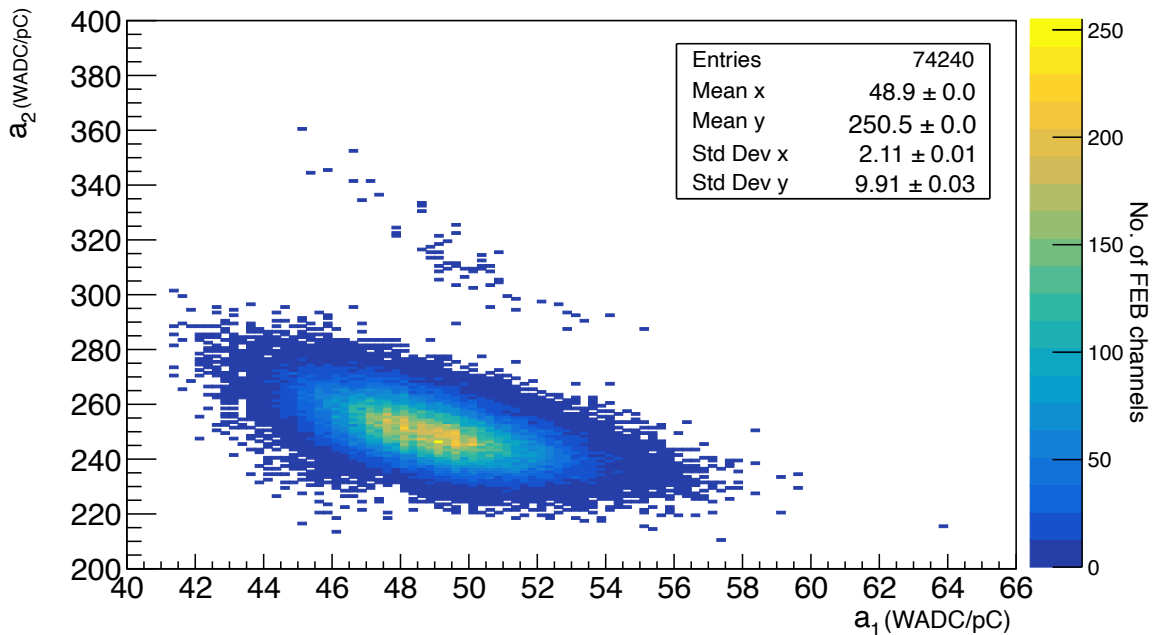
Figure 3.18 : *Comparison of a_1 and a_2 from charge calibration.*

to belong to the same FEB that showed a relatively high value of a_2 in the figure 3.16. These channels and the FEB were specifically noted, and this observation will be accounted during the FEB grading process.

3.1.5 Front-End Board Grading

Based on the comparison of results from various FEB tests and calibrations, it is possible to select a batch of 992 FEBs to ensure the highest level of consistency in the front-end electronics performance across the entire detector. To quantify the level of homogeneity among different FEBs, a grade G_j is calculated for the FEB j based on the test statistics. The grades were calculated based on the sum of squared relative deviations of the parameters $\langle a_1 \rangle$, $\langle a_2 \rangle$, $\langle \mu \rangle$ and $\langle \sigma \rangle$ of each FEB with respect to their respective means over all FEBs, as described below:

$$G_j = \sum_i \left(\frac{p_{i,j} - \bar{p}_i}{\bar{p}_i} \right)^2 + D_j. \tag{3.16}$$

The index $i : i \in \{\langle a_1 \rangle, \langle a_2 \rangle, \langle \mu \rangle, \langle \sigma \rangle\}$ is the parameter index, and $p_{i,j}$ is the value of parameter i of FEB j. $\bar{p}_i$ represents the corresponding mean value of the parameter i over all FEBs. D_j is an additional demerit value introduced to the grade of the FEBs that demonstrated clear deviations or other issues. It is used as a tool to distinguish such FEBs from the rest. Without the demerit term D_j, some FEBs that clearly deviated in performance for only one parameter (while performing well with respect to other parameters) were observed to have smaller G_j values compared to FEBs with no clear issues. This misleadingly suggested that
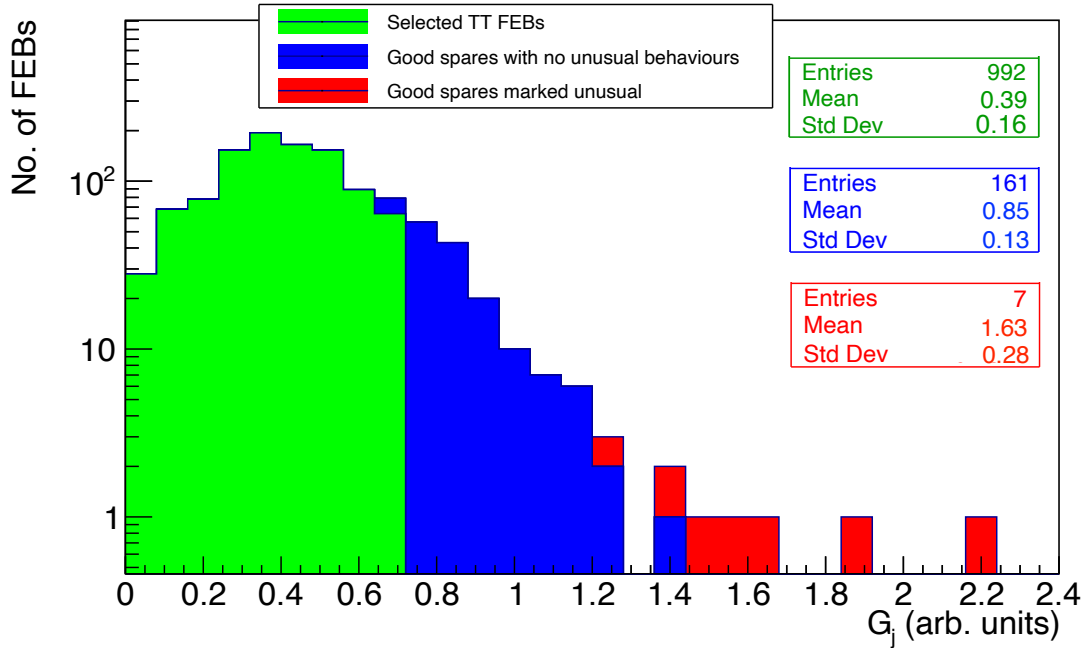
Figure 3.19 : *The distribution of grades for all tested TT FEBs (with lower grades being better) is shown as a stacked histogram, illustrating the various FEB categories identified during the grading process.*

the former FEBs had excellent, homogeneous performance across all parameters. However, for the sake of distinguishing such cards, the penalty term D_j is introduced. If a FEB has a handful of channels with unusual inconsistencies in performance with respect to other channels of the same FEB, D_j is incremented by 0.1 per each channel concerned. An increment of 0.1 per FEB channel was selected because for a given test, no FEB demonstrated more than 6 channels which misbehaved with respect to the other channels of the same FEB. Furthermore, for each FEB whose parameter values $\langle a_1 \rangle$, $\langle a_2 \rangle$, $\langle \mu \rangle$ or $\langle \sigma \rangle$ deviate significantly from that of the other FEBs, D_j is incremented by 1. Hence, a smaller G_j indicates that the measured calibration parameters of FEB j is closer to the respective global means, and hence a good candidate to be installed in the TT.

The grades distribution hence calculated is shown in figure 3.19. The FEBs selected for TT installation via this grading have $G_j < 0.69$. The selected FEBs have a good consistency in overall performance, and they have not been penalized for unusual performance in any way. Further, the distribution of G_j shows that there are 168 extra FEBs that perform almost similar to the chosen ones, 7 of which have been identified to have clear deviating performances with respect to the rest. It must be noted that it is possible to retain these FEBs as good replacements, if needed. Therefore, the performance of all the TT FEBs have been evaluated and graded, leading to the identification of the best TT FEBs as well as replacement FEBs for the installation and the operation of the TT.

3.1.6 Evaluation of front-end board performance at variable gains

Under section 2.5.3, it was introduced that the MA-PMT high voltage is common to all the 64 channels of a FEB, and the gain non-uniformities among different channels are compensated by tuning the MAROC3 preamplifier gain factors (p.g.f.) individually. The p.g.f. c_i that is required to correct the gain of the MA-PMT channel i is calculated as

$$c_i = \frac{J_{max}}{J_i}, \tag{3.17}$$

where J_i and J_{max} indicate the observed gains of the channel i and the channel with the highest gain, respectively, when the p.g.f. value is originally set to 1 for all the channels. The gain correction is chosen to be performed with respect to the gain of the channel with the highest gain, as it allows the operation of the MA-PMTs at the lowest high-voltage setting. As a result, the p.g.f.s will always be set to amplify the signal. The gain uniformity across each MA-PMT channel will be assessed and corrected monthly during when the JUNO data taking is stopped for CD calibration activities.

It is crucial to assess whether the applied p.g.f.s result in the expected behaviors in terms of the measured charge and their impact. To examine this, a FEB was injected with charges ranging from 0 to 10 pC at p.g.f.s of 0.5, 1, 2, and 3, and the measurements are depicted in figure 3.20. This illustrates the correlation between the linear regime and the p.g.f. value. Notably, the linearity diminishes and saturation is reached at a lower injected charge when using a higher p.g.f., in contrast to a lower p.g.f. Furthermore, the stability of the pedestal and saturation levels were evaluated at the aforementioned p.g.f.s, as shown in figure 3.21.
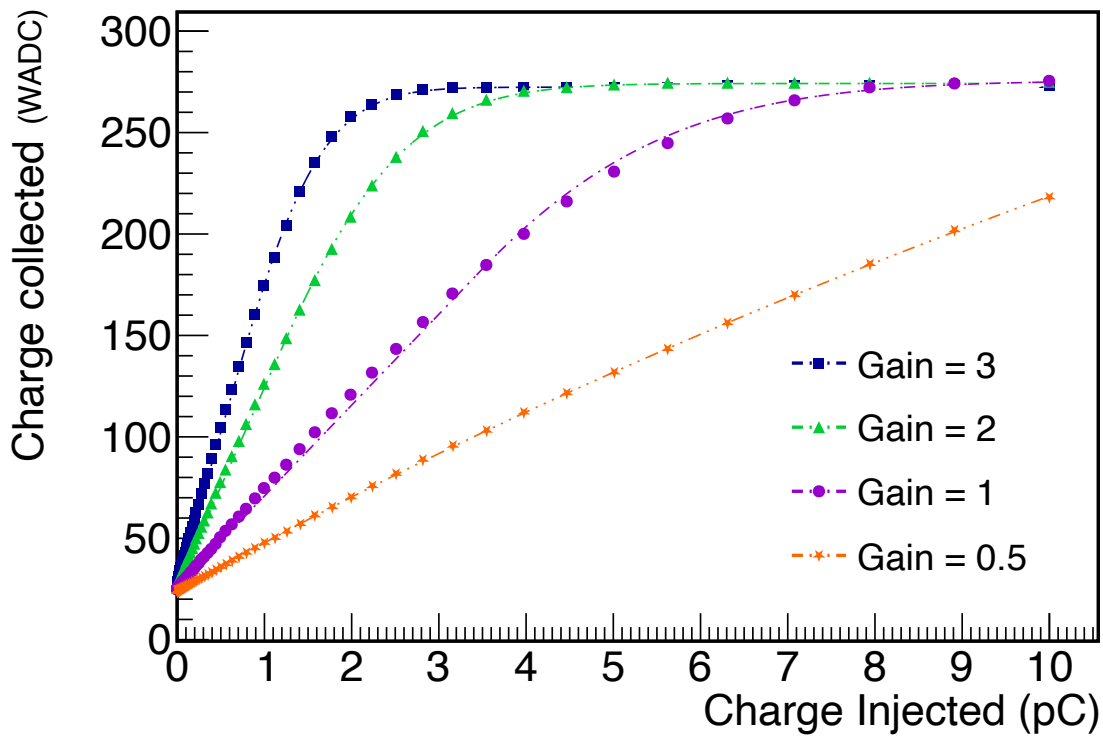
Figure 3.20 : *The charge calibration curves at different p.g.f. values of a FEB. The gain values in the legend correspond to the p.g.f. values.*
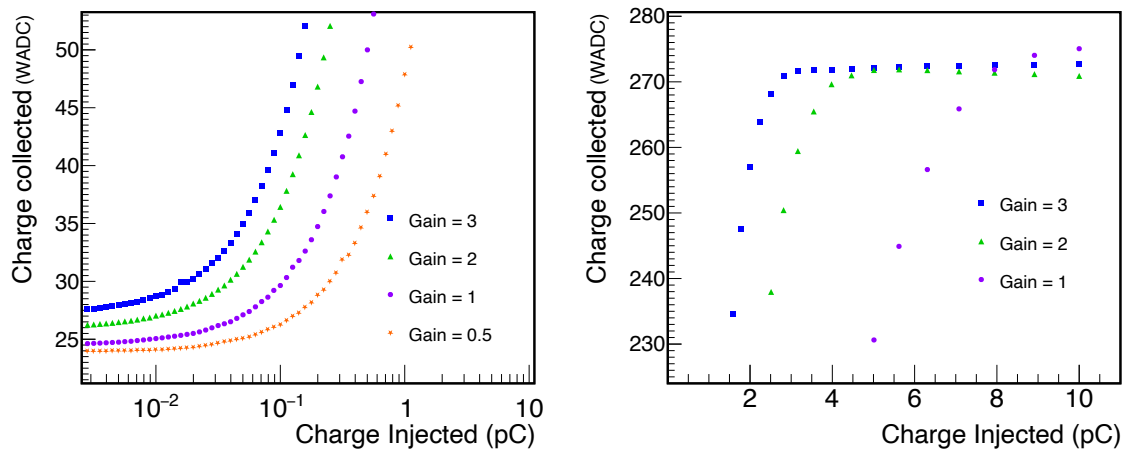
Figure 3.21 : *The zoomed plots of the pedestal (left) and saturation (right) regions of the charge calibration curves shown in the figure 3.20.*

It can be observed that the pedestal levels rise by 7 WADC units when the p.g.f. varies from 0.5 to 3. This change is due to the amplification of the noise level by the corresponding p.g.f. value. The corresponding variation in saturation level is observed to be 4 WADC.

For a detailed comparison of these curves, the pedestal measurements made at each respective values of p.g.f.s were subtracted. The resulting charge calibration curves are depicted in the figure 3.22. Here, charge input to the ADC of the FEB is obtained by taking the product of
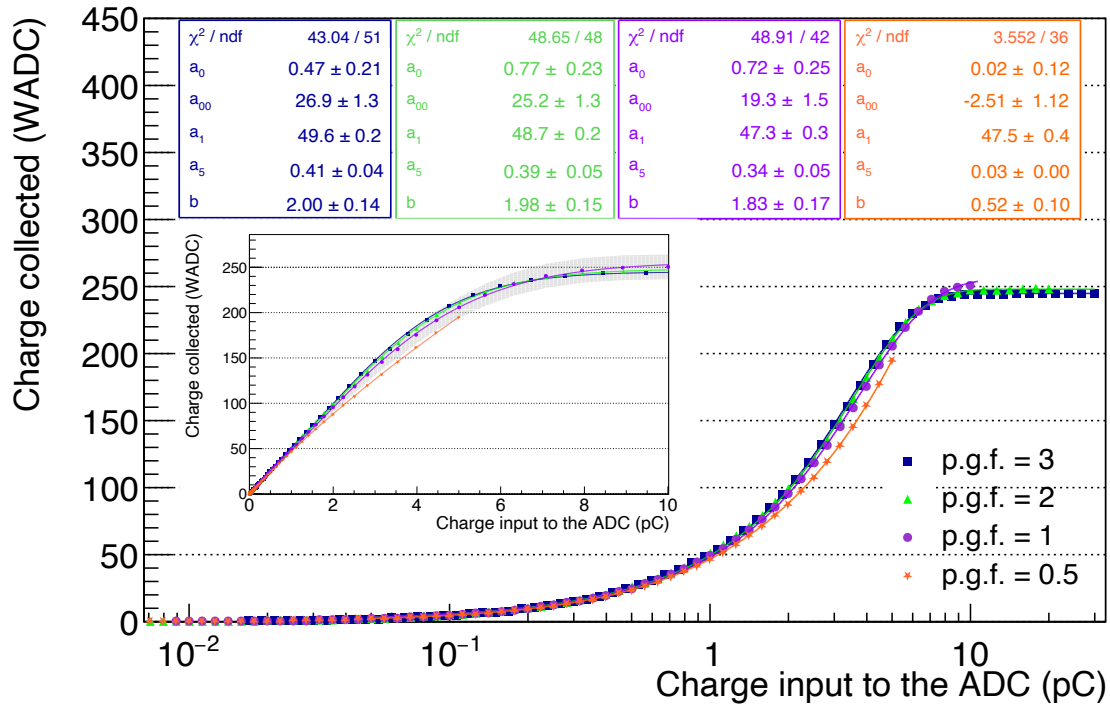
Figure 3.22 : *Comparison of the variation of charge measured by the ADC as a function of charge input to the ADC at different preamplifier gain factors. The inset shows the same information with the x-axis represented in linear scale. The grey shaded region indicates the 10% error band around the p.g.f.=1 curve.*

p.g.f. and the charge injected to the FEB. The curves were fitted with the expression 3.11, and the parameter b is left as a free parameter. Note that the value of b is found to be close to 2 pC in the curves where the saturation plateau is clearly evident. The mean value of a_1 among the four curves is 49.6 WADC/pC. The grey shaded region in the inset of figure 3.22 indicates the 10% error band around the measurements of p.g.f. = 1. The measurements for p.g.f. = 2 and p.g.f. = 3 are within the 10% error band, while some of the measurements at p.g.f. = 0.5 are found outside of it. It is important to note that, in the TT implementation, p.g.f.s will always be set to 1 or higher, as indicated by the expression 3.17. This indicates that, in the TT implementation, the FEB ADC charge reproducibility can be maintained within 10% of that measured when p.g.f.=1. For the purpose of muon tracking, the observed level of precision on the charge reproducibility is considered sufficient.

3.2 Estimation of the WLS fibre signal attenuation

3.2.1 Introduction

The WLS optical fibres mediate the transmission of the scintillation light signal from the scintillator strips to the MA-PMTs. During the extent of propagation of the light signal along the fibre, the intensity of the light signal is attenuated. This leads to the observation
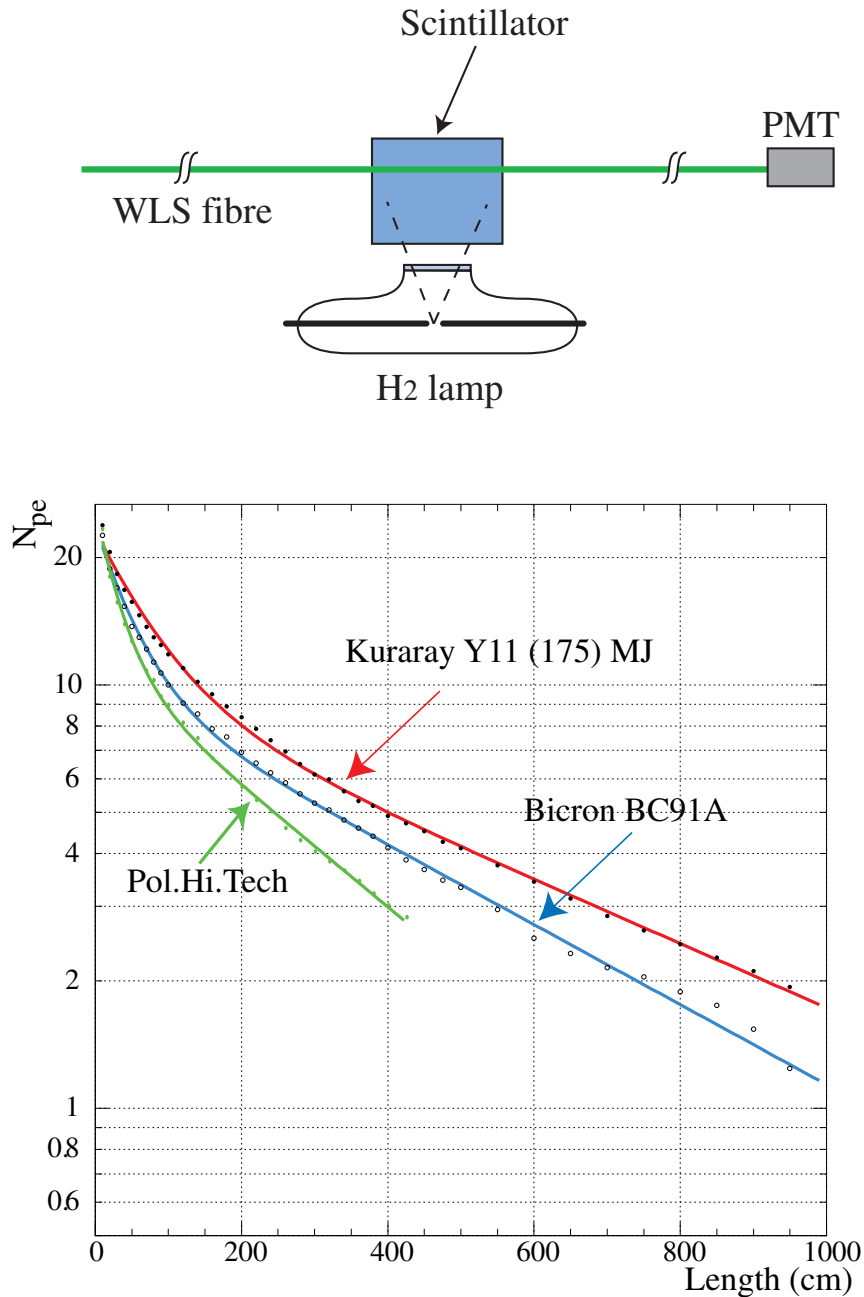
Figure 3.23 : *The setup for the WLS fibre attenuation study deployed by OPERA (top), and the corresponding measurements of the WLS fibre used in the OPERA Target Tracker (Kuraray Y11 (175) MJ) compared to two other commercially available optical fibres (bottom) [17, 148].*

of a much less light by the MA-PMT compared to the intensity of light originally collected by the optical fibre. Hence, the charge measured by the electronics readout is an under-estimation of the true scintillation signal. A high level of attenuation can degrade the signal quality and even loss of signal. Furthermore, it could lead to negatively influence the timing characteristics of the observed signals due to the MAROC3 trigger response time dependence on the incoming charge. This effect is known as time-walk, and it will be introduced in more detail under chapter 4. The attenuation of light within the optical fibre could be contributed

by factors such as self-absorption (absorption of photons by the optical fibre material itself), scattering (redirection of photons due to irregularities within the structure of the fibre), as well as reflection losses (loss of photons due to the reflections from the cladding as a result of fibre deformations). The degree of attenuation increases as the distance along which the optical signal propagated through the fibre increases.

3.2.2 Fibre signal attenuation in the TT modules

The attenuation length of the WLS fibres were measured during the initial stages of the OPERA experiment [17]. The fibres were placed into a 1 mm-diameter hole carved into a NE^{2}110 scintillator illuminated by an H_2 UV lamp, as illustrated in figure 3.23 (top). The measurements of the collected light intensity vs. the distance between the photodetector and the illumination spot along the Y11(175) MJ fibre from Kuraray used in the OPERA Target Tracker is shown in the figure 3.23 (bottom). The corresponding number of photoelectrons is provided for reference. The measured points have been fitted with a sum of two exponentials, given by

$$\mathrm{N}\left(x\right) = \exp\left(2.59 - \frac{x}{\lambda_s}\right) + \exp\left(2.29 - \frac{x}{\lambda_l}\right), \tag{3.18}$$

where $\mathrm{N}\left(x\right)$ represents the collected light intensity corresponding to a variable distance x travelled by the signal along the WLS fibre. The parameters λ_s = 79 cm and λ_l = 573 cm are known as the short absorption length and the long absorption length, respectively [17]. The short absorption component dominates for shorter propagation lengths (typically below 80 cm) while the long component becomes prominent at longer propagation lengths. Overall, the result indicates an attenuation of 48% over a propagation length of 1 m along the fibre. However, the aforementioned measurements have been conducted prior to 2007, and not much information about the procedure or the attenuation model used by OPERA is available.
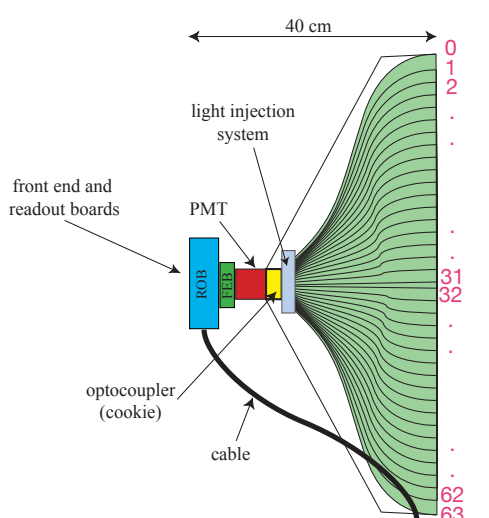
In the TT, the distance of transmission of the signal along the optical fibre (hence also the degree of WLS fibre signal attenuation) depends on the geometrical position of the muon crossing point on a TT module. On a given strip, a signal detected closer to the MA-PMT is subject to lesser attenuation compared to another similar signal on the same strip generated further away from the MA-PMT. Furthermore, the extra length of the WLS fibre in the end-cap of a TT module that extends from the end of the scintillator strip to the optocoupler of the MA-PMT also varies from strip to strip. This additional length of WLS fibre is shortest for the scintillator strips running through the middle of a TT module, and are longest for those placed towards the edges, as tabulated in the table 3.1. Therefore, the degree of attenuation of an optical signal also depends on the position of the scintillator strip. As a result, the charge signals observed by the TT require an additional correction in terms of the propagation length along the optical fibre.

The length of a plastic scintillator strip in the TT is 6.86 m. Hence, The distance of optical signal propagation within the optical fibre in the TT ranges from 0.22 m (at the nearer end of the scintillator strips 31-34) up to 7.9 m (at the farther end of the scintillator strips 1, 2, 63, 64). According to the OPERA calibration in the expression 3.18, this indicates a signal

---

[2]Nuclear Enterprise.

Table 3.1 : *The extra length of optical fibre in the end-cap of a TT module, extending from the exit of a scintillator strip to the optocoupler of the MA-PMT, for different scintillator strips. The diagram shows the variability in this extra length and the scintillator strip numbering. The extra length was calculated as half the difference between the fibre length and the plastic scintillator strip length (6860 mm). Fibre lengths and the scintillator strip length are from [148].*

Strip number		Length of fibre (mm)	Extra length of fibre (mm)
0,1	62,63	9004	1072
2,3	60,61	8891	1016
4,5	58,59	8778	959
6,7	56,57	8665	903
8,9	54,55	8552	846
10,11	52,53	8439	790
12,13	50,51	8326	733
14,15	48,49	8213	677
16,17	46,47	8100	620
18,19	44,45	7987	564
20,21	42,43	7874	507
22,23	40,41	7761	451
24,25	38,39	7648	394
26,27	36,37	7535	338
28,29	34,35	7422	281
30,31	32,33	7309	225

attenuation ranging from 16% up to 89%. However, since the electronic readout is done at either ends of the scintillator strips, the events that may suffer a higher level of attenuation as seen by the MA-PMT at the farther end suffer a much lower level of attenuation as seen by the MA-PMT at the nearer end. Therefore, the highest level of attenuation is expected when a muon crosses a TT module at the middle of a scintillator strip towards the edges of the module (equivalent to a propagation distance of 4.5 m), amounting to 80%.

The ageing of the plastic scintillator strips was tracked via the time evolution of the MA-PMT signal response over five years of OPERA beam (CERN Neutrinos to Gran Sasso, CNGS) runs in the period 2008-2012. Based on the findings, it is expected that there will be a 20% reduction in the mean charge deposition from the time of production of the scintillator strips, roughly 20 years ago, until the beginning of JUNO data collection. It is worthy to mention that, accounting for the scintillator strip ageing, it is expected to observe 4.8 PE from muon crossing events even in the most disfavoured case at the beginning of TT data acquisition [16].

3.2.3 The Top Tracker Prototype

A prototype of the TT (TTP) was constructed at IPHC using the least favourable modules manufactured for the OPERA experiment as a demonstrator of the TT. Moreover, the TTP
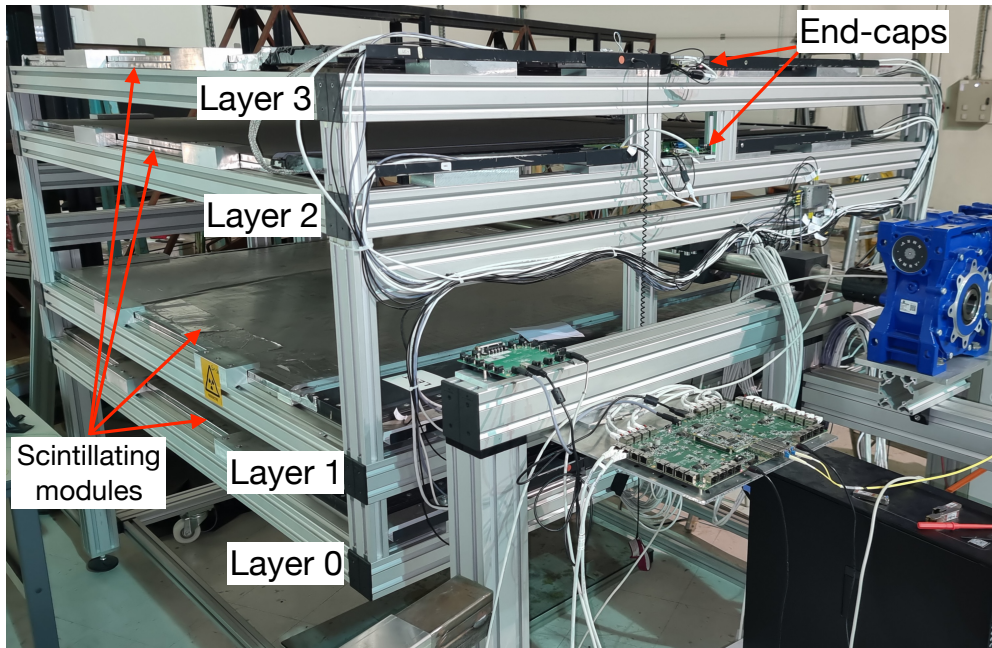
Figure 3.24 : *The Top Tracker Prototype.*
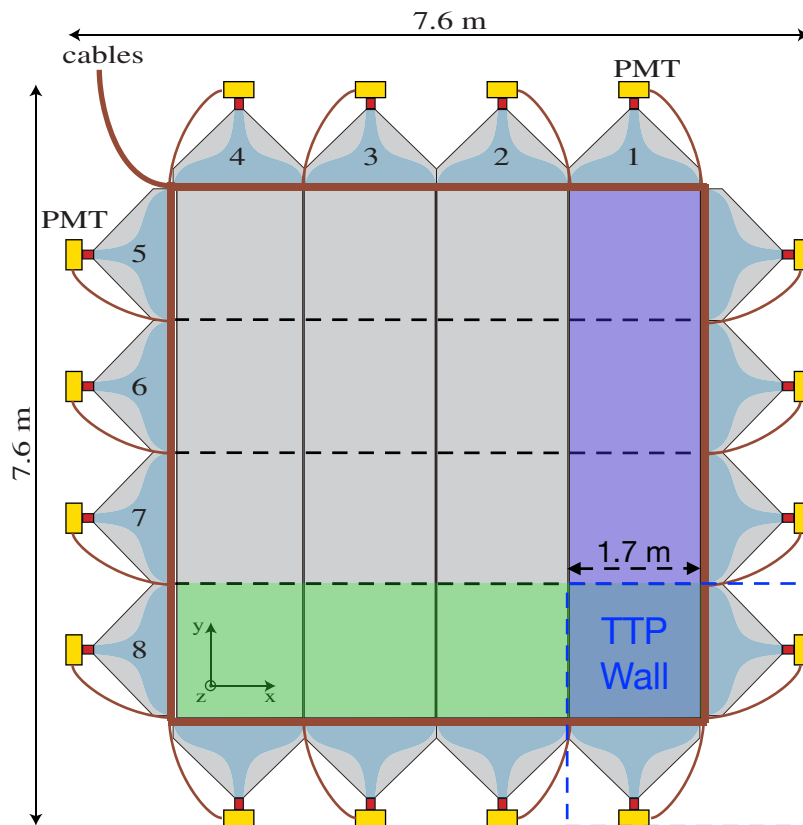
Figure 3.25 : *The schematic diagram of a wall of the Top Tracker Prototype with respect to a TT wall. Adapted from [16].*
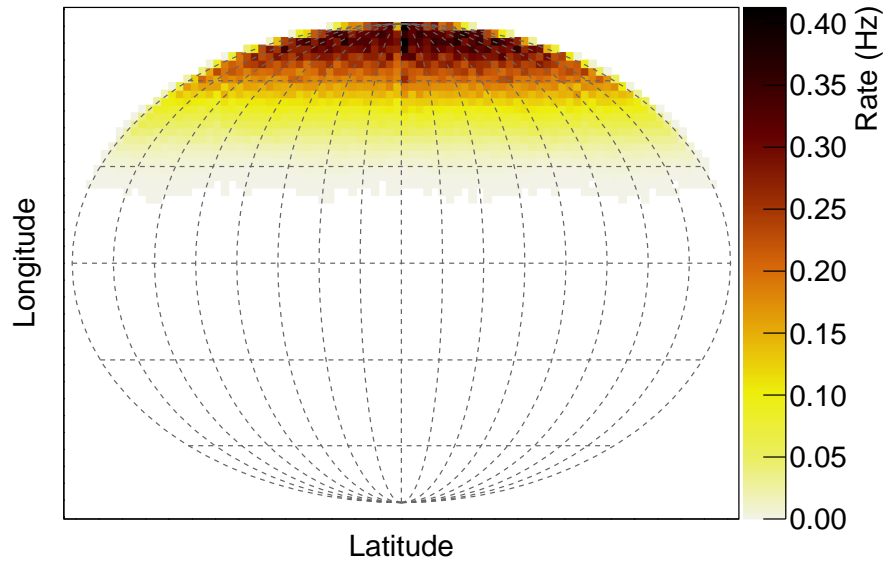
Figure 3.26 : *The distribution of observed muon directions in the TTP. The Mollweide projection projects the 3D sphere onto a plane. Longitude lines are displayed every 30°, and latitude lines every 22.5°. Colours indicate the observed muon rate [16].*
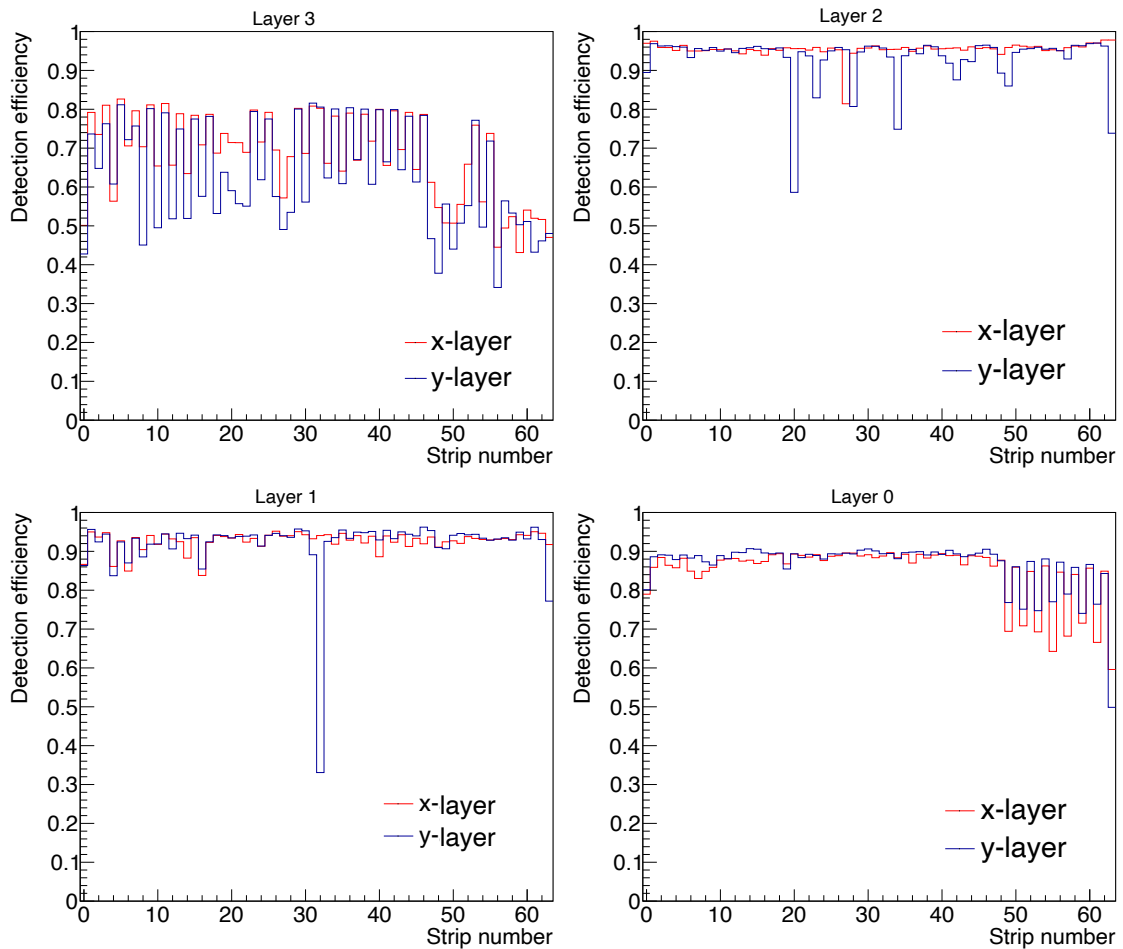
Figure 3.27 : *The muon hit detection efficiencies of plastic scintillator strips of different layers of the Top Tracker prototype.*

97

enables the development, fine-tuning, and evaluation of TT electronics components, along with the validation of TT electronics and hardware using the atmospheric muon flux in Strasbourg. Shown in the figure 3.24, the TTP consists of four layers. Each layer, akin to the TT design, comprises two planes oriented orthogonally. For the TTP, each plane was fashioned by segmenting a TT module into three parts, approximately 1.7 m from each end. The left and right end-caps of the divided modules serve as the x and y oriented planes, respectively, crucial for x-y coincidence selection akin to the TT. Consequently, each layer of the TTP originates from a single TT module, covering approximately 1/16 of the total surface area of a TT wall. The comparison of a TTP wall to a TT wall is shown in the figure 3.25. Unlike TT modules which feature electronics readout from either end, the electronic readout of TTP modules is performed on only one side. Given the requirement of 3 or 4 layers in coincidence for reconstruction, the field of view of the TTP is restricted to approximately 70° from the vertical. Figure 3.26 presents the directionality distribution of reconstructed muons as observed by the TTP. It is possible to expand this field of view with the aid of a motor incorporated into the TTP's rotation axis that enables the entire device to rotate.

Each end-cap of each TTP module are equipped with one MA-PMT, one FEB, and one ROB. All
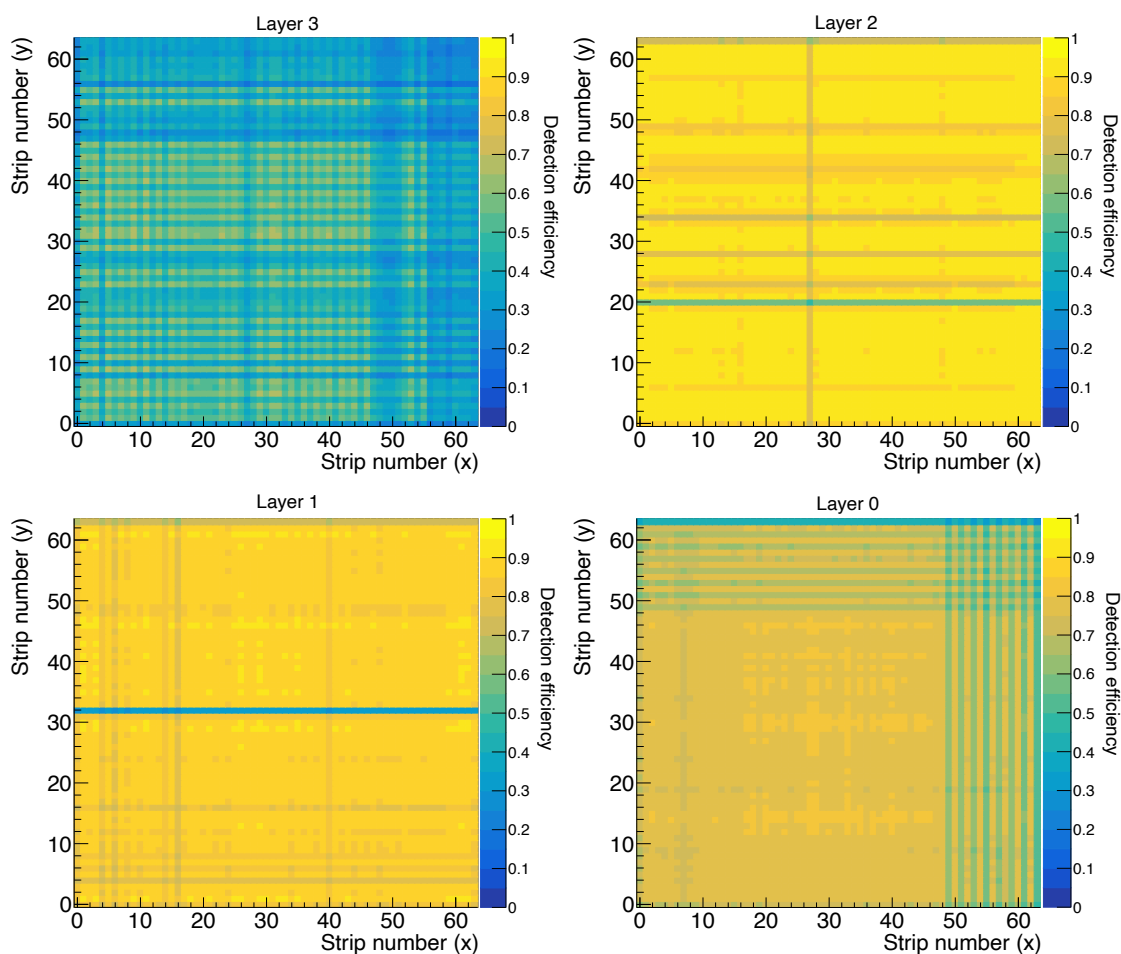
Figure 3.28 : *The muon hit detection efficiencies of 2D pixels of different layers of the Top Tracker prototype. The detection efficiency of each 2D pixel is the product of the individual detection efficiencies of the strips belonging to the x-module and the y-module that overlap to form the 2D pixel.*

8 ROBs are linked to a single CB positioned within the metal frame supporting the TTP. The TTP is capable of data acquisition in all the TT operation modes that were introduced under section 2.5.4. Through the TTP, calibration procedures have been successfully validated, and the interface between various electronic boards has been tested using real muon signals. All the TTP electronics have been calibrated prior to obtaining any physics data, as is described in detail in the reference [149].

A study performed prior to the doctoral thesis had revealed the muon hit detection efficiency of TTP scintillator strips. In this study, an atmospheric muon data sample obtained using the TTP was reconstructed using the JUNO Top Tracker muon reconstruction algorithm. From the results, a sample of reconstructed tracks that pass through all four TTP layers was selected. Hence, the detection efficiency of each scintillator strip, defined as

$$\text{detection efficiency} = \frac{\text{no. of muon hits observed}}{\text{no. of muon hits expected from reconstruction}}$$

was determined for each scintillator strip. The figure 3.27 depicts the strip-wise detection efficiencies of each layer. It indicates that most of the scintillation strips have detection efficiencies of the order of 85% or above. Layers 1 and 2 constitute the best scintillator strips which have efficiencies at or above 90%, with the exception of a few strips. In contrast, layer 3 is made up of strips of much worse efficiencies of around 70% on average. Scintillator strips of such poor detection efficiencies are as a result of aged scintillator strips and/or broken WLS fibres. The figure 3.28 illustrates the detection efficiencies of 2D pixels created by the perpendicular overlapping of scintillator strips from the x and y sub-layers in each TTP layer. The detection efficiency of the 2D pixels in layer 3 is approximately 50% on average due to the poor quality of the scintillator strips used in its formation. However, layers 1 and 2 demonstrate almost uniform detection efficiencies of the order of 80-90% throughout the surface, owing to the good quality of the scintillator strips that form them.

3.2.4 Procedure for estimating the WLS fibre attenuation

The atmospheric muon flux constitutes a free and readily available source of ionizing radiation that could produce scintillation events throughout the TTP modules, given sufficient exposure time. Therefore, the data sample for the analysis was obtained by continuously operating the TTP to perform data acquisition in the normal run mode (introduced under section 2.5.4) for 7 days. The muon tracks through the TTP were reconstructed using the JUNO official muon reconstruction algorithm.

The average energy of a muon at sea level is 4 GeV. At these energies, the range of muons through plastic (density ~ 1 g·cm^{-3}) is of the order of few hundreds of kilometres [25]. Thus, the plastic scintillator can be considered as a thin absorber with respect to the range of atmospheric muons. At such energies, muons can be treated as minimum ionizing particles, where the energy deposited in the scintillator strip per unit length is fairly independent of the energy of the muon. Therefore, the quantity of light produced within the scintillator strip increases in proportion to the increasing length of muon track within the strip. Hence, it is important to consider the charge observed per unit length of muon track within the
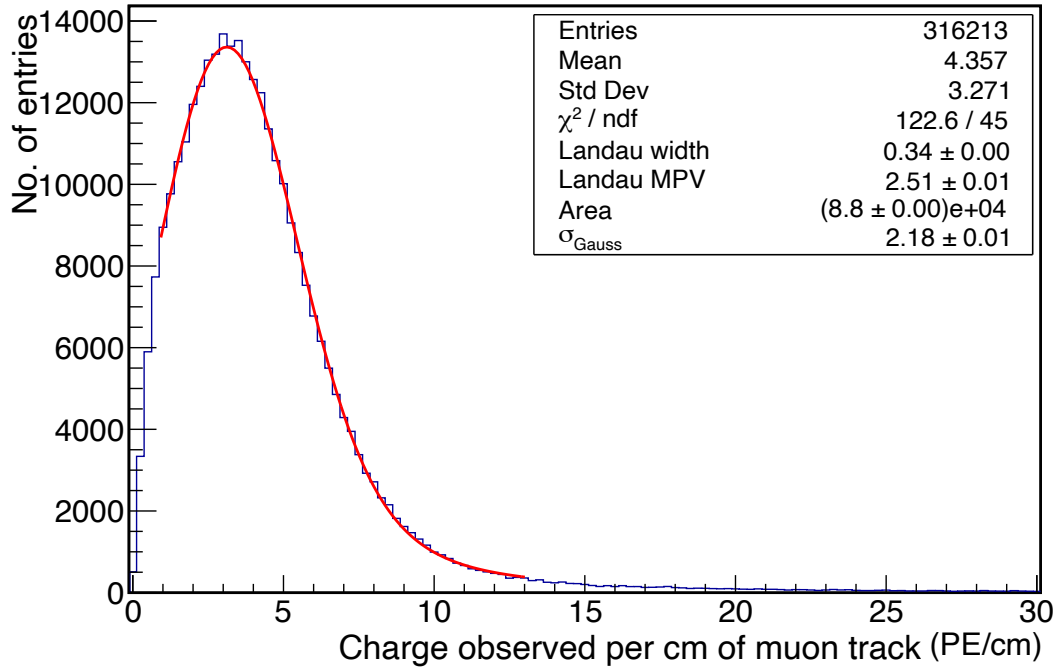
Figure 3.29 : *Distribution of observed charge per unit length of muon track through a section of a scintillator strip of the Top Tracker prototype. The distribution has been fitted with a Landau-Gauss convolution function in the range 1-13 PE/cm (red line).*

scintillator strip to eliminate bias in the observed charge due to varying muon track lengths within the scintillator strip. In this manner, the corresponding distributions of charge observed per unit length of muon track through different sections along the length of the scintillator strip was derived. Each strip is virtually sectioned into 64 parts of length 2.63 cm. The distribution of charge observed per unit length of muon track within the scintillator strip for one such section is depicted in figure 3.29.

In order to quantitatively characterize the attenuation of the optical signal due to the propagation through the optical fibre, a parametrization of the measured distribution of the observed charge per unit muon track length within the scintillator strip is needed. The inherent randomness of the ionization process when a fast charged particle traverses a thin material leads to significant fluctuations in the energy loss (Δ) within a thin absorber compared to the particle's range. The probability function $f(\Delta)$, known as the energy loss distribution or straggling function, may be characterized by the position of the most probable value (MPV) of the distribution function (Δ_p) and the full width at half maximum (w). Normally, Δ_p is found at a lower value compared to the mean value of the energy loss derived from the Bethe-Bloch function. Lev Landau was the first to calculate these energy loss fluctuations [150] by solving an integral transport equation given by

$$\frac{df(x, \Delta)}{dx} = \int_0^\infty W(E) \left[f(x, \Delta - E) - f(x, \Delta) \right] dE, \tag{3.19}$$

where $f(x, \Delta)$ represents the probability that the incident ionizing particle will lose a

Δ quantity of energy when traversing a x thickness of the medium, and $W(E)dE$ is the probability per unit length to transmit an energy E to an electron in the medium. Although a solution of $W(E)$ is not generally known, Landau's solution expressed $W(E)$ as

$$W(E) = \frac{\xi}{x} \cdot \frac{1}{E^2}.$$

(3.20)

The quantity ξ is described by

$$\xi = \frac{2\pi z^2 e^4}{m_e c^2 \beta^2} \cdot \frac{NZ\rho x}{A},$$

(3.21)

where z is the electric charge of the particle, m_e and e are the mass and the electric charge of an electron, respectively, c is the speed of light, β is the ratio of the particle velocity to the speed of light, N_A is the Avogadro number, and Z, A and ρ are the atomic number, mass number and the density of the material, respectively. Hence, the Landau distribution is given by

$$f_L(x, \Delta) = \frac{1}{\pi \xi} \int_0^\infty \exp\left(\frac{\pi y}{2}\right) \cos\left(y \ln(y) + \lambda y\right) dy,$$

(3.22)

where y is an arbitrary variable for the integration. The variable λ is defined such that

$$\lambda = \frac{\Delta - \langle \Delta \rangle}{\xi} - \beta^2 - \ln(k) - 1 + C_E,$$

(3.23)

in which $k = \frac{\Delta}{E_{max}}$, where E_{max} is the maximum energy transferable to an electron during a single collision, and C_E is the Euler's constant. The Landau distribution is an asymmetric distribution, featuring a tail that extends to E_{max}.

Theoretical predictions compared with experimental observations for solid-state materials show that the most probable energy loss usually matches theoretical expectations. However, the width of the experimentally observed energy loss distribution is broader than the Landau distribution, exceeding what can be attributed to electronic noise or resolution limitations. To address this, a modified cross-section approach is employed to incorporate electron binding energy, resulting in an improved energy loss distribution. Thus, the modified straggling function is expressed by convolving the Landau distribution with a Gaussian distribution defined by a standard deviation σ [151], as

$$f(x, \Delta) = \frac{1}{\sigma \sqrt{2\pi}} \int_{-\infty}^{+\infty} f_L(x, \Delta - \tau) \exp\left(-\frac{\tau^2}{2\sigma^2}\right) d\tau,$$

(3.24)

where τ serves as an arbitrary variable. The convolution yields a broader distribution, typically with a peak value slightly higher than predicted by the Landau theory.

The measured charge distributions, as was shown in the figure 3.29, were fitted using a C++/ROOT implementation of the Landau-Gauss convolution function given in the reference [152]. In this implementation, the fit is characterized by four parameters: w (width parameter of the Landau density), Δ_p (MPV of Landau density), total area, and σ (standard deviation of the convoluted Gaussian function). The Landau MPV is used as the parameter

to characterize the distribution of charge per unit length of muon track at each section of scintillator strip.

A poorly aged scintillator strip will have a low photon yield per unit of deposited energy in it, and a damaged fibre will lead to poor collection and/or transmission of photons to the MA-PMT. As a result, the quantity of photons transmitted to the MA-PMT via such scintillator strips is lower compared to the other strips of better quality for similar muon hits. Therefore, the charge deposition on such scintillator strips is always under-estimated. Additionally, muon hits with lower track lengths in the scintillator strip (which in turn deposits a lower quantity of energy) lead to producing a lower quantity of photons compared to other muon hits. In a scintillator strip of poor quality, the quantity of photons reaching the MA-PMT due to such hits is diminished even further. This may lead to such muon hits being completely lost. Furthermore, each 2D pixel of the TTP relies on the detection of the muon hits on both crossing scintillator strips to form a muon 3D point. If one of those strips did not detect a hit in coincidence with the strip perpendicular to it, then the muon 3D point cannot be reconstructed. As a result, the poor detection efficiency of one strip can bias the measurements made on the ones laid perpendicular to it.

Considering the aforementioned concerns, the sample of scintillator strips of the TTP that can be used for the current analysis was carefully chosen. Based on the detection efficiency measurements shown in the figures 3.27 and 3.28, a minimum requirement of 90% detection efficiency is established for the selection of scintillator strips. Furthermore, a similar level of detection efficiency is desired on the scintillator strips perpendicular to the selected ones. Thus, the scintillator strips of TTP layers 0 and 3 are rejected due to lower detection efficiencies as well as large fluctuations in the detection efficiencies among scintillator strips. Scintillator strips belonging to the sub-layer x of layer 2 demonstrates good consistency of the order of few percent except for one strip. However, large inconsistencies in detection efficiency is observed on the corresponding sub-layer y, deeming layer 2 unreliable for the study. Finally, the scintillator strips belonging to the sub-layer y of layer 1 have appreciable consistency, except for 1 strip, where the largest difference in detection efficiency between strips is around 10%. The corresponding sub-layer x has excellent consistency in detection efficiency as sub-layer y, where the largest difference in detection efficiency between strips is also around 10%. Therefore, the scintillator strips of sub-layer y of layer 1 with detection efficiency larger than 90% were chosen as the sample for the analysis.

Figure 3.30 depicts the variation of the optical signal propagation distance along the WLS fibre depending on the muon hit position on a sub-layer. Notice that the signal propagation distance along the WLS fibre is shortest when the muon passes through the scintillator strips in the middle of the sub-layer and close to the end-cap. Conversely, the signal propagation distance along the WLS fibre is longest when the muon passes through the strips towards the edges of the TTP and at the end of the sub-layer opposite to the end-cap. Moreover, the two outermost strips at either end of sub-layers x and y were excluded from this study, as they are prone to the shielding effects from the lining material at the edges of the TTP layer. These 4 strips corresponds to the longest lengths of fibre available on a TTP module. The red (black) shaded regions of the figure 3.30 indicate the sections of scintillator strips situated towards the edges of the shown sub-layer (the sub-layer perpendicular to the shown one) excluded from the analysis as mentioned above. Note that this exclusion narrows
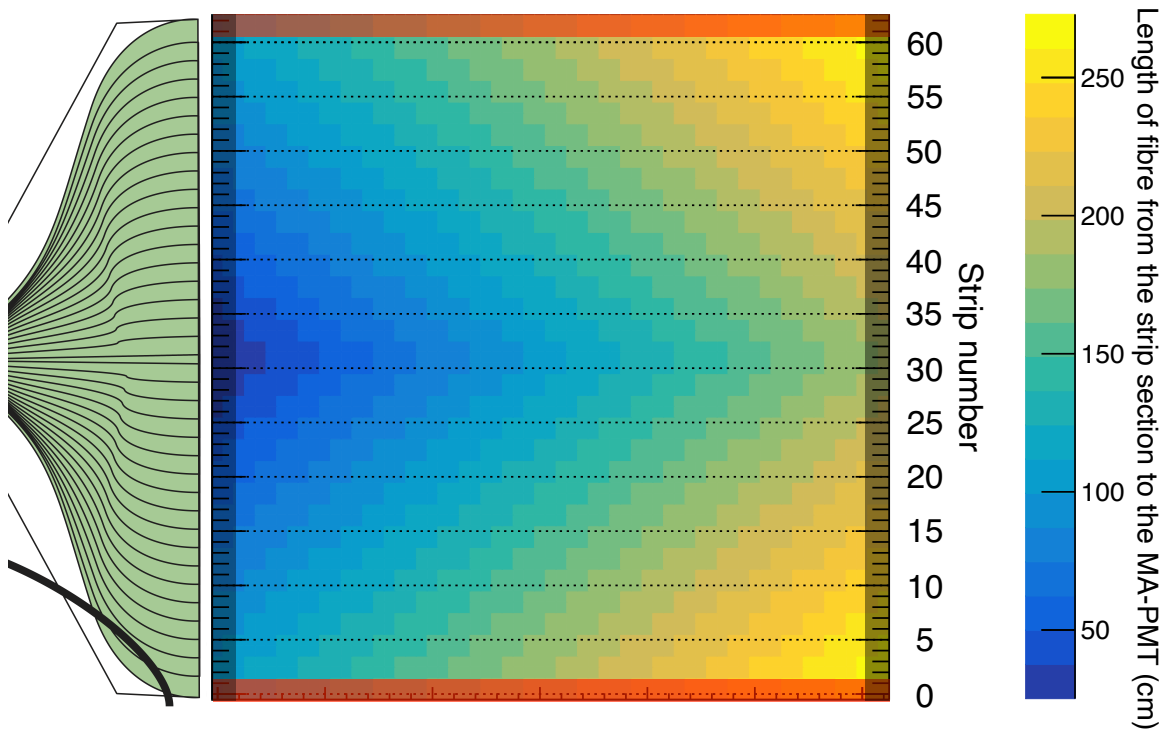
Figure 3.30 : *The variation of signal propagation distance along the WLS fibre at different sections of scintillator strips on a TTP sub-layer. The length is calculated from the centre of the strip section to the optocoupler of the MA-PMT in the end-cap. The end-cap region is depicted on the left of the figure. The red (black) shaded regions indicate the sections towards the edges of the sub-layer which are not considered for the estimation of WLS fibre signal attenuation.*
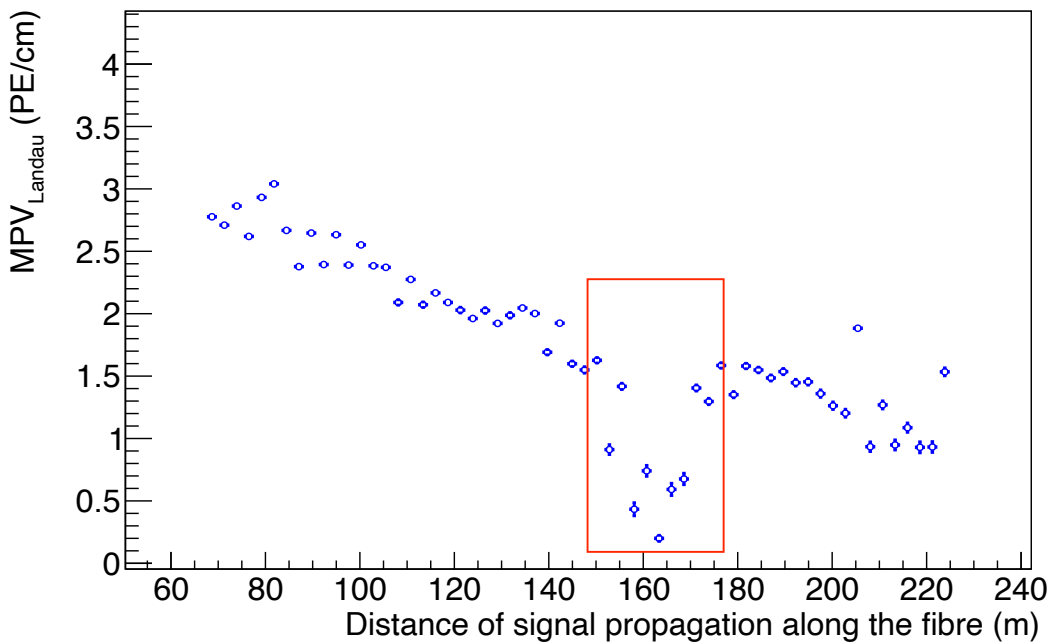
Figure 3.31 : *An example case of a rejected measurement of charge deposited by a muon through unit length of plastic scintillator strip. The red rectangle indicates the unusually low Landau MPV values observed on some sections of the scintillator strip.*

down the range of fibre propagation lengths, excluding 5.26 cm each at either end of each
selected scintillator strip. The charge deposited per unit length of muon track through the
scintillator strip at different sections of the selected strips were plotted as a function of the
distance of signal propagation along the fibre (i.e. length of fibre from the centre of the strip
section to the MA-PMT) for different scintillator strips. When plotting the Landau MPV
values as a function of signal propagation distance along the fibre for different sections of
the same scintillator strip, some strips showed unusually low MPV values in certain sections.
One such example is shown in the figure 3.31. The reason for this effect is not understood
clearly, and such strips were rejected from the sample. The distributions for the remaining
scintillator strips were individually fitted with the function

$$S(x) = A \cdot \exp\left(-x/\lambda_s\right) + B \cdot \exp\left(-x/\lambda_l\right), \tag{3.25}$$

that follows the form of the WLS fibre signal attenuation function used by OPERA, given
in the expression 3.18. Here, $S(x)$ is the variable Landau MPV corresponding to a variable
signal propagation distance x along the WLS fibre, and A and B represents the amplitudes
of the long and short exponential attenuation components, respectively. As seen in the
figure 3.30, most of the available scintillator strips do not sample fibre propagation lengths
sufficiently below 80 cm to be sensitive enough to estimate λ_s. Therefore, based on the
OPERA measurements, the ratio $\frac{A}{B}$ and λ_s were fixed to 1.35 and 79 cm, respectively.
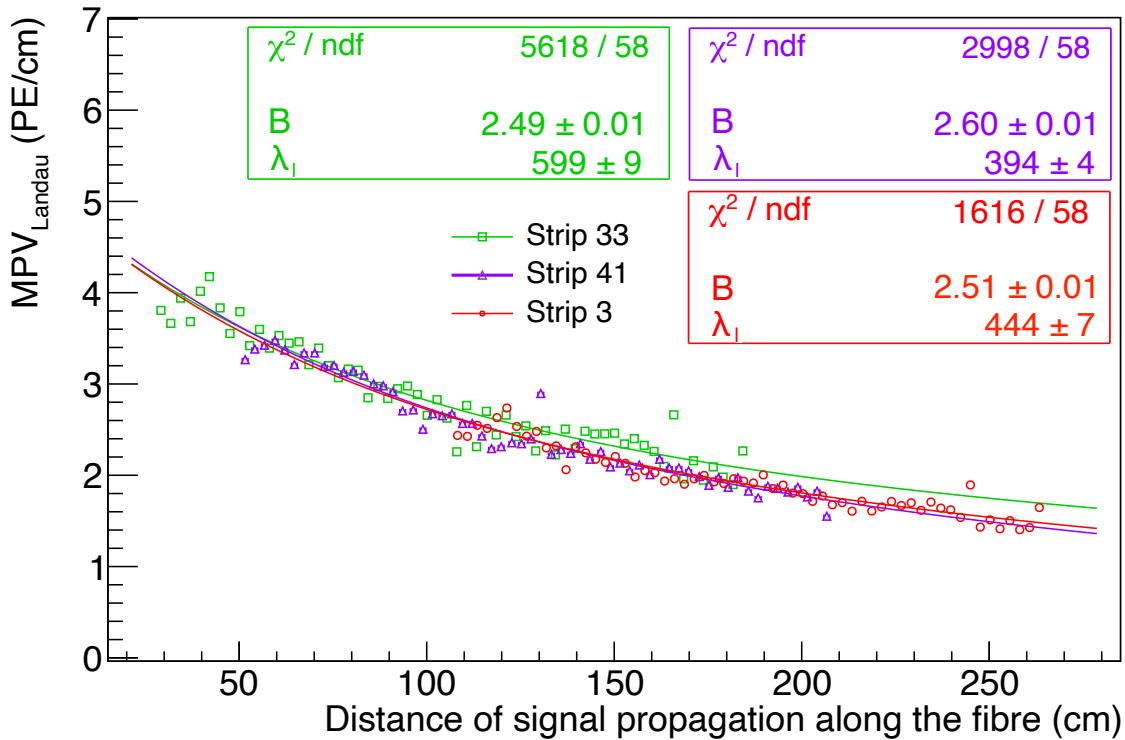
Figure 3.32 : *Variation of the Landau MPV over different sections of plastic scintillator strips of the
Top tracker prototype. The plot shows the measurements and the respective fits for three strips as an
example. The data points of each strip have been separately fitted with the expression 3.25.*
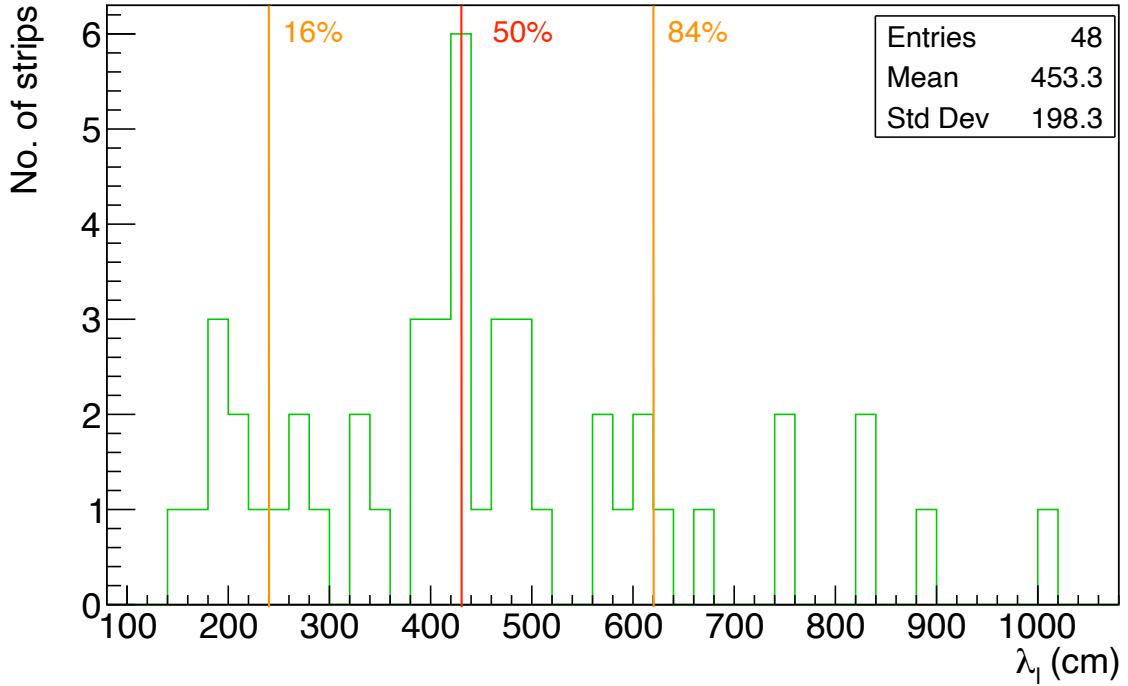
Figure 3.33 : *Distribution of the long attenuation coefficient estimated for different plastic scintillator strips of the x-sublayer of layer 1 of the Top Tracker prototype.*
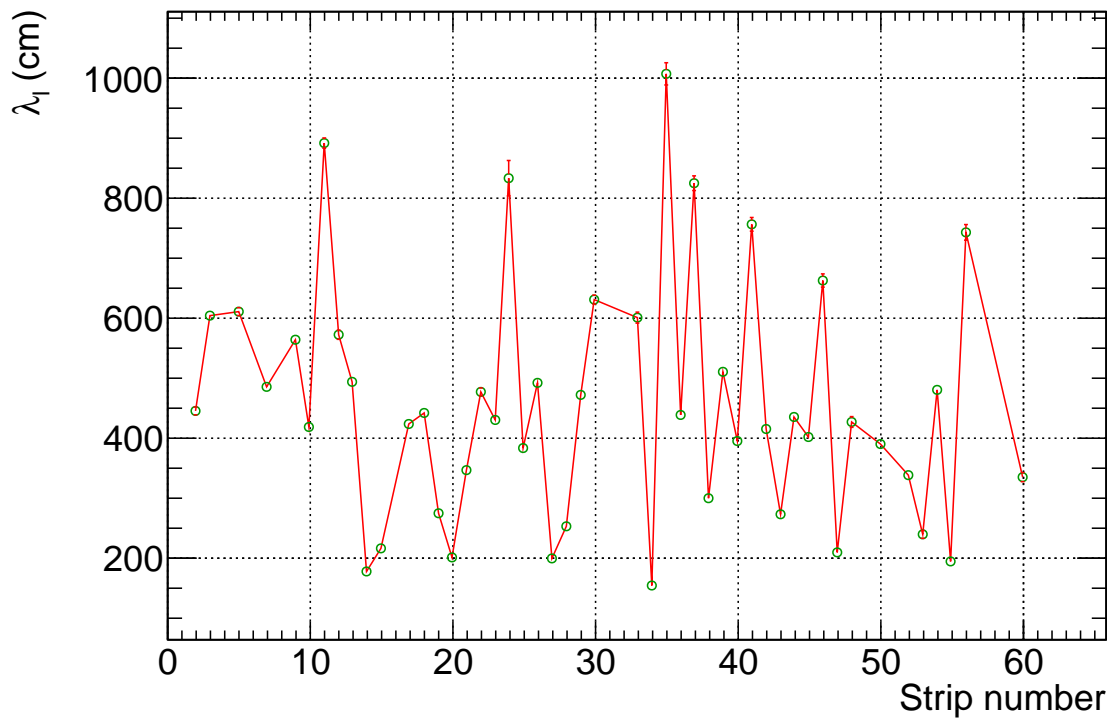
Figure 3.34 : *Graph of λ_l vs. strip number of layer 1 of the Top Tracker prototype.*

105

Then, the Landau MPV distributions were fitted to extract the value of λ_l, as shown in the figure 3.32.

The distribution of λ_l thus obtained from different scintillation strips yields an asymmetric distribution as shown in the figure 3.33. The observed distribution shows a wide range of values, spanning from as low as 140 cm up to as high as 1000 cm. This wide spread is due to the large systematic uncertainties associated with estimating λ_l which is about twice as much as the length of the WLS fibres available for the estimation. Since all of the plastic scintillator strips were produced with the same composition, under the same conditions and around the same period of time, the strips are expected to have similar behaviour with respect to each other. Therefore, it is reasonable to define a median λ_l using the distribution shown in the figure 3.33. The distribution yields a median λ_l of (4.3 ± 1.9) m. The uncertainties are defined by the bounds of the window that contains 68% of the statistics around the median λ_l. The estimate thus obtained via this method is statistically consistent with the the value measured by OPERA (λ_l = 5.73 m).

Figure 3.34 graphs the variation of λ_l against the scintillator strip number. It indicates that the estimation of λ_l is not biased with respect to the position of the scintillator strip. In conclusion, this estimation thus implies that the performance of the optical fibres has not deteriorated significantly in comparison to the OPERA measurements. At the estimated levels of attenuation, a muon passing through the TT will generate sufficiently high amount of photons so that the probability of detecting the signal is nearly perfect.

The estimation of λ_l from the TTP scintillator strips is subject to significant uncertainties due to the relatively short length of the strips in comparison to the estimated quantity. Furthermore, λ_s could not be measured using the TTP due to the lack of sufficient number of TTP scintillator strips that sample sufficiently low fibre propagation lengths below 80 cm. Given that the TT comprises many more scintillator strips, which are longer and of higher quality than those of the TTP, a more precise measurement of λ_l as well as λ_s can be achieved using the TT. Subsequently, these measured values can be globally adjusted in the JUNO TT simulation. Furthermore, as the plastic scintillator strips age, their scintillation light yield diminishes. Monitoring the time evolution of the attenuation lengths thus provide a means to quantitatively assess the ageing of the scintillator strips in the TT.

Résumé : Validations des cartes électroniques frontales du Top Tracker

Dans la chaîne électronique du Top Tracker (TT), le rôle de la carte frontale (FEB) est essentiel, car elle sert d'interface pour les signaux optiques provenant des canaux du tube photomultiplicateur à anode multiple (MA-PMT). La fonctionnalité de base de la FEB repose sur un circuit intégré à application spécifique, connu sous le nom de lecture multi-anode version 3 (MAROC3), qui fournit des outils essentiels pour l'interface avec les MA-PMT, la compensation des variations de gain inhérentes entre les différents canaux du MA-PMT et la mesure de la charge et le déclenchement spécifiques à chaque canal. Par conséquent, un étalonnage méticuleux de chaque FEB est essentiel pour l'interprétation précise des signaux détectés sur l'ensemble du TT.

Au total, 1200 FEB ont été produites pour le TT. À l'IPHC de Strasbourg, un banc d'essai automatisé a été mis en place pour les caractériser rapidement et complètement. À l'aide de ce banc d'essai, les performances des FEB ont été évaluées sur la base de divers critères, notamment les niveaux de piédestal (c'est-à-dire les mesures électroniques en l'absence de signaux d'entrée), la diaphonie (c'est-à-dire les fuites de signaux vers les canaux environnants), le réglage du seuil de déclenchement de l'électronique et la réponse à différentes charges injectées. Les mesures de charge sur le banc d'essai ont été effectuées à l'aide de l'ADC Wilkinson 8 bits interne des FEB. Dans le cadre de cette discussion, l'unité de charge mesurée par l'ADC Wilkinson est donc appelée WADC. Ce processus de test rigoureux a abouti à la sélection de 1160 FEB sur les 1200 FEB produites pour le TT. Le TT ne nécessite que de 992 des 1160 FEB sélectionnées. Grâce à une analyse complète des résultats des tests, il a été possible de classifier les FEB en fonction de leurs performances. Cela permet de sélectionner 992 FEBs pour les installer de manière à obtenir une réponse plus uniforme sur l'ensemble du TT. Ce processus de classement garantit non seulement l'homogénéité, mais facilite également l'identification rapide et sûre des FEB de remplacement en cas de besoin. Par conséquent, tout remplacement peut être géré avec une perturbation minimale de la configuration électronique d'origine du TT.

Les mesures du niveau du piédestal sont considérées comme une tâche intégrale à accomplir pendant les étalonnages et les essais de la FEB, ainsi que pendant les acquisitions de données de physique. Lors de la prise de données JUNO, il est prévu de collecter des informations sur le niveau du piédestal des FEB TT à intervalles réguliers tout au long des opérations du TT. Pour déterminer les niveaux de piédestal, l'acquisition de données a été réalisée sur tous les canaux des 1160 FEB en utilisant le banc d'essai en mode piédestal. La distribution de la charge est caractérisée par sa moyenne (Q_0) et son écart-type (σ_0). Les distributions de la moyenne Q_0 pour l'ensemble des FEB indiquent un écart-type relatif de l'ordre de 3%. Le σ_0 moyen du piédestal est de l'ordre de 0,26 WADC, ce qui est limité par granularité des ADCs à 8 bits. Cette mesure indique donc un niveau élevé de stabilité du piédestal pour l'ensemble des FEB.

Le niveau de déclenchement correspondant à une charge physique donnée est fixé par le convertisseur numérique-analogique (DAC) du MAROC3 en termes d'unité électronique

arbitraire (unités DAC). Il est commun à tous les canaux d'une FEB donnée. La distribution du bruit électronique inhérent à la FEB est censée se conformer à une distribution gaussienne, caractérisée par sa moyenne μ et son écart type σ.

Pour mesurer les niveaux de bruit électronique inhérents aux unités DAC de tous les canaux de chaque FEB, le nombre de déclenchements enregistrés sur une durée de 100 ms a été compté pour différentes valeurs DAC, à une fréquence d'auto-déclenchement de 8 MHz. La distribution du nombre de déclenchements en fonction de la valeur du DAC suit la forme d'une fonction d'erreur Gaussienne caractérisée par μ et σ. Les distributions de μ et σ ont donc été obtenues en ajustant les mesures de tous les canaux de chaque FEB. L'écart-type relatif de la moyenne de μ sur l'ensemble des FEB est d'environ 3,6%, tandis que l'écart-type de la moyenne de σ est d'environ 0,25 DAC, ce qui est limité par la granularité du DAC. Ces résultats soulignent collectivement que les FEB présentent un niveau élevé de concordance en termes de niveaux de bruit électronique intrinsèque entre les différents canaux au sein d'une même FEB ainsi qu'entre les différentes FEB.

La charge moyenne déposée par les muons atmosphériques dans les bandes de scintillateur en plastique du TT est d'environ 4,8 PE. Pour garantir une détection efficace, il est prévu que le seuil de déclenchement du MA-PMT soit fixé à 1/3 PE, ce qui assure une efficacité de sélection de >99% pour les véritables signaux muoniques. Comme le seuil DAC s'applique aux 64 canaux d'une FEB, il est important de vérifier la cohérence du seuil sur l'ensemble de ces canaux.

Pour déterminer le seuil en unités DAC correspondant à 1/3 PE (environ 56 fC à 10^6 de gain MA-PMT), des injections de charge équivalente à 1/3 PE ont été effectuées à 50 kHz dans tous les canaux de chaque FEB à des valeurs de seuil DAC variables. La distribution de la charge résultante suit une distribution gaussienne caractérisée par sa moyenne μ et son écart type σ. Ainsi, la distribution de l'efficacité de déclenchement en fonction de la valeur DAC suit une fonction d'erreur gaussienne caractérisée par μ et σ. Les distributions de μ et σ ont donc été obtenues en ajustant les mesures de tous les canaux FEB. Les valeurs de μ et σ étaient cohérentes entre les FEB, ne montrant aucune dépendance avec les canaux du MA-PMT. Une analyse de corrélation de μ et σ a identifié deux régions distinctes dans l'espace des paramètres. En effet, certains canaux s'écartant des tendances attendues à $\mu \sim$450 DAC, et nous avons pu identifier que ceci est du à la puce MAROC3. Ce changement dans la tendance vers 450 DAC identifié dans cette thèse a un effet négligeable sur la performance du TT. Les écarts types relatifs des μ et σ moyens sur l'ensemble des FEB étaient d'environ 4% et 5,3%, respectivement, ce qui confirme la cohérence des performances sur l'ensemble des FEB pour le seuil de 1/3 PE.

Pour interpréter la lecture numérisée de la charge par le MAROC3, un étalonnage pC↔WADC est nécessaire. Dans la configuration du banc d'essai, chaque canal de chaque FEB a été injecté avec des charges à cinq valeurs spécifiques dans la gamme 0-10 pC (0-63 PE) pour à un gain de 10^6. Un canal FEB a été injecté manuellement avec une gamme plus large de valeurs de charge distinctes et précisément calibrées. Les résultats montrent que la charge mesurée par l'ADC du MAROC3 augmente linéairement avec la charge injectée (régime linéaire), jusqu'à ce qu'elle atteigne la saturation (régime de saturation). Une fonction mathématique a été crée pour paramétrer la réponse du pC↔WADC en fonction de caractéristiques telles que la linéarité de la charge a_1 (c'est-à-dire le gradient du régime linéaire) et le degré de

saturation a_2 (c'est-à-dire la valeur du WADC à laquelle l'ADC MAROC3 sature). Cette fonction a été validée en comparant la courbe pC↔WADC ajustée à partir des données du banc d'essai avec celle des injections d'un quantité bien plus élévée de charges pour le même canal.

Par conséquent, les données du banc d'essai pour tous les canaux FEB ont été ajustées à l'aide de la fonction susmentionnée afin d'extraire les distributions a_1 et a_2 de toutes les FEB. Les analyses de corrélation de a_1 et a_2 entre les différentes FEB révèlent une excellente cohérence entre les FEB en ce qui concerne la réponse pC↔WADC, à l'exception d'une FEB dont la saturation est plus élevée. Hormis cette FEB, les mesures montrent que les écarts types relatifs des moyennes a_1 et a_2 sont de l'ordre de 2%. En outre, les valeurs de a_1 et a_2 ne dépendent pas des canaux MA-PMT.

Dans le but de sélectionner 992 FEBs pour garantir le plus haut niveau d'homogénéité des performances sur l'ensemble du détecteur, une note est calculée pour chaque FEB sur la base de la déviation des résultats susmentionnées de leur moyenne pour l'ensemble des FEBs susmentionnées. Les notes ont été calculées utilisant la somme des écarts relatifs au carré des paramètres a_1, a_2, μ et σ moyens (seuil DAC correspondant à 1/3 PE) de chaque FEB avec une valeur de démérite ajoutée pour les FEBs présentant des écarts évidents ou d'autres problèmes. Les FEB ainsi sélectionnées présentent une bonne cohérence dans leur performance globale. Il convient de noter qu'il est possible de conserver les 168 autres FEB comme de bonnes cartes de remplacement au cas où cela vienne à être nécessaire.

Dans le chapitre 2, il a été introduit que la haute tension du MA-PMT est commune aux 64 canaux d'un FEB, et que les non-uniformités de gain entre les différents canaux sont compensées par le réglage individuel des facteurs de gain du préamplificateur (p.g.f.) dans le MAROC3. Pour valider les performances des p.g.f., une FEB a été injectée avec des charges dans la gamme 0-10 pC à des p.g.f. de 0,5, 1, 2 et 3 et les courbes pC↔WADC correspondantes ont été mesurées. Notamment, l'inclinaison de la pente de linéarité augmente et la saturation est atteinte à une charge injectée plus faible lors de l'utilisation d'une p.g.f. plus élévée. Les mesures ont indiqué des niveaux de piédestal et de saturation stables pour différentes valeurs de p.g.f. Pour évaluer la reproductibilité de la charge à différentes valeurs de p.g.f., les mesures ont été soustraites du piédestal et remises à l'échelle en fonction des valeurs de p.g.f. Cela a indiqué que p.g.f. = 1, p.g.f. = 2 et p.g.f. = 3 se situent dans des bandes d'erreur de 10% l'une par rapport à l'autre. Ce niveau de reproductibilité de la charge à différentes p.g.f. est jugé suffisante pour l'objectif visé par le TT.

Les fibres optiques à décalage de longueur d'onde (WLS) assurent la transmission du signal lumineux de scintillation des bandes de scintillateurs aux MA-PMT. Au cours de la propagation du signal lumineux le long de la fibre, l'intensité du signal lumineux est atténuée en raison de facteurs tels que l'auto-absorption, la diffusion et les pertes par réflexion. Le degré d'atténuation augmente avec la distance sur laquelle le signal optique se propage dans la fibre. L'atténuation de la fibre WLS a été modélisée par les mesures de l'expérience OPERA comme une somme de deux fonctions exponentielles (avec des longueurs caractéristiques λ_s = 79 cm et λ_l = 573 cm).

Un prototype du TT (TTP) a été construit à l'IPHC en utilisant les modules les moins performants fabriqués pour l'expérience OPERA. Le TTP permet le développement, la mise

au point et l'évaluation des composants électroniques du TT, ainsi que la validation de l'électronique et du matériel du TT à l'aide du flux de muons atmosphériques à Strasbourg. Le TTP est constitué de 4 couches, dont la surface sensible est équivalente à 1/16 de la surface d'un mur du TT. La longueur de propagation du signal le long des fibres WLS varie entre 0,2 et 2,8 m, en fonction de la position de l'impact du muon dans la couche TTP.

Dans ce travail, le TTP a été utilisé pour estimer l'atténuation du signal optique due à la propagation dans les fibres WLS. Par conséquent, l'échantillon de données pour l'analyse a été obtenu en faisant fonctionner le TTP en continu pour effectuer l'acquisition de données en mode de fonctionnement normal pendant 7 jours. Les trajectoires des muons à travers le TTP ont été reconstruites à l'aide de l'algorithme officiel de reconstruction des muons de JUNO. Chaque bande est virtuellement divisée en 64 sections d'une longueur de 2,63 cm. Ainsi, les distributions correspondantes de la charge observée par unité de longueur de la trajectoire des muons à travers différentes sections le long de la bande de scintillateur ont été dérivées. L'étude a été limitée à un échantillon de bandes de scintillateurs dont l'efficacité de détection est supérieure à 90% afin d'éliminer les biais possibles dus à des bandes/fibres défectueuses ou mal vieillies. Pour éviter aussi des effets de bord, les bandes de scintillateurs dans les bords des couches du TTP n'ont également pas été utilisées dans cet étude. Les distributions de charge mesurées pour chaque section de bande ont été ajustées à l'aide d'une fonction de convolution de Landau-Gauss qui modélise le dépôt d'énergie par les muons à travers les bandes de scintillateur en plastique. La valeur la plus probable de la Landau (Landau MPV) est choisie comme sonde pour estimer l'atténuation du signal.

Pour toutes les bandes sélectionnées, les valeurs Landau MPV sont tracées en fonction de la distance de propagation du signal le long de la fibre. Ces distributions ainsi obtenues ont ensuite été ajustées à l'aide de la même fonction que celle utilisée pour l'expérience OPERA. Cependant, λ_s a été fixé à 79 cm parce que de nombreuses bandes n'ont pas de longueurs de fibres suffisamment courtes pour être sensibles à λ_s. La distribution de λ_l observée à partir des ajustements se situe entre 140 et 1000 cm. Cette large dispersion est attribuée aux grandes incertitudes systématiques associées à l'estimation de λ_l, qui sont approximativement deux fois la longueur des fibres WLS disponibles pour l'estimation. Étant donné que toutes les barreaux ont été produites avec la même fibre, on s'attend à ce que les bandes présentent un comportement similaire. Il est donc raisonnable de définir une valeur unique de λ_l = (4.3±1.9) m, ce qui est également cohérent avec le λ_l mesuré par OPERA. En outre, il a été vérifié que λ_l ne présente aucune corrélation avec la position de la bande de scintillateur.

<div style="text-align: right;">

CHAPTER 4

</div>

CONCENTRATOR BOARD VALIDATION

4.1 CB implementation in the Top Tracker prototype

 The Concentrator Boards are an integral part of the Top Tracker electronics chain. As detailed earlier in Section 2.5.3, the TT implementation places a CB on each TT wall. Each CB aggregates data from 16 FEB/ROB data streams on that wall, conducts L1 data selection, and transmits the charge and trigger information of the validated events to the DAQ system. This process reduces the TT data rate by an order of magnitude, and enhances the robustness of TT data handling. The CB is also responsible for event timestamping, utilizing the absolute time reference provided by the White Rabbit node implemented within it. Therefore, the validation of the CB performance in terms of the aforementioned aspects is essential. The purpose of this chapter is to present a detailed account of the CB validation tests performed as part of this doctoral research.
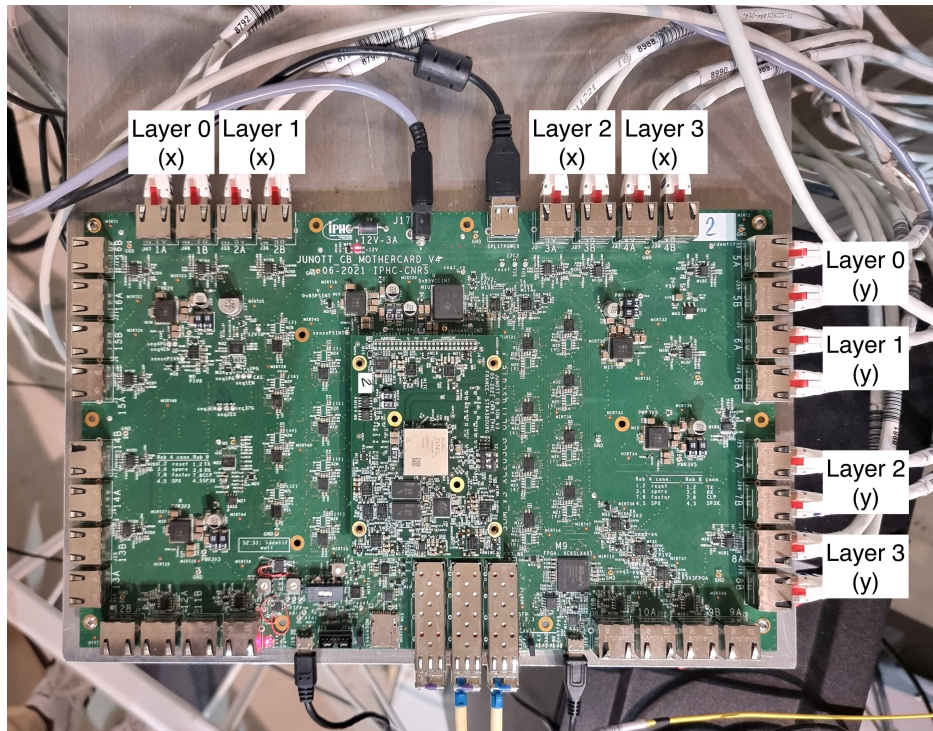
Figure 4.1 : *A photograph of the concentrator board installed in the TTP that shows how it is wired to different FEB/ROBs of different TTP layers.*

4.1.1 Introduction

As was introduced under section 3.2.3, the Top Tracker prototype is a useful tool to evaluate the performance of TT electronics under realistic conditions. Therefore, the TTP can be used to test the CB performance via the acquisition of muon data, as described under section 4.3. The figure 3.25 distinguishes the primary differences between a TT wall and a TTP wall. In a TT wall, the CB is responsible for aggregating data from each of the 16 FEB/ROB readouts belonging to four x-modules and four y-modules. In the TT, the CB concurrently searches for x-y coincident hits among all possible combinations of x-modules and y-modules. In contrast, a TTP wall is made up of only two perpendicular sub-layers, each with only one FEB/ROB readout. Therefore, with respect to the CB, the two FEB/ROB readouts of a TTP wall resembles one out of all possible combinations of x-modules and y-modules of a TT wall. Therefore, the TTP cannot be used to concurrently test the x-y coincidence selection performance of the CB across different x-modules and y-modules.

At the time of performing the studies mentioned in this chapter, the mass fabrication of the CBs had just commenced. Hence, only two CBs were available for testing. Although it was desirable to have one CB per TTP layer, the lack of CBs at the time required an alternative implementation. Unlike the CB implementation in the TT, where each wall has its own CB, a single CB was configured to aggregate data from all 8 FEB/ROBs across the different layers in the TTP. Figure 4.1 depicts the CB installed in the TTP and how it is wired to different FEB/ROBs from different TTP layers. Furthermore, the definition of an x-y coincidence was redefined accordingly for the TTP. An x-y coincidence in a TTP layer is thus defined

as two FEB/ROB triggers that occur within a sliding window of 100 ns and are linked to both modules within that TTP layer. The CB emulates this modified L1 trigger selection for each of the 4 TTP layers independently. In this implementation, the CB can be configured to operate in two different modes: x-y coincidence search mode (mode in which regular physics data acquisition is performed), or, validate-all mode (where all incoming data is accepted, without searching for x-y coincidences).

To perform CB tests using the TTP, a different ROB version (IPHC-ROB) developed by IPHC Strasbourg, was used. The IPHC-ROB was developed to provide a test platform to the FEB and CB, and so a few additional functionalities were implemented. First, the IPHC-ROBs also allow direct data reading, bypassing the CB. Second, the IPHC-ROB are also capable of data timestamping with the aid of an internal clock, unlike the ROBs that will be installed in the TT. This timestamp is different to how events are timestamped by the CB, which uses an internal clock synchronised with WRS. More details can be found under the section 4.1.2. Since neither of the aforementioned features were required in the official TT ROBs, those capabilities are not available in the official TT ROBs. It is also worth noting that IPHC ROBs do not have a separate ADC unlike TT ROBs. The IPHC-ROBs use Wilkinson ADCs for charge digitisation. Figure 4.2 shows a photograph of a IPHC-ROB installed in one of the end-caps of the TTP.

4.1.2 The timestamping structure

The CB is synchronised once per second via the WR switch. The CB has an internal clock of frequency 62.5 MHz (period=16 ns). The clock frequency is electronically multiplied by a factor of 16 using a clock multiplier, to simulate 1 ns clock pulses. This effective ns-clock keeps count of the number of ns elapsed since the last WR synchronisation. Therefore, a CB timestamp is composed of two parts: the time elapsed since UNIX epoch (provided by the WR system, in s), and, the time elapsed since the last WR synchronisation (in ns). Hence, a CB timestamp is an absolute timestamp. Furthermore, the pulses of the internal clock of the
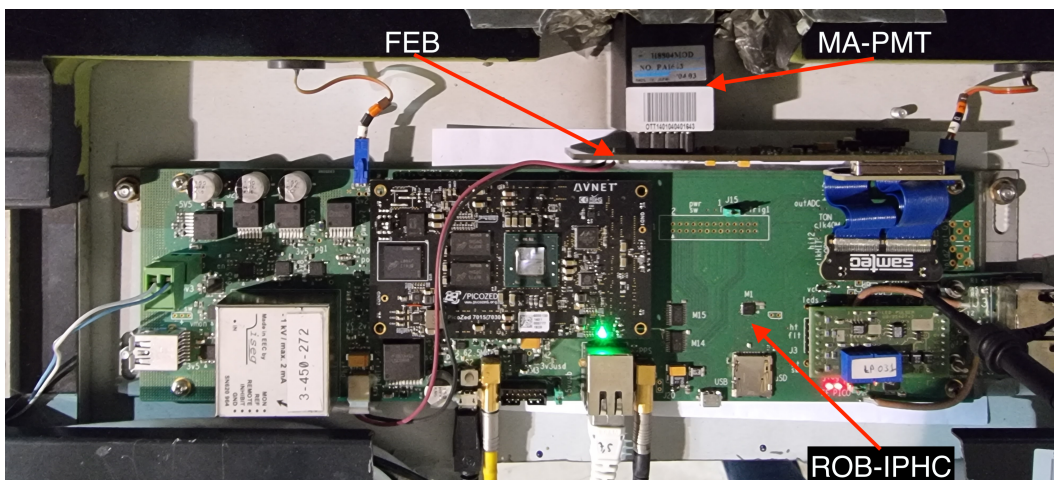
Figure 4.2 : *Photograph of an IPHC-ROB.*
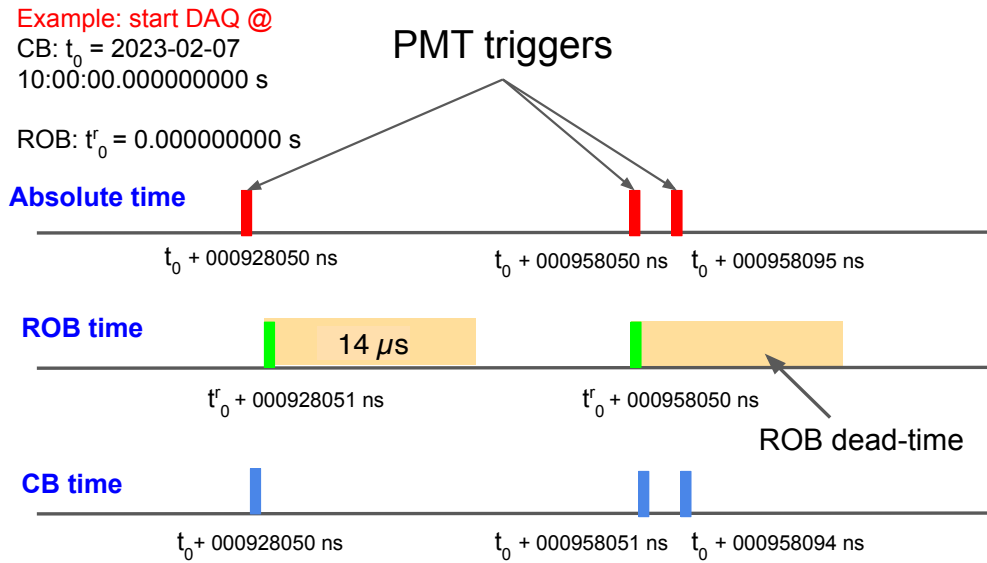
Figure 4.3 : *A schematic diagram comparing IPHC-ROB and CB timestamping, neglecting the impact of any constant time delays, such as due to cable lengths.*

CB are used by the IPHC-ROBs to generate its own ns-level timestamps. The IPHC-ROBs, however, only records the time since the beginning of the data acquisition, in units of ns, as a 32-bit integer. The clock overflows are handled in post-processing. Therefore, the timestamps provided by IPHC-ROBs are a measure of time relative to when the data acquisition commenced. Figure 4.3 serves as an example to distinguish the differences between the CB timestamps and IPHC-ROB timestamps. For the sake of a simplified illustration, let the impact of any constant delays (such as due to lengths of signal transmission cables) be ignored, and the PMT triggers illustrated in the example correspond to those of L1-validated events. Therefore, as illustrated in the figure 4.3, both the CB and the IPHC-ROB observe the MA-PMT trigger at the same moment of time. Although the ROBs do not respond to the MA-PMT triggers that arrive within the digitisation window, the CB will respond to all the FAST-ORs, generating a timestamp. Hence, an excess of CB timestamps with respect to the amount of ROB data packets is generally observed.

The CB data stream outputs two types of data packets. The first type, CB header data packets, contain the FEB identifier and the event-by-event charge and trigger information. The second type, the CB timestamp data packets, carries the FEB identifier, CB timestamp, as well as a CB validation status indicator that distinguishes whether the data packet was L1-validated by the CB or not. Both these data packets are saved into one file in the sequence of their arrival to the DAQ. The IPHC-ROBs output its own data packet that encapsulate the event-by-event charge and trigger information, as well as the IPHC-ROB timestamp. The IPHC-ROB data packets are saved into a separate file. Despite their differences, the event information recorded by the CB as well as the IPHC-ROBs correspond to the same physical events detected by the TTP. Therefore, the CB performance can be studied by correlating the IPHC-ROB data packets with the respective CB data packets.

It is planned not to store L1-rejected data in the TT. However, in the TTP implementation,

the trigger and timestamp information of the rejected data were still saved because the IPHC-ROBs did not fully implement the RESET functionality. Instead, all channel charges for L1-rejected events were reset to 0. Reading of the CB validation status indicator as well as the channel-by-channel charge information were found useful in revealing if the channels were reset properly, and, whether the CB validation status indicator has been appropriately assigned. These checks proved useful in debugging and improving the performance of CB firmware during the early stages of its development.

4.2 Validations of CB timestamping

4.2.1 Determination of the CB timestamping resolution

The TTP was operated in the normal run mode to make an hour-long measurement of atmospheric muons. For this measurement, the CB was configured to operate in x-y coincidence search mode. The data in the DAQ show no direct correlation among neither the CB header data packets, the CB timestamp data packets, nor the IPHC-ROB data packets. By comparing the channel-by-channel charge and trigger information, the CB header data packets and the IPHC-ROB data packets can be correlated. Due to the key differences between CB timestamps and IPHC-ROB timestamps identified earlier, it is not possible to directly compare them. Therefore, it is essential to establish a conversion to interpret IPHC-ROB timestamps as an absolute time, which could then be directly compared with the CB timestamps. In addition, the time measurements of different IPHC-ROBs are not perfectly aligned with each other. Therefore, individual conversions must be established for each IPHC-ROB separately.

A trio of CB header data-CB timestamp data-IPHC-ROB data packets were then chosen as
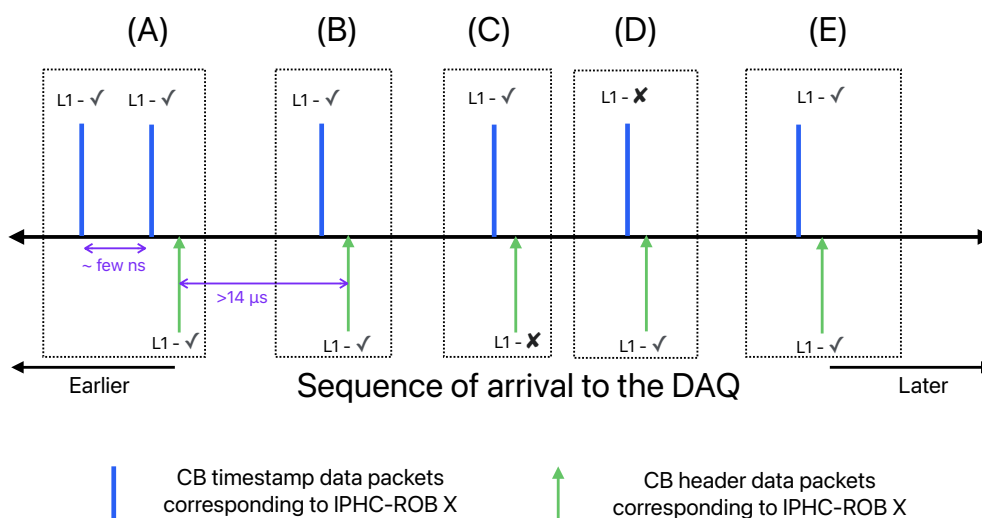
Figure 4.4 : A diagram depicting the method for aligning CB timestamp data packets with the corresponding CB header data packets.

follows, to serve as a reliable reference event to perform the conversion between IPHC-ROB timestamps↔absolute timestamps. Figure 4.4 serves as an example to illustrate the selection of the reference event. First, the reference event is required to be an L1-validated event. This condition is imposed because the channel-by-channel charges of all the L1-rejected events are reset to 0. As a result, it is impossible to neither distinguish nor directly correlate a CB header data packet to the corresponding IPHC-ROB data packet. Therefore, data packets labelled under (C) and (D) in the figure 4.4 do not qualify to be a part of a reference event. By considering the temporal sequence in which different data packets were saved into the CB data file, L1-validated CB data packets can be bundled together as the bundle (A) shown in the figure 4.4. Owing to the IPHC-ROB dead-time, the time span between CB timestamp data packets among two neighbouring L1-validated bundles is 14 μs or higher. Some bundles, like the one shown in (A), may contain multiple CB timestamp data packets. The extra packets could result from events unrelated to the original CB header data packet, such as due to electronic noise. These CB data packets are typically few ns apart from each other. Such data bundles are rejected to avoid the ambiguity of selecting one CB timestamp over the others within a bundle of two or more CB timestamps. This leaves bundles such as (B) or (E), with L1-validated CB header data packet with exactly one CB timestamp data packet. The earliest event that satisfies all the aforementioned requirement (in this example, (B)) is selected as the reference event.
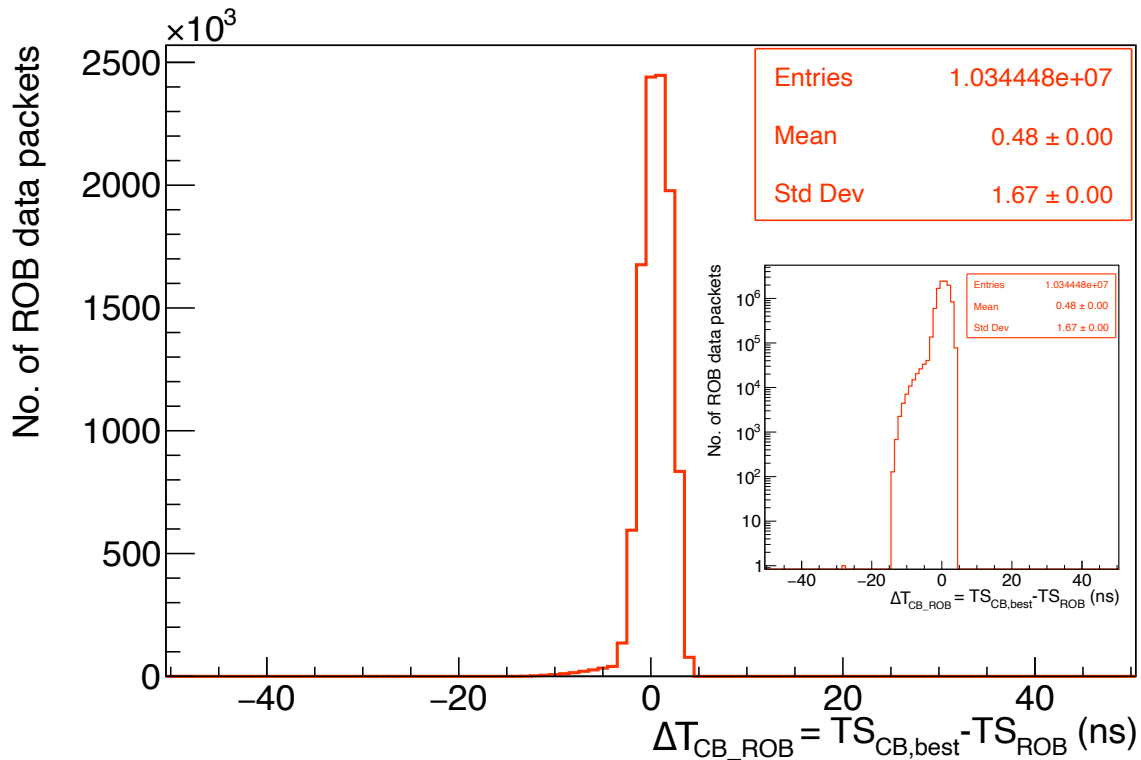
Figure 4.5 : *The distribution of time difference between the timestamp of a given IPHC-ROB data packet and the best candidate CB timestamp. The inset displays the same distribution with y-axis in log scale.*

From the acquired atmospheric muon data using the TTP, a bundle per each IPHC-ROB is obtained. Then, the IPHC-ROB data packet that corresponds to the CB header data packet is also obtained by comparing the charge and trigger information. Then the following assumption is made: for the IPHC-ROB concerned, the timestamp of the selected IPHC-ROB data packet and CB timestamp are in perfect temporal alignment (i.e. both the CB and IPHC-ROB timestamps represent the exact same moment in the absolute timeline). Based on this assumption, the IPHC-ROB timestamps can then be converted to an absolute timestamp (TS_{ROB}). Thus, for each IPHC-ROB data packet, the CB timestamp (TS_{CB}) with the correct CB validation indicator and the smallest $|\Delta T_{CB\_ROB}|$ (where $\Delta T_{CB\_ROB} = TS_{CB} - TS_{ROB}$) is selected as the best candidate CB timestamp ($TS_{CB,best}$) for that IPHC-ROB data packet.

The distribution of ΔT_{CB_ROB} thus obtained is shown in the figure 4.5. The results indicate that the CB timestamping resolution of 1.67 ns. Furthermore, a small tail that constitutes less than 1% of the events is seen at ΔT_{CB_ROB} below -5 ns. Upon investigation, it was understood that this results from how the triggers are handled by the CB. Since the CB clock period is 16 ns, it bundles together all the triggers observed between two clock pulses. If two or more triggers from the same FEB/ROB occur within this time window, the CB retains the latest trigger for that FEB/ROB, while the IPHC-ROB timestamp indicates the time of the earliest trigger. This leads to the observed tail of the figure 4.5.

4.2.2 Measurement of the CB timestamping stability

Time synchronisation among all trigger boards of the TT electronics chain is essential for the reliability and integrity of the TT data. Therefore, it is important to quantify the variability of the CB clocks, especially over long-term performance. For this purpose, the setup shown
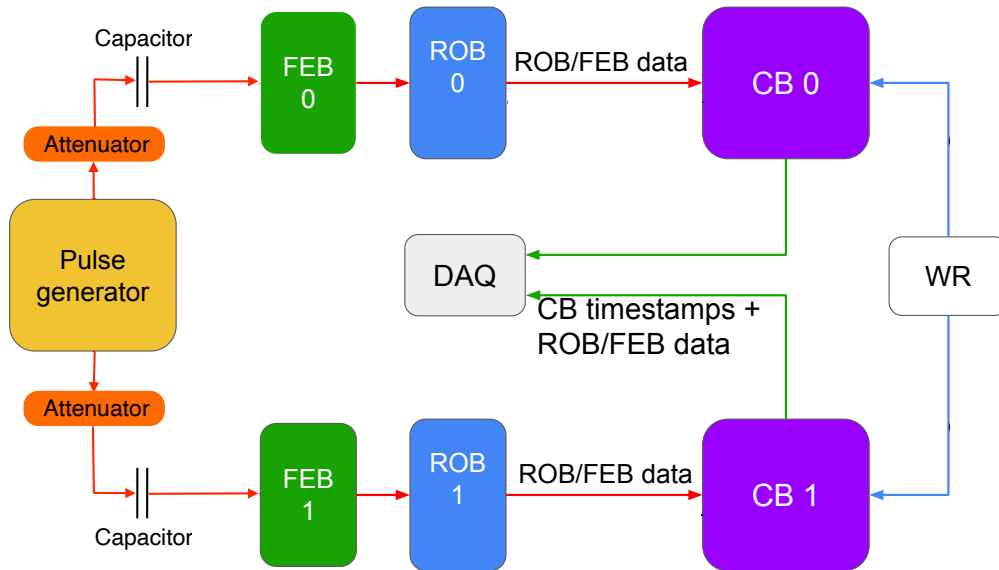
Figure 4.6 : *Schematic diagram of the setup used for the determination of the CB timestamping stability.*
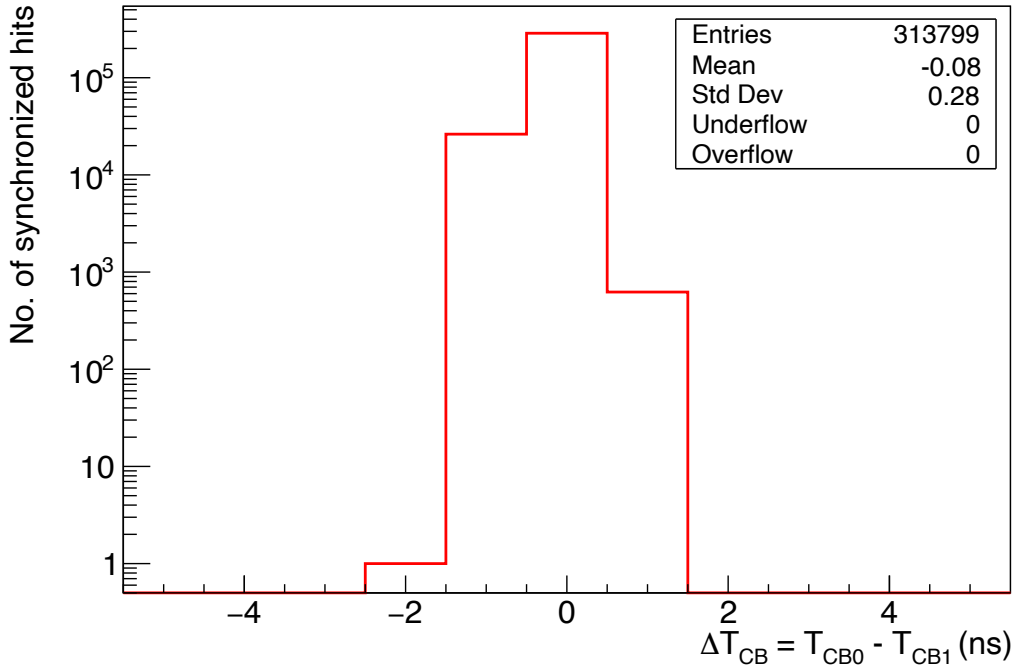
Figure 4.7 : *Distribution of the difference between timestamps corresponding to simultaneous injections as seen by two independent CBs.*

in the figure 4.6 was used. The pulse generator sends square-wave pulses to the attenuator. The attenuator is used to precisely control the amount of charge that is injected through the 10 pF capacitors. A pair of TT FEB/ROBs were concurrently injected with 1.6 pC of charge (about 10 PE) each using a pulse generator. The pair of TT FEB/ROBs are coupled to two independent CBs, which are synchronized via a WR timing system. Both CBs were configured to validate all incoming data, so that the charge injections do not get rejected by the L1 trigger. An initial data acquisition was performed such that the pulse generator simultaneously outputs injection pulses to both FEBs at the same frequency. The goal of this initial run was to determine possible constant time shifts t_{shift} between the times at which each FEB is triggered (such as due to cable lengths), given by

$$t_{shift} = t_{trig,1} - t_{trig,2},\tag{4.1}$$

where $t_{trig,1}$ ($t_{trig,2}$) represents the CB timestamp corresponding to the FEB 1 (2) trigger, given that the respective injection pulses were simultaneously output from pulse generator. The value of t_{shift} was thus determined to be 8 ns using the timestamps from the initial run. Then, a time delay of t_{shift} was applied via the pulse generator to the injection pulse of the FEB that triggers earlier than the other. This ensures that both the FEBs are triggered at the exact same ns. Following this calibration, the charge injection is performed at a frequency of 0.99 Hz. This specific injection frequency is chosen so as to be close yet different from the WR synchronisation frequency (1 Hz). Consequently, the time interval between each WR synchronization and the subsequent trigger (say, $\Delta T_{WR,trig}$) varies from one trigger to the next. This allows the sampling of CB timestamping performance at different values of $\Delta T_{WR,trig}$ with respect to the WR synchronisation time. The injection was performed for a

duration of 3 days.

Following the injection, the difference between timestamps recorded by the CB for the simultaneous injections was obtained and is shown in the figure 4.7. The distribution has a standard deviation of 0.28 ns, indicating a remarkable stability of the CB clocks.

4.2.3 Conclusion

The measurement ΔT_{CB_ROB} =1.67 ns which was determined under section 4.2.1 quantifies the dispersion of the CB timestamping with respect to the IPHC-ROB timestamps. Therefore, this measurement also includes the timing dispersion inherent to the IPHC-ROB timestamping as well. The measurement of ΔT_{CB} =0.28 ns quantifies the dispersion of the CB timestamping using CBs only. This reveals that the timing dispersion inherent to the CB is a fraction of a ns. Furthermore, these values are much smaller than the magnitudes of other sources that introduce timing uncertainties, such as the decay time in the scintillator strips (2.3 ns) and the WLS fibres (7.6 ns) [16]. Therefore, the level of CB timestamping precision and stability is sufficient for the intended purpose of the CBs in the JUNO TT.

4.3 Validations of CB x-y coincidence selection

4.3.1 CB x-y coincidence selection efficiency

As described earlier, the CBs have been entrusted with the important task of x-y coincidence selection. Since the x-y coincidence selection involves a sliding time window of 100 ns, it is
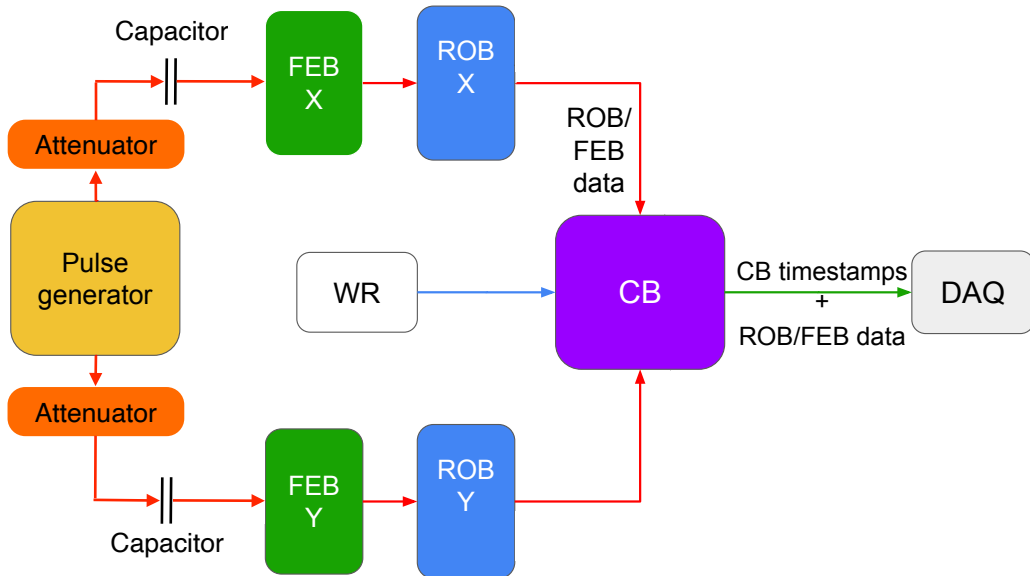
Figure 4.8 : *Schematic diagram of the setup used for the determination of the CB x-y coincidence selection efficiency.*

important to characterize the efficiency of validating true x-y coincidences at various time intervals between MA-PMT hits from different TT modules up to and beyond 100 ns. The x-y coincidence selection efficiency of the CB is defined as

$$\text{x} - \text{y coincidence selection efficiency} = \frac{\text{no. of true x} - \text{y coincidences validated}}{\text{total no. of true x} - \text{y coincidences}}. \quad (4.2)$$

For this study, the experimental setup shown in figure 4.8 was used. A pulse generator was used to inject a pair of TT FEB/ROBs (labeled x and y) with 1.6 pC of charge (about 10 PE) at a frequency of 10 kHz. In this configuration, each FEB/ROB was wired to the CB in a manner such that they resembled FEB/ROBs belonging to perpendicular TT modules (i.e., x- and y-modules). The CB was configured to operate in x-y coincidence search mode. The pulse generator was then configured to emit injection signals to the x-FEB/ROB (at time $T_{g,x}$) and y-FEB/ROB (at time $T_{g,y}$) at different values of time intervals ΔT_g (where $\Delta T_g = T_{g,y} - T_{g,x}$) in the range from -140 ns to 140 ns. At each value of ΔT_g, each FEB/ROB was injected with charge 10,000 times, and the corresponding number of L1-validated pairs of x-y coincident injections were counted. The x-y coincidence selection efficiencies were then calculated using equation 4.2. The variation of x-y coincidence selection efficiencies derived as a function of ΔT_g is shown in figure 4.9. Due to the symmetry of the measurement, only positive values of ΔT_g are shown. The plot indicates that the CB successfully validates all the pairs of x-y triggers with $\Delta T_g < 96$ ns. Beyond this point, the trigger efficiency undergoes a linear descent at a rate of 6.4% per ns from 1 to 0 in the range ($96 < \Delta T_g < 112$) ns, within a
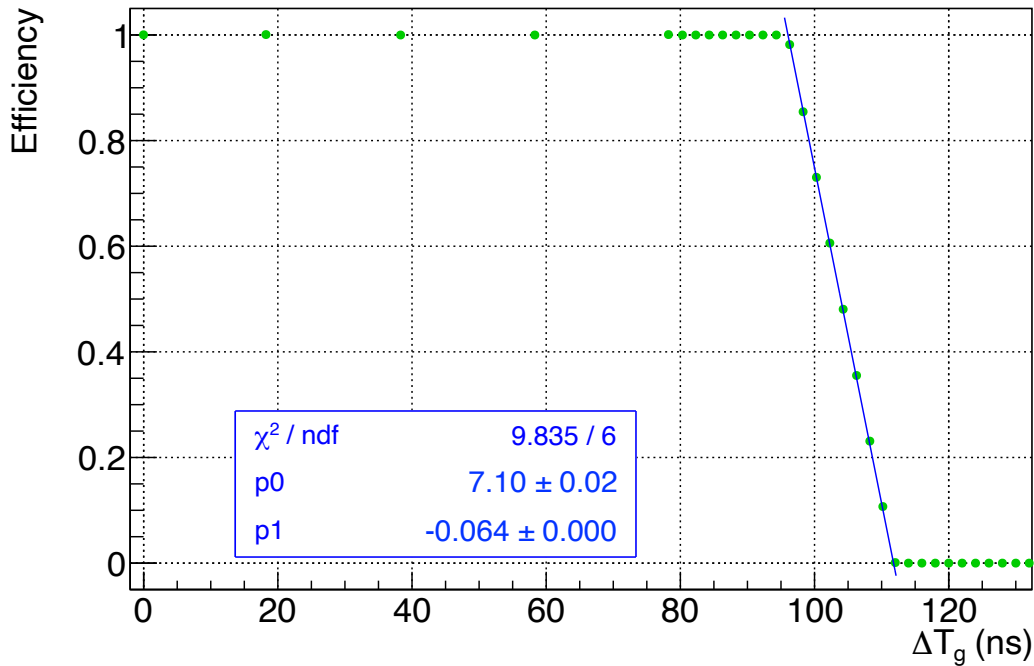
Figure 4.9 : *Graph of x-y coincidence selection efficiency vs. the time difference between the charge injections to the x-FEB/ROB and the y-FEB/ROB (ΔT_g). The data points in the range ($96 < \Delta T_g < 112$) ns is fitted with a function of the form y = [p0]+[p1]·x (blue line).*

span of 16 ns. As discussed in section 4.2.1, this observation is linked to the CB clock period of 16 ns and the associated trigger bundling. Consequently, ΔT_g=100 ns is found within the 7th CB clock cycle. Therefore, the CB validates all the x-y triggers found within 7 CB clock cycles. For events with (96<ΔT_g ≤112) ns, there is a non-zero probability that the pair of x-y triggers are found more than 7 CB clock cycles apart, leading to their rejection. Furthermore, the probability that the pair of triggers are separated by more than 7 CB clock cycles increases with increasing ΔT_g in that CB clock cycle. Therefore, a linear decline of the x-y coincidence selection efficiency as observed in figure 4.9 is expected as a consequence of the CB clock period.

## 4.3.2 Validation of CB x-y coincidence selection using the Top Tracker prototype

The TTP equipped with the IPHC-ROBs also offer a unique opportunity to evaluate the performance of the CB with respect to the x-y coincidence selection, using physics data. Hence, a 4-day-long atmospheric muon dataset was acquired using the TTP. For this acquisition, the CB was configured to operate in x-y coincidence search mode. The time of the x-hit (y-hit) of a given L1-validated pair of x-y coincident hits was obtained from the corresponding timestamps T_x (T_y). Thus, the distribution of $\Delta T = T_y - T_x$ was obtained for each TTP layer, using both the CB and IPHC-ROB timestamps.

The corresponding distribution of ΔT for the layer 1 of the TTP is shown in the figure 4.10. The results indicate a strong level of agreement between the distributions obtained using CB and IPHC-ROB timestamps, which bolsters confidence in both the CB x-y coincidence selection and the accuracy of the timestamping performance. The mean value of ΔT is measured to be 0.5 ns according to both the CB and IPHC-ROB timestamps, which indicates that there is no significant asymmetry between the average time of arrival of the signal on one module versus the other. With respect to the CB (IPHC-ROB) timestamps, the standard deviation ΔT indicates a variability of 11.28 ns (11.67 ns) on average between the detections of the x-trigger and the y-trigger. The integral indicates the rate of detection of valid x-y coincidences, which amounts to 349 Hz.

It was discussed in detail under section 3.2 that the distance of optical signal transmission along the WLS fibres of the scintillator strips depends on the geometrical position of the muon crossing point on a module. Therefore, the times at which the x-signal and the y-signal take to reach the respective MA-PMTs, and the corresponding ΔT value, also vary depending on the geometrical position on the TTP where the muon crosses the module. This effect is illustrated in the figure 4.11 for three example regions on the TTP, labelled A, B, and, C. Note that for events occurring in region A (B), the x-signal has to travel a much shorter (longer) distance along the WLS fibre compared to the y-signal for the same muon event. Consequently, for events in region A (B), the trigger on the x-module (y-module) is observed earlier than the other, resulting in $\Delta T<0$ ($\Delta T>0$) on average for events in that region. However, when muons cross regions on the TTP such as C where the distance of signal propagation along the fibre on both modules is similar, both triggers are produced almost concurrently, leading to a mean $\Delta T \sim 0$.
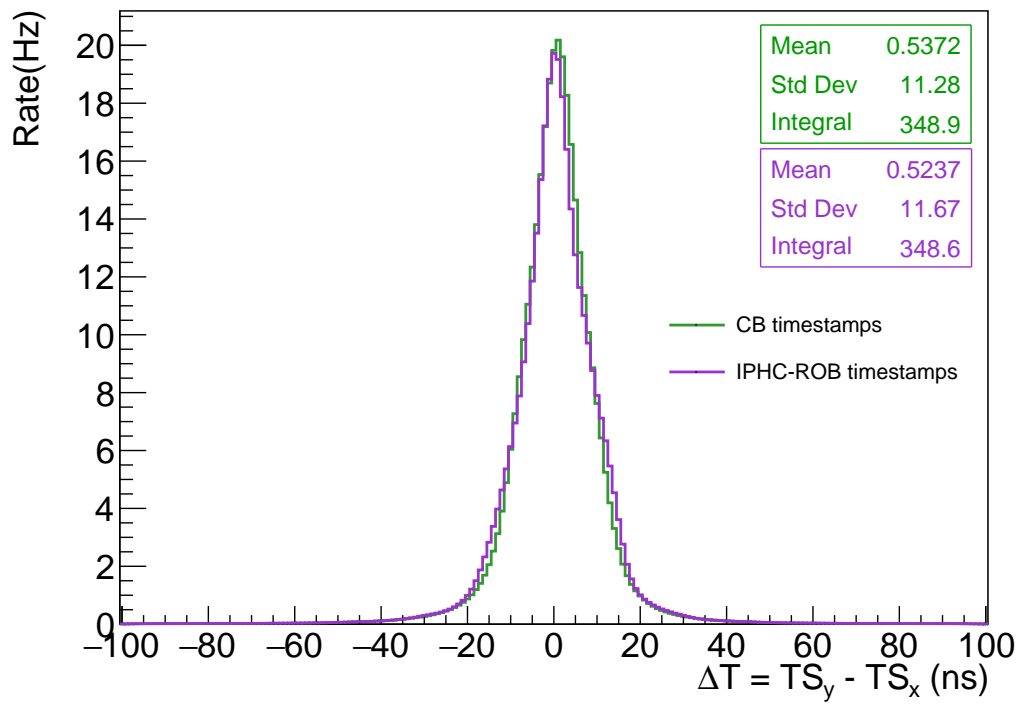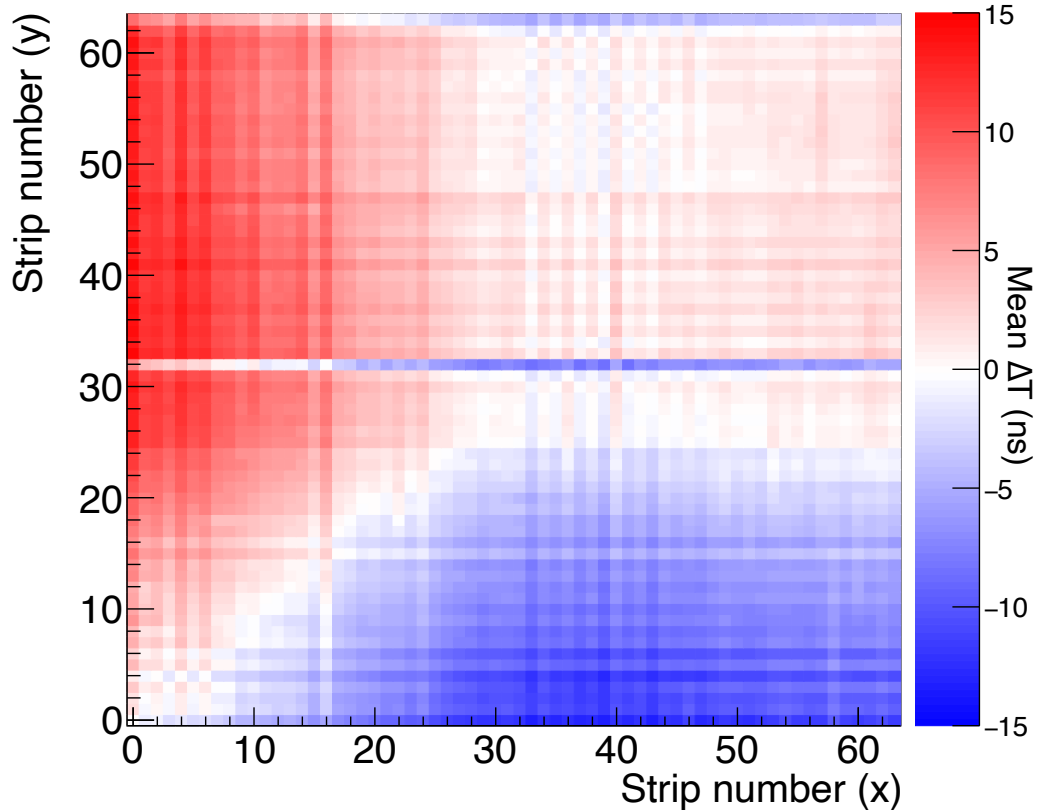
Figure 4.10 : *Distribution of time difference between the x-y coincident pairs of FEB/ROB triggers for a TTP layer 1.*
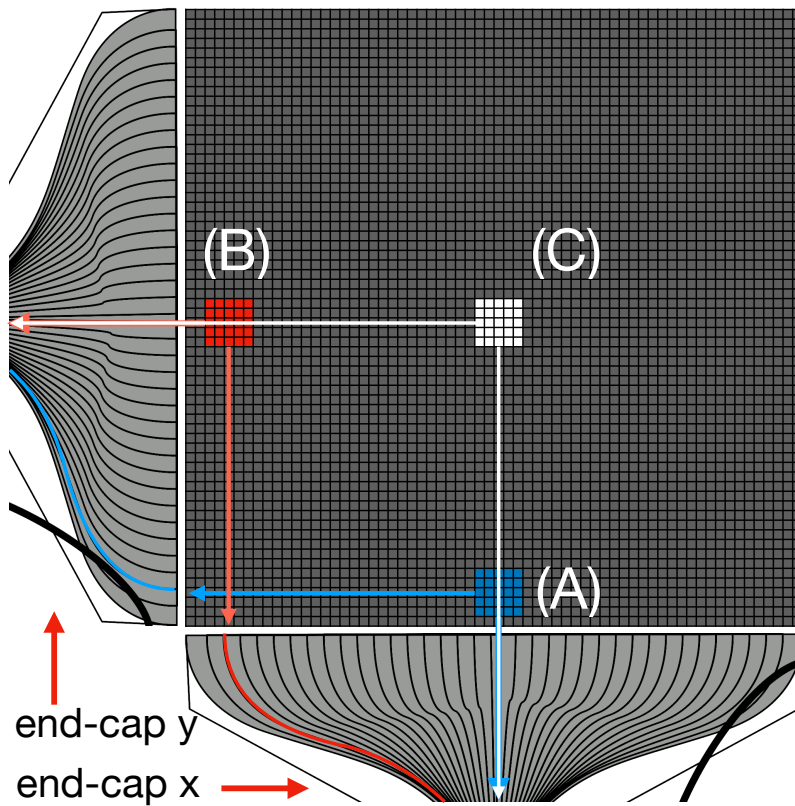
Figure 4.11 : *Illustration of how ΔT varies as a function of the position of the x-y coincident event on a TTP module.*

Therefore, it is possible to map the variation of observed mean ΔT as a function of the 2D position on a TTP layer. Hence, the variation of the mean ΔT measured using CB timestamps at each 2D pixel of the layer 1 of the TTP is plotted as shown in the figure 4.12. The orientation of these plots are identical to that shown in the figure 4.11. The color axis (Mean ΔT) is centred on 0, which represents that both optical signals corresponding to an x-y coincident events reach the MA-PMT at the same time, while blue (red) represents that the x (y) signal reach the respective MA-PMT before the other. It can be observed that the x-y coincidences that occur close to a given end-cap reaches that particular end-cap earlier than that of the module perpendicular to it, as expected. The fluctuations observed in the ΔT distributions are due to the variation of the event detection efficiencies of different scintillator strips. The mean ΔT values along the scintillator strips 32 and 63 on the y-modules indicate that these two strips do not function properly, and are excluded from the rest of this study.

The standard deviation of the ΔT distributions shown in figure 4.10 is an admixture of multiple contributions. Based on figure 4.12, it can be observed that the standard deviation of the ΔT distribution is significantly influenced by the variation in the optical signal propagation distance along the WLS fibres. This variation depends on the geometric location on the TTP where an x-y coincident event takes place. Additionally, the x-y coincidences validated by the CB are not purely from muons, but may also contain false coincidences due to accidental correlation of physically uncorrelated events, such as radioactivity, electronics

Figure 4.12 : *Distribution of mean time difference between the x-y coincident pairs of FEB/ROB triggers per each 2D pixel for the TTP layer 1 based on CB timestamps.*

noise and MA-PMT channel cross-talk. Moreover, physical effects such as the optical response of the scintillator strip and the WLS fibres, as well as electronics effects such as MAROC3 time-walk (introduced under section 4.3.3), also introduce timing uncertainties. By applying appropriate corrections, the effect of different external factors that contribute to the ΔT distributions can be gradually eliminated. This allows for a more in-depth analysis of the CB's potential and its impact on the measurement of pure physics events.

4.3.3   Correction of x-y coincidence time interval

Rejecting accidental x-y coincidences

Since accidentals coincidences are random events, they are somewhat uniformly distributed over ΔT. Hence, their contribution could also lead to an increase of the standard deviation of the ΔT distributions given in the figure 4.10. Therefore, with the aim of selecting events purely due to the atmospheric muons, a subset of x-y coincidences such that

1. each x-y coincidence must be found together with two or more other x-y coincidences found on at least three different TTP layers, within a sliding window of 100 ns, and,

2. charge on each MA-PMT trigger must be 1 PE or higher.

The x-y coincidences that do not satisfy the aforementioned conditions are rejected. The set of x-y coincidences thus selected will be used for the remainder of this study. The selection of x-y coincidences in correlation with other TTP layers, as outlined in criterion (1), results in the rejection of x-y coincidences caused by atmospheric muons that did not traverse three or more layers. However, this method ensures that the selected x-y coincidences are from actual muon events and not from accidentally correlated noise.

Signal propagation length within the WLS fibre

The distance of propagation of the optical signal within the WLS fibre can be calculated by combining the x-y coincident event position information as well as the extra length of fibre of each scintillator strip at the end-cap region. Additionally, the speed of light within the WLS fibre (v_f) can be derived from its refractive index [141] to be 18.73 cm/ns, assuming propagation along a straight line within the optical fibre. However, the photons do not travel along the fibre in a linear trajectory, but rather a helical path, thereby decreasing their effective longitudinal speeds. Therefore, based on measurements of speed of light within Kuraray Y11 WLS fibres found in the references [153, 154] v_f = 16 cm/ns is used as an approximation for the speed of optical signal propagation along the WLS fibre. Based on the information above, the value of ΔT corrected for the optical signal propagation within the WLS fibre (ΔT$_f$) can be obtained as

$$\Delta\text{T}_f = \Delta\text{T} - \left(\frac{l_{f,y} - l_{f,x}}{v_f}\right),$$

(4.3)

where $l_{f,x}$ and $l_{f,y}$ represent the distances along which the x and y optical signals propagated along the WLS fibres, respectively.

MAROC3 time-walk

Figure 4.13 illustrates two example charge response curves of the MAROC3 with respect to two signals that differ with respect to the quantity of input charge. Notice that the response curve of the high charge signal surpasses the trigger threshold at a time earlier than that of the low charge signal. Thus, the time at which a trigger is issued with respect to the initiation of the signal depends on the quantity of total charge input to the MAROC3 by that signal. This is known as the time-walk. Due to the difference between the charges
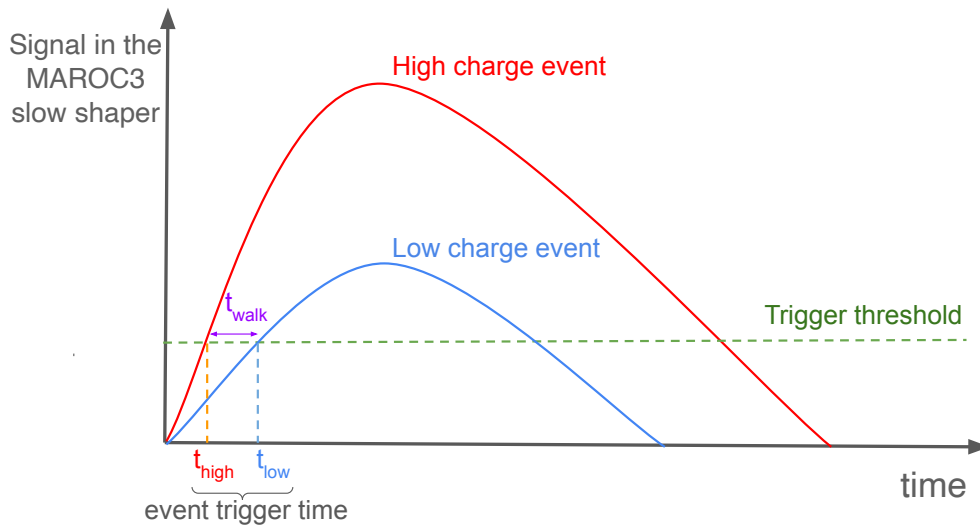
Figure 4.13 : *Illustration of the MAROC3 time-walk effect.*
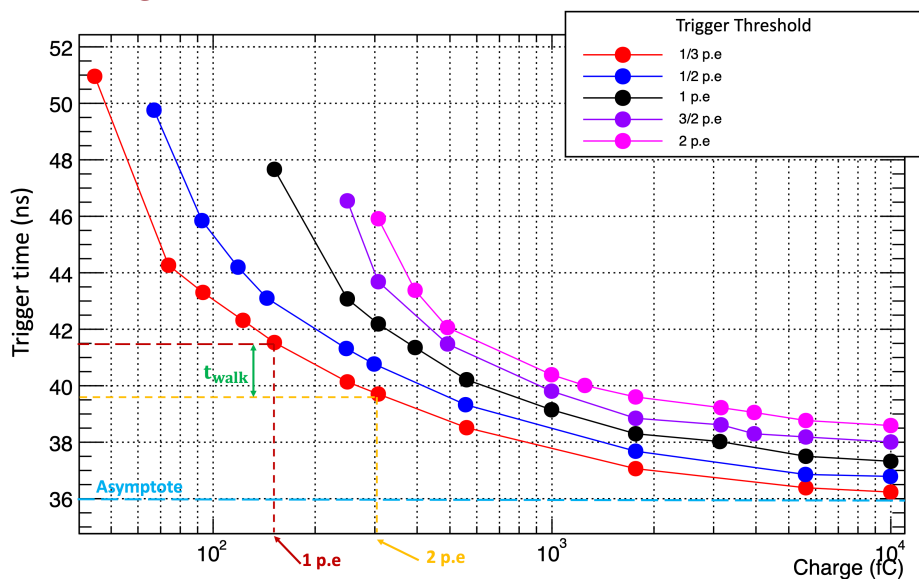
Figure 4.14 : *Measurement of trigger time vs. injected charge, for time-walk calibration [149].*

measured on the x-module and the y-module for x-y coincident events, this effect may lead to timing uncertainties. The degree of MAROC3 time-walk for different input charges at various trigger threshold has been determined earlier [149], as shown in the figure 4.14. The trigger times measured in the aforementioned study also includes the constant time delay due to the signal propagation time along the cables. The results indicate that, two signals of charge 1 PE and 2 PE at a trigger threshold of 1/3 PE would see a time-walk of 2 ns between them. Notice that the effect of time-walk varies with different trigger threshold levels. The time-walk between two signals (for a given charge difference between them) is larger when their magnitudes are smaller, than when they are larger.

Recognizing the importance of the time-walk correction highlighted in [149], a more detailed measurement was recently conducted[1] using 28 different charges, instead of the 11 charges shown in figure 4.14, spanning the range [0.063, 62.5] PE at a trigger threshold of 1/3 PE. This measurement utilized a similar setup but with different cabling compared to [149], focusing on minimizing timing differences from sources other than the MAROC3, which accounts for the different offset between the two datasets. The newer dataset, with its broader energy range and larger number of measured charges, will be used in the remainder of the discussion unless noted otherwise. The variation of mean trigger times (corrected for constant cable delay) thus obtained is plotted in the figure 4.15. In order to correct the ΔT
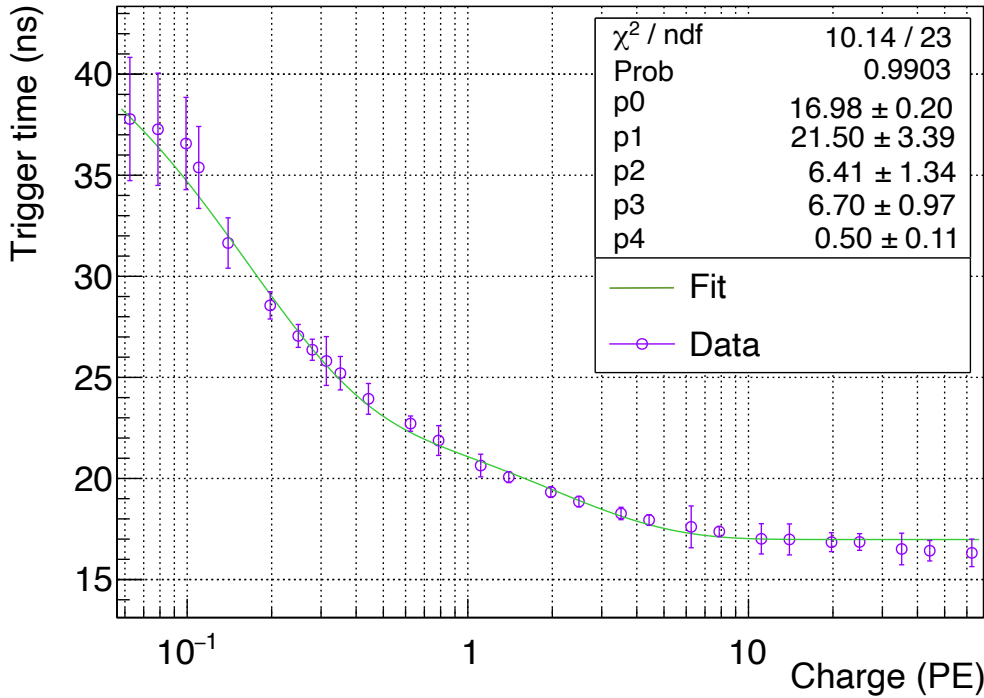
Figure 4.15 : *MAROC3 time-walk calibration curve (for 1/3 PE trigger threshold) used for the time-walk correction. The data has been corrected for constant delay due to cable lengths. The data has been fitted with the expression 4.4.*

---

[1]Measurement done by Min Li et al. (IPHC).

distribution with respect to the time-walk, the measurements were fitted with the function

$$t_{trig} = p_0 + p_1 \cdot \exp\left(-p_2 \cdot x\right) + p_3 \cdot \exp\left(-p_4 \cdot x\right) \tag{4.4}$$

where x represents the charge in units of PE is used to characterize the measurements. The best-fit curve for the measurements is also shown in the figure 4.15. Note that the MAROC3 trigger time reaches an asymptote of 17 ns (indicated by parameter p0) as the input charge increases. It corresponds to the constant intrinsic delay of the MAROC3.

Then, the magnitude of time-walk (i.e. the value of t_{trig}) for each MA-PMT signal were calculated individually using the best-fit curve. Hence, the time difference between the x-signal and the y-signal of an x-y coincident event following the corrections for the propagation along the WLS fibre and the MAROC3 time walk (ΔT_{corr}) is given by

$$\Delta T_{corr} = \Delta T_f - \left(t_{trig,y} - t_{trig,x}\right), \tag{4.5}$$

where $t_{trig,x}$ and $t_{trig,y}$ represent the MAROC3 trigger times corresponding to the x-signal and the y-signal of a given x-y coincidence, respectively. The value of ΔT_{corr} is determined by the respective charges of the x- and y-signals, as well as the parameters p1, p2, p3 and p4, except p0. Note that p0, which is a constant delay, gets cancelled out among the terms $t_{trig,y}$ and $t_{trig,x}$ in the aforementioned correction.

Results

The ΔT distributions for TTP layer 1 obtained using CB timestamps at different stages of corrections is presented in the figure 4.16. The procedure applied for the rejection of accidentals yield a ΔT distribution with a standard deviation of 7.64 ns, which corresponds to a 32% reduction of the standard deviation. Figure 4.16 demonstrates that this selection process has reduced the number of events in the (-30<ΔT<30 ns) range by about an order of magnitude. This reduction is due to the loss of x-y coincidences from atmospheric muons, which results from the limited field of view of the TTP and the inefficiencies of its scintillator strips. Additionally, this selection has decreased the number of x-y coincidences in the tail regions (i.e. ΔT<-30 ns and ΔT>30 ns) by up to two orders of magnitude, where accidental coincidences are expected to be more prevalent. Thus, the procedure for rejection of accidentals also reduces the rate of x-y coincidences from 349 Hz down to 45 Hz.

The time correction with respect to the propagation length along the WLS fibres narrows the standard deviation down to 6.49 ns, corresponding to a further reduction of 15% (overall reduction of 42% with respect to the uncorrected distribution). When the correction against time-walk is introduced, the standard deviation of the ΔT distribution diminishes down to 5.91 ns, marking a further 9% reduction (overall reduction of 48% with respect to the uncorrected distribution) in the standard deviation. The correction due to time-walk was calculated with respect to both the measurement quoted in [149], as well as the measurement shown in the figure 4.15. The impact of the correction derived from either of the measurements were found to be almost identical (differing by only about 1%). The reduction in the dispersion of the ΔT distribution after each correction reflects the extent of timing
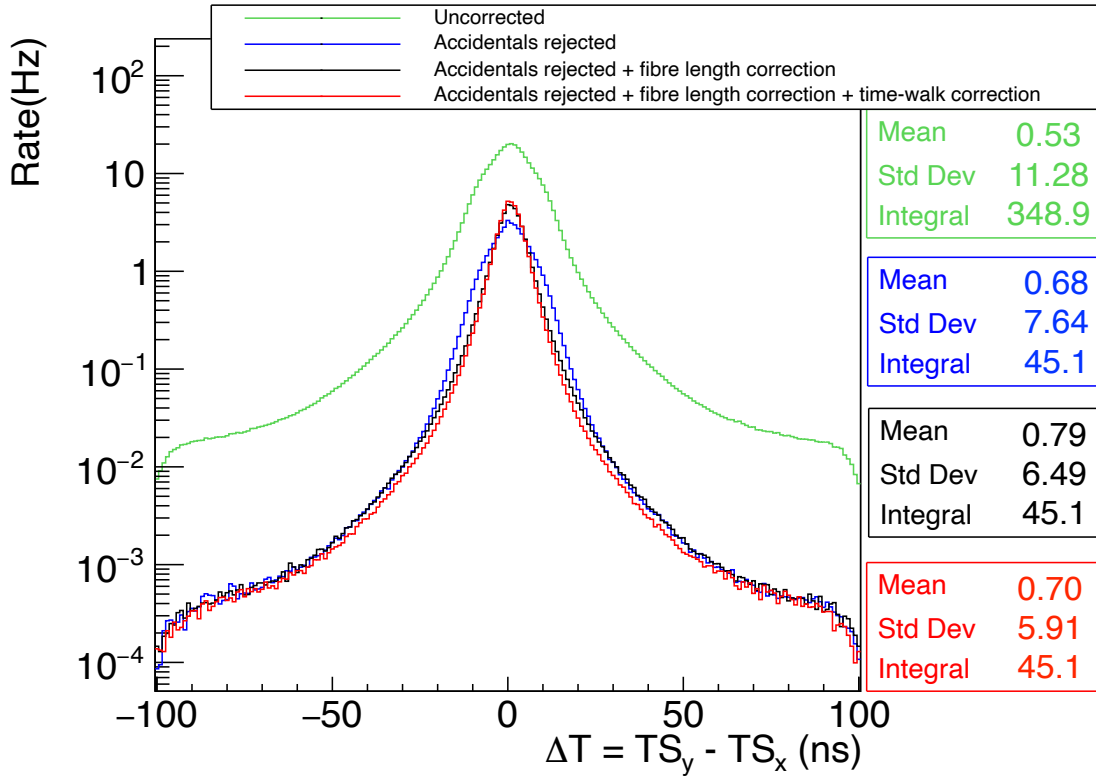
Figure 4.16 : *Distribution of time difference between the CB timestamps of x-y coincident pairs for the TTP layer 1 following different stages of time corrections.*

uncertainty contributed by each respective source. The optical emission decay times of the plastic scintillator strips and the WLS fibres, the timestamping resolution of the CB itself, and, the residual accidentals account for the dispersion in the ΔT distribution that remained following all the aforementioned corrections.

The distribution of mean ΔT values per each 2D pixel of the TTP layer 1 is depicted in the figure 4.17. The mean ΔT values along the faulty strips 32 and 63 on the y-module of the TTP layer 1 have been set to 0. The comparison of mean ΔT variation per each 2D pixel before and after corrections (figure 4.12 and figure 4.17 respectively, which share the same mean ΔT scaling) reveals the impact of the corrections. Following the corrections, the mean ΔT values of all the 2D pixels have converged towards 0 (white) as expected, apart from the fluctuations of the order of a few ns. These fluctuations arise from various sources, such as variations of the scintillation signal detection efficiencies of different scintillator strips, variations in the optical signal attenuation levels among different optical fibres, scintillation losses, variations of the effective speed of light within different fibres, among others. These remaining fluctuations could, in principle, be corrected with more detailed modelling of each individual effect involved; however, this is beyond the scope of this thesis. The vertical distance between the top and bottom layers of the TT is 3 m. Assuming muons travel at the speed of light, it takes at least 9 nanoseconds for a muon to pass through the TT. Two types of muons are relevant to the TT: down-going and up-going muons. Up-going atmospheric neutrinos can interact with the JUNO liquid scintillator through charged-current weak interactions, producing secondary charged leptons of the same flavour as the original
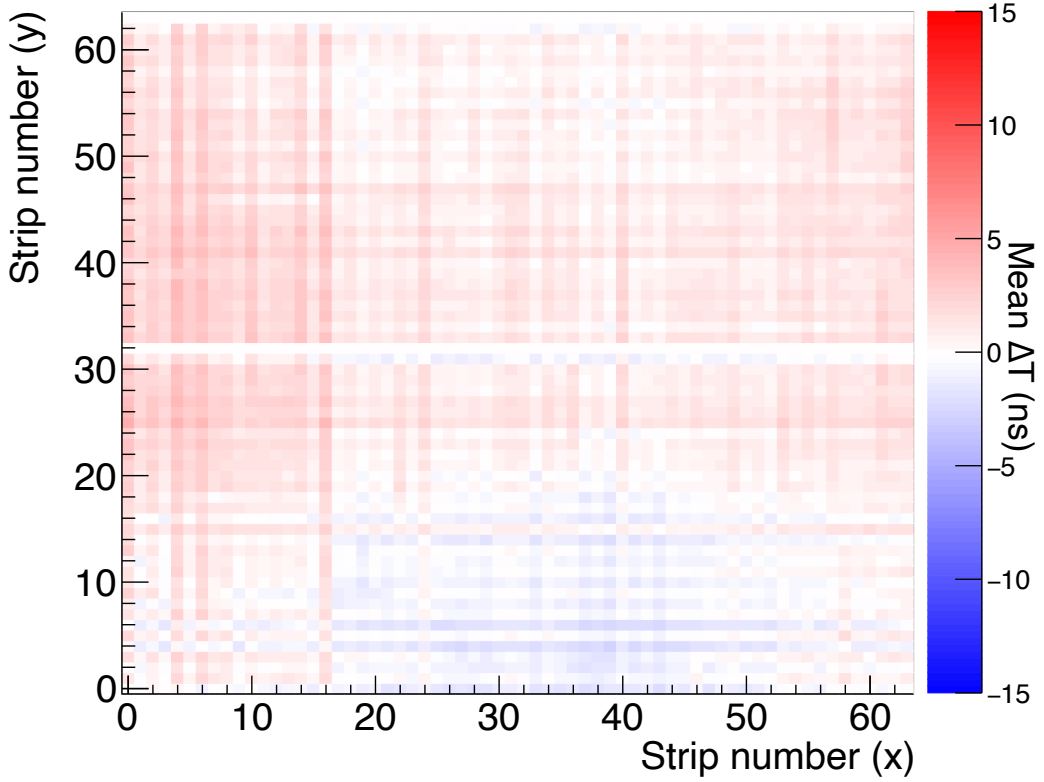
Figure 4.17 : *Distribution of mean time difference between the x-y coincident pairs of FEB/ROB triggers per each 2D pixel for the TTP layer 1 based on CB timestamps following all the corrections.*

neutrino. Up-going muons could, for instance, originate from such interactions in the JUNO liquid scintillator or surrounding area and then traverse the Top Tracker. Define ΔT_{tb} as $\Delta T_{tb} = T_t - T_b$, where T_t and T_b are the times when a muon crosses the top and bottom layers of the TT, respectively. The difference in the ΔT_{tb} values of an up-going muon and a down-going muon is expected to be at least 18 nanoseconds. With a time resolution of approximately 6 nanoseconds, the TT can distinguish between these two types of muons with at least 3 times the standard deviation of the ΔT distribution. Thus, the TT should be effective in identifying atmospheric muon neutrinos in JUNO, where the outgoing muon traverses the TT, as well as in similar studies.

To achieve better separation between up-going and down-going muons, stricter charge cuts on x-y coincident events can improve timestamping precision in the TT. Higher-charge events correspond to muon hits with more scintillation photons. The presence of more photons reduces the impact of the intrinsic time resolution of the plastic scintillator and WLS fibres by triggering on the first photon produced, which is more likely to be closer to the actual time the muon crossed the TTP layer. Figure 4.18 shows the impact of different charge cuts (ranging from 5 PE to 10 PE) on the ΔT distribution for layer 1 of the TTP, after all previously discussed corrections (red). The variation of the standard deviation of the ΔT distribution following each charge cut is depicted in the figure 4.19. A 5 PE (6 PE) cut decreases the standard deviation of the ΔT distribution by approximately 6% (11%), reducing it to 5.5 ns (4.9 ns) when compared to the pre-cut distribution. This leads to a
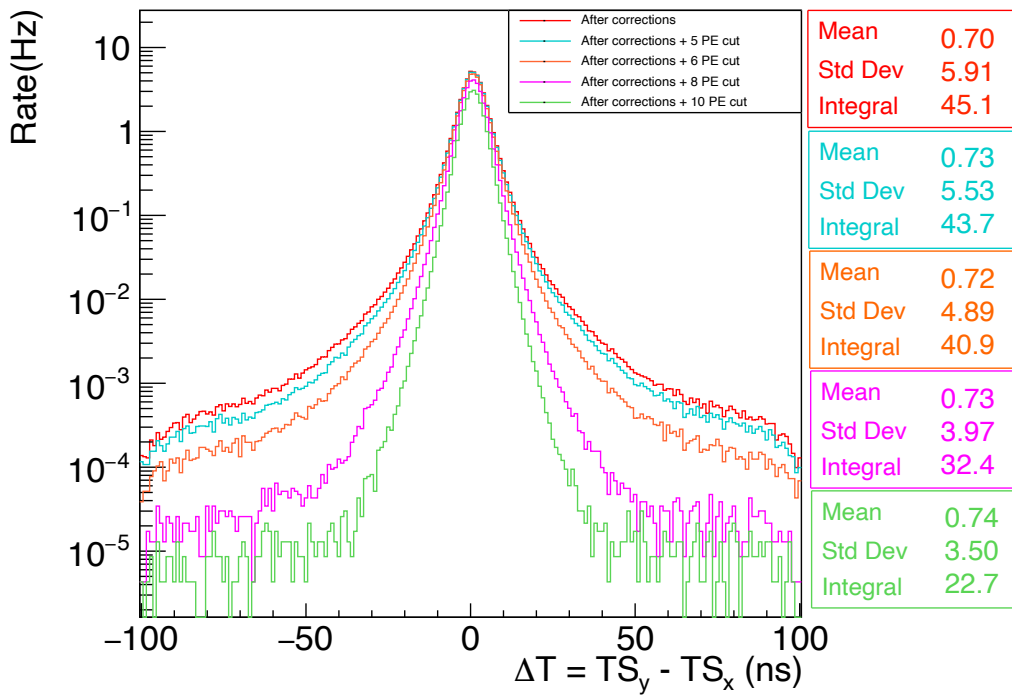
Figure 4.18 : *Distribution of time difference between the CB timestamps of x-y coincident pairs (after rejecting accidentals as well as correcting for propagation length along the WLS fibre and electronics time-walk) for the TTP layer 1 at different charge cuts on each MA-PMT triggers.*
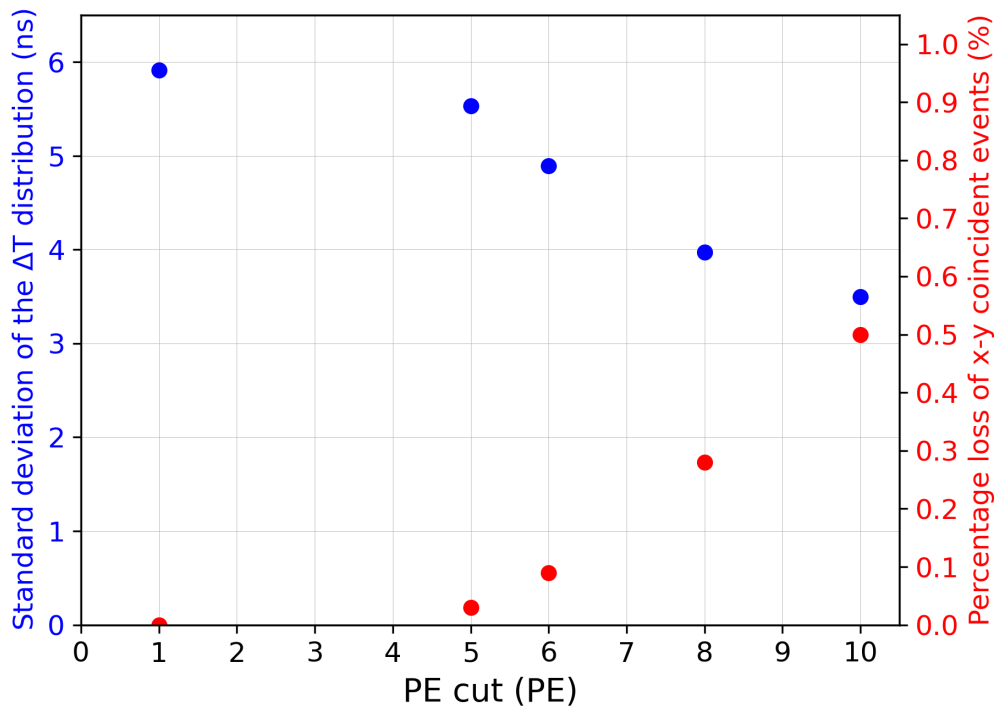
Figure 4.19 : *Graph of standard deviation of the ΔT distributions obtained after all the corrections (blue) as well as the corresponding percentage loss of x-y coincident events (red) at different MA-PMT trigger charge cuts.*

reduction in the observed x-y coincidence rate to 44 Hz (41 Hz). With a 5 PE (6 PE) cut, the TT will be able to distinguish up-going muons from down-going muons by at least 3.3 (3.7) times the standard deviation of the resulting ΔT distribution. These cuts mainly suppress the tail regions (ΔT<-30 ns and ΔT>30 ns) while leaving the central region (-30<ΔT<30 ns) largely unaffected. With an extreme cut of 8 PE (10 PE), the tails of the ΔT distribution are significantly suppressed, reducing the standard deviation to 3.9 ns (3.5 ns), which is 33% (41%) narrower. The corresponding rate of x-y coincidence selection drops to 32.4 Hz (23 Hz). With a 8 PE (10 PE) cut, the TT will be able to better distinguish up-going muons from down-going muons by at least 4.6 (5.1) times the standard deviation of the resulting ΔT distribution.

4.4 Future prospects

As was introduced under section 4.1, the CB implementation used in the TT is different with respect to that used in the TTP. Consequently, while the CB x-y coincidence selection performance has been validated using the TTP, it is crucial to re-evaluate the CB performance by considering the differences among the implementations. It was introduced under section 4.1 that the CB simultaneously looks for x-y coincident hits across all combinations of x-modules and y-modules. This function could not be validated using the TTP as each TTP module has only one electronics readout, representing one out of all possible combinations of x and y modules. The performance of the CB in this aspect must be validated by simulating random triggering of different combinations of x and y modules via charge injection, as well as using atmospheric muons at the JUNO site, prior to the start of data acquisition. Additionally, due to the differences in the signal propagation lengths in the TT modules with respect to the TTP, the observed ΔT distributions will also differ. Consequently, it is important to verify whether the ΔT distributions following corrections as well as charge cuts can be replicated using the TT. These additional validations can be performed during the TT commissioning stages.

Résumé : Validation de la carte concentrateur

Les cartes concentrateur (CB) font partie intégrante de la chaîne électronique du Top Tracker (TT). La mise en œuvre du TT place une carte concentratreur sur chaque mur du TT. Chaque CB regroupe les flux de données de 16 paires de carte FEB/ROB dans le mur du TT. Utilisant ces signaux, la CB sélectionne les événements coïncidents x-y dans le mur du TT et transmet les charges mésurées par la FEB/ROB, ainsi que quelles voies du PMT ont décléché, des événements validés au système d'acquisition de données. Une coïncidence x-y dans le TT est définie comme la détection de 2, 3 ou 4 déclenchements FEB/ROB dans une fenêtre de temps glissante de 100 ns, dans deux modules perpendiculaires dans le mur. Cette sélection réduit le débit de données du TT d'un ordre de grandeur. Le CB est également responsable de l'horodatage des événements, en utilisant la référence temporelle absolue fournie par le nœud White Rabbit implémenté dans la CB. Il est donc essentiel de valider les performances de la CB en ce qui concerne les aspects susmentionnés.

Le prototype Top Tracker (TTP), a été utilisé pour évaluer les performances du CB dans des conditions réalistes. Un mur du TTP est constitué de seulement deux sous-couches perpendiculaires, chacune équipée d'une seule lecture FEB/ROB. Au moment des études présentées dans ce chapitre, seuls deux CBs étaient disponibles pour les essais. Dans l'idéal, un CB serait affecté à chaque couche du TTP, mais en raison de la disponibilité limitée des CB, une autre approche s'est avérée nécessaire. Contrairement à la configuration TT, où chaque mur a sa propre CB, une unique CB a été configurée pour agréger les données de 8 FEB/ROB à travers les différentes couches du TTP. Dans cette configuration, une coïncidence x-y au sein d'une couche du TTP est définie comme deux déclenchements FEB/ROB survenant dans une fenêtre glissante de 100 ns, correspondant aux deux modules de cette couche. La CB émule cette sélection modifiée de coïncidence x-y indépendamment pour chacune des quatre couches du TTP. La CB peut fonctionner en deux modes : le mode de recherche des coïncidences x-y (utilisé pour l'acquisition de données physiques normales) et le mode où tous les triggers sont validés.

Pour effectuer des tests de la CB à l'aide du TTP, une version différente de la ROB (IPHC-ROB) développée par l'IPHC Strasbourg a été utilisée. Les IPHC-ROB permettent également la lecture directe des données, en contournant la CB. Deuxièmement, les IPHC-ROB sont également capables d'horodater les données à l'aide d'une horloge interne, contrairement aux ROB qui seront installés dans le TT. Étant donné qu'aucune des caractéristiques n'était requise pour le TT, ces capacités ne sont pas disponibles dans les ROB officiels du TT. Comme la CB et les IPHC-ROB enregistrent les mêmes événements physiques, les horodatages des IPHC-ROB peuvent être utilisés pour évaluer les performances d'horodatage du CB.

Afin de déterminer la résolution temporelle de l'horodatage des événements de la CB, le TTP a été utilisé en mode de normal pour mesurer des muons atmosphériques pendant une heure. Pour cette mesure, la CB a été configurée pour fonctionner en mode de recherche de coïncidence x-y. L'horodatage de la CB et l'horodatage de la IPHC-ROB ont été associés de façon que l'horodatage de la CB corresponde au mieux à un paquet de données de la

IPHC-ROB. La distribution de la différence entre l'horodatage IPHC-ROB et l'horodatage CB indique que la résolution de l'horodatage CB est, au maximum, d'environ 1,67 ns.

Pour évaluer la variabilité des horloges des CB, une charge d'environ 10 PE a été injectée de manière synchronisée dans deux FEB/ROB à une fréquence de 0,99 Hz. Ce processus a été réalisé sur une période de trois jours, les deux FEB/ROB étant connectés à des CB distincts fonctionnant en mode que valide tous événements. Cette fréquence spécifique est choisie de manière à être proche mais différente de la fréquence de synchronisation White-Rabbit (WR) (1 Hz) afin que les performances d'horodatage du CB puissent être évaluées à différents intervalles de temps depuis la dernière synchronisation WR. Après l'injection, la différence entre les horodatages enregistrés par la CB pour les injections simultanées a été obtenue. La distribution a un écart-type de 0,28 ns, ce qui indique une stabilité remarquable des horloges du CB. Il faut noter que la résolution de l'horodatage de la CB et la variabilité des horloges de la CB sont beaucoup plus faibles que les magnitudes d'autres sources qui introduisent des incertitudes temporelles, telles que le temps de décroissance dans les bandes de scintillateur (2,3 ns) et les fibres WLS (7,6 ns). Par conséquent, le niveau de précision et de stabilité de l'horodatage des CBs est suffisant pour leur utilisation prévue dans le JUNO TT.

Pour valider l'efficacité de la sélection des coïncidences x-y du CB, une charge d'environ 10 PE a été injectée dans une paire de FEB/ROB à 10 kHz. Ces cartes étaient connectées à une CB pour simuler des événements sur des modules TT perpendiculaires. Le délai ΔT_g entre les injections dans chaque FEB/ROB a varié de -140 ns à 140 ns, et la CB a fonctionné en mode de recherche de coïncidence x-y. En raison de la symétrie de la mesure, les résultats sont discutés par rapport aux valeurs positives de ΔT_g uniquement. Pour chaque valeur de ΔT_g, 10000 injections ont été effectuées et l'efficacité a été déterminée en comptant les coïncidences x-y validées. Les résultats montrent une efficacité de 100% (0%) pour ΔT_g<96 ns (ΔT_g>112 ns). Les résultats montrent une chute linéaire 6.4% par ns pour (96 ns<ΔT_g<112 ns) en raison du cycle d'horloge de la CB de 16 ns. Étant donné que la fenêtre de coïncidence x-y de 100 ns dure 7 cycles d'horloge, la CB valide tous les déclenchements x-y trouvés avec un décalage de 7 cycles ou moins 7 cycles. Le déclin de l'efficacité sur 16 ns autour de 100 ns a peu d'effet sur la sélection des événements muoniques dans le TT, car la plupart des coups corrélés x-y se produisent bien en dessous de 100 ns.

Un ensemble de données muoniques atmosphériques d'une durée de 4 jours a été acquis à l'aide du TTP, en faisant fonctionner la CB en mode de recherche de coïncidence x-y. La distribution de l'intervalle de temps entre les détections x et y des événements coïncidents x-y validés (ΔT) a donc été mesurée en utilisant à la fois l'horodatage de la CB et de l'IPHC-ROB. Les differences de temps mesurés avec les deux systèmes sont en accord. L'écart-type de la distribution de différence de temps indique une variabilité d'environ 11 ns en moyenne entre les détections dans le module x et y. Cette variabilité de ΔT est dû à un mélange de contributions multiples, telles que la variation de la distance de propagation du signal optique le long des fibres WLS, la corrélation accidentelle d'événements physiquement non corrélés, les effets de l'électronique, ainsi que la réponse optique de la bande de scintillateur et des fibres WLS. En appliquant des corrections appropriées, l'effet des différents facteurs externes qui contribuent aux distributions ΔT peut être progressivement éliminé. Cela permet une analyse plus approfondie du potentiel de la CB et de son impact sur la mesure des événements de physique pure. L'impact de ces corrections a été étudié en considérant

uniquement l'horodatage de la CB.

Pour sélectionner les événements purement dus aux muons atmosphériques, un sous-ensemble d'événements coïncidents x-y a été sélectionné de manière à ce que seuls soient retenus les groupes événements avec au moins 3 couches du TTP en coïncidence dans une fenêtre de 100 ns. En plus de cela, seulement les événements avec une charge d'au moins 1 PE ont été sélectionnés. Ces critères de sélection entraînent la réduction du taux de coïncidentes x-y. Suite au réjet de ces événements, la distance de propagation du signal le long de la fibre sur chaque module TTP peut être obtenue grace à la position du signal correspondant dans la couche perpendiculaire du TTP. Par conséquent, utilisant de la vitesse effective de la lumière dans la fibre, la correction temporelle de chaque résultat due à la longueur de propagation peut être calculée. Finalement, un effet électronique connu sous le nom de « time-walk » (c'est-à-dire la variabilité du temps de déclenchement en fonction de la charge d'entrée) entraîne un biais dans le temps observé. Des mesures de ce "time walk" ont été ajustées en utilisant la somme de deux fonctions exponentielles. La correction du "time walk" a été calculée en utilisant les résultats de l'ajustement.

Après le rejet des signaux accidentels, la correction de la longueur de propagation le long des fibres et la correction de l'effect de "time walk", l'écart-type de la distribution de ΔT est passé de 11,28 ns à 7,64 ns, 6,49 ns et 5,91 ns, respectivement. Cela indique que le TT sera capable de distinguer les muons atmosphériques verticalement ascendants et verticalement descendants avec une précision supérieure à trois fois l'écart-type de cette distribution après corrections. Pour obtenir une meilleure séparation entre les muons ascendants et descendants, des réductions de charge plus strictes sur les événements coïncidents x-y améliorent la précision de l'horodatage dans le TT, bien qu'au prix d'une perte d'événements.

Part III

Atmospheric muon-induced backgrounds in JUNO

CHAPTER 5

ESTIMATION OF THE ^{9}LI/^{8}HE BACKGROUND WITH THE TOP TRACKER

5.1 Atmospheric muon-induced backgrounds

5.1.1 Introduction

The success of achieving JUNO's primary physics goals relies on the precision measurement of the antineutrino spectrum from its source reactors via the IBD channel. As was discussed under chapter 2, different sources and processes lead to generate signatures in the detector that resemble the IBD prompt-delayed spatial and temporal coincidences, formulating backgrounds to the JUNO reactor antineutrino spectrum. These sources constitute accidental coincidences, ^{9}Li/^{8}He isotopes, fast neutrons, and, ^{13}C$(\alpha, n)^{16}$O.

Significant efforts have been dedicated to the design and construction of the JUNO experiment to effectively suppress the aforementioned background contributions. These measures include the strict radiopurity control and maintenance of cleanliness, among others. The particles emitted by the decays of residual radioactive impurities in the PMTs and other materials outside the JUNO LS usually do not penetrate far into the LS, depositing their energies near the LS boundary. Therefore, the accidentals, fast neutron background, and, the ^{13}C$(\alpha, n)^{16}$O background can be suppressed via a fiducial volume cut. Selection of IBD candidates based on spacial and temporal correlations among prompt-delayed events as well as their respective energies are employed in the antineutrino selection process to further reduce accidental background. JUNO IBD selection criteria for the NMO determination is discussed in detail under section 5.1.2.

The atmospheric muons can induce a variety of radioisotopes in the JUNO LS, which are listed in the table 5.1. The isotopes that undergo β^-n decay, highlighted in red, can form prompt-delayed correlated background signals by themselves that mimic the IBD prompt-delayed coincidence signature in the JUNO detector. JUNO's 700-meter overburden suppresses the atmospheric muon flux reaching the detector to 4.1×10^{-3} Hz·m^{-2} [112]. The average energy of atmospheric muons at the JUNO detector is about 207 GeV [13]. Table 5.1 also presents the event rates expected in the JUNO LS due to each atmospheric muon-induced radioisotope. Out of them, ^{9}Li/^{8}He isotopes have the highest estimated event rates. In comparison, the other β^-n-emitting isotopes have significantly smaller contributions. Moreover, the Q-values of their β^-n decay modes are high enough such that the energies carried by the decay electrons span the energy range of interest for the prompt IBD signal. Based on simulation studies, the expected rate of true reactor antineutrino IBD events and the rate of ^{9}Li/^{8}He background events are estimated to have comparable rates [12]. Therefore, the ^{9}Li/^{8}He isotopes represent the most significant background prior to applying the muon veto criteria (outlined in the section 5.1.2) for the measurement of reactor antineutrino spectrum in JUNO. The rest of the isotopes which are not β^-n emitters can not form correlated backgrounds by themselves, but could contribute towards the accidental background.

Hence, atmospheric muon veto cuts are necessary to suppress the correlated backgrounds arising from ^{9}Li/^{8}He isotopes. Reactor antineutrino experiments such as Daya Bay [86], Double Chooz [155], RENO [156], and KamLAND [77] have shown that the atmospheric muon-induced neutron background can be significantly reduced by vetoing the entire detector volume for a period proportional to the characteristic neutron capture time since

Table 5.1 : *The estimated rates for radioactive isotopes induced by atmospheric muons in JUNO LS [12]. The decay modes and Q-values are from TUNL Nuclear Data Group [159].*

Isotopes	Q (MeV)	$T_{1/2}$	Rate (per day)
^{3}H	$0.0186(\beta^-)$	12.31 years	1.14×10^4
^{6}He	$3.508(\beta^-)$	0.807 s	544
^{7}Be	Q_{EC}=0.862 (10.4 % γ, E_γ=0.478)	53.22 day	5438
^{8}He	$10.66(\beta^-\gamma : 84\ \%)$, $8.63(\beta^-$n: 16 %)	0.119 s	11
^{8}Li	$16.0(\beta^-)$	0.839 s	938
^{8}B	$16.6(\beta^+)$	0.770 s	225
^{9}Li	$13.6(\beta^-: 49\ \%)$, $11.94(\beta^-$n: 51 %)	0.178 s	94
^{9}C	$15.47(\beta^+$ p: 61.6 %, $\beta^+\alpha$: 38.4 %)	0.126 s	31
^{10}Be	$0.556(\beta^-)$	1.51×10^6 year	1419
^{10}C	$2.626(\beta^+\gamma)$	19.29 s	482
^{11}Li	$20.55(\beta^-$n: 83 %, β^-2n: 4.1 %)	0.00875 s	0.06
^{11}Be	$11.51(\beta^-\gamma$: 96.9 %), $2.85(\beta^-\alpha$: 3.1%)	13.76 s	24
^{11}C	$0.960(\beta^+)$	20.36 min	1.62×10^4
^{12}Be	$11.708(\beta^-\gamma$, β^-n: 0.5 %)	0.0215 s	0.45
^{12}B	$13.37(\beta^-\gamma)$	0.0202 s	966
^{12}N	$16.316(\beta^+\gamma)$	0.0110 s	17
^{13}B	$13.437(\beta^-\gamma)$	0.0174 s	12
^{13}N	$1.198(\beta^+)$	9.965 min	19
^{14}B	$20.644(\beta^-\gamma$, β^-n: 6.1 %)	0.0126 s	0.021
^{14}C	$0.156(\beta^-)$	5730 years	132
^{15}C	$9.772(\beta^-)$	2.449 s	0.6
^{16}C	$8.010(\beta^-$n: 99 %)	0.747 s	0.012
^{16}N	$10.42(\beta^-\gamma)$	7.130 s	13
^{17}N	$8.680(\beta^-\gamma$: 5 %), $4.536(\beta^-$n: 95 %)	4.173 s	0.42
^{18}N	$13.896(\beta^-\gamma$: 93 %), $5.851(\beta^-$n: 7 %)	0.620 s	0.009
neutron			155000

when the muon was tagged. However, this approach cannot fully reject the ^{9}Li/^{8}He background as these isotopes have longer half-lives. Experiments such as KamLAND, Super-Kamiokande [114] and Borexino [157] have explored the possibility of exploiting the fact that the muon-induced isotopes are produced close to and along the direction of the parent muon. The measurements of atmospheric muon spallation products in the KamLAND [158] and Borexino [157] detectors have revealed that the lateral distance between the background events and the muon track is approximately exponentially distributed.

5.1.2 JUNO IBD selection criteria for NMO determination

Using state-of-the-art simulations, refined IBD event selection criteria for the purpose of NMO determination using JUNO have been designed by the collaboration. These criteria have been chosen by considering the spatial and temporal correlations and the expected energy ranges for the prompt and delayed signals of true IBD events, along with the impact

of various background components discussed earlier. They are listed as follows [112]:

- Fiducial volume cut: r<17.2 m (over the JUNO acrylic sphere of radius 17.7 m);

- Prompt energy cut: 0.7 MeV<E_p<12 MeV;

- Delayed energy cut: (1.9 MeV<E_d<2.5 MeV) $\cup$ (4.4 MeV<E_d<5.5 MeV);

- Time interval between the prompt and the delayed signal: ΔT_{p-d}<1.0 ms;

- Spatial separation between the prompt and the delayed vertices: d_{p-d}<1.5 m;

- Muon veto criteria:

  1. Veto the entire fiducial volume for a duration of 1 ms for all muons passing through the WCD and/or the CD;

  2. For well-reconstructed muon tracks in the CD, vetoes are applied to candidate events based on their proximity to the tracks: 0.6 s for vertices within 1 m, 0.4 s for vertices within 2 m, and 0.1 s for vertices within 4 m;

  3. For events involving two close and parallel muons (less than 3 m apart), which account for approximately 0.6% of muon-related events, a single track is often reconstructed. The veto is applied around this track as described above, but the distance of the veto cut is increased based on the separation between the two muon tracks, which can be inferred from the PMT charge pattern at the entrance and exit points;

  4. For events where a track cannot be properly reconstructed, a 0.5 s veto is applied across the entire fiducial volume;

  5. A 1.2 s veto is applied to any candidate events reconstructed within a 3 m radius of spallation neutron capture events.

The fiducial volume cut defined above will be further optimised following initial stages of data acquisition depending upon the final radiopurity of the PMTs and the detector materials. The delayed candidates are chosen in two discrete energy windows which are centred around 2.2 MeV and 4.95 MeV, which correspond to the energy of the photon released upon the neutron capture on hydrogen and carbon, respectively.

The veto criterion (1) is applied to suppress the background due to spallation neutrons and short-lived radioisotopes induced in the CD by muons crossing the CD and/or the WCD. The muon tagging efficiency of the WCD is better than 99.5% [112]. The inefficiency mainly arises from atmospheric muons in the WCD whose path length in the WCD is shorter than 0.5 m [13]. The 1 ms veto duration of criterion (1) is long enough to allow the thermalisation and capture of most of the fast neutrons and for the depletion of short-lived isotopes. However, this is not sufficient to suppress the backgrounds due to longer-lived radioisotopes, such as ^{9}Li/^{8}He. Therefore, the veto criteria (2) and (3), which are cylindrical veto volume cuts around well-reconstructed muon tracks in the CD for specific durations, are applied to efficiently reject the backgrounds due to longer-lived isotopes. Simulation of atmospheric muon flux at the JUNO detector using the JUNO official simulation software

Table 5.2 : *Summary of cumulative reactor antineutrino selection efficiencies. The reported IBD rates refer to the expected events per day after the selection criteria are progressively applied. These rates are calculated for nominal reactor power, and do not include any reactor time off [112].*

Selection Criterion	Efficiency (%)	IBD Rate / day $^{-1}$
All IBDs	100.0	57.4
Fiducial Volume	91.5	52.5
IBD Selection	98.1	51.5
- Energy Range	99.8	-
- Time Correlation (ΔT_{p-d})	99.0	-
- Spatial Correlation (ΔR_{p-d})	99.2	-
Muon Veto (Temporal $\oplus$ Spatial)	91.6	47.1
Combined Selection	82.2	47.1

Table 5.3 : *The rates of different backgrounds in JUNO and the associated uncertainties [112].*

Background	Rate / day $^{-1}$	Rate Uncertainty (%)	Shape Uncertainty (%)
Geoneutrinos	1.2	30	5
World reactors	1.0	2	5
Accidentals	0.8	1	negligible
$^{9}Li/^{8}He$	0.8	20	10
Atmospheric neutrinos	0.16	50	50
Fast neutrons	0.1	100	20
$^{13}C(\alpha, n)^{16}O$	0.05	50	50

reveals that about 92%, 6%, and, less than 2% of the muon flux is composed of single muons, muon pairs, and, muon events with more than two muons, respectively. The study also reports that the CD is capable of reconstructing 97%-99% (94%-97%) of the single muon tracks (double muon tracks), with a mean angular resolution of about 0.5° (1.0°) [160]. Moreover, the TT covers only about 60% of the top surface of the JUNO CD. Thus, coupled with the geometrical acceptance, the TT can track only about 30% of the total muon flux crossing the CD with an efficiency of about 97%, at a mean angular resolution of about 0.2° [16].

However, not all muon tracks can be properly reconstructed. When two or more muons traverse the CD simultaneously, they leave a number of charge patterns corresponding to the muon entry and exit points, making individual muon track reconstruction extremely complicated. As previously noted, the WCD is unable to tag the majority of muons with path lengths shorter than 0.5 m in the WCD [13]. Consequently, criterion (4) is applied to reject background potentially induced in the CD by muons for which individual track reconstruction is highly uncertain or impossible. Criterion (5), which deploys a spherical veto around spallation neutron capture events, is introduced to further reject backgrounds due to atmospheric muon-induced isotopes.

The breakdown of IBD selection efficiencies of different IBD selection criteria is presented

in the table 5.2, and the residual background rates and uncertainties following JUNO antineutrino selection are presented in the table 5.3. The muon veto criteria are estimated to be 91.6% efficient in preserving the true IBDs. Along with the muon veto cuts, the fiducial volume cut (91.5% efficiency) introduces the largest impact on the measured IBD rate. The combined JUNO antineutrino selection criteria is able to measure 47.1 IBD events per day, at a selection efficiency of 82.2%. In contrast, the corresponding total residual background rate amounts to about 4.1 events per day. The refined muon veto strategy has been instrumental in suppressing the ^{9}Li/^{8}He down to 0.8 events per day. Following all the selection criteria, the highest contributors to the JUNO reactor antineutrino spectrum are $\bar{\nu}_e$ from geo-neutrinos and distant nuclear reactors. Compared to other underground LS experiments, the influence of backgrounds on the precision of measuring oscillation parameters is minimal. This is because JUNO utilizes the significant spectral shape distortion of the IBD spectrum as the main method for extracting the oscillation parameters.

The veto volumes defined by the muon veto criteria are rich in ^{9}Li/^{8}He events. This makes the information of events within these veto volumes valuable for a data-driven estimation of ^{9}Li/^{8}He production in the JUNO detector. A precisely reconstructed muon track leads to a well-defined veto volume around the true muon track. Therefore, the precise muon reconstruction capabilities of the TT can be utilized to perform an accurate estimation of the ^{9}Li/^{8}He background. Section 5.3 explores the role of the TT as a precise muon tracker for this estimation under realistic conditions. The TT partially covers the top surface of the WCD. Thus, the TT can assist in accurately tracking certain muons that have short paths in the WCD. Since the TT also partially covers the top surface of the rock, it is the only sub-detector that is capable of tagging a portion of the muons passing through the surrounding rock. Consequently, this information can be used to estimate the fast neutron background.

5.1.3 Impact of ^{9}Li/^{8}He background uncertainty on JUNO NMO sensitivity

As highlighted earlier, JUNO aims to determine the NMO via precisely measuring the difference of reactor antineutrino oscillation pattern driven by Δm_{31}^2 in the NO and IO cases. An excellent energy resolution is crucial for the effective discrimination of the NMO signature among the two possible scenarios. The relative energy resolution for the visible energy of a neutrino (E_{vis}) in the JUNO detector is parametrized as

$$\frac{\sigma_{E_{vis}}}{E_{vis}} = \sqrt{\left(\frac{a}{\sqrt{E_{vis}}}\right)^2 + b^2 + \left(\frac{c}{E_{vis}}\right)^2}, \tag{5.1}$$

where term a represents the Poisson statistical fluctuation of the number of detected photoelectrons, term b is driven by residual effects after correcting the detector's spatial non-uniformity, and, term c represents the contributions of the background noises [125]. Based on comprehensive simulations and the latest updates on the detector's design and construction, the energy resolution of the detector has been determined to be 2.95% at 1 MeV [140].

To compare the JUNO's observed antineutrino spectra to NO and IO hypothetical models, a function $\mathscr{T}$ is defined based on the least-squares method, given by [125]

$$\mathscr{T}\left(\vec{\vartheta}, \sin^2\theta_{13}, \vec{\eta}, \vec{\zeta}\right) \equiv \sum_d \left(\mu^d\left(\vec{\vartheta}, \sin^2\theta_{13}, \vec{\eta}, \vec{\zeta}\right) - D^d\right)^T \cdot \left(V_{stat}^d + V_{b2b}^d\right)^{-1} \cdot \left(\mu^d - D^d\right)$$
$$+ \chi_{osc}^2\left(\sin^2\theta_{13}\right) + \chi_{nuis}^2\left(\vec{\eta}\right) + \chi_{corr.nuis}^2\left(\vec{\zeta}\right),$$
(5.2)

where $\vec{\vartheta}$ represents a set of free parameters, including Δm_{31}^2, Δm_{32}^2, and $\sin^2\theta_{12}$, $\vec{\eta}$ represents a set of uncorrelated nuisance parameters, and $\vec{\zeta}$ represents a set of partially correlated parameters. The index d represents the detectors JUNO and TAO. These detectors are treated together in a simultaneous fit, where both models share a common reactor antineutrino component. This joint analysis functions as a far/near measurement: the TAO data provides greater sensitivity to the reactor antineutrino spectrum, while the JUNO data is more sensitive to neutrino oscillations. The column μ represents the expected event spectrum, while the column D contains the observed data. The diagonal matrix V_{stat} contains the statistical uncertainties. The matrix V_{b2b} represents the bin-to-bin uncertainties. The elements of V_{b2b}^{JUNO} capture the background shape uncertainties specific to the JUNO detector, whereas V_{b2b}^{TAO} includes the background shape uncertainties for the TAO detector, as well as uncertainties arising from the fiducial volume cut and additional fission fraction uncertainties. The term χ_{nuis}^2 represents the nuisance term due to uncorrelated parameters, and the term $\chi_{corr.nuis}^2$ represents the nuisance term due to partially correlated parameters. The parameter $\sin^2\theta_{13}$ is constrained in the term $\chi_{osc}^2(\sin^2\theta_{13})$, using the central value and uncertainty from [113]: $\sin^2\theta_{13} = (2.18\pm0.07)\times10^{-2}$.

The best-fit of the function $\mathscr{T}$ to the measured reactor antineutrino spectrum under the NO (IO) hypothesis yields the corresponding minimum value of $\mathscr{T}$, given by $\min\mathscr{T}_{NO}(D)$ ($\min\mathscr{T}_{IO}(D)$). Hence, the NMO discriminator is defined as

$$\Delta\mathscr{T} = \min\mathscr{T}_{NO}(D) - \min\mathscr{T}_{IO}(D),$$
(5.3)

where $\mathscr{T}>0$ (<0) indicates that the data follows NO (IO), with an estimated sensitivity of $n\sigma$ where $n = \sqrt{|\Delta\mathscr{T}|}$.

Figure 5.1 displays the median NMO sensitivity as a function of JUNO and TAO data collection time for both the NO and IO hypotheses, comparing scenarios with and without all systematic uncertainties. The analysis used Asimov data generated with the oscillation parameters from PDG2020 [113]. The results suggest that JUNO will reach an NMO sensitivity of 3σ (3.1σ) after 7.1 years of data taking with 11/12 duty factor for the source reactors (equivalent to a continuous exposure of 6.5 years $\times$ 26.6 GW$_{th}$) in the case of NO (IO). Table 5.4 presents the breakdown of the impact of systematic uncertainties on the NMO sensitivity after 7.1 years of data collection. The sensitivity is calculated by cumulatively considering the statistical uncertainty of the reactor antineutrino sample along with each individual source of systematic uncertainty. It indicates that the uncertainty associated with the ^{9}Li/^{8}He background reduces JUNO's NMO sensitivity by 0.1. Note that this assumes the shape of this systematic can be controlled to 10% precision.
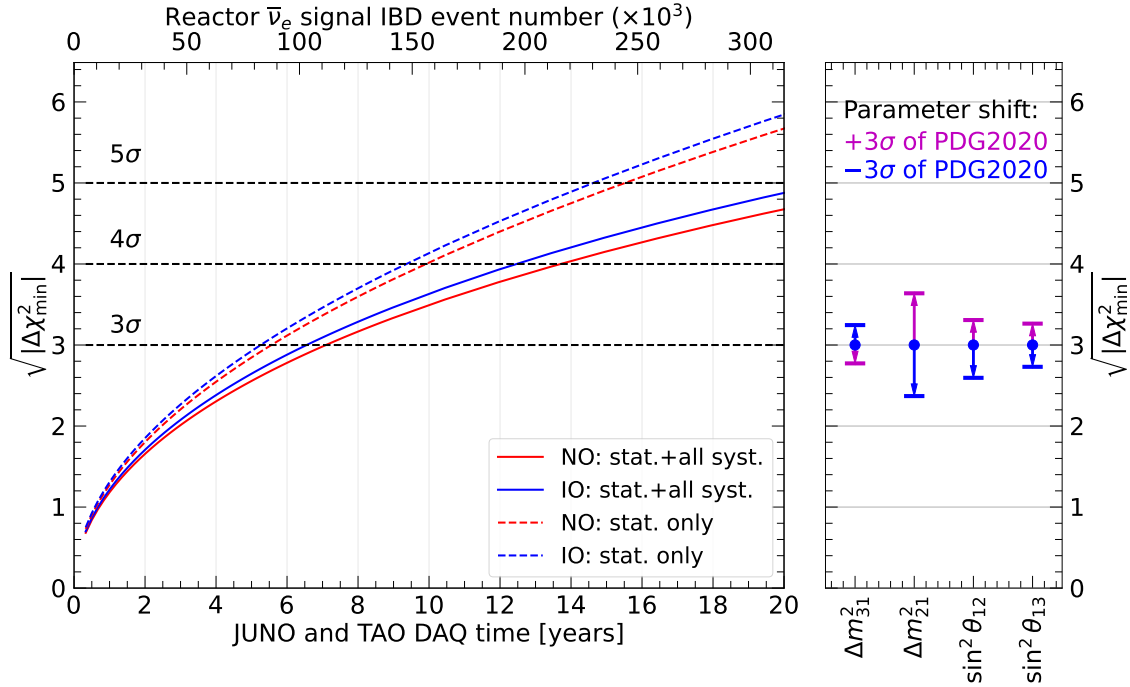
Figure 5.1 : *Variation of JUNO's median NMO sensitivity ($|\Delta\chi^2_{min}| = \overline{\Delta\mathcal{T}}$ from Asimov data) as a function of JUNO and TAO data collection time for both the NO (red) and IO (blue) scenarios, with (solid lines) and without (dashed lines) systematics. The plot has been produced assuming that JUNO and TAO begin data acquisition simultaneously [125].*

Table 5.4 : *The relative impact of individual sources of uncertainty ($|\Delta\chi^2_{min}|$ change) on JUNO's NMO sensitivity ($|\Delta\chi^2_{min}|$) for an exposure of 6.5 years $\times$ 26.6 GW$_{th}$. $|\Delta\chi^2_{min}| = \overline{\Delta\mathcal{T}}$ from Asimov data [125].*

Uncertainties	$|\Delta\chi^2_{min}|$	$|\Delta\chi^2_{min}|$ change
Statistics of JUNO and TAO	11.5	
+ Common uncertainty	10.8	-0.7
+ TAO uncertainty	10.2	-0.6
+ JUNO geoneutrinos	9.7	-0.5
+ JUNO world reactors	9.4	-0.3
+ JUNO accidental	9.2	-0.2
+ JUNO ^{9}Li/^{8}He	9.1	-0.1
+ JUNO other backgrounds	9.0	-0.05
Total	9.0	

5.2 Previous measurements of the ^{9}Li/^{8}He background

Due to the threat posed by atmospheric muon-induced radioisotopes in reactor antineutrino oscillation experiments, various efforts were put forward during the past few decades to measure their production yields in various neutrino experiments as well as accelerator beams. In 1997, the production of various muon-induced radioisotopes and the subsequent secondaries were experimentally studied by irradiating LS samples using the NA54 experiment at the Super Proton Synchrotron muon beam at CERN [161]. A combined production cross-section for ^{9}Li+^{8}He data was derived, using a 190 GeV muon beam. The respective cross-sections at other energies were derived by extrapolation, assuming a power-law dependence of the production cross-section on the energy of the muons, whose precision depends on the energy range as well as the radioisotope concerned. The yield of radioactive isotopes can be estimated, albeit with large uncertainty, using simulations based on MUSIC [162], FLUKA [163], and GEANT4 [164].

During the last decade, several underground LS neutrino experiments have published their experimental measurements of the muon-induced ^{9}Li and ^{8}He yields. Experiments such as KamLAND [158], Borexino [157], Daya Bay [165], and Double Chooz [166] employed somewhat similar techniques to measure the respective ^{9}Li and ^{8}He yields. Each experiment selected prompt-delayed candidate pairs in the entire detector fiducial volume such that the visible energies and the time of detection since the muon event fall within respective ranges characteristic of ^{9}Li and ^{8}He events, yielding ^{9}Li/^{8}He-rich samples. Events at low
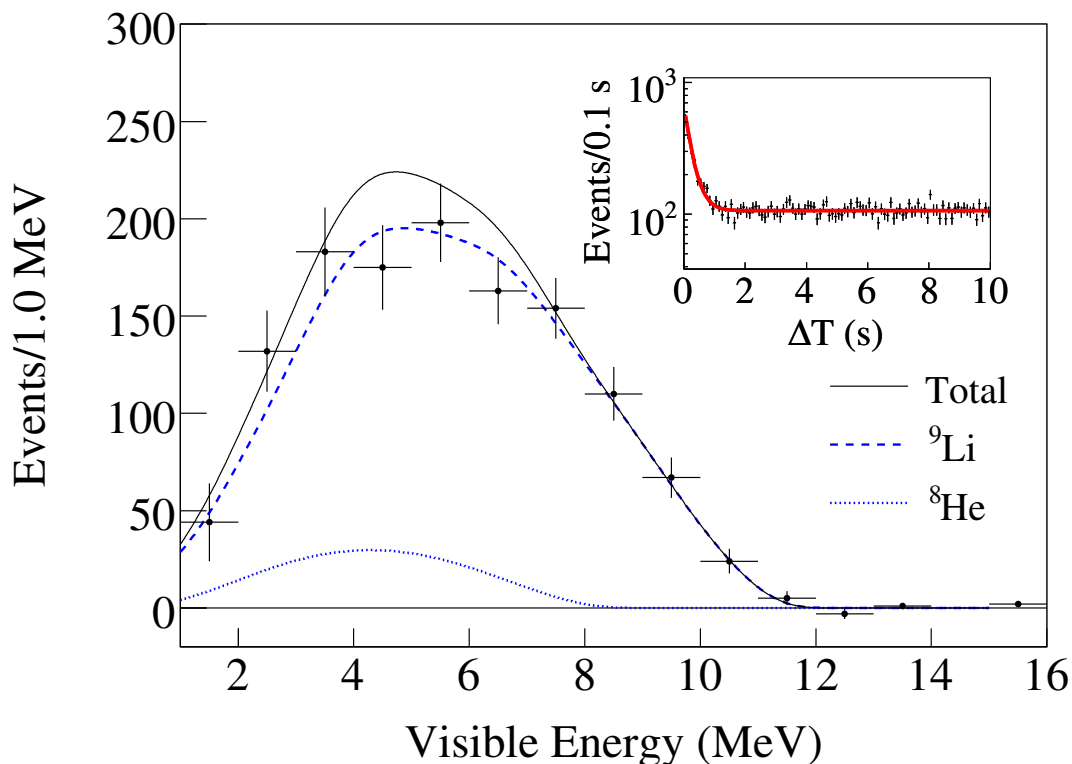
Figure 5.2 : *High-purity ^{9}Li/^{8}He visible energy spectra above 1 MeV as measured by KamLAND experiment. The inset shows the simultaneous fit to the distribution of time since muon event (ΔT) [158].*

timescales since the muon (typically of the order of few ms to few tens of ms) were excluded from this selection, in order to reject the contribution of short-lived radioisotopes. The RENO experiment [167] selected ^{9}Li/^{8}He candidates by requiring an additional spatial and temporal correlation between the prompt and the delayed candidates.

Borexino, Daya Bay, and Double Chooz experiments measured the ^{9}Li/^{8}He yields to the samples obtained as mentioned earlier and performing spectral fits on the time and/or visible energy distributions, taking into account different contributions present. In contrast, KamLAND and RENO experiments defined ^{9}Li/^{8}He-depleted samples, where the time windows were measured at timescales much larger than the half-lives of ^{9}Li/^{8}He isotopes (typically after few seconds since the muon). Since the occurrence of true IBD events are independent of the muon events, the presence of true IBDs in the ^{9}Li/^{8}He-enhanced and the ^{9}Li/^{8}He-depleted samples must be similar. Therefore, a high-purity ^{9}Li/^{8}He spectrum is obtained by subtracting the ^{9}Li/^{8}He-depleted sample from the ^{9}Li/^{8}He-enhanced sample, which was subsequently fit with model spectral functions to determine the respective isotope yields. Figure 5.2 shows the ^{9}Li/^{8}He visible energy spectra and the distribution of time to the prompt signal since the muon measured by the KamLAND experiment.

5.3 Data-driven estimation of ^{9}Li/^{8}He background in JUNO

As was introduced under the section 5.1.2, JUNO employs a topological veto selection, where both the temporal and spatial correlation of the signals due to muon-induced isotopes and the parent muon tracks is taken into account. Due to its excellent muon track reconstruction capabilities, JUNO offers a unique opportunity to perform data-driven estimation of the background due to muon-induced radioisotopes. Under this section, a template to perform a data-driven estimation of the ^{9}Li/^{8}He background, whose procedure is defined using Monte-Carlo simulations, is presented. Once JUNO begins data acquisition, the final template can be defined based on real data.

5.3.1 The dataset

The dataset used for this study consists of two main ingredients: atmospheric muons as well as the associated muon spallation events induced in the JUNO LS, and, IBD events. The data of atmospheric muons and the associated muon spallation events is based on a Monte Carlo simulation of atmospheric muons passing through the JUNO detector and its surroundings. The muons were propagated using MUSIC, accounting for the local geology of the region up to the JUNO experimental site, and from that point onward, their propagation was handled by GEANT4. The simulation indicates that the rate of ^{9}Li/^{8}He events in the JUNO CD is 567 events/day, which is inconsistent with the expectation. Based on the measurements from KamLAND and Borexino, the production yield of ^{9}Li/^{8}He in the JUNO detector is expected to be about 167 events/day [125]. The prompt energy (E_p) spectrum of the simulated IBD events correspond to that of an unoscillated reactor antineutrino flux. The rate of IBD events derived is 3469 events/day. This approach of having excess events has been adopted to optimize the use of limited simulation data by increasing the event rates, provided that the

events are properly re-weighted to ensure the accuracy of the final calculations.

The simulated information includes energy, position, and time data for energy depositions in the JUNO LS by the IBD products as well as muon spallation products. However, this sample does not include any photon propagation from any of the energy deposits due to the high computational power required for propagating every photon produced by a muon passing through the JUNO CD. The dataset only holds truth-level information, which means that it does not include neither the detector response, nor the impact of muon track and CD event vertex reconstruction. The total dataset corresponds to a detector exposure of about 3525 days. Taking into account the time limitation for this study (including the re-simulation and reconstruction of the dataset as discussed under section 5.3.7), a sub-sample of the dataset which corresponds to an exposure of about 325 days is used for this study. For simplicity, this study only concerns the single muon tracks (which constitutes about 89.3% of the total muon flux), and the contribution from other sources of backgrounds are not considered.

In the study of the ^{9}Li/^{8}He yield, the true IBD events stand as the major contaminant against the extraction of a pure sample of ^{9}Li/^{8}He events. Due to the rate discrepancies identified earlier, the dataset was appropriately re-adjusted. First, the IBD E_p spectrum was re-weighted to include the oscillations. Figure 5.3 illustrates the variation of the electron antineutrino disappearance probability at the JUNO baseline, which is calculated using the expression 2.1 assuming normal ordering. Secondly, the E_p spectra of IBD events and ^{9}Li/^{8}He events were re-normalized to represent the expected rates of events, as shown in the figure 5.4. All the analyses presented here onwards were conducted using the dataset
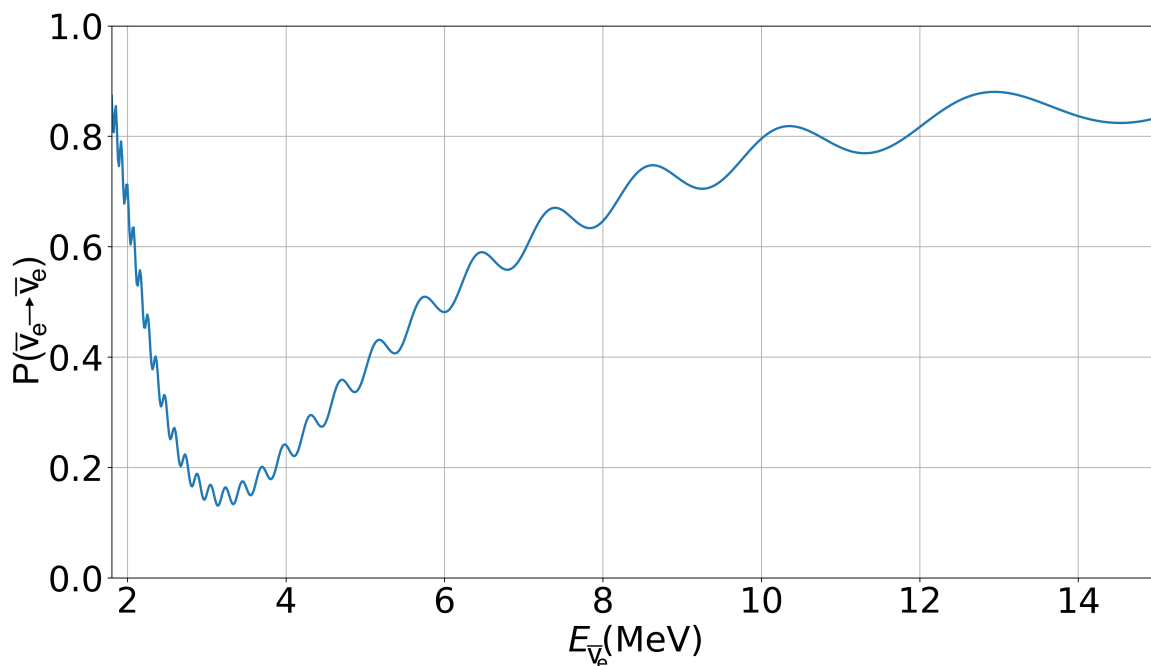
Figure 5.3 : *The variation of the reactor electron antineutrino disappearance probability as a function of the energy of the antineutrino, corresponding to the JUNO baseline, assuming normal ordering.*
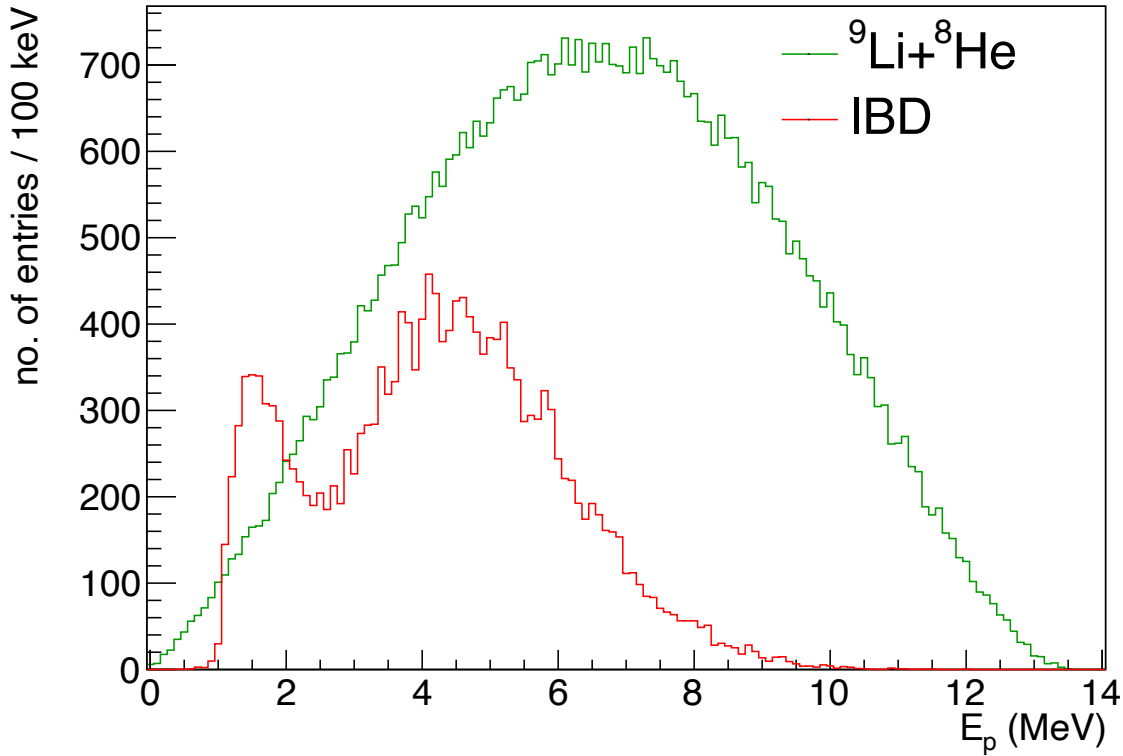
Figure 5.4 : *The re-normalised* E_p *distributions of prompt* $^9Li/^8He$ *events and the IBD events.*

obtained after the appropriate application of antineutrino oscillations as well as the rate re-normalisations.

Figure 5.5 depicts the distributions of the time difference between the prompt signal and the muon event ($\Delta T_{\mu-p}$) for the ^{9}Li/^{8}He events. The median value of $\Delta T_{\mu-p}$ is about 0.15 s, which is in the same order of magnitude as the ^{9}Li/^{8}He decay half-lives. Figure 5.6 depicts the distributions of the lateral distance between the prompt energy deposition vertex and the muon track ($d_{\mu-p}$) for the ^{9}Li/^{8}He. The distributions of $\Delta T_{\mu-p}$ and $d_{\mu-p}$ for the ^{9}Li/^{8}He events highlight the spatial-temporal correlation of the ^{9}Li/^{8}He to the parent muons.

Figures 5.7 and 5.8 demonstrate the correlation among the prompt and delayed signals of the ^{9}Li/^{8}He and the IBD events. The distribution of temporal correlation among the prompt-delayed signals (ΔT_{p-d}) are almost indistinguishable between the ^{9}Li/^{8}He and the IBD events. The median value of ΔT_{p-d} for both the ^{9}Li/^{8}He and the IBD events is about 0.21 ms, which corresponds to the median thermalisation time for a neutron prior to being captured by a proton. However, the distributions of spatial separation between the prompt signal vertices and the corresponding delayed signal vertices (d_{p-d}) have distinct characteristics for ^{9}Li/^{8}He and IBD events. The d_{p-d} distribution for the ^{9}Li/^{8}He events peak just below d_{p-d}=0.1 m, and falls sharply within 0.5 m. In contrast, the d_{p-d} distribution for the IBD events peaks at about d_{p-d}=0.2 m, and continues to fall thereafter, albeit much less rapidly, resulting in a longer tail. Section 5.3.2 introduces a method for selecting ^{9}Li/^{8}He candidate events by utilizing the spatial and temporal correlations between prompt and delayed signals and their associated muons, with a focus on optimizing based on $\Delta T_{\mu-p}$ and $d_{\mu-p}$. Although
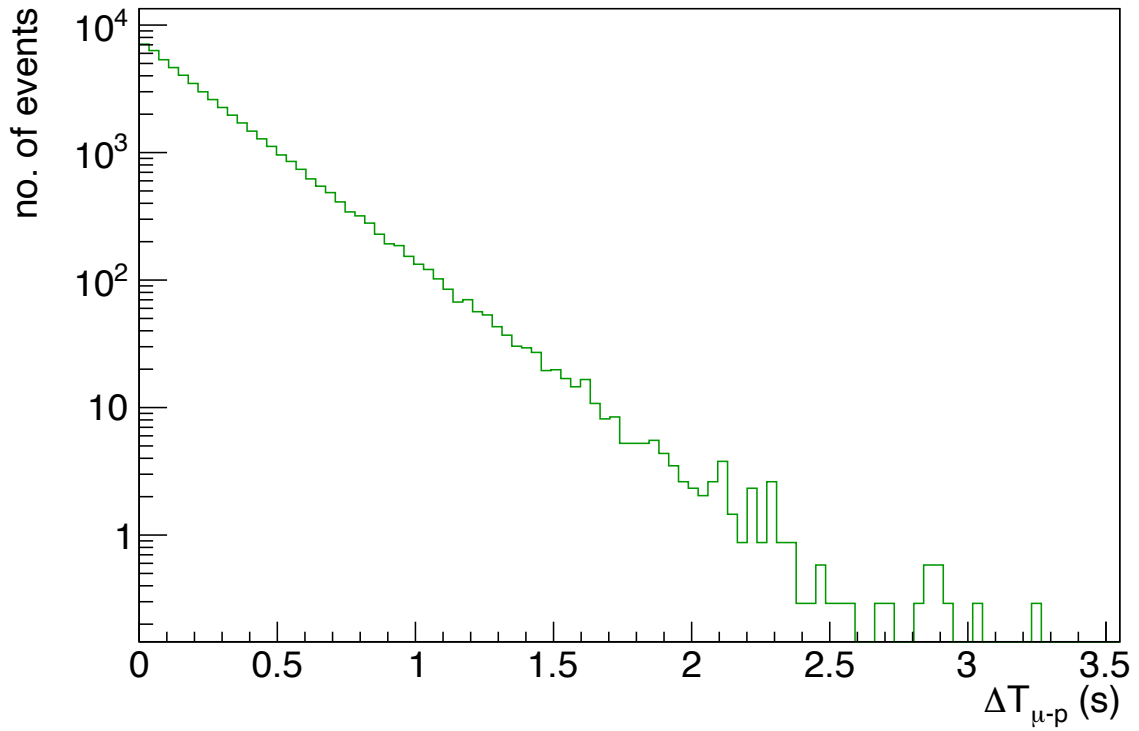
Figure 5.5 : *Distribution of time interval between the the prompt signal of $^9Li/^8He$ decay events and the corresponding muon event.*
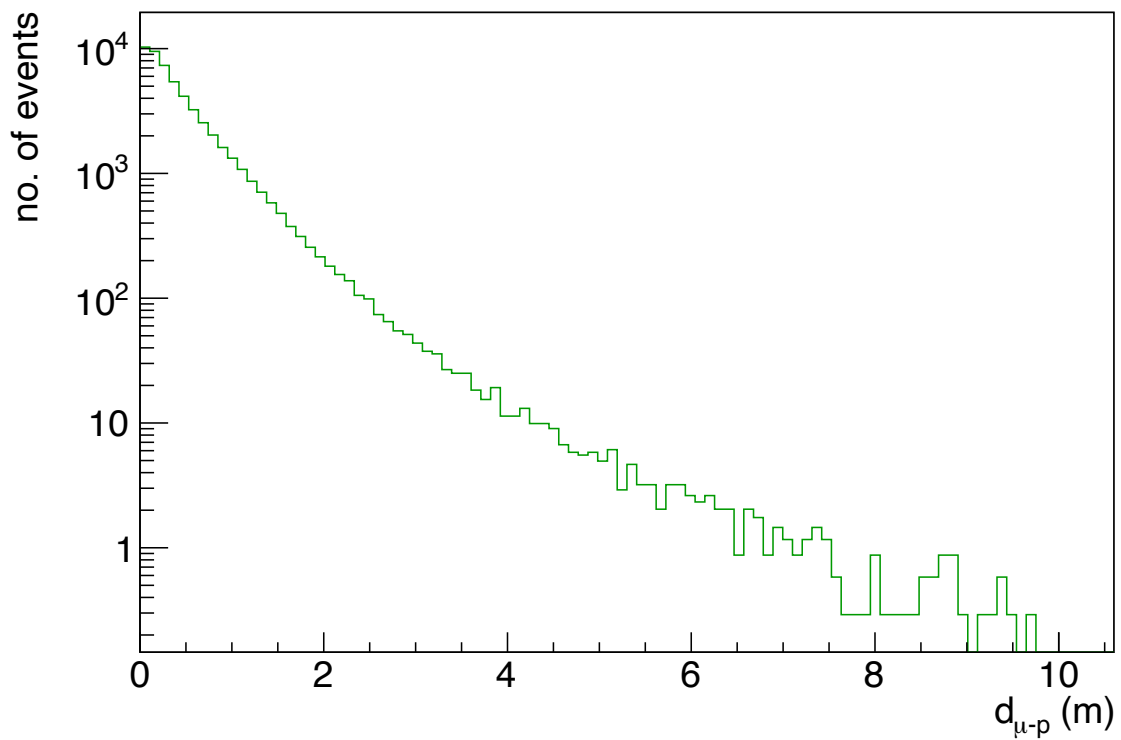
Figure 5.6 : *Distribution of lateral distance between the prompt signal vertices of $^9Li/^8He$ decay events and the parent muon tracks.*
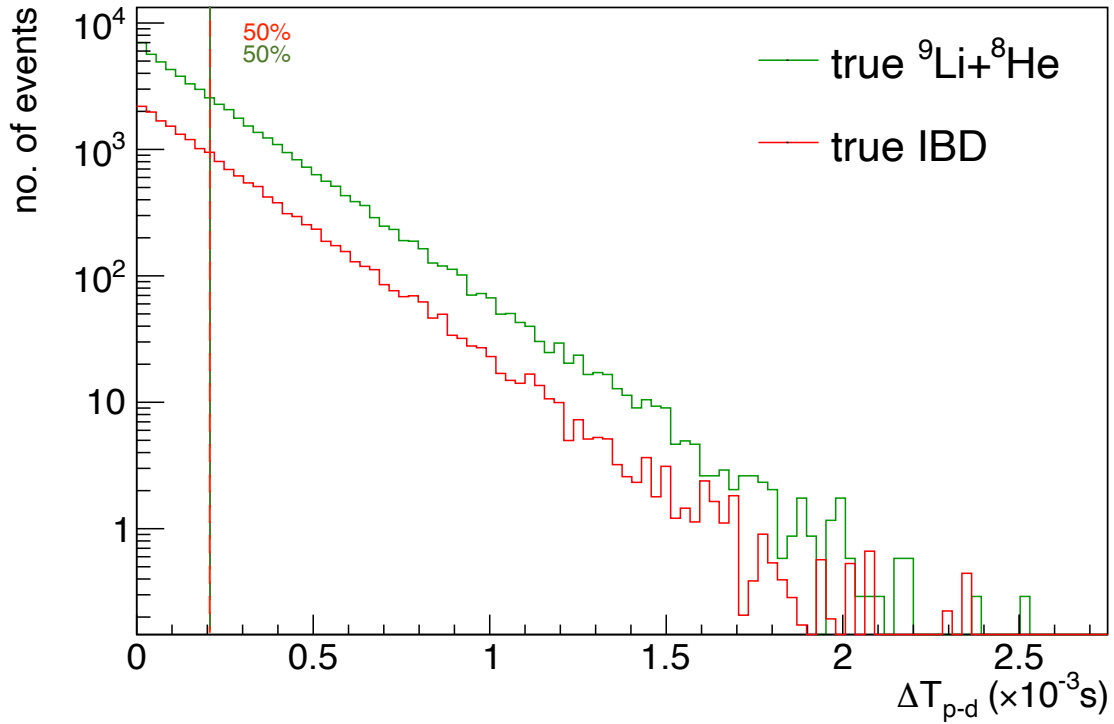
Figure 5.7 : *Distribution of time difference between the prompt signal and the delayed signal of ^{9}Li/^{8}He decay events and IBD events. The vertical lines represent the median values of the distribution for each respective type of event.*
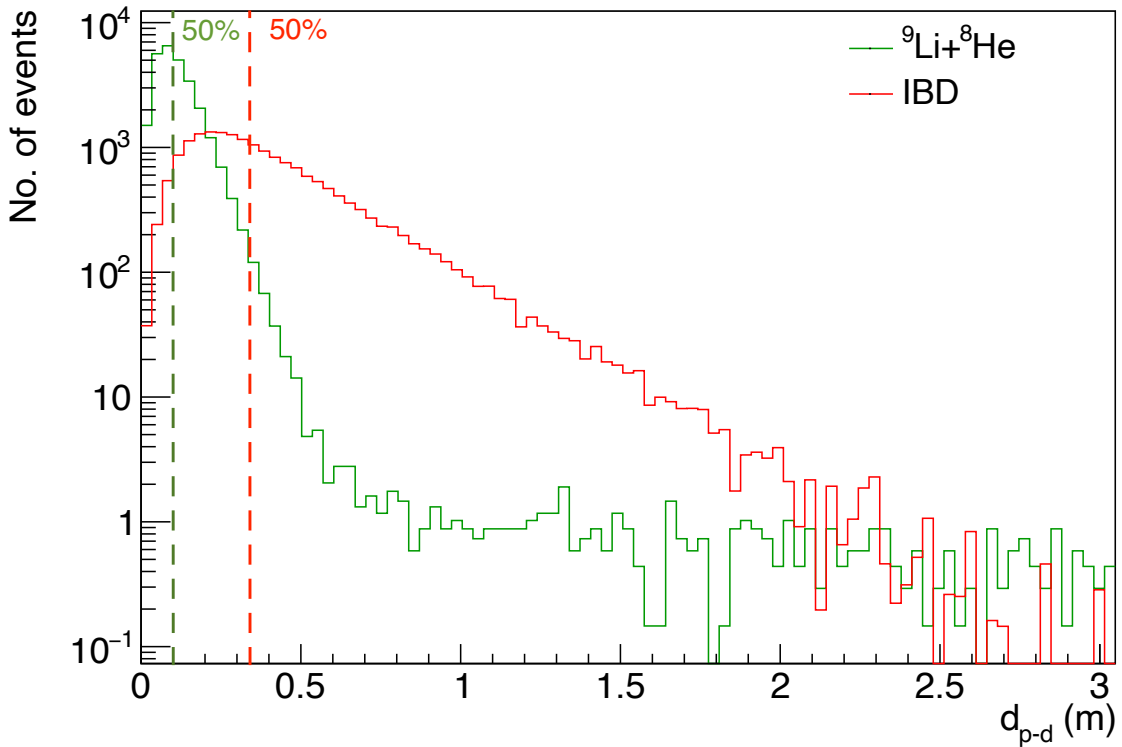
Figure 5.8 : *Distribution of spatial separation between the prompt signal vertex and the delayed signal vertex of ^{9}Li/^{8}He decay events and IBD events. The vertical lines represent the median values of the distribution for each respective type of event.*

152

further optimization using d_{p-d} is possible, this study prioritizes $\Delta T_{\mu-p}$ and $d_{\mu-p}$ as they directly capture the correlation between candidate events and muons.

5.3.2 The method

The suppression of the ^{9}Li/^{8}He background in the JUNO IBD spectrum using the event selection described previously is based on the fact that the prompt and delayed events from ^{9}Li/^{8}He isotope decays are spatially and temporally correlated to the parent muon track. Therefore, by defining a strategy similar to an inverted veto selection (i.e. selecting IBD-like events from within the veto volume surrounding the well-tracked muon tracks), a ^{9}Li/^{8}He-enhanced sample can be obtained. Therefore, an initial set of ^{9}Li/^{8}He candidates selection criteria is defined based on the IBD candidate selection criteria listed earlier under section 5.1.2. The comparison of ^{9}Li/^{8}He candidates selection criteria against the JUNO IBD selection criteria for NMO analysis is presented in the table 5.5.

To select the IBD candidates for the JUNO NMO analysis, the veto volume around well-reconstructed muon tracks is defined to exclude events based on specific cuts: $d_{\mu-p}$<4 m for $\Delta T_{\mu-p}$<0.1 s, $d_{\mu-p}$<2 m for $\Delta T_{\mu-p}$<0.4 s, and $d_{\mu-p}$<1 m for $\Delta T_{\mu-p}$<0.6 s. Reference [12]

Table 5.5 : *Comparison of criteria for selecting IBD candidates for JUNO NMO analysis, $^9Li/^8He$ candidate events, and true $^9Li/^8He$ events within the IBD selection volume used in the study. Text highlighted in red (blue) denotes criteria for selecting $^9Li/^8He$ candidates (true $^9Li/^8He$ events within the IBD selection volume) that differ from those used for selecting IBD candidates.*

Selection criterion	For IBD candidates	For ^{9}Li/^{8}He candidates	For true ^{9}Li/^{8}He events in the IBD selection volume
Inverted cuts from muon veto criteria for NMO analysis:			
Lateral distance between the muon track and the prompt vertex	$(d_{\mu-p}$ > 1 m, $\Delta T_{\mu-p}$ > 0.6 s) + $(d_{\mu-p}$ > 2 m, $\Delta T_{\mu-p}$ > 0.4 s) + $(d_{\mu-p}$ > 4 m, $\Delta T_{\mu-p}$ > 0.1 s)	$d_{\mu-p}$ < 3 m	$d_{\mu-p}$ > 3 m
Time interval to the prompt event since the muon tag		$\Delta T_{\mu-p}$ < 1.2 s	$\Delta T_{\mu-p}$ > 1.2 s
Inherited cuts from JUNO IBD selection criteria for NMO analysis:			
Fiducial volume cut	r < 17.2 m		
Prompt energy cut	0.7 MeV < E_p < 12 MeV	0 MeV < E_p < 15 MeV	0 MeV < E_p < 15 MeV
Delayed energy cut	(1.9 MeV < E_d < 2.5 MeV) + (4.4 MeV < E_d < 5.5 MeV)		
Prompt-delayed time cut	ΔT_{p-d} < 1.0 ms		
Prompt-delayed distance cut	d_{p-d} < 1.5 m		

outlines a simpler preliminary muon veto criterion, excluding events within $d_{\mu-p}$<3 m for $\Delta T_{\mu-p}$<1.2 s. Although this preliminary veto cut is less optimized for ^{9}Li/^{8}He background rejection, it is straightforward to invert it for ^{9}Li/^{8}He candidate selection. Consequently, this study defines the ^{9}Li/^{8}He candidate selection volume by inverting the preliminary criterion, resulting in a cylindrical volume with a radius of 3 m and duration of 1.2 s around well-tracked single muons in the CD fiducial volume.

From the detector's perspective, the ^{9}Li/^{8}He events generate a prompt-delayed coincidence signature that closely resembles IBD events. Therefore, the IBD selection criteria which are not designed to reject ^{9}Li/^{8}He events are used here for the selection of ^{9}Li/^{8}He candidates. Thus, the same fiducial volume cut, prompt-delayed time cut, and prompt-delayed distance cut used to select IBD candidates for NMO analysis are also applied to select ^{9}Li/^{8}He candidates. However, as highlighted in the table 5.5, the prompt energy cut is broadened to measure the prompt energy spectrum of ^{9}Li/^{8}He events over the full range.

5.3.3 The results

The aforementioned selection criteria were applied on the dataset concerned, and a ^{9}Li/^{8}He-enhanced sample, labelled as the control sample, was obtained. The distribution of E_p of the ^{9}Li+^{8}He candidates of the control sample is shown in the figure 5.9. Two parameters, sample purity and sample efficiency, are defined to characterise the performance of ^{9}Li/^{8}He candidate selection, as follows:

$$\text{Purity} = \frac{\text{no. of true } ^9\text{Li}/^8\text{He events in the sample}}{\text{Total no. of } ^9\text{Li}/^8\text{He candidates in the sample}},$$

and,

$$\text{Efficiency} = \frac{\text{no. of true } ^9\text{Li}/^8\text{He events in the sample}}{\text{Total no. of true } ^9\text{Li}/^8\text{He events generated}}.$$

The purity and efficiency of the control sample thus obtained was found to be 96.6% and 90.3%, respectively. The control sample also contained 9.2% of all the true IBDs. This is a clear indication of the capability of the current approach to obtain samples of ^{9}Li/^{8}He candidates which are of high purities while preserving statistics. Since the contribution of the E_p of the true IBDs is most significant in the range 1 MeV< E_p <6 MeV, the distribution of E_p of all candidates deviates from that of the true ^{9}Li/^{8}He events in this energy range. The distribution of $\Delta T_{\mu-p}$ following the selection of ^{9}Li/^{8}He candidates are shown in the figure 5.10. It indicates that the number of true ^{9}Li/^{8}He events falls rapidly as $\Delta T_{\mu-p}$ increases. In contrast, the true IBD events are distributed uniformly over $\Delta T_{\mu-p}$. The volume of the cylinder defined by the radius $d_{\mu-p}$ around the muon track, used for selecting ^{9}Li/^{8}He candidates, is proportional to $d_{\mu-p}^2$. To verify whether the true ^{9}Li/^{8}He events are uniformly distributed within this cylindrical volume, the number of candidate events of the control sample was plotted against $d_{\mu-p}^2$, as shown in the figure 5.11. It indicates that the number of true ^{9}Li/^{8}He events falls rapidly as $d_{\mu-p}^2$ increases, while the true IBD events are distributed uniformly over $d_{\mu-p}^2$. These observations indicate that the true ^{9}Li/^{8}He events are strongly correlated with the parent muon tracks in terms of position and time, while
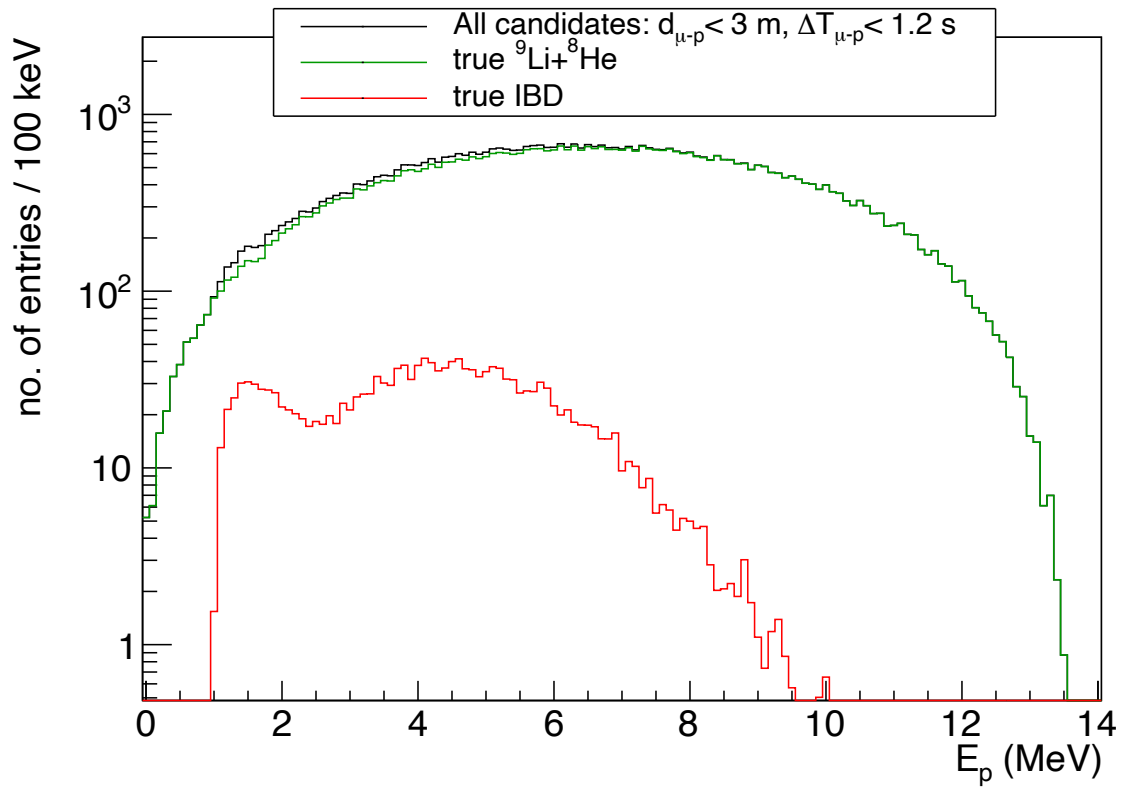
Figure 5.9 : *The distribution of energy of the prompt events of the $^9Li/^8He$ candidates in the control sample.*
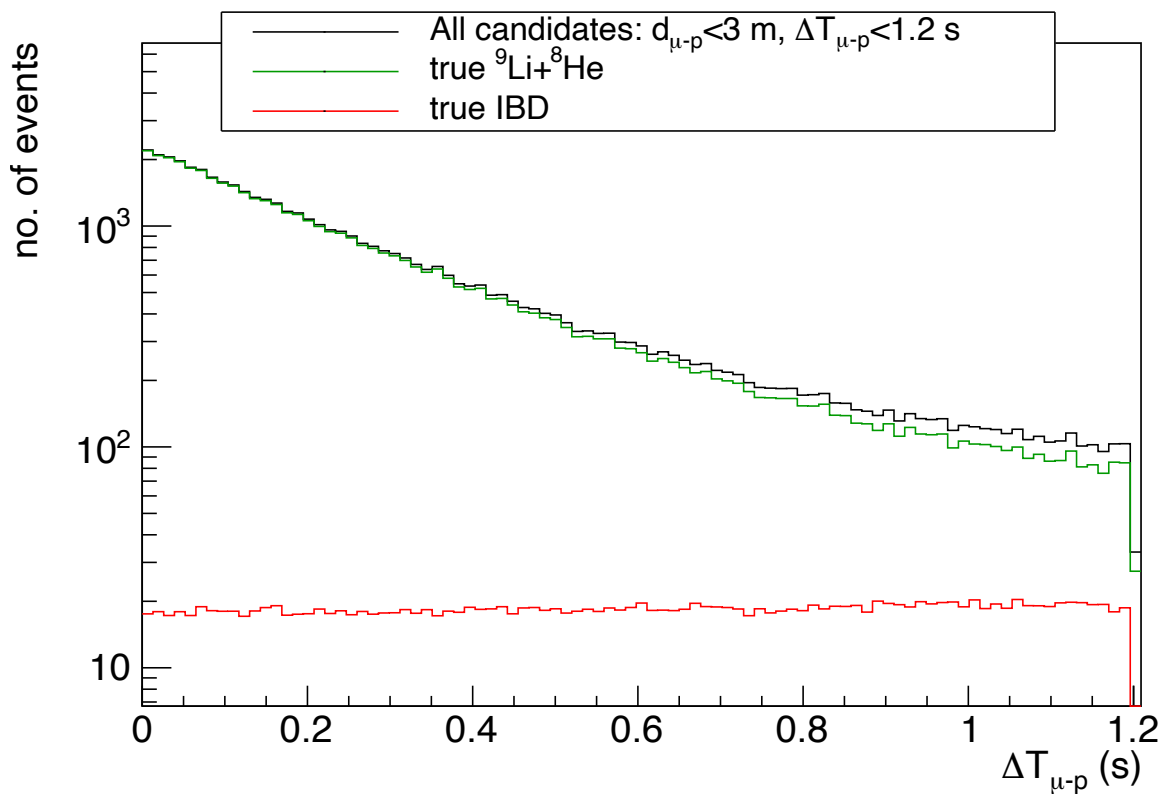
Figure 5.10 : *Distribution of time difference between the prompt candidate signal and the muon event of the $^9Li/^8He$ candidates in the control sample.*
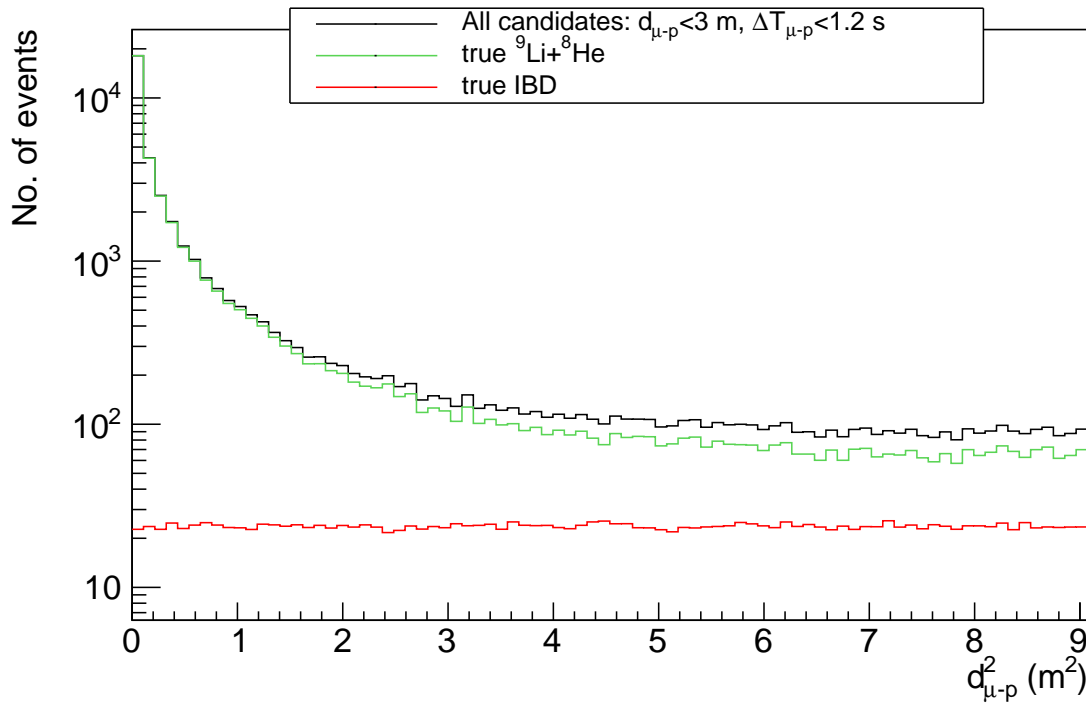
Figure 5.11 : *Distribution of the squared lateral distance between the parent muon track and the prompt candidate signal vertex of the $^9Li/^8He$ candidates in the control sample.*

IBD events are independent of the muon tracks, as expected.

It is important to quantify the level of compatibility of the control sample as an estimate of the true ^{9}Li/^{8}He background in JUNO's antineutrino spectrum. For this purpose, a sample of true ^{9}Li/^{8}He events, labelled as the reference sample, were selected. The criteria to select the reference sample is given in the fourth column of the table 5.5. It is important to note that the criteria for $\Delta T_{\mu-p}$ and $d_{\mu-p}$ are consistent with the preliminary selection criteria for IBD candidates outlined in reference [12], as previously discussed under section 5.3.2. Consequently, the events in the reference sample accurately represent true ^{9}Li/^{8}He events within the IBD candidate selection volume for the JUNO NMO analysis. This makes the reference sample a reliable proxy for the true ^{9}Li/^{8}He background in JUNO's antineutrino spectrum. The rate of true ^{9}Li/^{8}He events in the reference sample is approximately 2.6 events per day. Note that this value is different compared to rate of residual ^{9}Li/^{8}He background in JUNO's antineutrino measurements for the NMO analysis (0.8 events per day) quoted in the table 5.3. This is because the criteria for the reference sample are different with respect to $\Delta T_{\mu-p}$, $d_{\mu-p}$, and E_p compared to those used for selecting IBD candidates in JUNO's NMO analysis.

For the purpose of quantifying the level of compatibility of the control sample as an estimate of the true ^{9}Li/^{8}He background, the E_p spectrum derived from the high-purity sample as well as that of the reference sample were normalized with respect to the event rates. The comparison of the normalized E_p spectra is shown in figure 5.12. Since the reference sample contains a small number of events, a 100keV binning is used instead of the prompt-energy
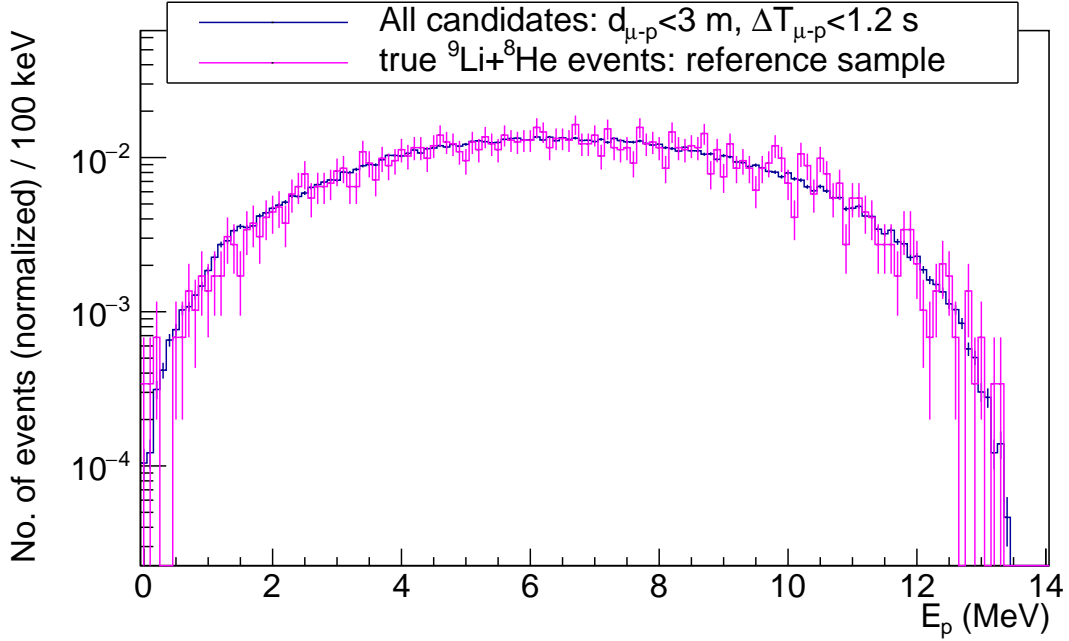
Figure 5.12 : *Comparison of* E_p *distributions of all the* $^9Li/^8He$ *candidates of the control sample (blue), against that of the reference sample (magenta).*

binning defined for JUNO NMO analysis. This increases the number of events per bin and reduces the bin-to-bin uncertainty in the reference sample. A χ^2-comparison among the two distributions yields $\chi^2/\mathrm{NDF} = 0.99$, indicating a good compatibility among the control and the true ^{9}Li/^{8}He events.

As highlighted earlier, the E_p spectrum of the control sample deviates from the sample of true ^{9}Li/^{8}He events outside the veto volume at 1 MeV < E_p < 6 MeV. According to the figure 5.9, this is primarily because of the prominence of the contamination due to IBD events. If the relative sample contamination due to true IBDs can be minimized, the resulting sample would yield a better estimate of the true ^{9}Li/^{8}He events. Under this study, two possible approaches are considered: optimisation of $\Delta T_{\mu-p}$ and $d_{\mu-p}$ selection criteria, and, contamination subtraction. Although true ^{9}Li/^{8}He events and their parent muons are correlated to each other with respect to $\Delta T_{\mu-p}$ and $d_{\mu-p}$, the IBD events are independent of the muon events. This property can be exploited to yield samples with lower levels of contamination due to true IBDs via further constraining $\Delta T_{\mu-p}$ and $d_{\mu-p}$ selection criteria. However, this constraint leads to the loss of true ^{9}Li/^{8}He events in the sample. Therefore, optimizing the selection criteria for $\Delta T_{\mu-p}$ and $d_{\mu-p}$ allows for a more accurate estimation of the true ^{9}Li/^{8}He background, while balancing the trade-off between purity and efficiency. This is discussed in detail under section 5.3.4.

The second approach is similar to the methods employed by the KamLAND and RENO experiments to estimate ^{9}Li/^{8}He yields in their studies. This approach involves the definition of two regions: a ^{9}Li/^{8}He-enhanced region, and, a ^{9}Li/^{8}He-depleted region, with respect the muon tracks. Since the atmospheric muon-induced isotopes are highly correlated to the

parent muon in terms of space and time, the cylindrical volume defined earlier for the sample selection can be considered as a ^{9}Li/^{8}He-enhanced region. Similarly, by defining the same physical cylindrical volume around each track but at a time prior to the arrival of muons for the same length of time can be considered a ^{9}Li/^{8}He-depleted region. The contribution of IBDs or any other backgrounds uncorrelated with the muons in either of these volumes can be considered similar, as they are homogeneously distributed in the detector with respect to both space and time. Therefore, by performing a selection of ^{9}Li/^{8}He candidates in both regions for all muons, followed by the subtraction of the ^{9}Li/^{8}He-depleted sample from the ^{9}Li/^{8}He-enhanced sample can yield a sample almost free of true IBDs. This is discussed in detail under section 5.3.5.

5.3.4 Approach 1: Optimization of $\Delta T_{\mu-p}$ and $d_{\mu-p}$ cuts for the selection of ^{9}Li/^{8}He candidates

The optimization of the ^{9}Li/^{8}He candidate selection criteria involves finding the best combination of $\Delta T_{\mu-p}$ and $d_{\mu-p}$ cut values that produce a ^{9}Li/^{8}He candidate sample that is high in purity while maintaining a robust efficiency. The variation of efficiency and purity for different combinations of $\Delta T_{\mu-p}$ and $d_{\mu-p}$ cuts is plotted in figures 5.13 and 5.14, respectively.
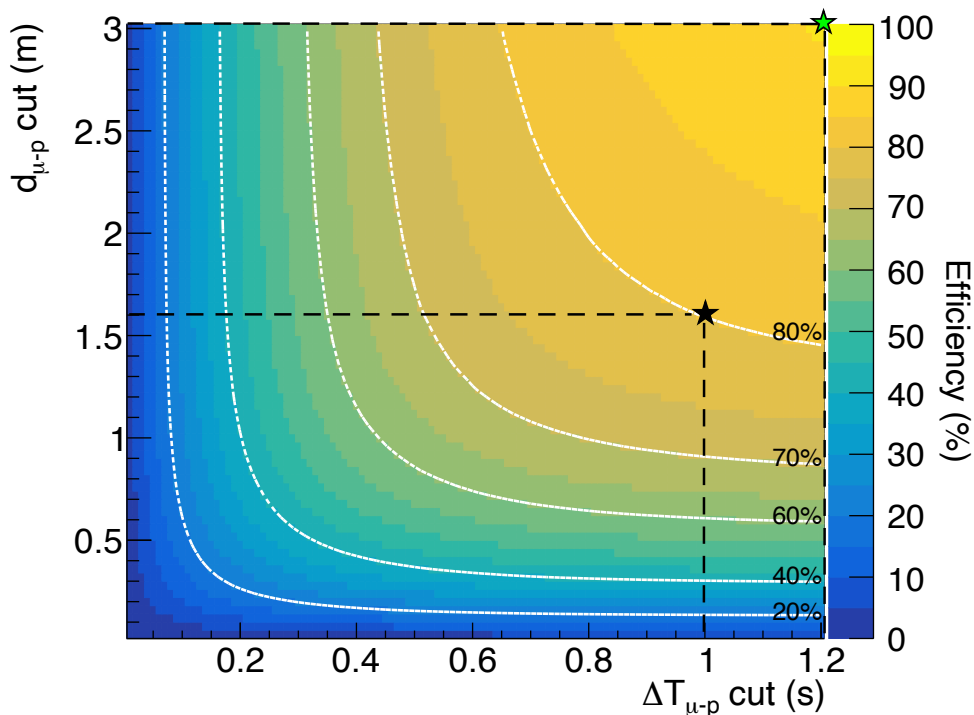
Figure 5.13 : *The distribution of sample efficiency upon different combinations $\Delta T_{\mu-p}$ and $d_{\mu-p}$ cuts to select ^{9}Li/^{8}He candidates. Each 2D point represents a specific $\Delta T_{\mu-p}$ and $d_{\mu-p}$ cut. The color scale indicates the efficiency. The white lines indicate the contours for the indicated efficiency levels. The green (black) star indicates the combination of cuts for the control (optimized) scenario.*
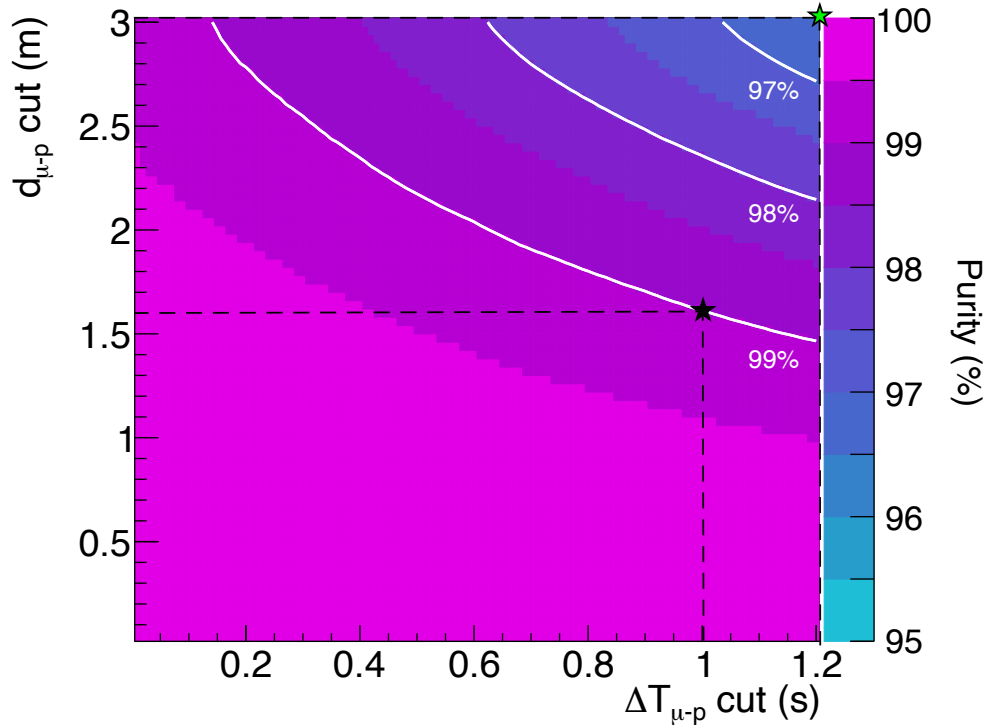
Figure 5.14 : *The distribution of sample purity upon different combinations $\Delta T_{\mu-p}$ and $d_{\mu-p}$ cuts to select $^9Li/^8He$ candidates. Each 2D point represents a specific $\Delta T_{\mu-p}$ and $d_{\mu-p}$ cut. The color scale indicates the purity. The white lines indicate the contours for the indicated purity levels. The green (black) star indicates the combination of cuts for the control (optimized) scenario.*
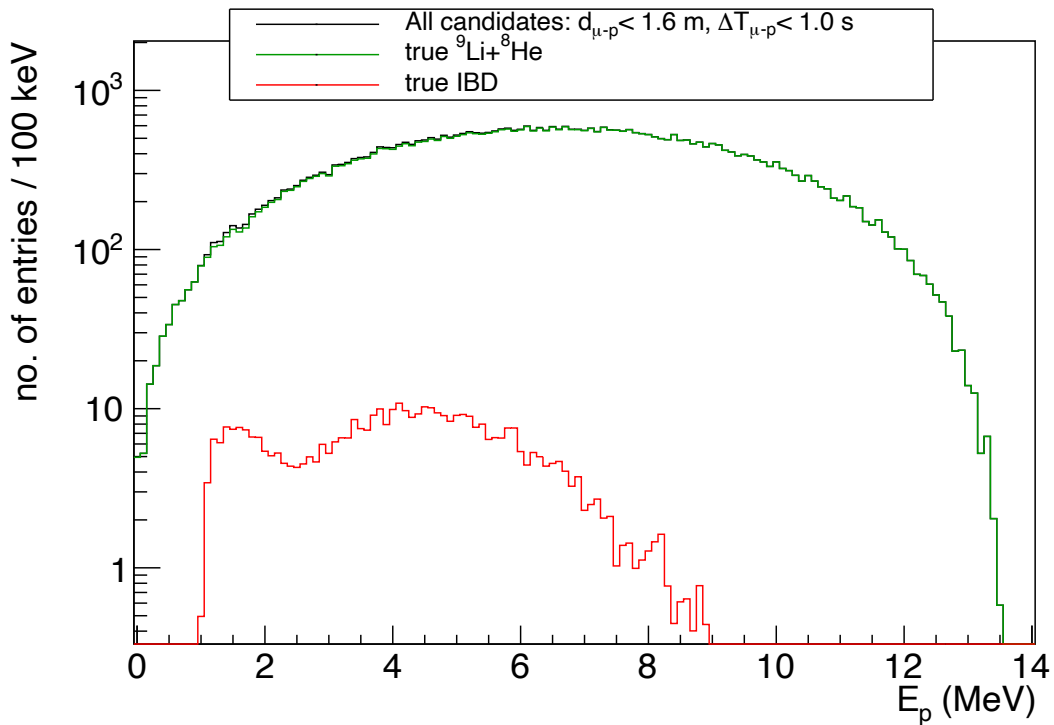
Figure 5.15 : *The E_p distribution of the $^9Li/^8He$ candidates of the high-purity sample.*

Each point on each of these 2D plots corresponds to a unique combinations of $\Delta T_{\mu-p}$ and $d_{\mu-p}$ cuts. The white contours indicate different efficiency and purity contours in respective plots. The top-right corner of each plot corresponds to the selection criteria of the control sample (indicated by the green star).

A higher purity sample contains more events of interest and fewer contaminants. The purer the sample, the more accurately it reflects the true events of interest. Therefore, a data sample with excellent purity is best for analyses. Thus, a new scenario is considered, where the base requirement of purity is lifted to be at least 99%. However, high purity comes at the cost of loss of statistics, as evident from the figures 5.13 and 5.14. Therefore, the $\Delta T_{\mu-p}$ and $d_{\mu-p}$ cuts were optimized to maximize efficiency, while meeting the aforementioned minimum requirement of purity. The $\Delta T_{\mu-p}$ and $d_{\mu-p}$ selection contour that gives 99% purity is shown in the figure 5.14. The optimum combination is marked with a black star in the figures 5.13 and 5.14, found at $\Delta T_{\mu-p} < 1.0$ s, and $d_{\mu-p} < 1.6$ m. This selection corresponds to an efficiency of 80.1% and a purity of 99%. The E_p distribution of all the ^{9}Li/^{8}He candidates selected using the aforementioned cuts, labelled as high-purity sample, is shown in the figure 5.15. Notice that the contamination from true IBDs is suppressed in comparison to the control sample, whose E_p spectra were shown in the figure 5.9. Hence, in contrast to the control, the E_p spectrum of the high-purity sample more closely resembles that of the true ^{9}Li/^{8}He events.

To assess the compatibility of the high-purity sample with true ^{9}Li/^{8}He events, it was compared to the reference sample as shown in the figure 5.16. The χ^2 comparison yields χ^2/NDF=0.88, indicating good statistical agreement between the two samples.
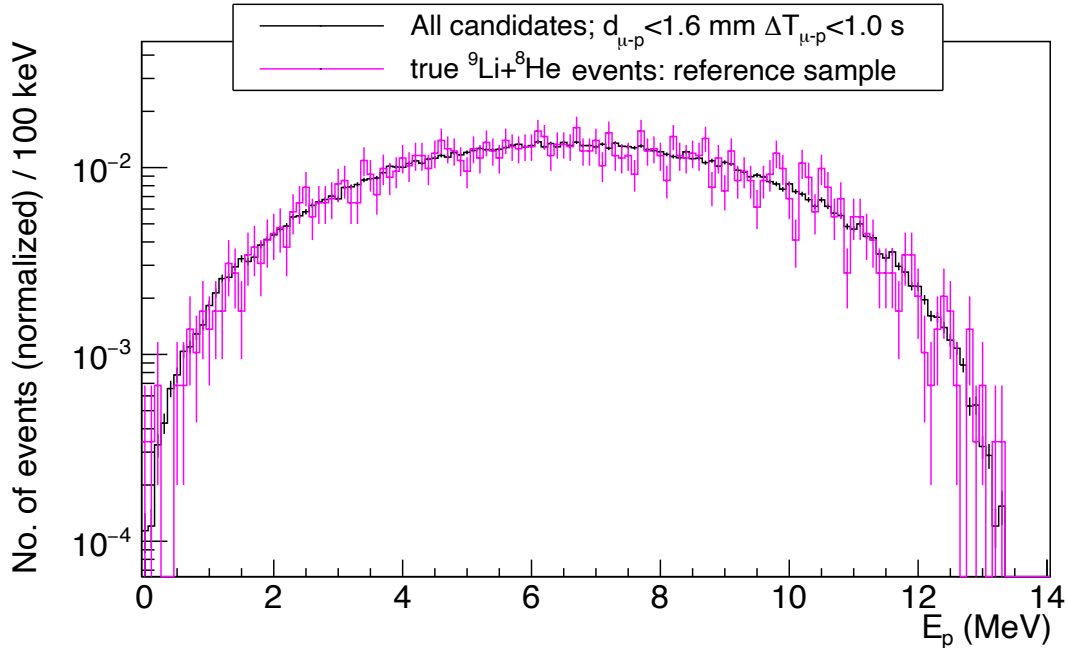
Figure 5.16 : *Comparison of E_p distributions of all the ^{9}Li/^{8}He candidates of the high-purity sample (black), against that of the reference sample (magenta).*

5.3.5 Approach 2: Subtraction of IBD contamination

Let the space-time volume defined by the ^{9}Li/^{8}He candidate selection criteria under section 5.3.2 (i.e. 0.001 s < $\Delta T_{\mu-p}$< 1.2 s, and $d_{\mu-p}$< 3 m) be labelled as region A. The sample of ^{9}Li/^{8}He candidates selected from this region, labelled as sample A, is rich with true ^{9}Li/^{8}He events, as discussed previously. Another space-time volume of same dimensions as the region A is defined at the same spatial volume but at a time period 0.5 s prior to the passage of the muon (i.e. -1.7 s <$\Delta T_{\mu-p}$< -0.5 s, and $d_{\mu-p}$< 3 m). Let this region be labelled as region B, and the sample of ^{9}Li/^{8}He candidates selected from this region as sample B. Subtracting sample B from sample A yields a new sample, labelled sample (A-B), that is significantly suppressed of IBDs. Hence, the sample (A-B) can be considered as a sample which is further enriched of true ^{9}Li/^{8}He events. Note that sample A is equivalent to the control sample discussed in the previous section, whose E_p spectra are depicted in the figure 5.9.

The E_p spectrum of the ^{9}Li/^{8}He candidate events of sample B is depicted in the figure 5.17. The rate of IBD events in the samples A and B were found to be about 5.2 events/day and 5.1 events/day, respectively, indicating almost the same number of IBD contaminants in either of the samples as expected. Sample B was then subtracted from the sample A to obtain sample (A-B). Figure 5.18 depicts the E_p spectra of the sample (A-B) thus obtained. Notice that the E_p spectrum of all the ^{9}Li/^{8}He candidates in sample (A-B) is dominated by true ^{9}Li/^{8}He events, in comparison to that of sample A. The "purity" of true ^{9}Li/^{8}He events in
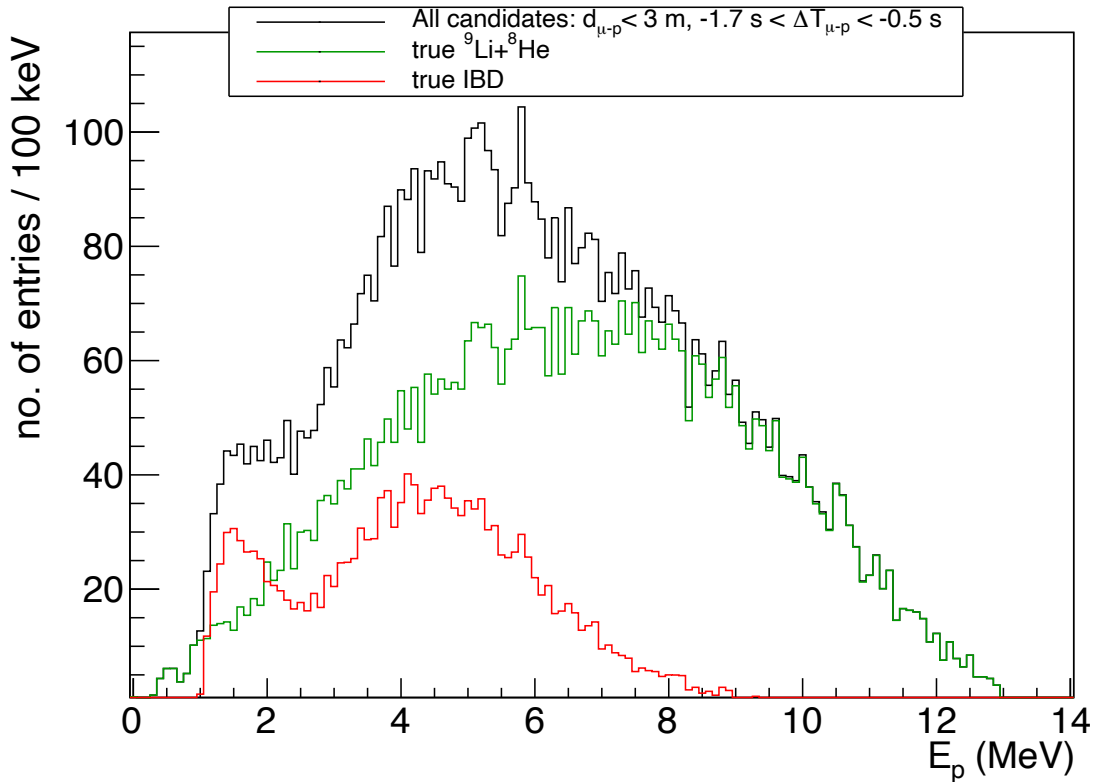
Figure 5.17 : *The E_p distribution of the ^{9}Li/^{8}He candidates of the sample B.*
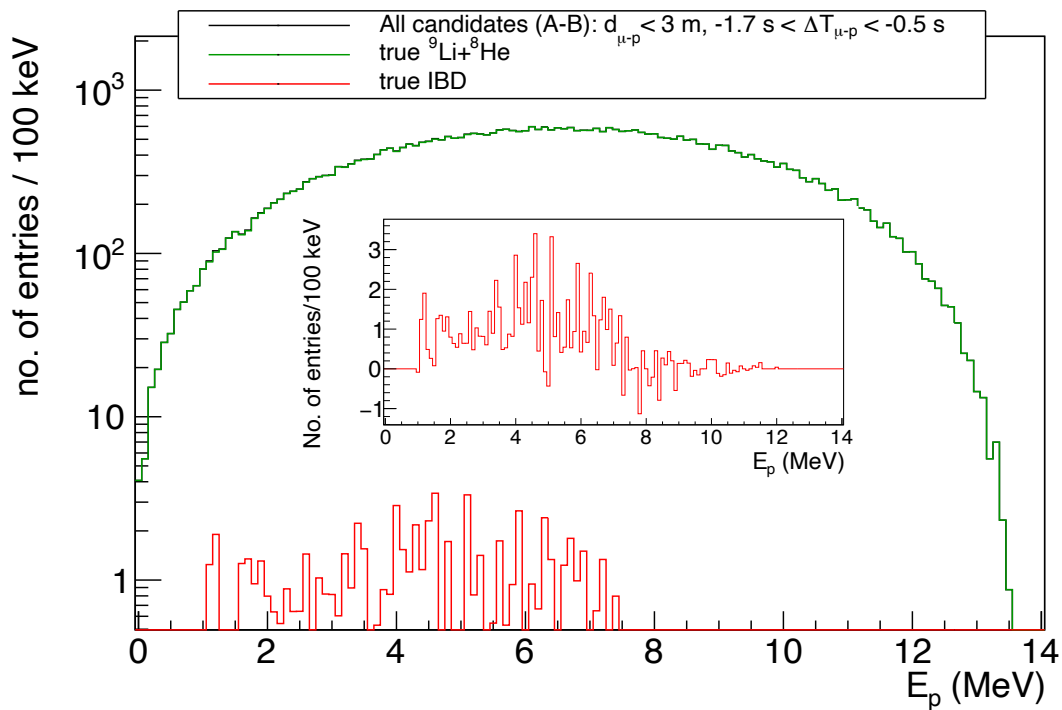
Figure 5.18 : *The* E_p *distribution of the* $^9Li/^8He$ *candidates of the sample (A-B). The inset shows the distribution of residual true IBD events in the sample (A-B).*
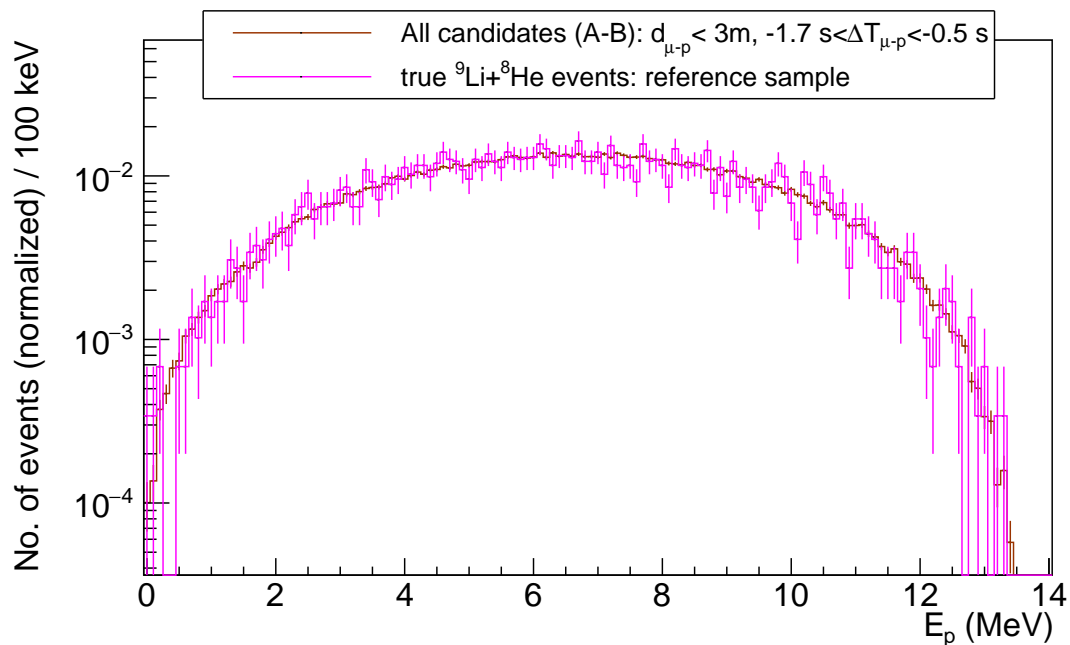
Figure 5.19 : *Comparison of* E_p *distributions of all the* $^9Li/^8He$ *candidates of the (A-B) sample (brown), against that of the reference sample (magenta).*

sample (A-B) is 99.8%[1], which corresponds to an "efficiency" of 81%[2]. This indicates that this approach, under the same selection criteria as for sample A, has yielded a new sample (A-B) which has a much lower contamination of true IBDs compared to the high-purity sample discussed in the previous section, while maintaining a level of similar sample size as the high-purity sample.

To further establish the validity of this approach, the E_p spectrum of sample (A-B) was normalized with respect to the total number of events, and compared with that of the reference sample, as shown in the figure 5.19. A similar agreement is observed between the two spectra, compared to the both scenarios discussed earlier. This agreement was evaluated using a χ^2-test, which yielded a χ^2/NDF of 0.87.

5.3.6 Comparison: Approach 1 vs. Approach 2

As discussed under sections 5.3.4 and 5.3.5, both approaches for a data-driven estimation of the ^{9}Li/^{8}He background produce reliable estimations. The χ^2-tests to compare the E_p spectra produced from either estimate against that of the reference spectrum yielded comparable χ^2/NDF values. In a scenario where low statistics are not a concern, further tightening the selection criteria for ^{9}Li/^{8}He candidates based on $\Delta T_{\mu-p}$ and $d_{\mu-p}$ can effectively lead to a precise estimation of the ^{9}Li/^{8}He background. Therefore, approach 1 is better suited for such situations. In contrast, contamination suppression method as used in the second approach is much more suited for low-statistics scenarios to achieve an effective suppression of backgrounds which are not correlated to the muons, while preserving most of the true ^{9}Li/^{8}He events. Section 5.3.8 examines the potential of using the TT's precise muon reconstruction to estimate the ^{9}Li/^{8}He background in the JUNO antineutrino spectrum by selecting single muons that pass through the TT. Since only about a third of the atmospheric muons passing through the CD also traverse the TT, the size of the selected ^{9}Li/^{8}He candidate sample will be reduced by roughly a third. Additionally, detector response and reconstruction effects (discussed under the next section) will further decrease the sample size. Therefore, the study given in section 5.3.8 is demonstrated using the second approach only.

---

[1]Purity cannot be properly defined for the sample (A-B). The presented "purity" is calculated as:

$$\mathrm{Purity} = \frac{\text{True } ^9\mathrm{Li}+^8\mathrm{He} \text{ events in sample A} - \text{True } ^9\mathrm{Li}+^8\mathrm{He} \text{ events in sample B}}{\text{Total no. of candidates in sample A} - \text{Total no. of candidates in sample B}}.$$

[2]Efficiency cannot be properly defined for the sample (A-B). The presented "efficiency" is calculated as:

$$\mathrm{Efficiency} = \frac{\text{True } ^9\mathrm{Li}+^8\mathrm{He} \text{ events in sample A} - \text{True } ^9\mathrm{Li}+^8\mathrm{He} \text{ events in sample B}}{\text{Total no. of True } ^9\mathrm{Li}+^8\mathrm{He} \text{ events generated}}.$$

5.3.7   Inclusion of detector electronics and reconstruction effects

As mentioned earlier, the dataset used for the aforementioned analyses does not account for any detector reconstruction effects. In practice, the success of the aforementioned data-driven estimation techniques depend on the reconstruction capabilities of the detector. Factors such as the precision and efficiency of muon track reconstruction as well as vertex position and energy reconstruction capabilities of the detector play a significant role that determines the practical validity of the estimation technique. A worse muon reconstruction precision and/or efficiency translates into badly defined veto volumes, that leads to an unreliable estimation of the true ^{9}Li/^{8}He background. However, the excellent muon tracking efficiency and precision of the TT can be utilized to obtain a sub-sample of very well-defined muon tracks. This translates to well-defined veto cylinders around the muon tracks that lead to an efficient extraction of true ^{9}Li/^{8}He events. Therefore, the TT presents an excellent opportunity to perform high-precision data-driven estimation of ^{9}Li/^{8}He backgrounds using well-tracked muons that pass through it.

To estimate the impact of muon track reconstruction as well as the ^{9}Li/^{8}He prompt-delayed energy and vertex position reconstruction capabilities, the events of interest of the aforementioned dataset was re-simulated to include electronics simulation effects, and reconstructed using JUNO official reconstruction software. The ^{9}Li/^{8}He events, IBD events and muons were extracted into separate datasets, and simulated and reconstructed independently. As the following study aims to explore the TT's potential to perform a data-driven estimation of the ^{9}Li/^{8}He background to the JUNO antineutrino spectrum, only the muons which pass through all three layers of the TT were re-simulated and reconstructed. The true event position, energy, momentum and time information from the original dataset were used as the inputs to the simulation. A new dataset was then formed by taking into account the output from the simulation and the reconstruction.

5.3.8   Data-driven estimation of the ^{9}Li/^{8}He background using the Top Tracker

The ^{9}Li/^{8}He-enhanced region is defined at $\Delta T_{\mu-p} < 1.2$ s, and $d_{\mu-p} < 3$ m, and the corresponding sample of ^{9}Li/^{8}He candidates, labelled sample A', was obtained. Sample A' has a purity of 96.1%, which corresponds to an efficiency of 22.8%. This reduction in sample efficiency is due to the geometric acceptance when only muons passing through all three layers of the TT and the CD are considered, combined with detector and reconstruction inefficiencies.

Afterwards, ^{9}Li/^{8}He candidates were chosen from the same physical volume as sample A' but during an earlier time window (-1.7 s< $\Delta T_{\mu-p}$ < -0.5 s) of the same duration. This sample, labelled sample B', was subtracted from sample A' to obtain a new sample of ^{9}Li/^{8}He candidates, labelled sample (A'-B'). The "purity" of true ^{9}Li/^{8}He events in the sample (A'-B') is 99.9%, and it corresponds to an "efficiency" of 21.9%. Quantifying the compatibility of the sample as an estimate of the true ^{9}Li/^{8}He background in JUNO's antineutrino spectrum is crucial. To do this, a sample of true ^{9}Li/^{8}He events was selected from the new dataset using
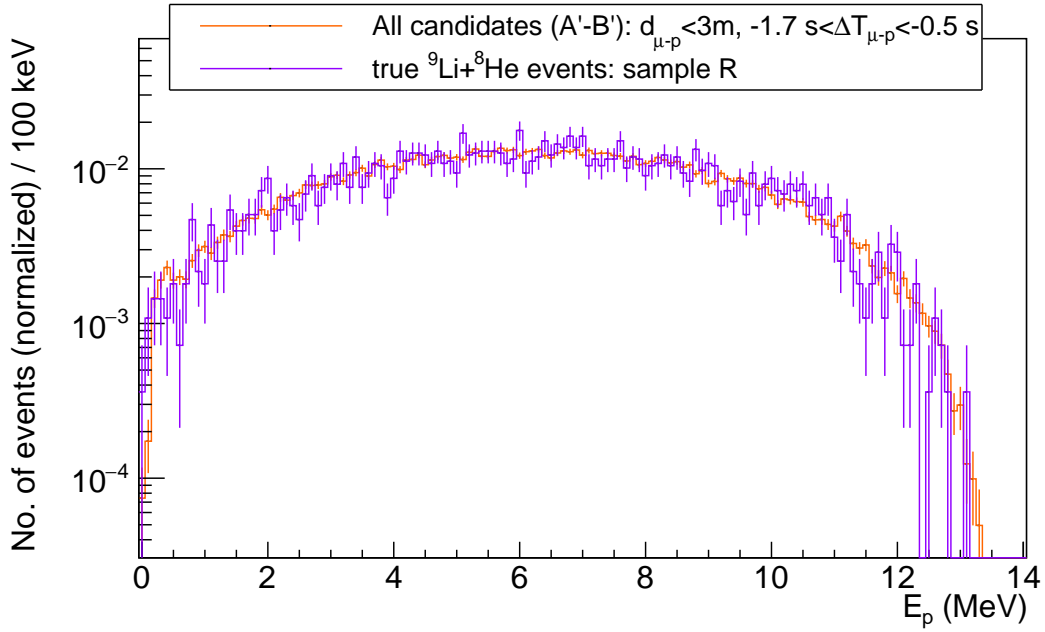
Figure 5.20 : *Comparison of* E_p *distributions of all the* $^9Li/^8He$ *candidates of the (A′-B′) sample (orange), against that of the true* $^9Li/^8He$ *events (purple) of sample R, following the inclusion of detector electronics and reconstruction effects.*

the selection criteria from the fourth column of the table 5.5. This sample is labelled as the sample R. The E_p spectrum of sample (A′-B′) was then normalized with respect to the total number of events, and compared with that of the sample R, as shown in the figure 5.20. The compatibility of the estimation was quantified using a χ^2-test, which yielded a χ^2/NDF of 1.22. It indicates a good statistical agreement among the two samples. Therefore, these results firmly establish the validity of performing a data-driven estimation of the ^{9}Li/^{8}He background using the TT muon track information, under realistic conditions.

Furthermore, this estimation of the ^{9}Li/^{8}He background can be used to calculate the bin-to-bin shape uncertainty on the ^{9}Li/^{8}He background. The relative Poisson uncertainty of the ith E_p bin for Y years of data acquisition using JUNO can be estimated using the sample (A′-B′) as

$$\frac{\sigma_{i,Y}}{N_{i,Y}} = \frac{\sqrt{N_{i,y}^{A'} + N_{i,y}^{B'}}}{\sqrt{\frac{Y}{y} \cdot \left(N_{i,y}^{A'} - N_{i,y}^{B'}\right)}}. \tag{5.4}$$

The terms $\sigma_{i,Y}$ and $N_{i,Y}$ represent the uncertainty and the number of entries expected in the ith E_p bin for Y years of data collection, respectively. The terms $N_{i,y}^{A'}$ and $N_{i,y}^{B'}$ represent the number of events in the ith E_p bin for samples A′ and B′, respectively, after y years of data collection which correspond to the available sample size (y = 0.89 years, or 325 days). The bin-to-bin shape uncertainty on the ^{9}Li/^{8}He background was determined for different durations of data acquisition, as shown in the figure 5.21. The top panel shows the bin-to-bin shape uncertainties for 100 keV E_p binning which was used for the comparison of samples so far. Notably, this estimation using the TT muon information can achieve a shape
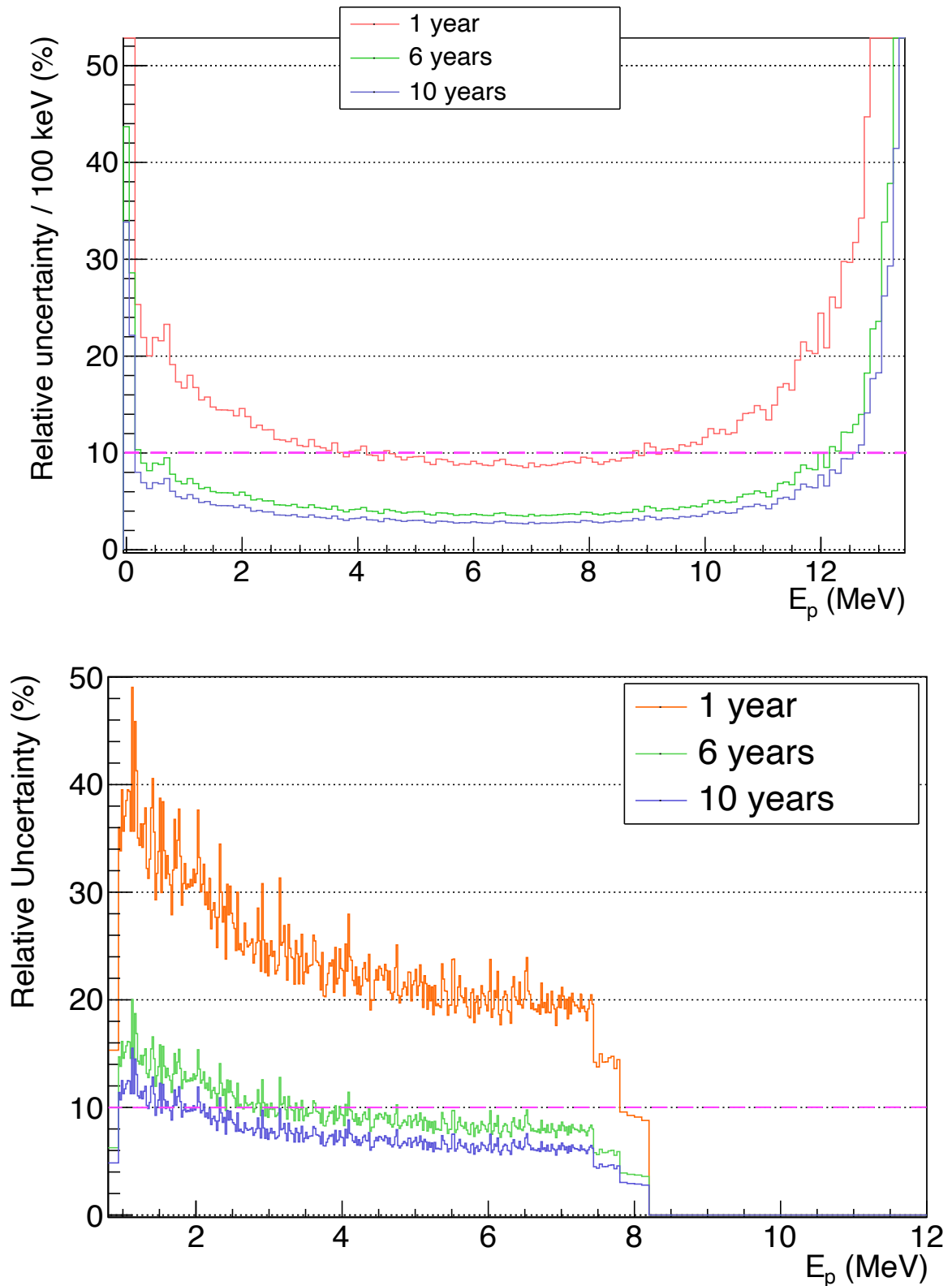
Figure 5.21 : *The distributions of bin-to-bin shape uncertainties of the $^9Li/^8He$ background for different durations of data acquisition using JUNO for 100 keV energy binning (top), and, the IBD prompt energy binning defined for the JUNO NMO analysis (bottom), assuming non-stop operation of the reactors at full power. The magenta dashed line represents JUNO's assumed shape uncertainty quoted in [125]. The definition of bins for the bottom figure is described in the table 5.6.*

Table 5.6 : *The definition of the bins of the histograms for the IBD prompt energy used in the JUNO NMO analysis. The total number of bins is 340 [125].*

Bin edges (MeV)	0.8 ...	0.94 ...	7.44 ...	7.8 ...	8.2 ...	12
Bin width (keV)	140	20	40	100	3800	
Number of bins	1	325	9	4	1	

uncertainty close to 10% or better within just one year, with the potential to reach 5% within six years. The bin-to-bin shape uncertainty on the ^{9}Li/^{8}He background was also determined using the IBD prompt energy binning defined for the JUNO NMO analysis, as given in the table 5.6. Wider bins are chosen to ensure that each contains at least 500 events, preventing any bias in the χ^2 calculation [125]. The bin-to-bin shape uncertainty thus calculated is shown in the bottom panel of the figure 5.21. It demonstrates that over six years of data collection, with the IBD prompt energy binning defined for the JUNO NMO analysis, the bin-to-bin shape uncertainty of the ^{9}Li/^{8}He background can be determined to within 10% for most of the energy range relevant to the NMO determination. Therefore, the results indicate that the proposed strategy for data-driven estimation of the ^{9}Li/^{8}He background using the Top Tracker has great potential to more accurately determine the bin-to-bin shape uncertainty of the ^{9}Li/^{8}He background than the value currently assumed by JUNO.

As demonstrated, coupled with the precise muon track reconstruction capabilities, JUNO possesses a great potential to perform an excellent data-driven estimation of ^{9}Li/^{8}He background. It also shows promise that by the time when JUNO has gathered sufficient statistics to reach 3σ significance on the NMO determination, the bin-to-bin shape uncertainty on the ^{9}Li/^{8}He background can be determined to better than the current uncertainty assumed by JUNO so far. Through continued data acquisition, this estimation can be further refined. Therefore, the impact of JUNO's NMO sensitivity can be re-evaluated using a detailed bin-to-bin shape uncertainty measurement as time progresses.

Résumé : Estimation du bruit de fond ^{9}Li/^{8}He avec le Top Tracker

La réalisation des objectifs de physique primaire de JUNO repose sur la mesure précise du spectre des antineutrinos provenant de ses réacteurs sources. Comme présenté dans le chapitre 2, différentes sources et différents processus génèrent des signatures dans le détecteur qui ressemblent aux coïncidences spatiales et temporelles promptes-retardées de l'IBD, constituant les bruits de fond du spectre antineutrino observé par JUNO. Ces sources sont les coïncidences accidentelles, les isotopes ^{9}Li/^{8}He, les neutrons rapides et ^{13}C$(\alpha, n)^{16}$O.

En plus de choix de design du détecteur pour garder ces bruits de fond sous controle, il s'avère nécessaire de les filtrer utilisant la topologie des événements. En demandant que les signaux prompte et retardé ressemblent à celui d'un IBD et en utilisant un volume fiduciaire, il est possible de réduire à des taux suffisamment bas les bruits de fond dus aux coïncidences accidentelles, les neutrons rapides et le ^{13}C.

Les muons atmosphériques peuvent induire une variété de radio-isotopes dans le LS de JUNO. Les isotopes qui subissent la désintégration de β^-n peuvent former eux-mêmes des signaux de fond corrélés à retardement qui imitent la signature de coïncidence à retardement de l'IBD dans le détecteur JUNO. Parmi eux, les isotopes ^{9}Li/^{8}He présentent les taux d'événements estimés les plus élevés dans le détecteur JUNO, comparables à ceux des IBD. Il est donc nécessaire de procéder à des coupures de veto muon atmosphérique pour supprimer les bruits de fond corrélés provenant des isotopes ^{9}Li/^{8}He. Une stratégie préliminaire proposée en 2016 consiste à rejeter les événements qui se trouvent à l'intérieur d'un volume cylindrique de 3 m de rayon défini autour des muons bien suivis dans le détecteur central (CD) de JUNO pendant une durée de 1,2 s depuis le passage du muon. Une stratégie affinée a été introduite en 2022, qui concerne la définition de plusieurs volumes de veto cylindriques (de rayons et de durées variables depuis le marquage du muon).

JUNO vise à déterminer l'ordre de masse des neutrinos (NMO) en mesurant précisément oscillation des antineutrinos de réacteur pour pouvoir distinguer le cas de l'ordre normal (NO) et celui de l'ordre inversé (IO). Une excellente résolution en énergie est cruciale pour une discrimination efficace de la signature NMO entre les deux scénarios possibles. Sur la base de simulations complètes et des dernières mises à jour sur la conception et la construction du détecteur, la résolution en énergie du détecteur a été évaluée comme étant de 2,95% à 1 MeV, surpassant l'exigence de résolution en énergie de base de JUNO pour la détermination des NMO.

Pour comparer les spectres d'antineutrinos observés par JUNO aux modèles hypothétiques NO et IO, une fonction $\mathscr{T}$ est définie sur la base de la méthode des moindres carrés. La fonction $\mathscr{T}$ est paramétrée en termes de paramètres d'oscillation des neutrinos, d'incertitudes statistiques, d'incertitudes sur la forme du bruit de fond, ainsi que de paramètres de nuisance. L'ajustement traite conjointement les mesures et les systématiques du détecteur JUNO et de l'observatoire antineutrino de Taishan (TAO) dans un ajustement simultané les données de TAO servent à contraindre le spectre des antineutrinos du réacteur, tandis que les données

de JUNO permettent de mesurer les oscillations des neutrinos.

Le meilleur ajustement de la fonction $\mathscr{T}$ au spectre antineutrino du réacteur mesuré dans l'hypothèse NO (IO) donne la valeur minimale correspondante de $\mathscr{T}$, donnée par $\min \mathscr{T}_{NO}(D)$ ($\min \mathscr{T}_{IO}(D)$). Par conséquent, le discriminant NMO est défini comme $\Delta \mathscr{T} = \min \mathscr{T}_{NO}(D) - \min \mathscr{T}_{IO}(D)$, où $\mathscr{T} > 0$ (<0) indique que les données suivent NO (IO), avec une sensibilité estimée de $n\sigma$ où $n = \sqrt{|\Delta \mathscr{T}|}$. Par conséquent, une sensibilité de la NMO de 3σ correspond à $\Delta \mathscr{T}$ = 9. JUNO suppose une incertitude de forme de 10% sur le bruit de fond ^{9}Li/^{8}He, ce qui réduit $\Delta \mathscr{T}$ de 0,1.

Les radio-isotopes atmosphériques induits par les muons constituent un défi pour les expériences sur l'oscillation des neutrinos des réacteurs. Pour y remédier, diverses expériences ont mesuré leurs rendements de production au cours des dernières décennies. En 1997, l'expérience NA54 au CERN a étudié les radio-isotopes induits par les muons en irradiant des échantillons de scintillateurs liquides (LS). Plus récemment, des expériences souterraines sur les neutrinos comme KamLAND, Borexino, Daya Bay et Double Chooz ont mesuré les ^{9}Li et ^{8}He en sélectionnant des paires candidates promptement retardées sur la base de critères d'énergie et de temps. Afin d'exclure les isotopes à courte durée de vie, les événements survenant peu après le muon ont été rejetés. RENO a encore affiné sa sélection en exigeant des corrélations spatiales et temporelles entre les événements prompts et retardés.

Les expériences Borexino, Daya Bay et Double Chooz ont mesuré les rendements en ^{9}Li/^{8}He en analysant les distributions du temps et de l'énergie visible dans les échantillons et en effectuant des ajustements spectraux, en tenant compte de diverses contributions. En revanche, KamLAND et RENO ont créé des échantillons appauvris en ^{9}Li/^{8}He en utilisant des fenêtres temporelles beaucoup plus longues que les demi-vies de ces isotopes (généralement plusieurs secondes après le muon). Étant donné que les véritables événements IBD sont indépendants des muons, leur présence dans les échantillons enrichis en ^{9}Li/^{8}He et appauvris en ^{9}Li/^{8}He devrait être similaire. Un spectre ^{9}Li/^{8}He de grande pureté est obtenu en soustrayant l'échantillon appauvri de l'échantillon renforcé et en ajustant le résultat pour déterminer les rendements isotopiques.

Les expériences LS souterraines évoquées ci-dessus ont utilisé le veto sur l'ensemble du volume sensible du détecteur pendant une certaine durée afin de rejeter le bruit de fond dû aux radio-isotopes atmosphériques induits par les muons. Cependant, JUNO utilise une sélection topologique du veto, où la corrélation temporelle et spatiale des signaux dus aux isotopes induits par les muons et aux traces des muons parents est prise en compte. Ici est présenté un modèle d'estimation du bruit de fond ^{9}Li/^{8}He utilisant par les données, dont la procédure est définie à l'aide de simulations. Lorsque JUNO commencera à acquérir des données, le modèle final pourra être défini sur la base de données réelles.

Le jeu de données de cette étude comprend les muons atmosphériques et les événements de spallation de muons qui leur sont associés. Les données sur les muons atmosphériques sont basées sur des simulations de Monte Carlo, fournissant des informations sur l'énergie, la position et le temps pour les dépôts d'énergie dans le LS par IBD et les produits de spallation. La propagation des photons est exclue en raison des limites de calcul, et seules les informations au niveau de ce qu'a été simulé sont utilisées, sans prendre en compte ni la réponse du détecteur ni la reconstruction de l'événement. L'étude utilise un échantillon

correspondant à environ 325 jours d'exposition, en se concentrant uniquement sur les traces de muons uniques (89,3% du flux total de muons). Dans l'étude du rendement de ^{9}Li/^{8}He, les véritables événements IBD constituent le principal contaminant qui empêche l'extraction d'un échantillon pur d'événements ^{9}Li/^{8}He. Le spectre d'énergie des événements IBD a été repondéré pour inclure les oscillations des antineutrinos. Ensuite, les spectres de l'énergie déposée par l'événement prompt dans le détecteur JUNO (E$_p$) des événements IBD et des événements ^{9}Li/^{8}He ont été renormalisés pour représenter les taux d'événements attendus.

Un ensemble initial de critères de sélection des candidats ^{9}Li/^{8}He est basé sur la sélection préliminaire IBD de 2016, inversée pour définir un volume cylindrique (rayon de 3 m, durée de 1,2 s) autour des traces de muons uniques dans le volume fiduciaire du CD. La coupure sur la variable E$_p$ est élargie à 0-15 MeV pour capturer le spectre d'énergie ^{9}Li/^{8}He complet. L'application de ces critères a permis d'obtenir un échantillon de contrôle d'une pureté de 96,6% et d'une efficacité de 90,3%. Pour quantifier le niveau de compatibilité de l'échantillon de contrôle en tant qu'estimation du véritable bruit de fond ^{9}Li/^{8}He dans le spectre antineutrino de JUNO, un échantillon d'événements ^{9}Li/^{8}He restant dans l'échantillon utilisé pour les analyses d'oscillation, appelé échantillon de référence, a été sélectionné. Les critères de sélection de l'échantillon de référence sont les mêmes que ceux de la stratégie de sélection de l'IBD 2016, à l'exception de l'enlargissement de la fenêtre d'énergie décrite préalablement. Une comparaison entre les spectres E$_p$ de l'échantillon de contrôle et de l'échantillon de référence à l'aide d'un test χ^2 (χ^2/NDF=0,99) montre une bonne compatibilité. Deux approches permettant d'améliorer encore l'estimation du bruit de fond en supprimant la contamination par les IBD sont examinées.

Les événements IBD ^{9}Li/^{8}He sont corrélés avec leurs muons parents, tandis que les événements IBD sont indépendants des muons. En resserrant la sélection de la séparation temporelle (ΔT$_{\mu-p}$) et spatiale ($d_{\mu-p}$), la contamination IBD peut être réduite. Par contre, cela supprime également les véritables événements ^{9}Li/^{8}He. L'optimisation de ces critères permet une estimation plus précise du véritable bruit de fond ^{9}Li/^{8}He, tout en équilibrant le compromis entre pureté et efficacité. Pour obtenir une pureté d'au moins 99%, nous avons déterminé que la meilleure combinaison est d'avoir ΔT$_{\mu-p}$<1,0 s et $d_{\mu-p}$<1,6 m, permettant d'atteindre une efficacité de 80,1%. Un test de χ^2 montre un bon accord (χ^2/NDF=0,88) entre ce nouvel échantillon (nommé échantillon de haute pureté) et celui de référence.

La seconde approche est similaire à celles utilisées par les expériences KamLAND et RENO pour estimer leurs rendements en ^{9}Li/^{8}He. Deux régions (A et B) sont définies. La région A, englobe un volume spatio-temporel (0,001 s < ΔT$_{\mu-p}$ < 1,2 s et $d_{\mu-p}$ < 3 m) après le passage d'un muon. Cette region contient une majorité d'événements ^{9}Li/^{8}He. La région B est définie avec le même volume spatial mais 0,5 s avant le muon. Cette region sert d'échantillon pour mesurer le bruit de fond à la mesure de ^{9}Li/^{8}He dans la région A. En soustrayant l'échantillon B de l'échantillon A, on obtient l'échantillon (A-B), qui présente une "pureté" de 99,8% ^{9}Li/^{8}He et une "efficacité" de 81%. Une comparaison des spectres E$_p$ de l'échantillon de référence et de l'échantillon (A-B) donne un χ^2/NDF de 0,87, ce que, à nouveau, correspond à un bon accord entre ces échantillons. Il est utile de noter que la contamination IBD de l'échantillon (A-B) est inférieure à celle de l'échantillon de haute pureté, tout en maintenant une efficacité similaire.

Comme indiqué précédemment, l'ensemble de données utilisé pour les analyses susmen-

tionnées ne tient pas compte des effets de reconstruction du détecteur. En pratique, le succès des techniques d'estimation basées sur les données mentionnées ci-dessus dépend des capacités de reconstruction du détecteur. Une précision et/ou une efficacité moindre de la reconstruction des muons se traduit par des volumes de veto mal définis, ce qui conduit à une estimation peu fiable du véritable bruit de fond ^{9}Li/^{8}He. Toutefois, l'efficacité et la précision excellentes du TT en matière de suivi des muons peuvent être utilisées pour obtenir un sous-échantillon de traces de muons très bien définies. Le TT offre donc une excellente occasion d'effectuer une estimation de haute précision des bruits de fond ^{9}Li/^{8}He à partir de données, en utilisant les muons bien suivis qui le traversent.

Afin d'estimer l'impact de la reconstruction de la trajectoire des muons ainsi que des capacités de reconstruction de l'énergie prompte et retardée et de la position des événements de ^{9}Li/^{8}He, les événements d'intérêt de l'ensemble de données susmentionné ont été re-simulés afin d'inclure les effets de la simulation électronique et reconstruits à l'aide du logiciel de reconstruction officiel de JUNO. Comme l'étude suivante vise à explorer le potentiel du TT pour réaliser une estimation pilotée par les données du bruit de fond du ^{9}Li/^{8}He dans le spectre antineutrino vu par JUNO, seuls les muons qui traversent les trois couches du TT ont été re-simulés et reconstruits. Les informations relatives à la position, à l'énergie, à la quantité de mouvement et au temps de l'événement réel provenant de l'ensemble de données originaux ont été utilisées comme données d'entrée pour la simulation. Un nouvel ensemble de données a ensuite été formé en tenant compte des résultats de la simulation et de la reconstruction. Étant donné qu'un tiers seulement des muons atmosphériques passant par le CD traversent également le TT, la taille de l'échantillon candidat ^{9}Li/^{8}He sélectionné sera réduite d'environ un tiers. En outre, la réponse du détecteur et les effets de la reconstruction réduiront encore la taille de l'échantillon. C'est pourquoi l'étude suivante a été démontrée en utilisant uniquement l'approche (A-B).

La région renforcée par ^{9}Li/^{8}He est définie avec $\Delta T_{\mu-p}$ <1,2 s et $d_{\mu-p}$ <3 m, ce qui donne l'échantillon A$'$. Un deuxième échantillon, B$'$, a été sélectionné dans le même volume physique mais dans une fenêtre temporelle antérieure (-1,7 s< $\Delta T_{\mu-p}$ <-0,5 s). La soustraction de B$'$ de A$'$ a produit un nouvel échantillon, (A$'$-B$'$), d'une pureté de 99,9% et d'une efficacité de 21,9%. Pour quantifier la compatibilité de l'échantillon en tant qu'estimation du véritable bruit de fond ^{9}Li/^{8}He, un échantillon d'événements ^{9}Li/^{8}He a été sélectionné dans le nouvel ensemble de données (étiqueté échantillon R) en utilisant les mêmes critères que ceux utilisés pour l'échantillon de référence présenté plus haut. Une comparaison entre les spectres E_p de l'échantillon (A$'$-B$'$) et de l'échantillon R à l'aide d'un test χ^2 (χ^2/NDF=1,22) montre toujours une bonne compatibilité.

Cette estimation du bruit de fond ^{9}Li/^{8}He peut être utilisée pour calculer l'incertitude de forme dans le spectre de ^{9}Li/^{8}He après 1, 6 et 10 années de collecte de données. En utilisant un binning de E_p de 100 keV, il est montré que l'approche basée sur les données peut atteindre une précision de 5% en six ans. En appliquant le binning de E_p utilisé lors de la dernière étude de sensitivité à la NMO de JUNO, l'incertitude de forme bin-à-bin du bruit de fond ^{9}Li/^{8}He peut être déterminée avec une précision de 10% pour la majeure partie du domaine d'énergie pertinent pour cet étude au bout de six ans. Ces résultats suggèrent que la stratégie proposée, utilisant le Top Tracker, répond aux exigences de précision de JUNO sur le bruit de fond ^{9}Li/^{8}He pour la mesure de la NMO.

Summary and Conclusions

The Jiangmen Underground Neutrino Observatory (JUNO) is an upcoming underground Liquid Scintillator (LS) detector which looks forward to resolve the Neutrino Mass Ordering (NMO) with a significance of 3σ within approximately seven years of data collection. Additionally, JUNO aims to surpass the current precision of the oscillation parameters Δm^2_{31}, Δm^2_{21}, and $\sin^2 \theta_{12}$, achieving sub-percent accuracies. The success of the experiment will be driven by its cutting-edge design, including a 20 kton LS neutrino target, an outstanding energy resolution of 2.95% at 1 MeV, less than 1% energy non-linearity, and over 75% photocathode coverage. Via precise measurement of reactor antineutrino oscillations at a baseline of 53 km, JUNO not only targets to determine the NMO, but also deploy a broad physics program to explore other fields of physics, such as astrophysics, geophysics, cosmology, among others.

The Water Cherenkov detector and the Top Tracker (TT) form the muon veto system of the JUNO detector. The TT is a 3-layer grid of plastic scintillator strips designed to precisely track atmospheric muons and aids the mitigation of consequent backgrounds. Scintillation light produced by muons passing through the TT scintillator strips is collected by wavelength-shifting fibres and transmitted to Multi-Anode Photomultiplier Tubes (MA-PMT). The resulting signal is then digitized by Front-End electronics Boards (FEB), with the aid of an embedded application-specific integrated circuit known as the Multi-Anode Read-Out Circuit (MAROC3). The FEBs transfer the digitized information to the Read-Out Boards (ROB) that aid MA-PMT interfacing, MAROC3 control, high voltage regulation and TT calibration. One of the key focuses of this doctoral research was on the validation of the performance of the FEBs. The FEBs, facilitated by the MAROC3, are responsible for setting the MA-PMT trigger, event digitization, and, transmission of the event information to the next stages of the TT electronics chain. Extensive evaluations of the FEBs were conducted, focusing on aspects such as trigger threshold, gain compensation, electronics background, charge calibration, and electronics saturation. The results demonstrated excellent homogeneity and consistency across all the FEBs and FEB channels, with only a few exceptions. This is important to ensure a homogeneous electronics response across the entire TT detector. Based on these performance metrics, the FEBs for installation in the TT, along with spare units, were identified. Additionally, the Top Tracker prototype, a demonstrator and test environment re-purposed from suboptimal strips of the de-commissioned OPERA Target Tracker, was used to observe the muon flux in Strasbourg under realistic conditions. This data helped estimate the performance of the optical fibres embedded in the scintillator strips. The estimated optical signal attenuation length was found to be statistically consistent with the original OPERA measurements, indicating that the performance of the fibres have not deteriorated significantly since the OPERA detector construction about 20 years ago.

In the TT electronics chain, the Concentrator Board (CB) is responsible for aggregating 16 data streams, selecting valid x-y coincidences within its respective TT wall, and performing event timestamping. To minimize detector dead time, the CB issues a RESET command to the read-out boards (ROB) when no valid x-y coincidences are detected, preparing it to accept new signals. Injecting charges into two CBs using a charge injection system over three days, revealed a CB timestamping stability of approximately 0.28 ns. The x-y coincidence tagging

173

efficiency of a CB was also assessed by injecting charges into two FEB/ROBs to emulate x and y hits from the CB's perspective. The tests showed that the CB is 100% efficient in event validation as expected when the time difference between x and y hits is under 96 ns, with a linear decline in efficiency by 6.4% per ns from 96 ns to 112 ns. This observation attributed to the CB's clock period of 16 ns defines the x-y coincidence time window. The TT prototype was also used to validate the CB performance using atmospheric muons, which revealed a CB timestamping resolution of 1.67 ns. The results from the aforementioned studies indicate that the CB's timestamping precision and stability are sufficient for its role in the JUNO TT. Moreover, the standard deviation of the time difference distribution between the x and y hits of x-y coincidences tagged by the CB was found to be approximately 11.3 ns. By removing accidental coincidences, followed by corrections for the propagation time along the optical fibres as well as MAROC3 time-walk, the standard deviation narrows down to 5.9 ns (reduction of 48%). It ensures that the up-going and down-going muons in the perspective of the TT can be distinguished to better than 3 times the CB timestamping resolution.

JUNO detects electron antineutrinos via IBD reactions, where an antineutrino interacts with a proton in the JUNO LS. However, atmospheric muons that reach the LS can induce spallation of carbon atoms, producing radioisotopes like ^{9}Li and ^{8}He. These isotopes decay in a way that mimics the IBD signal, creating the most problematic background for JUNO's antineutrino spectrum measurements. The rate of these events is comparable to that of the IBDs. To address this, JUNO uses a veto strategy within a cylindrical volume around well-tracked muons. This volume can be considered a ^{9}Li/^{8}He-enhanced volume. Two methods for estimating this background by selecting ^{9}Li/^{8}He candidate events within the veto volume were demonstrated using a simulated dataset. Both methods produced almost identical energy spectra that closely matched the true ^{9}Li+^{8}He energy spectrum. To evaluate the TT's precision muon tracking capabilities under realistic conditions, the dataset was re-simulated to incorporate detailed TT information for the muons, along with electronics and reconstruction effects associated with the CD and the TT. The estimation was repeated using the new dataset, and the results confirmed that these methods could provide a reliable estimate of the ^{9}Li/^{8}He background. The bin-to-bin shape uncertainty of the ^{9}Li/^{8}He background was calculated. It was found that, using the Top Tracker, this shape uncertainty can be determined to better than the JUNO assumed value of 10% across most of the energy range of the prompt signal.

Through detailed testing, calibration, and validation of the Top Tracker's electronics, the work presented in this thesis ensures the optimal performance of the Top Tracker. Through this study, it has been demonstrated that the Top Tracker's outstanding muon track reconstruction capabilities can be used to generate a reliable data-driven estimate of the ^{9}Li/^{8}He background for JUNO's NMO analysis. This method can achieve a shape uncertainty better than the JUNO assumed value of 10% with six years of data, enhancing JUNO's sensitivity to NMO. Consequently, these efforts not only support JUNO's primary mission but also set the stage for future discoveries that could significantly advance our understanding of particle physics and beyond.

Bibliography

1. Fermi, E. Trends to a Theory of beta Radiation. *Il Nuovo Cimento* **11,** 535 (1934).

2. Bethe, H. & Peierls, R. The neutrino. *Nature* **133,** 689–690 (1934).

3. Cowan Jr, C. *et al.* Detection of the free neutrino: a confirmation. *Science* **124,** 103–104 (1956).

4. Davis, R. A review of the Homestake solar neutrino experiment. *Progress in Particle and Nuclear Physics* **32,** 13–32 (1994).

5. Koshiba, M. *et al.* Kamioka nucleon decay experiment. *Il Nuovo Cimento* **9,** 141–158 (1986).

6. Maki, Z., Nakagawa, M. & Sakata, S. Remarks on the unified model of elementary particles. *Progress of Theoretical Physics* **28,** 870–880 (1962).

7. Pontecorvo, B. Neutrino Experiments and the Question of Leptonic-Charge Conservation. *Old and New Problems in Elementary Particles,* 251–261 (1968).

8. Fukuda, S. *et al.* The Super-Kamiokande detector. *Nuclear Instruments and Methods in Physics Research A: Accelerators, Spectrometers, Detectors and Associated Equipment* **501,** 418–462 (2003).

9. Fukuda, Y. *et al.* Evidence for Oscillation of Atmospheric Neutrinos. *Physical Review Letters* **81,** 1562 (1998).

10. Boger, J. *et al.* The Sudbury Neutrino Observatory. *Nuclear Instruments and Methods in Physics Research A: Accelerators, Spectrometers, Detectors and Associated Equipment* **449,** 172–207 (2000).

11. Ahmad, Q. *et al.* Direct evidence for neutrino flavor transformation from neutral-current interactions in the Sudbury Neutrino Observatory. *Physical Review Letters* **89,** 011301 (2002).

12. An, F. *et al.* Neutrino Physics with JUNO. *Journal of Physics G: Nuclear and Particle Physics* **43,** 030401 (2016).

13. Abusleme, A. *et al.* JUNO physics and detector. *Progress in Particle and Nuclear Physics* **123,** 103927 (2022).

14. Abusleme, A. *et al.* The Design and Technology Development of the JUNO Central Detector. *arXiv:2311.17314* (2023).

15. Lu, H. *et al.* The JUNO water Cherenkov detector system. *Nuclear Instruments and Methods in Physics Research A: Accelerators, Spectrometers, Detectors and Associated Equipment* **1056,** 168623 (2023).

16. Ahmed, R. *et al.* The JUNO experiment Top Tracker. *Nuclear Instruments and Methods in Physics Research A: Accelerators, Spectrometers, Detectors and Associated Equipment* **1057,** 168680 (2023).

17. Adam, T. *et al.* The OPERA experiment target tracker. *Nuclear Instruments and Methods in Physics Research A: Accelerators, Spectrometers, Detectors and Associated Equipment* **577,** 523–539 (2007).

18. Li, K. *et al.* GDML based geometry management system for offline software in JUNO. *Nuclear Instruments and Methods in Physics Research A: Accelerators, Spectrometers, Detectors and Associated Equipment* **908,** 43–48 (2018).

19. Lubej, M. Standard Model. last accessed on 2024-08-28. https://www.physik.uzh.ch/groups/serra/StandardModel.html.

20. Fermi, E. Sulla quantizzazione del gas perfetto monoatomico. *Rendiconti Lincei* **145** (1926).

21. Dirac, P. A. M. On the theory of quantum mechanics. *Proceedings of the Royal Society of London. Series A, Containing Papers of a Mathematical and Physical Character* **112,** 661–677 (1926).

22. Pauli, W. Pauli exclusion principle. *Naturwiss* **12,** 741 (1924).

23. Bose, S. Plancks gesetz und lichtquantenhypothese. *Zeitschrift für Physik* **26,** 178–181 (1924).

24. Einstein, A. *Quantum Theory of a Monoatomic Ideal Gas A translation of Quantentheorie des einatomigen idealen Gases (Einstein, 1924)* **1** (Sitzungsberichte Der Preuss. Akad. Der Wissenschaften, 1925).

25. Workman, R. *et al.* Review of particle physics. *Progress of Theoretical and Experimental Physics* **2022,** 083C01 (2022).

26. Ahmad, Q. R. *et al.* Direct evidence for neutrino flavor transformation from neutral-current interactions in the Sudbury Neutrino Observatory. *Physical Review Letters* **89,** 011301 (2002).

27. Schwinger, J. The theory of quantized fields. I. *Physical Review* **82,** 914 (1951).

28. Lüders, G. On the equivalence of invariance under time reversal and under particle-antiparticle conjugation for relativistic field theories. *Danske Matematisk-Fysiske Meddelelser* **28,** 1–17 (1954).

29. Bohr, N. *et al.* Niels Bohr and the Development of Physics. Essays Dedicated to Niels Bohr on the Occasion of His Seventieth Birthday. (1955).

30. Glashow, S. The renormalizability of vector meson interactions. *Nuclear Physics* **10,** 107–117 (1959).

31. Salam, A. & Ward, J. C. Weak and electromagnetic interactions. *Il Nuovo Cimento* **11,** 568–577 (1959).

32. Weinberg, S. A model of leptons. *Physical Review Letters* **19,** 1264 (1967).

33. Englert, F. & Brout, R. Broken symmetry and the mass of gauge vector mesons. *Physical Review Letters* **13,** 321 (1964).

34. Higgs, P. Broken symmetries and the masses of gauge bosons. *Physical Review Letters* **13,** 508 (1964).

35. Guralnik, G. S., Hagen, C. R. & Kibble, T. W. Global conservation laws and massless particles. *Physical Review Letters* **13,** 585 (1964).

36. Pontecorvo, B. Inverse–process. *Chalk River Laboratory Report PD-205* (1946).

37. Goldhaber, M., Grodzins, L. & Sunyar, A. W. Helicity of neutrinos. *Physical review* **109,** 1015 (1958).

38. Antusch, S., Drees, M., Kersten, J., Lindner, M. & Ratz, M. Neutrino mass operator renormalization revisited. *Physics Letters B* **519,** 238–242 (2001).

39. Majorana, E. Teoria simmetrica dell'elettrone e del positrone. *Il Nuovo Cimento* **14,** 171–184 (1937).

40. Soleti, S. Are neutrinos their own antiparticles? last accessed on 2024-08-28. https://next-experiment.org/experiment/neutrinoless-double-beta-decay/.

41. Abgrall, N. *et al.* LEGEND-1000 preconceptual design report. *arXiv:2107.11462* (2021).

42. Abe, S. *et al.* Search for the Majorana nature of neutrinos in the inverted mass ordering region with KamLAND-Zen. *Physical Review Letters* **130,** 051801 (2023).

43. Albanese, V. *et al.* The SNO+ experiment. *Journal of Instrumentation* **16,** P08059 (2021).

44. Anton, G. *et al.* Search for neutrinoless double-β decay with the complete EXO-200 dataset. *Physical Review Letters* **123,** 161802 (2019).

45. Canonica, L. *et al.* Search for Majorana neutrinos exploiting millikelvin cryogenics with CUORE. *Nature* **604,** 53–58 (2022).

46. Lee, M. AMoRE: A search for neutrinoless double-beta decay of 100Mo using low-temperature molybdenum-containing crystal detectors. *Journal of Instrumentation* **15,** C08010 (2020).

47. Arnold, R. *et al.* Results of the search for neutrinoless double-β decay in Mo 100 with the NEMO-3 experiment. *Physical Review D* **92,** 072011 (2015).

48. Bonn, J. *et al.* Newest results from the Mainz neutrino-mass experiment. *Physics of Atomic Nuclei* **63,** 969–974 (2000).

49. Lobashev, V. *et al.* Direct search for neutrino mass and anomaly in the tritium beta-spectrum: Status of "Troitsk neutrino mass" experiment. *Nuclear Physics B-Proceedings Supplements* **91,** 280–286 (2001).

50. Aker, M. *et al.* Direct neutrino-mass measurement based on 259 days of KATRIN data. *arXiv:2406.13516* (2024).

51. Aker, M. *et al.* KATRIN: status and prospects for the neutrino mass and beyond. *Journal of Physics G: Nuclear and Particle Physics* **49,** 100501 (2022).

52. Bates, C. *et al.* Reproducibility and calibration of MMC-based high-resolution gamma detectors. *Applied Physics Letters* **109** (2016).

53. Alpert, B. *et al.* HOLMES: The electron capture decay of ^{163}Ho to measure the electron neutrino mass with sub-eV sensitivity. *The European Physical Journal C* **75,** 1–11 (2015).

54. Croce, M. *et al.* Development of Holmium-163 electron-capture spectroscopy with transition-edge sensors. *Journal of Low Temperature Physics* **184,** 958–968 (2016).

55. Segal, T. Mass Measurements of Neon Isotopes at THe-Trap. last accessed on 2024-08-28. https://archiv.ub.uni-heidelberg.de/volltextserver/27321/1/PhD%20Thesis%20Tom%20Segal.pdf.

56. Aghanim, N. *et al.* Planck 2018 results-VI. Cosmological parameters. *Astronomy & Astrophysics* **641,** A6 (2020).

57. Xu, H. *et al.* DESI Legacy Imaging Surveys Data Release 9: Cosmological constraints from galaxy clustering and weak lensing using the minimal bias model. *Science China Physics, Mechanics & Astronomy* **66** (2023).

58. Noriega, H. E. & Aviles, A. Unveiling Neutrino Masses: Insights from Robust (e)BOSS Data Analysis and Prospects for DESI and Beyond. *arXiv:2407.06117* (2024).

59. Gell-Mann, M. & Pais, A. Behavior of neutral particles under charge conjugation. *Physical Review* **97,** 1387 (1955).

60. Pontecorvo, B. Mesonium and antimesonium. *Zhurnal Éksperimental'noi i Teoreticheskoi Fiziki* **33** (1957).

61. Thomson, M. Modern particle physics. *Cambridge University Press* (2013).

62. Guenther, D., Demarque, P, Kim, Y.-C. & Pinsonneault, M. Standard solar model. *Astrophysical Journal, Part 1* **387,** 372–393 (1992).

63. Bahcall, J. N. & Davis Jr, R. Solar neutrinos: a scientific puzzle. *Science* **191,** 264–267 (1976).

64. Abdurashitov, J. *et al.* Results from SAGE (The Russian-American gallium solar neutrino experiment). *Physics Letters B* **328,** 234–248 (1994).

65. Anselmann, P. *et al.* Solar neutrinos observed by GALLEX at Gran Sasso. *Physics Letters B* **285,** 376–389 (1992).

66. Aharmim, B. *et al.* Determination of the ν_e and total ^{8}B solar neutrino fluxes using the Sudbury Neutrino Observatory Phase I data set. *Physical Review C* **75,** 045502 (2007).

67. Fukuda, S. *et al.* Solar ^{8}B and hep Neutrino Measurements from 1258 Days of Super-Kamiokande Data. *Physical Review Letters* **86,** 5651 (2001).

68. Bionta, R. M. *et al.* Search for Proton Decay into $e^+\pi^0$. *Physical Review Letters* **51,** 27–30 (1983).

69. Hirata, K. *et al.* Experimental study of the atmospheric neutrino flux. *Physics Letters B* **205,** 416–420 (1988).

70. Casper, D. *et al.* Measurement of atmospheric neutrino composition with the IMB-3 detector. *Physical Review Letters* **66,** 2561 (1991).

71. Kajita, T. Nobel Lecture: Discovery of atmospheric neutrino oscillations. *Reviews of Modern Physics* **88,** 030501 (2016).

72. Esteban, I. *et al.* The fate of hints: updated global analysis of three-flavor neutrino oscillations. *Journal of High Energy Physics* **2020,** 1–22 (2020).

73. Wolfenstein, L. Neutrino oscillations in matter. *Physical Review D* **17** (1978).

74. Wolfenstein, L. Neutrino oscillations and stellar collapse. *Physical Review D* **20,** 2634 (1979).

75. Borexino Collaboration. Comprehensive measurement of pp-chain solar neutrinos. *Nature* **562,** 505–510 (2018).

76. Smirnov, A. The MSW effect and solar neutrinos. *arxiv:0305106* (2003).

77. Abe, S. *et al.* Precision measurement of neutrino oscillation parameters with Kam-LAND. *Physical Review Letters* **100,** 221803 (2008).

78. Bergström, J. *et al.* Updated determination of the solar neutrino fluxes from solar neutrino data. *Journal of High Energy Physics* **2016,** 1–19 (2016).

79. Wester, T. *et al.* Atmospheric neutrino oscillation analysis with neutron tagging and an expanded fiducial volume in Super-Kamiokande I–V. *Physical Review D* **109,** 072014 (2024).

80. Ahn, M. *et al.* Measurement of neutrino oscillation by the K2K experiment. *Physical Review D* **74,** 072003 (2006).

81. Adamson, P. *et al.* Measurement of neutrino oscillations with the MINOS detectors in the NuMI beam. *Physical Review Letters* **101,** 131802 (2008).

82. Abe, K. *et al.* T2K measurements of muon neutrino and antineutrino disappearance using 3.13×10^{21} protons on target. *Physical Review D* **103,** L011101 (2021).

83. Acero, M. *et al.* Improved measurement of neutrino oscillation parameters by the NOvA experiment. *Physical Review D* **106,** 032004 (2022).

84. Adrián-Martínez, S. *et al.* Measurement of atmospheric neutrino oscillations with the ANTARES neutrino telescope. *Physics Letters B* **714,** 224–230 (2012).

85. Aartsen, M. *et al.* Measurement of atmospheric neutrino oscillations with IceCube. *Physical Review Letters* **111,** 081801 (2013).

86. Adey, D. *et al.* Measurement of the electron antineutrino oscillation with 1958 days of operation at Daya Bay. *Physical Review Letters* **121,** 241805 (2018).

87. Abe, K. *et al.* Indication of electron neutrino appearance from an accelerator-produced off-axis muon neutrino beam. *Physical Review Letters* **107,** 041801 (2011).

88. Akiri, T. *et al.* The Double Chooz experiment. *Nuclear Physics B-Proceedings Supplements* **215,** 69–71 (2011).

89. Cao, J. & Luk, K.-B. An overview of the Daya Bay reactor neutrino experiment. *Nuclear Physics B* **908,** 62–73 (2016).

90. Jeon, E.-J., Collaboration, R., *et al.* Status of RENO Experiment. *Nuclear Physics B-Proceedings Supplements* **217,** 137–139 (2011).

91. Abe, Y. *et al.* Reactor ν_e disappearance in the Double Chooz experiment. *Physical Review D* **86,** 052008 (2012).

92. Ahn, J. *et al.* Observation of reactor electron antineutrinos disappearance in the RENO experiment. *Physical Review Letters* **108,** 191802 (2012).

93. An, F. *et al.* Observation of electron-antineutrino disappearance at Daya Bay. *Physical Review Letters* **108,** 171803 (2012).

94. Acero, M. *et al.* Improved measurement of neutrino oscillation parameters by the NOvA experiment. *Physical Review D* **106,** 032004 (2022).

95. Abe, K. *et al.* Improved constraints on neutrino mixing from the T2K experiment with $3.13 \times 10\ 21$ protons on target. *Physical Review D* **103** (2021).

96. Kudenko, Y. Neutrino Oscillations: Status and Prospects. *Physics of Particles and Nuclei* **53,** 820–824 (2022).

97. Abi, B. *et al.* Long-baseline neutrino oscillation physics potential of the DUNE experiment. *The European Physical Journal C* **80,** 1–34 (2020).

98. Alekou, A. *et al.* The European Spallation Source neutrino super-beam conceptual design report. *The European Physical Journal Special Topics* **231,** 3779–3955 (2022).

99. Abe, K. *et al.* Hyper-Kamiokande Design Report. *arXiv:1805.04163* (2018).

100. Alekou, A. *et al.* The ESSnuSB design study: overview and future prospects. *Universe* **9,** 347 (2023).

101. Majhi, R. *et al.* Constraining C P T violation with Hyper-Kamiokande and ESSnuSB. *Physical Review D* **104,** 055002 (2021).

102. Gómez-Cadenas, J. J. *et al.* The search for neutrinoless double-beta decay. *La Rivista del Nuovo Cimento* **46,** 619–692 (2023).

103. Kismalac. Neutrino mass hierarchy. last accessed on 2024-08-28. https://en.wikipedia.org/wiki/File:NeutrinoHierarchy.svg.

104. Abi, B. *et al.* Long-baseline neutrino oscillation physics potential of the DUNE experiment. *The European Physical Journal C* **80,** 1–34 (2020).

105. Raut, S. Matter effects at the T2HK and T2HKK experiments. *Physical Review D* **96,** 075029 (2017).

106. Aiello, S. *et al.* Determining the neutrino mass ordering and oscillation parameters with KM3NeT/ORCA. *The European Physical Journal C* **82,** 26 (2022).

107. Choubey, S., Ghosh, M. & Raikwal, D. Neutrino mass ordering: Circumventing the challenges using synergy between T2HK and JUNO. *Physical Review D* **106,** 115013 (2022).

108. Ballett, P., King, S. F., Pascoli, S., Prouse, N. W. & Wang, T. Sensitivities and synergies of DUNE and T2HK. *Physical Review D* **96,** 033003 (2017).

109. Aartsen, M. *et al.* Combined sensitivity to the neutrino mass ordering with JUNO, the IceCube Upgrade, and PINGU. *Physical Review D* **101,** 032006 (2020).

110. Aiello, S. *et al.* Combined sensitivity of JUNO and KM3NeT/ORCA to the neutrino mass ordering. *Journal of high energy physics* **2022,** 1–31 (2022).

111. Adam, T. *et al.* JUNO conceptual design report. *arXiv:1508.07166* (2015).

112. Abusleme, A. *et al.* Sub-percent precision measurement of neutrino oscillation parameters with JUNO. *Chinese Physics C* **46,** 123001 (2022).

113. Zyla, P. *et al.* Review of particle physics. *Progress of Theoretical and Experimental Physics* **2020,** 1–2093 (2020).

114. Abe, K. *et al.* Solar neutrino measurements in Super-Kamiokande-IV. *Physical Review D* **94,** 052010 (2016).

115. Abusleme, A. *et al.* Feasibility and physics potential of detecting ^{8}B solar neutrinos at JUNO. *Chinese Physics C* **45,** 023004 (2021).

116. Zhao, J. *et al.* Model-independent Approach of the JUNO ^{8}B Solar Neutrino Program. *The Astrophysical Journal* **965,** 122 (2024).

117. Abusleme, A. *et al.* JUNO sensitivity to 7Be, pep, and CNO solar neutrinos. *Journal of Cosmology and Astroparticle Physics* **2023,** 022 (2023).

118. Al Kharusi, S. *et al.* SNEWS 2.0: a next-generation supernova early warning system for multi-messenger astronomy. *New Journal of Physics* **23,** 031201 (2021).

119. Han, R. *et al.* Potential of geo-neutrino measurements at JUNO. *Chinese Physics C* **40,** 033003 (2016).

120. Gando, A. *et al.* Partial radiogenic heat model for Earth revealed by geoneutrino measurements. *Nature Geoscience* **4** (2011).

121. Agostini, M. *et al.* Comprehensive geoneutrino analysis with Borexino. *Physical Review D* **101,** 012009 (2020).

122. Strati, V. *et al.* Expected geoneutrino signal at JUNO. *Progress in Earth and Planetary Science* **2,** 1–7 (2015).

123. Huang, Y., Chubakov, V., Mantovani, F., Rudnick, R. L. & McDonough, W. F. A reference Earth model for the heat-producing elements and associated geoneutrino flux. *Geochemistry, Geophysics, Geosystems* **14,** 2003–2029 (2013).

124. Abusleme, A. *et al.* TAO conceptual design report: a precision measurement of the reactor antineutrino spectrum with sub-percent energy resolution. *arXiv:2005.08745* (2020).

125. Abusleme, A. *et al.* Potential to Identify the Neutrino Mass Ordering with Reactor Antineutrinos in JUNO. *arXiv:2405.18008* (2024).

126. Vogel, P., Wen, L. & Zhang, C. Neutrino oscillation studies with reactors. *Nature Communications* **6,** 6935 (2015).

127. Vogel, P. & Beacom, J. The angular distribution of the reaction $\nu_e + p \rightarrow e + n$. *Physical Review D* **60,** 053003 (1999).

128. Huber, P. & Jaffke, P. Neutron capture and the antineutrino yield from nuclear reactors. *Physical Review Letters* **116,** 122503 (2016).

129. Dye, S. & Barna, A. Global antineutrino modeling for a web application. *arXiv:1510.05633* (2015).

130. Abusleme, A. *et al.* Radioactivity control strategy for the JUNO detector. *Journal of High Energy Physics* **2021,** 1–39 (2021).

131. Zhang, P. Progress of Veto Detector of JUNO. *Journal of Physics: Conference Series* **1468,** 012188 (2020).

132. Wonsak, B. *et al.* A container-based facility for testing 20'000 20-inch PMTs for JUNO. *Journal of Instrumentation* **16,** T08001 (2021).

133. Cao, C. *et al.* Mass production and characterization of 3-inch PMTs for the JUNO experiment. *Nuclear Instruments and Methods in Physics Research Section A: Accelerators, Spectrometers, Detectors and Associated Equipment* **1005,** 165347 (2021).

134. Abusleme, A. *et al.* Mass testing and characterization of 20-inch PMTs for JUNO. *The European Physical Journal C* **82,** 1–42 (2022).

135. He, M. Double calorimetry system in JUNO. *Radiation Detection Technology and Methods* **1,** 1–3 (2017).

136. Zhang, G. *et al.* The study of active geomagnetic shielding coils system for JUNO. *Journal of Instrumentation* **16,** T10004 (2021).

137. Zhang, Y. *et al.* A complete optical model for liquid-scintillator detectors. *Nuclear Instruments and Methods in Physics Research A: Accelerators, Spectrometers, Detectors and Associated Equipment* **967,** 163860 (2020).

138. Abusleme, A. *et al.* Optimization of the JUNO liquid scintillator composition using a Daya Bay antineutrino detector. *Nuclear Instruments and Methods in Physics Research A: Accelerators, Spectrometers, Detectors and Associated Equipment* **988,** 164823 (2021).

139. Abusleme, A. *et al.* The design and sensitivity of JUNO's scintillator radiopurity pre-detector OSIRIS. *The European Physical Journal C* **81,** 973 (2021).

140. Abusleme, A. *et al.* Prediction of Energy Resolution in the JUNO Experiment. *arXiv: 2405.17860* (2024).

141. Kuraray. Plastic Scintillator Fibres. last accessed on 2024-08-28. https://www.kuraray.com/uploads/5a717515df6f5/PR0150_psf01.pdf.

142. Kuraray. Multianode photomultiplier tube assembly. last accessed on 2024-08-28. https://www.hamamatsu.com/eu/en/product/optical-sensors/pmt/pmt-assembly/metal-package-type/H7546B-100.html.

143. Lin, T. *et al.* Simulation software of the JUNO experiment. *The European Physical Journal C* **83,** 382 (2023).

144. Blin, S., Barrillon, P. & de La Taille, C. MAROC, a generic photomultiplier readout chip. *Journal of Instrumentation* **5,** C12007 (2010).

145. Lipiński, M. *et al.* White rabbit: a PTP application for robust sub-nanosecond synchronization. *2011 IEEE International Symposium on Precision Clock Synchronization for Measurement, Control and Communication* (2011).

146. Analog Devices. AD9629 Datasheet. last accessed on 2024-08-28. https://www.analog.com/en/products/ad9629.html#product-overview.

147. Ullrich, T. & Xu, Z. Treatment of errors in efficiency calculations. *arXiv:0701199* (2007).

148. Dracos, M. The OPERA Target Tracker Technical Design Report. last accessed on 2024-08-28. http://sbgopera.in2p3.fr/general/TDR/target_tracker.htm#tthFtNtAAF.

149. Rico, L. Track reconstruction for the Top Tracker of the JUNO Neutrino experiment. *HAL:tel-04103506* (2022).

150. Landau, L. On the energy loss of fast particles by ionization. *Journal of Physics* **8,** 201–205 (1944).

151. Hancock, S. *et al.* Energy loss and energy straggling of protons and pions in the momentum range 0.7 to 115 GeV/c. *Physical Review A* **28,** 615 (1983).

152. Pernegger M. Friedl, R. langaus.C: Convoluted Landau and Gaussian Fitting Function. last accessed on 2024-08-28. https://root.cern/doc/master/langaus_8C.html.

153. Baldini, W. *et al.* Measurement of parameters of scintillating bars with wavelength-shifting fibres and silicon photomultiplier readout for the SHiP Muon Detector. *Journal of Instrumentation* **12,** P03005 (2017).

154. Zhang, H. *et al.* Design and test for muon detectors based on extruded scintillator and SiPM. *arXiv:2312.02553* (2023).

155. Gonzalez, G. *et al.* Double Chooz θ_{13} measurement via total neutron capture detection. *Nature Physics* **16,** 558–564 (2020).

156. Bak, G. *et al.* Measurement of reactor antineutrino oscillation amplitude and frequency at RENO. *Physical Review Letters* **121,** 201801 (2018).

157. Bellini, G. *et al.* Cosmogenic Backgrounds in Borexino at 3800 m water-equivalent depth. *Journal of Cosmology and Astroparticle Physics* **2013,** 049 (2013).

158. Abe, S. *et al.* Production of radioactive isotopes through cosmic muon spallation in KamLAND. *Physical Review C* **81,** 025807 (2010).

159. Triangular Universities Nuclear Laboratory (TUNL), the Nuclear Data Evaluation Group. last accessed on 2024-08-28. https://nucldata.tunl.duke.edu.

160. Yang, C.-F. *et al.* Reconstruction of a muon bundle in the JUNO central detector. *Nuclear Science and Techniques* **33,** 59 (2022).

161. Hagner, T. *et al.* Muon-induced production of radioactive isotopes in scintillation detectors. *Astroparticle Physics* **14,** 33–47 (2000).

162. Kudryavtsev, V. Muon simulation codes MUSIC and MUSUN for underground physics. *Computer Physics Communications* **180,** 339–346 (2009).

163. Ferrari, A. *et al.* FLUKA: A multi-particle transport code (Program version 2005) (2005).

164. Allison, J. *et al.* Geant4 developments and applications. *IEEE Transactions on nuclear science* **53,** 270–278 (2006).

165. An, F. *et al.* Measurement of electron antineutrino oscillation based on 1230 days of operation of the Daya Bay experiment. *Physical Review D* **95,** 072006 (2017).

166. De Kerret, H. *et al.* Yields and production rates of cosmogenic ^{9}Li and ^{8}He measured with the Double Chooz near and far detectors. *Journal of High Energy Physics* **2018,** 1–20 (2018).

167. Lee, H. *et al.* Measurement of cosmogenic ^{9}Li and ^{8}He production rates at RENO. *Physical Review D* **106,** 012005 (2022).

P. S. Deshan Sandanayake

The Top Tracker of the JUNO neutrino experiment: Mitigating atmospheric muon-induced backgrounds

JUNO est une expérience de scintillation liquide souterraine à venir avec une masse cible de 20 kton et une résolution énergétique de 2,95 % à 1 MeV, visant à déterminer l'ordre de masse des neutrinos. Le Top Tracker, un détecteur à trois couches de bandes de scintillateur plastique, suit les muons atmosphériques avec une grande précision pour caractériser le bruit de fond induits par les muons qui pourraient affecter les objectifs physiques de JUNO.

Dans cette thèse, les performances des systèmes électroniques du Top Tracker ont été validées par des tests dédiés. Ces performances ont été déterminées dans des conditions réalistes en utilisant des mesures de muons atmosphériques faites avec le prototype du Top Tracker.

À l'aide de simulations de Monte Carlo, des modèles basés sur les données pour mesurer le fond ^{9}Li/^{8}He ont été étudiés. Les capacités de reconstruction des muons du Top Tracker permettent d'estimer l'incertitude du spectre énergétique du ^{9}Li/^{8}He à mieux de 10%, répondant aux exigences de JUNO pour la mesure de l'ordre de masse des neutrinos.

Mots-clés : JUNO, ordre de masse des neutrinos, Top Tracker, électronique, ^{9}Li/^{8}He fond.

JUNO is an upcoming underground liquid scintillator experiment with a 20 kton target mass and an energy resolution of 2.95% at 1 MeV, aimed at determining the neutrino mass ordering. The Top Tracker, a three-layer array of plastic scintillator strips, tracks atmospheric muons with high precision to mitigate muon-induced backgrounds that could impact JUNO's physics goals.

In this thesis, the performance of the Top Tracker electronics was validated through dedicated tests. Their performance was demonstrated under realistic conditions using atmospheric muon measurements with the Top Tracker prototype.

Using Monte Carlo simulations, data-driven templates for measuring the ^{9}Li/^{8}He background were studied. The Top Tracker's muon reconstruction capabilities allow for estimating the ^{9}Li/^{8}He energy spectrum better than 10%, meeting JUNO's requirements for neutrino mass ordering sensitivity.

Keywords: JUNO, neutrino mass ordering, Top Tracker, electronics, ^{9}Li/^{8}He background.